Politecnico di Bari

Department of Mechanics, Mathematics and Management
MECHANICAL AND MANAGEMENT ENGINEERING

Ph.D. Program
SSD: ING-IND/16 – MANUFACTURING TECHNOLOGY AND SYSTEMS

Final Dissertation

Monitoring and sustainability assessment of the Direct Laser Metal Deposition process

by
MARCO MAZZARISI

Referees:

Prof.ssa Fabrizia CAIAZZO

Prof. Giampaolo CAMPANA

Supervisors:

Prof.ssa Sabina Luisa CAMPANELLI

Prof. Michele DASSISTI

Coordinator of Ph.D. Program:
Prof. Giuseppe Pompeo DEMELIO

Course n°33, 01/11/2017 - 31/12/2020

ABSTRACT

The advent of the Industry 4.0 paradigm has upset the Italian and global industrial sector. Thanks to it, increasing attention is being paid to innovation, digitization and sustainability of production processes. The concept of industrial production has radically changed so much until calling this current historical period the "fourth industrial revolution".
One of the seven pillars of the Industry 4.0 paradigm is Additive Manufacturing (AM). Within this ecosystem, AM plays a key role in the development and production of prototypes and final components, characterised by extreme customization and complex geometries, which cannot be achieved by means of traditional production techniques.
This innovative technology contrasts with the traditional conception of the production processes, which has characterised the last few centuries. The idea of producing components not by subtracting material from a bulk, but by selective addition, inexorably changes all the main principles of industrial production. AM has not only changed the way of producing, but the whole production and distribution chain connected to it, starting from the supply chain for raw materials, up to ad-hoc production and distribution by makers.
All of this has been possible thanks to the concomitant development of mechanics, robotics, sensors and software design fields. The most recent innovations in these sectors have been combined in the various technologies that make up the AM world, decreeing its worldwide success and allowing the creation of components, not imaginable up to 50 years ago. These indisputable potentials have attracted the attention of various industrial sectors, including architectural, aerospace, automotive and biomedical design.
Currently, Direct Laser Metal Deposition (DLMD) is undoubtedly among the AM processes that are gaining more interest from the scientific and industrial sectors. This technology uses the potentiality and flexibility given by a laser beam to produce, layer by layer, free-form 3D components or functionally recovered worn components. The capability to process a wide selection of materials (metallic, polymeric and ceramic) is leading to the development of components characterised by extreme performances. However, this technology has only a few decades of life behind it, still has several critical issues that characterise it, and that the scientific world is trying to solve.
The present doctoral thesis tries to face, with a rigorous scientific method, the challenges that still preclude the diffusion of the DLMD on an industrial level.
The first chapters start with a careful analysis of the state of the art in the Additive Manufacturing sector. Then, focusing on an in-depth study of DLMD technology, this work examines the components of the system, analyses the workable materials and the main feasible applications. After this indispensable survey of the state of the art, attention shifted to the focal points of the doctoral activities.
Different modelling practices related to the DLMD process were analysed. The main parameters involved in the process were identified and their effects on the mechanical characteristics and quality of the deposition were evaluated. The different deposition models of single traces were catalogued according to the methodology and the pursued objectives. A phenomenological model was developed, which correlate the main process parameters to the quality of the deposition, in an efficient and computationally convenient way.
Further process parameters involved in the production of multilayer components were investigated, which incorrect setting may lead to process failure. An innovative method was therefore evaluated to mitigate variations in the working distance, by varying the laser spot dimension.
The fourth chapter of the thesis is dedicated to the monitoring of the process. DLMD is a very flexible but also extremely delicate and complex technology. Nowadays, the search for the quality of components inexorably passes through a rigorous process control that may ensure excellent working conditions. The in-process and post-process monitoring methods applied to the technology were then analysed and classified.
Thanks to collaborations with external research centres, such as the ENEA centre of Brindisi, it was possible to carry out an in-depth thermal monitoring campaign of single-pass and multi-pass depositions. The influence of process parameters and deposition strategies on the thermal field generated during the processing of nickel-based superalloy, which has a significant influence on the final product quality is highlighting.
The DLMD process was also monitored by an optical method, via a coaxial CCD camera mounted on the laser head, capable of visualizing the molten pool and detect the geometric changes during processing.
The quality of the laser deposition was also evaluated in a post-process step by ultrasonic techniques, which are useful for mechanically characterizing the specimens and identifying some deposition defects.
In the last chapter of the thesis, the sustainability of the DLMD processes is assessed. First of all, an analysis of the literature was carried out to detect works related to the AM domain and methods for assessing economic, social and environmental impacts. Considerable differences with respect to traditional production techniques were discovered, which

under certain conditions, make the AM techniques the best choice from various points of view. Several techniques for assessing sustainability were explored, especially for the assessment of the environmental impact. It is highlighted that some of them are now globally recognized, while others are currently under development, albeit showing considerable advantages. Starting from the last point, an Exergetic Analysis was finally developed on the prototype DLMD system present in the laboratories of the Department of Mechanics, Mathematics and Management (DMMM) of the Polytechnic University of Bari.

SOMMARIO

L'avvento del paradigma dell'Industria 4.0 ha stravolto il settore industriale italiano e mondiale. Grazie ad esso si sta rivolgendo una crescente attenzione all'innovazione, digitalizzazione e sostenibilità dei processi produttivi. Il concetto stesso di produzione industriale si sta pian piano modificando radicalmente, tanto da denominare questo periodo la "quarta rivoluzione industriale".
Uno dei sette pilastri fondanti del paradigma della Industria 4.0 è l'Additive Manufacturing (AM). All'interno di questo ecosistema, l'AM gioca un ruolo chiave per lo sviluppo e la produzione di prototipi e componenti finali, caratterizzati da un'estrema personalizzazione e da geometrie complesse, irrealizzabili con le tradizionali tecniche produttive.
Questa tecnologia innovativa si contrappone alla concezione tradizionale di processo produttivo, che ha contraddistinto gli ultimi secoli. L'idea di produrre componenti non per sottrazione di materiale da un grezzo di partenza, ma per selettiva aggiunta, stravolge inesorabilmente tutti i principi cardine della produzione industriale. L'AM non ha modificato solo il modo di produrre, ma tutto la catena di produzione e distribuzione ad essa collegata, partendo dalla supply chain per le materie prime, fino alla produzione e distribuzione ad-hoc da parte dei makers.
Tutto ciò si è potuto realizzare grazie al concomitante sviluppo dei settori della meccanica, robotica, sensoristica e della progettazione software. Le più recenti innovazioni in questi settori si sono combinate nelle diverse tecnologie che compongo il mondo dell'AM, decretandone il successo a livello mondiale e permettendo la realizzazione di componenti, inimmaginabili fino a 50 anni fa. Queste indiscutibili potenzialità hanno attratto l'attenzione di diversi settori industriali, tra i quali spiccano la progettazione architettonica, aerospaziale, automobilistica e biomedicale.
Attualmente, tra i processi AM che stanno riscuotendo maggiore interesse da parte del settore scientifico ed industriale, vi è senza alcun dubbio la Direct Laser Metal Deposition (DLMD). Questa tecnologia utilizza le potenzialità e la flessibilità date da un fascio laser per produrre, strato per strato, componenti 3D free-form o recuperare funzionalmente componenti usurati. La capacità di poter lavorare una selezione molto ampia di materiali (metallici, polimerici e ceramici) sta portando allo sviluppo di componenti caratterizzati da prestazioni estreme. Tale tecnologia, però, avendo alle spalle pochi decenni di vita, ha ancora diverse criticità che la caratterizzano e che il mondo scientifico sta tentando di risolvere. La presente tesi di dottorato ha cercato di affrontare, con rigoroso metodo scientifico, le sfide che ancora impedisco la diffusione a livello industriale del DLMD.
Si è partiti nei primi capitoli da un'attenta analisi dello stato dell'arte del settore dell'Additive Manufacturing. Concentrandosi successivamente sullo studio approfondito della tecnologia DLMD, sviscerandone i componenti che costituiscono il sistema, analizzando i materiali utilizzabili e le principali applicazioni realizzabili. Dopo quest'imprescindibile analisi dello stato dell'arte, l'attenzione si è spostata sui punti focali dell'attività di dottorato.
Si sono analizzate le diverse modellazioni relative al processo DLMD. Sono stati individuati i principali parametri coinvolti nel processo e valutati i loro effetti sulle caratteristiche meccaniche e la qualità della deposizione.
Sono stati catalogate le diverse modellazioni di deposizione di singole tracce in funzione della metodologia e degli obiettivi perseguiti. Si è deciso quindi di elaborare un modello fenomenologico che possa correlare i principali parametri di processo alla qualità della deposizione, in maniera efficiente e computazionalmente conveniente.
Ci si è rivolti successivamente agli ulteriori parametri di processo coinvolti nella produzione di componenti multilayer, il cui errato settaggio può comportare il fallimento della produzione. È stato quindi valutato un metodo innovativo per mitigare le variazioni della distanza di lavoro, mediante variazione dello spot laser.
Il quarto capitolo della tesi è dedicato al monitoraggio di processo. Il DLMD è una tecnologia molto flessibile ma anche estremamente delicata e complessa. Al giorno d'oggi la ricerca della qualità dei componenti, passa inesorabilmente da un controllo del processo che possa assicurare ottime condizioni di lavoro.
Sono stati quindi analizzati e classificati i metodi di monitoraggio in-process e post-process applicati alla tecnologia. Grazie a collaborazioni con centri di ricerca esterni, quali l'ENEA di Brindisi, è stato possibile eseguire un'approfondita campagna di monitoraggio termico di deposizioni a singola passata e multi passata. Evidenziando l'influenza dei parametri di processo e delle strategie di deposizione sul campo termico, che ha una notevole influenza sulla qualità del prodotto finale.
Il processo di DLMD è stato monitorato anche con metodologia ottica, tramite una videocamera coassiale solidale con la testa laser, in grado di visualizzare la pozza fusa e di metterne in evidenza le modifiche geometriche nel corso della lavorazione.
La qualità della deposizione laser è stata valutata anche post-process con tecniche ultrasoniche, che si rivelano utili per caratterizzare meccanicamente i provini realizzati e identificare alcuni difetti.

Nell’ultimo capitolo della tesi è stata valutata la sostenibilità delle lavorazioni DLMD. Innanzitutto, è stata effettuata un’analisi della letteratura per mettere in mostra i lavori relativi al mondo AM e i metodi di valutazione degli impatti di tipo economico, sociale ed ambientale. Sono state scoperte ragguardevoli differenze rispetto alle tradizionali tecniche produttive, che in determinate condizioni di produzione, rendo le tecniche AM superiori sotto diversi punti di vista. Sono state sviscerate le diverse tecniche di valutazione della sostenibilità, utili a valutare soprattutto l'impatto ambientale. Si è messo in evidenza come alcune siano ormai riconosciute a livello globale, mentre altre siano in fase di sviluppo seppur mostrando notevoli vantaggi. Partendo da quest’ultimo punto, si è infine sviluppata un'analisi exergetica sul sistema prototipale presente nei laboratori del Dipartimento di Meccanica, Matematica e Management (DMMM) del Politecnico di Bari.

TABLE OF CONTENTS

TABLE OF FIGURES

1 INTRODUCTION ON ADDITIVE MANUFACTURING

The Additive Manufacturing (AM) was defined by the ISO/ASTM standard as "a process of joining materials to create objects using data from a 3D model, usually layer-by-layer, as opposed to material subtraction and moulding production methods" such as machining (Gibson et al., 2015).
AM or 3D printing are names of a category of processes in which a three-dimensional object is created using a filler material (in form of liquid or powder grains)that is melted and solidified under computer control. As shown in Figure 1, additive manufacturing is a completely different procedure compared to traditional subtractive processes, in which starting from a bulk raw material, the desired shape is reached by subtraction (Lundbäck and Lindgren, 2017). The technologies that are part of the AM sector are different, but all are based on the principles of rapid prototyping.
Rapid Prototyping (RP) is a concept born different decades ago, which differs from traditional production techniques of prototypes, which are a first or preliminary version of a component from which other forms are developed. RP techniques operate on an inverse conceptual base, in which the object is built by addition of material layer by layer, stratifying and stacking the "slices" that compose the output. The possibility of obtaining even very complex shapes, impossible to achieve with traditional processes, is one of the main advantages of this method. In fact, in some cases, it is called Layered Manufacturing. The rapid prototyping is usually used in the industry for the production of on-demand prototypes, following the evolution of design until the implementation of the final composition (Bak, 2003).
Therefore, RP refers to the production of preliminary components, characterised by poor quality compared to the final component. With the advancement of technology, the development of skills and new devices, it was possible to improve and expand the production process characteristics: precision, repeatability, and range of adoptable materials. As a result, this technique was introduced for the production of end-use objects. The term no longer adequately describes some of the newer applications of the technology and was modified in recent years in Rapid Manufacturing (RM). Hence, RM or AM refer to the use of techniques for the on-demand production of final products by layered manufacturing (Hopkinson et al., 2006).

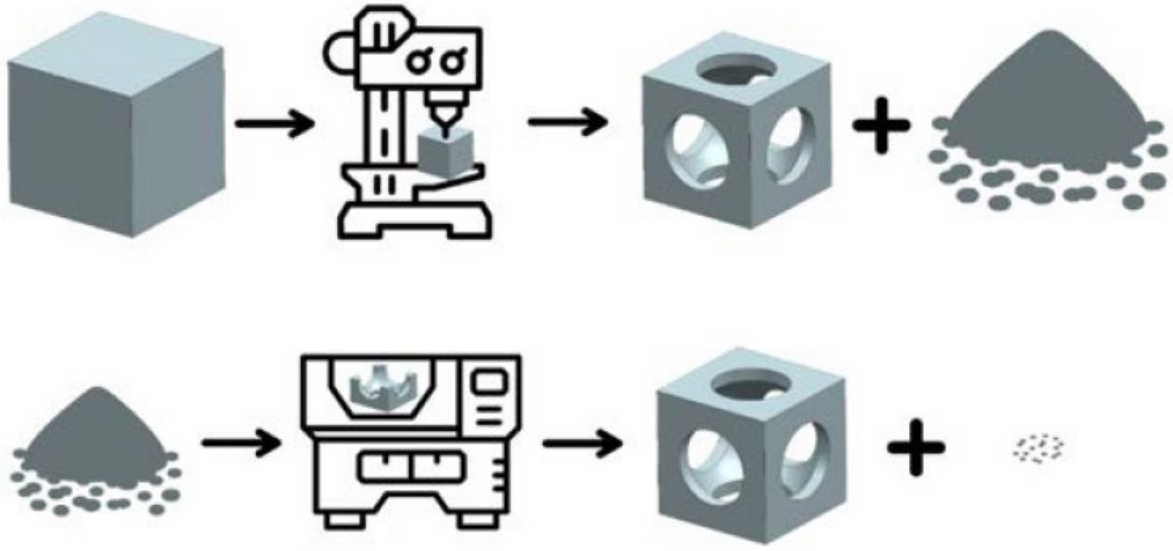

Figure 1 Illustration of conventional subtractive manufacturing and additive manufacturing (Lundbäck and Lindgren, 2017).

Rapid prototyping concerns very different technologies for the production of components intended for the most disparate fields of the market. Despite this, the phases that lead to the realization of prototypes (in the case of RP) or final products (in the case of RM) are almost the same (Khorram Niaki and Nonino, 2018), as shown in Figure 2:

1. **From CAD to STL file.** This is a pre-prototype phase and consists of generating of the STL file and its verification. The STL (Standard Triangulation Language) file is a graphic standard that describes the 3D object by decomposing its surfaces. Basically, the surfaces of the piece are entirely broken down into triangular-shaped meshes. Approximately the number of triangles is greater, the better the approximation of the surface is requested. The STL file generation phase can be split into two sub-processes: realization by means of CAD software or through the use of reverse engineering techniques. While the first method provides for a fully CAD-

driven implementation, the second method involves the use of a scanner that returns a certain number of points belonging to the surfaces of the object, in slang "point cloud". The cloud is processed using dedicated software to obtain the three-dimensional mathematical model.

2. **Management of the STL file.** Useful to verify that the file is free from errors. The control is performed through dedicated software, which identifies and corrects the errors present, and also allows the possibility to design supports for the cantilevered parts and orient the objects (an operation that can strongly influence the final result). This software also performs and modifies the slicing process, i.e. generate the slices superimposed on each other to generate the final object. Slicing is a critical operation because it determines the surface characteristics of the part and is closely linked to the production features of the technology employed. This operation can be uniform or "adaptive" when the thickness of the slices is variable and is chosen according to the curvature of the surface to better arrange the final geometry and reducing the staircase effect (the inclined surfaces are approximated by steps).
3. **Build of the component.** It consists of sending the STL or compatible files to the machine and proceeding with the deposition of the material layer by layer until the object is completed. This phase can last many hours depending on the size of the object (in particular the height of the component), therefore an accurate choice of the orientation of the object is essential both for the surface finish and to reduce the overall time and processing cycles.
4. **Post-processing.** It usually consists of manual operations which purpose is to remove the printed object from the machine, free it from the support and excess material and possibly carry out further finishing operations. These can be simple operations, when it is necessary only to remove the excess powders from the prototype, or more complex, in case it is necessary to use a pressure washer or a milling machine to remove supports. It is also possible to improve the surface quality by resorting to surface treatments such as the use of abrasive paper or painting.

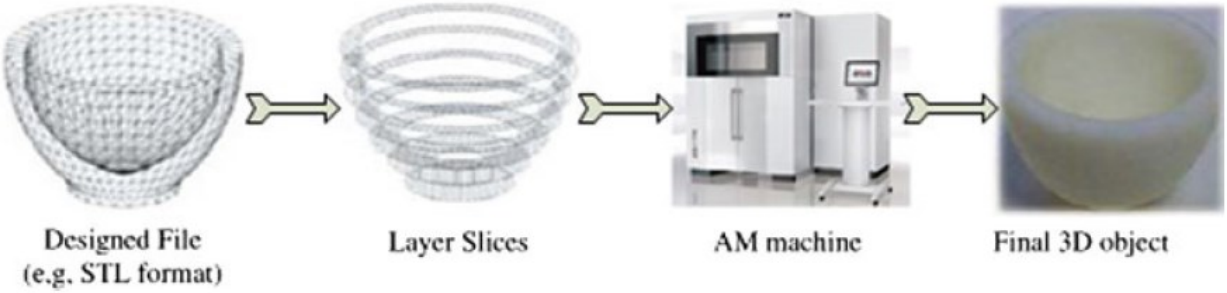

Figure 2 General additive manufacturing process(Khorram Niaki and Nonino, 2018)

1.1 History and technological background

The development of Additive Manufacturing technologies has rapidly progressed since a primordial technology that took hold on the world stage in the 1960s. However, it was in 1981 when Hideo Kodama of Nagoya Municipal Industrial Research Institute devised two methods for the additive manufacturing of three-dimensional plastic components by photo-curing of a thermosetting polymer, where the exposure of the area to UV rays was controlled by a fiber transmitter scan (Kodama, 1981). Traces of these technologies began to appear already in the late 1960s, albeit in a very veiled way. The first attempt to fabricate solid objects using photopolymer materials was at the Battelle Memorial Institute. DuPont invented the photopolymer resins used in the process, a type of polymer that changes its properties when exposed to light. The process involved two laser beams with different wavelengths operating in a container full of resin, solidifying the material at the point of intersection. As stated by Wohlers, in the early 1970s, Formigraphic Engine Co. employed the dual-laser approach in their first commercial laser prototyping project. In 1974, Formigraphic presented the 3D object production using a rudimentary system. In the late 1970s, Dynell Electronics Corp. awarded several patents on “Solid photograph”. This technology produced a 3D object by cutting cross-sections of thin layers using a milling machine or laser and then stacking it to form the final object (Wohlers, 2014).

Hideo Kodama was among the first inventors of the single beam laser polymerization method. In the early 1980s, publications and discoveries followed one another at a fast pace. On July 16, 1984, Alain Le Méhauté, Olivier de Witte, and Jean Claude André filed their patent for the stereolithography process. Three weeks later, Chuck Hull of 3D Systems

Corporation filed his patent for a stereolithography fabrication system, in which layers are added by photopolymerizing polymers by ultraviolet light lasers. Hull's contribution was the STL file format and digital cut and fill strategies common to many processes today.

AM processes for sintering or melting metals usually went through their system names in the 1980s and 1990s. At the time, metal processing was performed using traditional processes (casting, stamping and machining). The growing automation of the industrial sector led to the development of tools capable of working within a 3D work area, building a component with the desired shape from a mass of raw material following tool patterns. This idea was initially associated with machining processes, such as CNC milling. Although, automated metal addition techniques, which would later be called additive manufacturing, were starting to question that assumption. In the mid-1990s, new techniques for depositing materials were developed at Stanford University and Carnegie Mellon University, including casting and spraying processes. Compatible materials have also become more common, allowing for a disruptive development of the technology.

It is important to observe the price of AM systems during this period. In February 1999, 3D Systems launched its SLA 7000 system (stereolithography apparatus) for approximately $800,000, making it the most expensive polymer-based AM system of the time. Today, developers are attempting to lower the price of desktop 3D printers so that they are affordable for end consumers.

The 2010s were the first decade in which metal components such as engine brackets were produced by AM techniques. Nowadays, casting and machining are still prevalent in metalworking, but AM is starting to make significant strides and, with the benefits of design for additive manufacturing, engineers are beginning to be clear about the significant room for improvement in the industry (Khorram Niaki and Nonino, 2018).

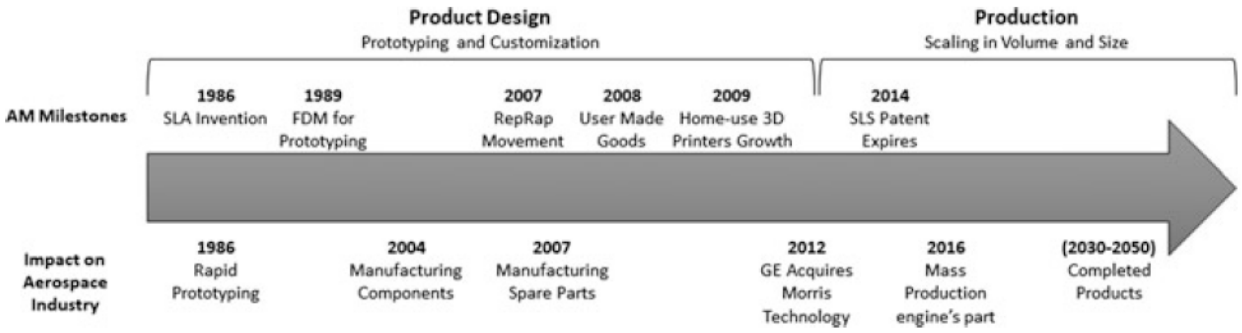

Figure 3 AM technology evolution and aerospace industry (Khorram Niaki and Nonino, 2018).

1.2 Industry 4.0

The manufacturing sector has evolved extraordinarily over the course of history. Several milestones were set and characterised these periods. In 1700, the First Industrial Revolution that involved textile manufacturing, with the steam energy and the mechanization of production. The introduction of electricity and oil as new energy sources and the idea of mass production in the following century, started the Second Industrial Revolution. In the Third Industrial Revolution (known as the Digital Revolution), during the second half of the twentieth century, a whole series of transformation processes arose, which involved the automation and computerization of the production and the transformation of the socio-economic condition of the population (Bonilla et al., 2018; Stock and Seliger, 2016; Tay et al., 2018). In the new millennium, the focus on process technology innovation and sustainability has increased exponentially, giving rise to the Industry 4.0 paradigm, defined for the first time in the Hannover Fair in 2011 in Germany. The core of the paradigm is the digitalization, which concerns all sectors of the economy: from production to consumption, from transport to telecommunications, from the primary sector to all areas of services. This led to an easy exchange of information and system integration, with manufacturing products and machines acting simultaneously and smartly (Butt, 2020; Vaidya et al., 2018). Industry 4.0 is not just about the production system, but it also innovates in education, research and development. The paradigm encompasses several Key Enabling Technologies (KET) that are oriented toward automation and data exchange in manufacturing technologies and processes. These include several latest technological developments such as cyber-physical systems, digital twins, Internet of things, cloud computing, cognitive computing, and artificial intelligence, as shown in Figure 4.

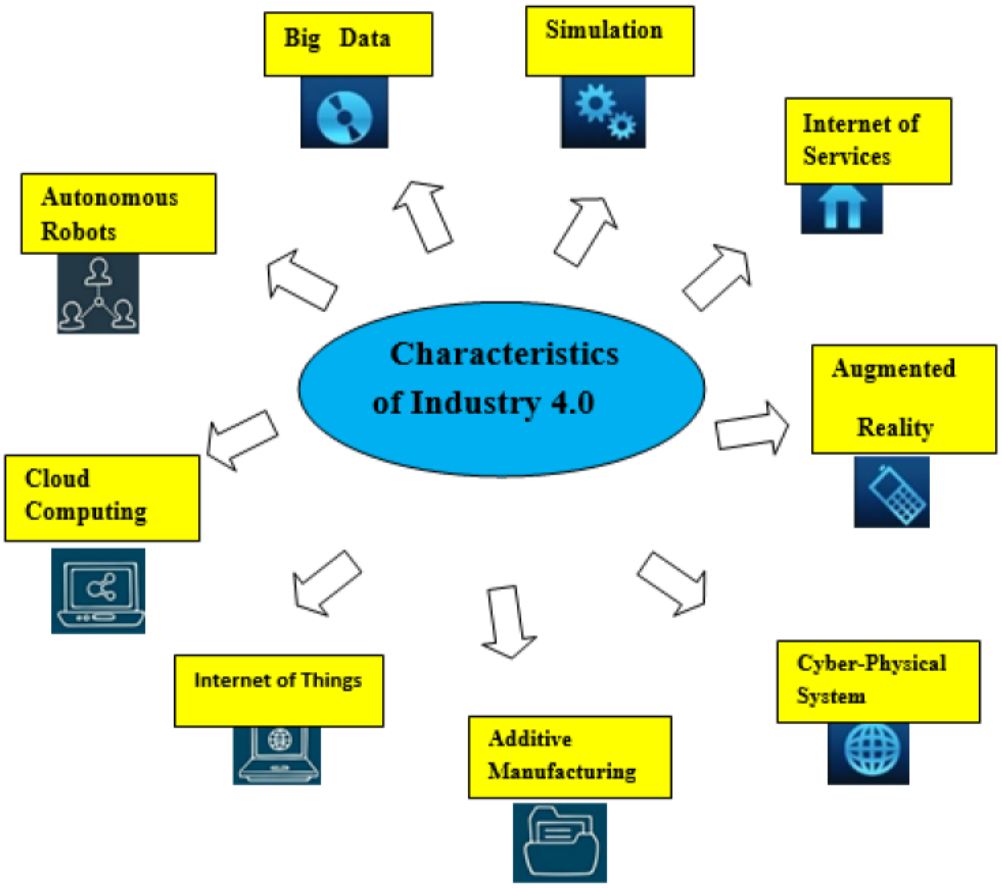

Figure 4 Key enabling technologies and characteristics of Industry 4.0 (Tay et al., 2018)

Among the KET of Industry 4.0, Additive Manufacturing (or 3D printing) is considered as a key factor for the implementation of the new production paradigm. This achieves requirements of Industry 4.0 such as customization, efficiency, quick delivery, waste reductions. In the Factory 4.0 ecosystem, AM plays an paramount role inside the Advanced Manufacturing Systems for the development of prototypes, or for producing customized components (Ghobakhloo, 2018). The concurrent development of hardware, software, and the intense research for adopting new materials has been key of success of AM technologies, so that multi-material components become possible, broadening the application field. It has in fact found applications in the fields of medicine, engineering, aerospace, automotive, design, food industry. This technology overcome the current barrier of mass production with personal and customized fabrication (Dilberoglu et al., 2017; Haleem and Javaid, 2019). However, AM still has room for improvement, especially in the implementation within the production chain, which could increase the economic benefits which are currently relatively low (Di Pierro et al., 2019).

1.3 Classification of AM technologies

The first classification of AM technologies came in the early 1990s, when Kruth categorized additive manufacturing processes from different points of view. According to the form of the building materials, he distinguished: liquid-based, discrete-based (powders), molten-based and solid-based systems. A second classification was made according to the construction method, which included 1D-channel, array-channel, and 2D-channel (Gao et al., 2015). Most recently, the International Organization for Standardization (ISO) and ASTM International (ISO and ASTM International, 2015) classified AM technologies into seven categories as shown in Table 1.

In this section, the AM technologies of polymers, metallic, and ceramic materials were analysed. However, it should be kept in mind that there are many other printable materials used in AM systems: natural fibers, sand, cement, and other biological materials (Gibson et al., 2015).

CATEGORIES	TECHNOLOGIES	PRINTED "INK"	POWER SOURCE	STRENGTHS / DOWNSIDES
Material Extrusion	Fused Deposition Modeling (FDM)	Thermoplastics, Ceramic slurries, Metal pastes	Thermal Energy	• Inexpensive extrusion machine • Multi-material printing • Limited part resolution • Poor surface finish
	Contour Crafting			
Powder Bed Fusion	Selective Laser Sintering (SLS)	Polyamides /Polymer	High-powered Laser Beam	• High Accuracy and Details • Fully dense parts • High specific strength & stiffness • Powder handling & recycling • Support and anchor structure • Fully dense parts • High specific strength and stiffness
	Direct Metal Laser Sintering (DMLS)	Atomized metal powder (17-4 PH stainless steel, cobalt chromium, titanium Ti6Al-4V), ceramic powder		
	Selective Laser Melting (SLM)			
	Electron Beam Melting (EBM)		Electron Beam	
Vat Photopolymerization	Stereolithography (SLA)	Photopolymer, Ceramics (alumina, zirconia, PZT)	Ultraviolet Laser	• High building speed • Good part resolution • Overcuring, scanned line shape • High cost for supplies and materials
Material Jetting	Polyjet / Inkjet Printing	Photopolymer, Wax	Thermal Energy / Photocuring	• Multi-material printing • High surface finish • Low-strength material
Binder Jetting	Indirect Inkjet Printing (Binder 3DP)	Polymer Powder (Plaster, Resin), Ceramic powder, Metal powder	Thermal Energy	• Full-color objects printing • Require infiltration during post-processing • Wide material selection • High porosites on finished parts
Sheet Lamination	Laminated Object Manufacturing (LOM)	Plastic Film, Metallic Sheet, Ceramic Tape	Laser Beam	• High surface finish • Low material, machine, process cost • Decubing issues
Directed Energy Deposition	Laser Engineered Net Shaping (LENS) Electronic Beam Welding (EBW)	Molten metal powder	Laser Beam	• Repair of damaged / worn parts • Functionally graded material printing • Require post-processing machine

Table 1 *Classification of additive manufacturing processes by ASTM International* (Gao et al., 2015).

1.3.1 Material extrusion

The material extrusion is an AM process that deposits a thermoplastic filament according to a toolpath in order to produce 3D components. Fused Deposition Modeling (FDM) technology was invented in the 1980s by Scott Crump. The process involves the use of wire that is melted and subsequently extruded through a nozzle, to print a cross-section of an object, moving vertically and reiterate the process until the object is completed. The most exploited materials in FDM are ABS, PLA, and PC (Polycarbonate), but it is possible to find innovative mixtures containing wood, stone, and filaments with rubbery characteristics. The support material often consists of a second material and is removable (or soluble) from the final component at the end of the manufacturing process. A schematic representation of the fused deposition process is displayed in Figure 5. The main drawback of the technology is the low resolution compared to other processes. It is therefore impossible to obtain a product ready for use, in case a surface finish is required. The finishing process is a slow procedure that sometimes takes days for more complex geometries. FDM technology is the most popular among desktop 3D printers and less expensive professional printers (Anakhu et al., 2018; Gibson et al., 2015).

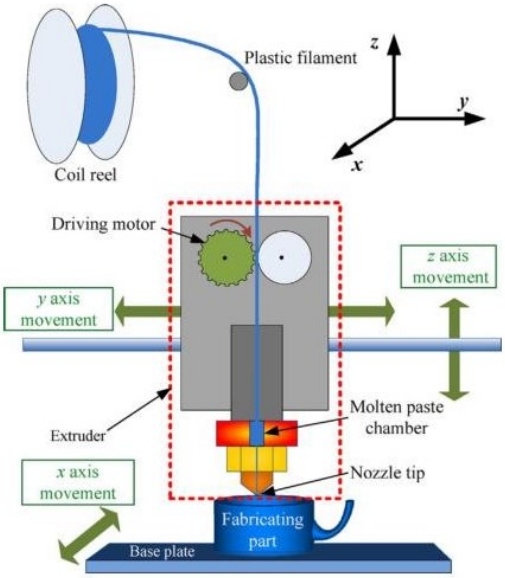

Figure 5 Schematic representation of the fused deposition process (Anakhu et al., 2018)

1.3.2 Powder bed fusion

In general, Powder Bed Fusion (PBF) techniques use an energy beam to selectively melt a powder bed. The process requires high temperatures to completely sinter or melt the powder. After the high-energy beam (laser for SLM, electron beam for EBM) melts the first layer of powder, following the digital model information, the work platform holding the powder bed is lowered and the roller (or cutter) passes across the workstation adding a new powder layer (see Figure 6). The energy beam scans the layers thanks to galvanometric mirrors (SLM) or magnetic deflection coil (EBM) and the process is repeated until the object is completed. The process can be used to work metal, ceramic, and polymer blends, in general, using polyamides and polymer composites. Direct Metal Laser Sintering (DMLS), Selective Laser Melting (SLM) and Electron Beam Melting (EBM) are the most popular PBF techniques. The process is carried out in a vacuum (EBM) or inert environment using nitrogen (SLM) to avoid the oxidation of metals. The DMLS realizes sintering at high temperatures, such as fusion at the "solid-state" of powder particles without melting. Parts produced by using SLM and EBM are completely dense with high mechanical characteristics. A scheme of powder bed system is shown in Figure 6 (Bhavar et al., 2017; Gibson et al., 2015).

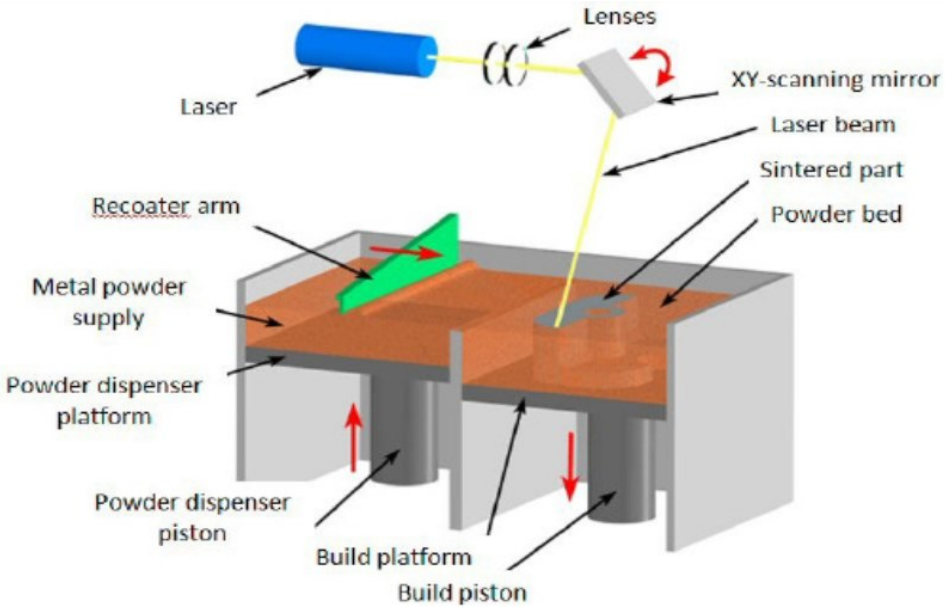

Figure 6 Laser based powder bed fusion technology (Bhavar et al., 2017).

1.3.3 Vat photopolymerization

The Vat photopolymerization (VP) category is usually utilized for conceptual and functional polymer prototypes. It uses an ultraviolet laser, focused on a photo-polymerizable liquid (radiation-curable resins) to build a solid object. The VP adopt several methods to illuminate photopolymers, including vector scan point-wise processing (using a galvanometric mirror), mask projection layer-wise processing, and two-photon approaches that focus on the same point to polymerize the part. The first patent related to the VP category was the Stereolithography (SLA). This is the most widely used additive system and was the first commercialized AM process. Invented by Charles Hull it was introduced by 3D Systems, Inc. in 1987. The SLA process uses a CAD file to guide the laser into a selected portion of the surface of a resin vat, which is cured and solidified on the platform. The platform is then lowered (typically 100 μm) and a new layer of liquid resin is deposited on the previous layer (see Figure 7). SLA can create very precise and detailed polymer objects with a relatively good surface finish. Furthermore, with this process, it is possible to create components using a number of different materials and it is easily integrated with other operations within a production chain. It can produce both semi-finished products from bulk and existing components. SLA is also considered a process with short lead times. The main limitations of the technology are given by the supports, which must be removed by consuming raw materials and increasing production times, and by the poor long-term stability of the components, which limits their application in prototyping. Another disadvantage of SLA is the long and complex procedure of replacing different type of resin (Chartrain et al., 2018; Gibson et al., 2015).

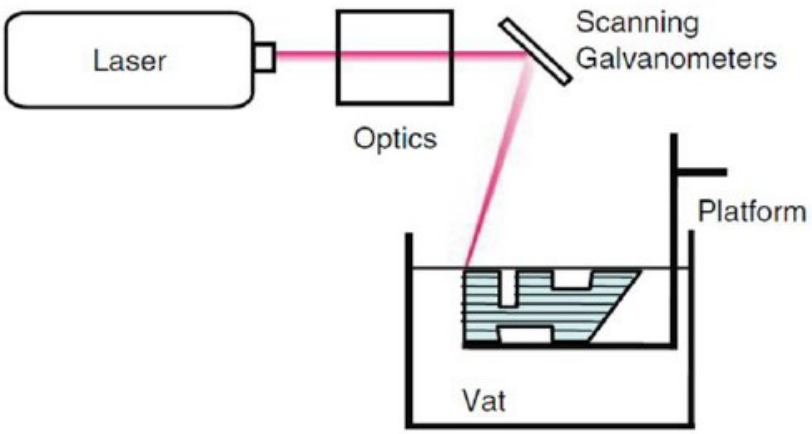

Figure 7 Vat polymeralization scheme (Chartrain et al., 2018).

1.3.4 Material jetting

Material Jetting (MJ) technology deposits droplets of photopolymer materials (continuously or on-demand) through multiple nozzles, in thin layers on a construction platform. Two different photopolymer materials are used for the construction, one for the main component and another gel-like material for the support. The layers are cured by UV lamps while the gel-like polymer supports the complexity of the geometry in the shell. The soluble gel (support material) is then removed by machining or water jet. Materials that can be processed by MJ technology are basically polymeric, but ceramic and metallic materials have also been recently investigated. The compatible materials are characterised by specific thresholds of printable viscosity, liquid density, or surface tension. One of the most representative systems is the Multi-Jet Modeling from 3D Systems. A graphic representation of the material jetting process is presented in Figure 8 (Gibson et al., 2015; Sireesha et al., 2018).

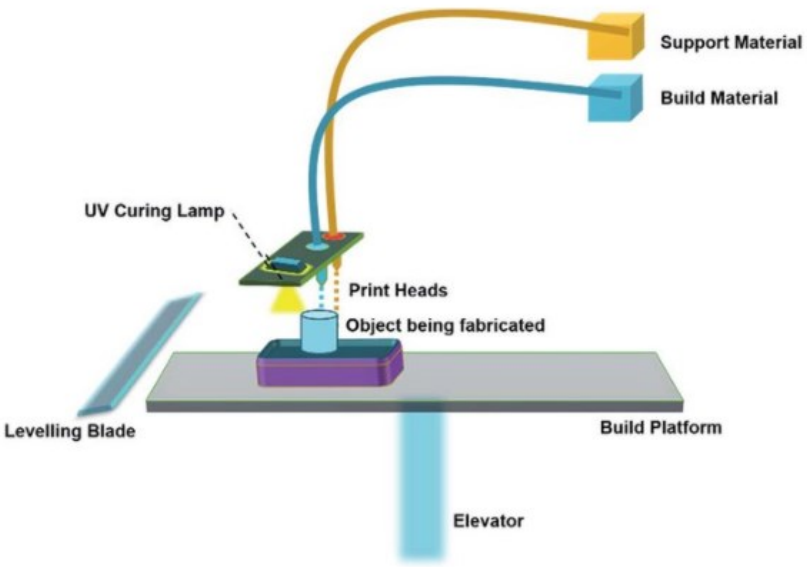

Figure 8 Schematic representation of the material jetting process (Sireesha et al., 2018)

1.3.5 Binder jetting

The leading exponent of the Binder Jetting category is 3D Printing (3DP), also known as Color Jet Printing (CJP), which combines powders and binders to create parts. The 3DP was developed by MIT. Each layer is created by spreading a thin layer of powder with a powder spreader that is selectively blended with a jet of binder droplets. The build plate is lowered to create the next level until the object is completed (see Figure 9). This process has been used to fabricate numerous metal, ceramic, and polymer components of any geometry for a wide range of applications. The BJ technology enabling to obtain slurries with higher solids loadings, thus parts with a better mechanical characteristic. Innovative compounds have been tested to make wood products. The 3DP can print in multicolour, directly in the mould during the construction process, thanks to a colour loader. The final model has then been extracted from the powder bed and, in some cases, an infiltration with liquid glue is performed. The infiltrants improve the definition of the colour and the mechanical characteristics of the piece. 3DP can provide architects a useful tool to quickly create a realistic model (Gibson et al., 2015; Sireesha et al., 2018).

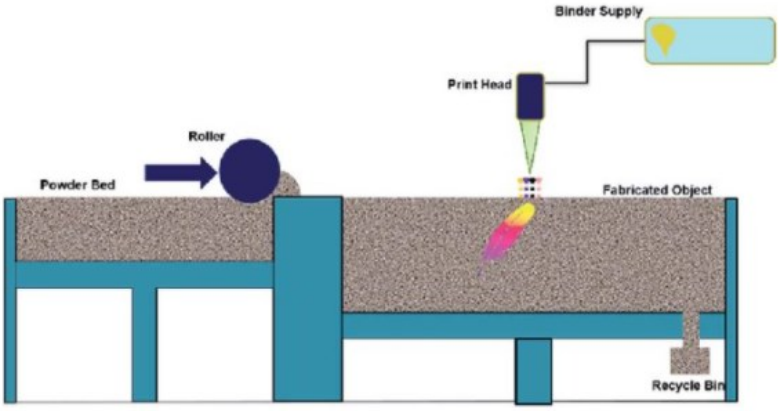

Figure 9 Schematic representation of binder jetting (Sireesha et al., 2018).

1.3.6 Sheet Lamination

Sheet Lamination is a category of rapid prototyping processes in which an object is built by stacking layers cut according to 3D model and then joined together. Michael Feygin invented the most famous sheet lamination system in 1985, the Laminated Object Manufacturing (LOM), which was commercialized by Helisys in 1991. LOM involves stacking layers of laser-cut material to create the final component. The system includes an x-y plotter device positioned above the mobile work surface, consisting of a laser or cutter, to create a layer from a sheet of material placed on the work surface. The

layers are bonded together by heat-sensitive adhesives. A roller or a fuser moves across the work surface applying pressure and heat, to allow the bonding of each layer. The layers are superimposed to form the final object and its resolution is defined by the thickness of the sheets. The LOM system has been used for both RP and RM but has fewer applications in final product manufacturing. The limitations, as other AM systems, involved the mechanical and thermal properties of the materials that are not homogeneous. Furthermore, the reproducibility of details and the life of small parts are relatively low. However, the main problem regards the complex geometries. For example, for those products with thin walls, post-processing is difficult, takes time, and can damage the object. Ultrasonic Additive Manufacturing (UAM) is an alternative sheet lamination system, which involves the production of the component by stacking thin metal sheets bonded together through a sonotrode. Rolling on the sheets, the device applies an orthogonal pressure and a vibration given by transverse oscillations at very high frequencies, which lead to the bonding of layers by plastic deformation and intimate contact. A schematic of the LOM process can be seen in Figure 10 (Gibson et al., 2015).

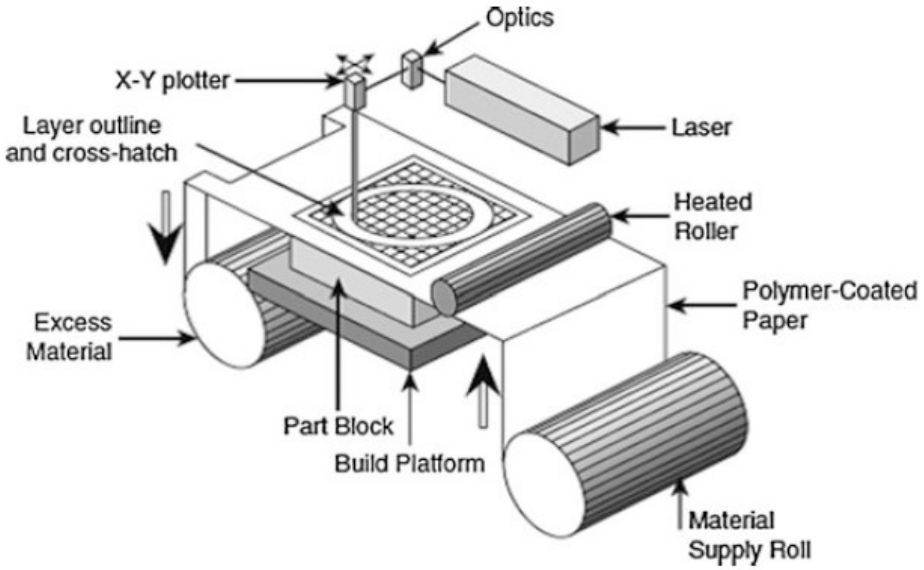

Figure 10 Schematic of the LOM process (Gibson et al., 2015).

1.3.7 Direct Energy Deposition

Direct Energy Deposition (DED) is an AM process in which a focused energy source is used to create a melt pool on a substrate. The filler material is injected by means of a nozzle and a shielding gas is usually adopted to prevent oxidisation. The feedstock material can be used in form of wire or powder (see Figure 11).

Although this technique can work employing polymers, ceramics, and metal matrix composites, it is predominantly used for metals. In the process both the filler material and the energy source can move, according to the paths, to define the desired shape. Depending on the mode of handling the terminals, it can have two main types of systems. In the first, the product remains stationary, and the deposition nozzle moves simultaneously with the energy beam. In the second case, the substrate is moving while the deposition head remains fixed. DED can achieve a theoretical material density of up to 99.9%. Thanks to local melting and rapid cooling, therefore, the microstructure resulting from this process consists of a fine grains and well-finished parts and shows a resistance comparable or superior to those created by casting. This process is used for creation of 3D components, repair of damaged parts and clading of existing surfaces having even complex geometries.

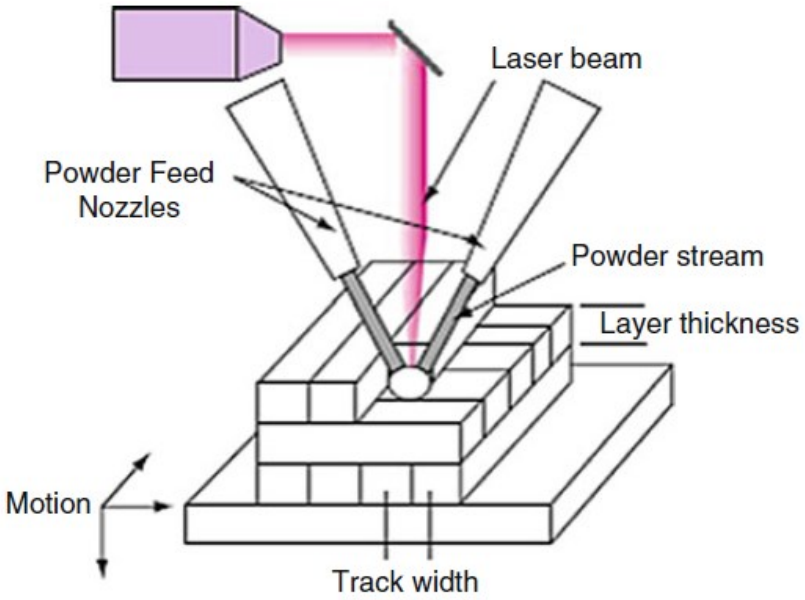

Figure 11 Schematic of a typical laser powder DED process (Gibson et al., 2015)

As shown in the graph in Figure 12, the DED covers a wide range of systems that can be classified as melt-based DED, which uses thermal energy sources, such as plasma, electric arc, electron beam, and laser beam, and kinetic energy-based DED, which utilizes the kinetic energy generated by a pump to deposit the metal powder (Dass and Moridi, 2019). This last category includes the DED system called Cold Spray. Instead, many systems belong to the melt-based DED technology. The Electron-Beam Additive Manufacturing (EBAM), implement a high energy focused electron beam to melt the feedstock metal material in a vacuum. EBAM is mainly used for manufacturing near-net shape parts. The Ion Fusion Formation (IFF) melts a metal wire or powder material by means of a plasma welding torch to create 3D components. The Wire Arc Additive Manufacturing (WAAM) works by melting metal wire using an electric arc as heat source, typically controlled by a robotic arm. It takes advantage of the principle of electric arc welding and the flexibility of the robotic arm to produce large-scale metal parts (Knezović and Topić, 2019).

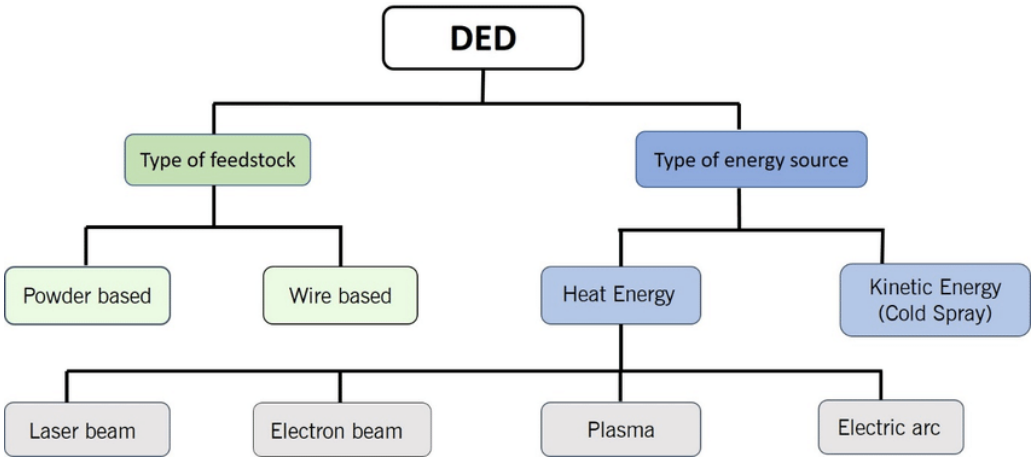

Figure 12 Classification of Directed Energy Deposition (DED) systems (Dass and Moridi, 2019).

The techniques that are having the most success in the scientific and industrial manufacturing sector in recent years are laser-based DED systems, thanks also to the enormous development that laser sources have had in last decades. This subcategory includes many systems and patents which will be extensively described in the following chapter.

2 DIRECT LASER METAL DEPOSITION PROCESS

The Direct Laser Metal Deposition (DLMD from now on) process is an innovative technology that combines laser technology, robotics, process control, powder metallurgy, and computer-aided design and manufacturing (CAD/CAM) (Steen and Mazumder, 2010). As shown in Figure 13, the DLMD system consists of a set of interconnected subsystems that normally consist of:

- *Control workstation*
- *Multi-axis CNC system*
- *Powder feed system*
- *Nozzle*
- *Laser system*

In addition to the main components, the DLMD system is equipped with auxiliary devices to carry out specific activities, such as:

- *Feedback control system*
- *Controlled atmosphere chamber*

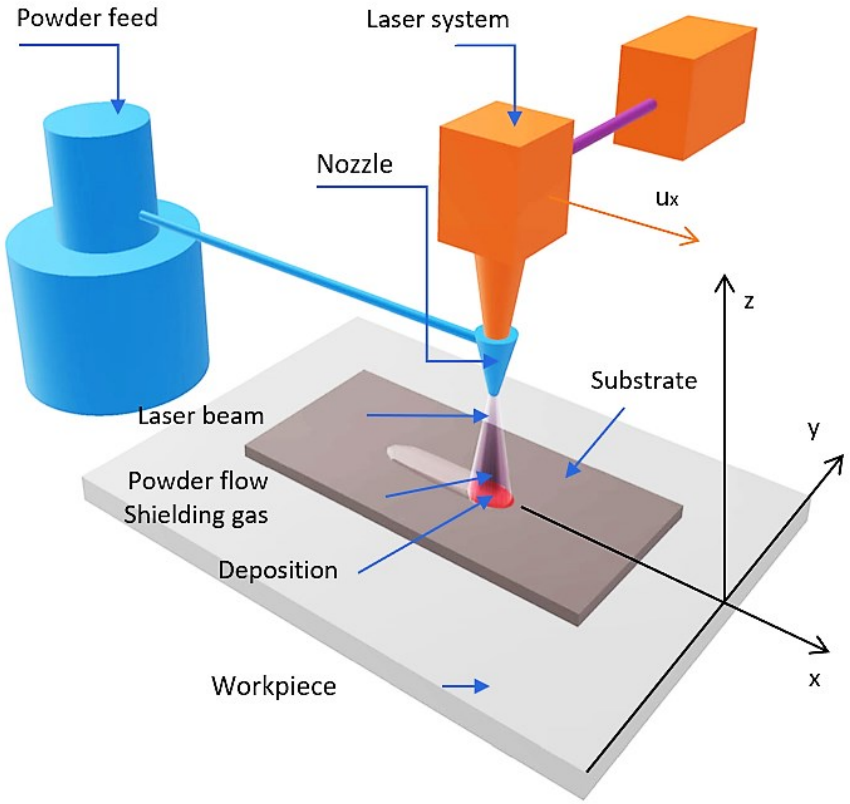

Figure 13 Schematic process of Direct Laser Metal Deposition.

2.1 The control workstation

The control workstation is a custom PC designed to monitor and control all the component of the DLMD system. This device is set to report any system alerts or errors, predisposing the related maintenance routines. It also receives data relating to the deposition process in CNC instructions format (G-code), derived from the 3D model developed by means of CAD/CAM software.

2.2 The multi-axis handling system

The multi-axis handling system determine position, speed, and motion path of the deposition head. The translation path is implemented using a CNC machine that converts a G-code obtained by slicing the STL model or directly

from the CAD/CAM software. The most adopted handling system for DLMD applications implement 3 - 5 axis gantry machine or multi-axis anthropomorphic robot.

2.3 Powder feeding system

The powder feed system has the purpose of delivering the metal powders in the working area and prevent dispersion into the environment. Generally, it consists of one or more containers, a powder feeder, sensors for the mass flow control, and the nozzle.

The powder flow that reaches the working area is regulated by the powder feeders. These devices take the powders from one or more containers in which different kinds of powders are stored and conveyed them to the nozzle separately or simultaneously to create a mixture. This approach makes the process capable to produce different types of alloys or to gradually vary the material composition of the workpiece under construction, depending on the desired properties. Basically, there are two types of feeders which are distinguished by the method of dosing the powders. The first one consists of a container from which the powder flows by gravity into a groove created in a rotating disk. Subsequently, the powder is conveyed by a suction unit, which transports it to the nozzle through a flow of inert gas (*Figure 14*(a)). The volumetric flow rate of the powder is therefore regulated by the size of the groove and the speed of rotation of the disc.

In the second type, the dosage of the powders is regulated by a pneumatic screw (*Figure 14*(b)). The volumetric flow rate is a function of the rotation speed and the geometry of the screw (Toyserkani et al., 2005). The gas pushes the powder through thin tubes towards the splitters and then into the nozzle at the set pressure.

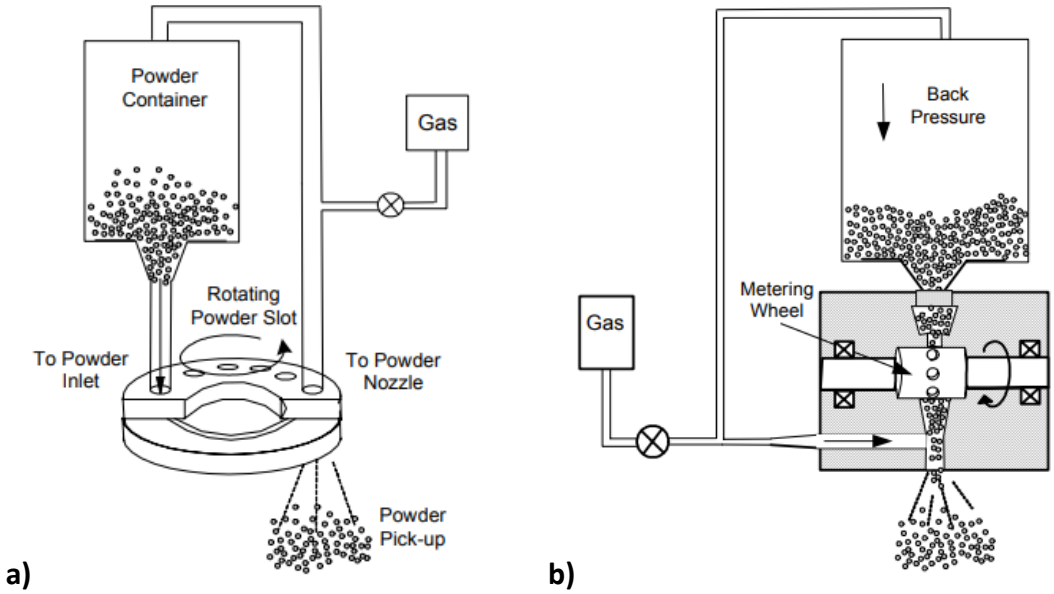

Figure 14 a) Gravity feeder and b) pneumatic screw feeder (Toyserkani et al., 2005)

2.4 Nozzle

The powder feeding system ends in the nozzle, which has the task of injecting the powder into the melting pool. The nozzle is generally made of brass to resist the thermal load generated by the laser beam and to better reflect the light radiation returning from the melting pool (Toyserkani et al., 2005). Depending on the configuration of the powder flow with respect to the laser beam, there are three different nozzle typology:

- coaxial
- lateral
- multijet

The coaxial powder supply provides for the toroidal emission of the powder around the laser beam. This type of nozzle has a conical shape with two internal annular interstices. The external cavity allows the flow of carrier gas and powder, while the internal cavity lets the transition of laser beam and shielding gas. The shielding gas protects the molten pool from oxidation (when the process is carried out in the presence of air) and prevents the powder flow from diverging towards the optics and being easily confined in the molten pool. The shielding gases usually adopted in this kind of

processes are argon, nitrogen, or helium. A further advantage of coaxial feeding is its independence from the direction of advancement of the head, as well as favouring a more effective orientation of the powders towards the molten pool. A feature that enables obtaining very high powder capture efficiencies.
The disadvantage of this category of nozzle concerns the difficulty of accessing some areas of the components due to the considerable size of the device. Usually, for complex machining, specific nozzles are made with specially produced geometries (Torims, 2013).
In the second case, the powder is fed into the working area through a separate channel from the nozzle, which through a carrier gas injects the powders laterally to the laser beam. This type of powder supply focuses on the simplicity of the equipment, which provides a nozzle with a single internal cavity, and the consequent reduction in costs. It also facilitates deposition in hard-to-reach places, such as inside pipes. The main drawback is the positioning of the powder flow during processing, which gives rise to a phenomenon of shadowing of the laser beam.
In this type of nozzle, the filler material can also be supplied in form of wire. This method emphasizes the phenomenon of shadowing but on the other hand causes extremely reduced pollution of the surrounding environment compared to the powder feeding (de Oliveira et al., 2005). The described configurations are shown in Figure 15.

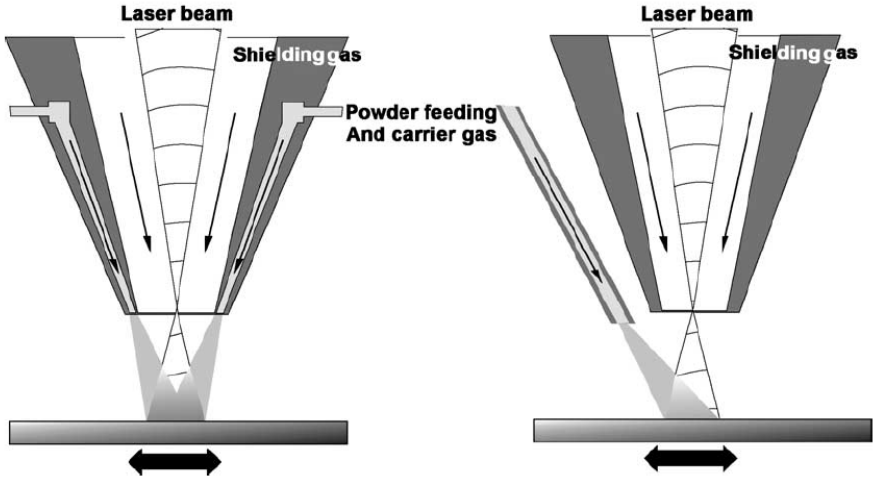

Figure 15 a) Coaxial nozzle, and b) side nozzle (de Oliveira et al., 2005).

Multi-jet feeding is a combination of previous technologies. In fact, the powder flow is injected into the molten pool by means of 3 or 4 side nozzles directed to the same focus point. This powder supply approach is nowadays the most employed in the manufacturing sector thanks to the excellent performance and the robustness of the system. The device has other advantages, being substantially independent to the working direction and having significantly lower costs for nozzle production than the coaxial one. However, it shows disadvantages in processing very complex geometries and has a lower degree of protection from oxidation of the molten pool than that of coaxial nozzles.
An innovative category of nozzles provides a new design with the powder flow in the central part and the laser beam set externally and coaxially to it. In this case, the powder does not exhibit problems of focusing, since the flow keeps almost the same distribution on each work plane. On the other hand, the laser beam presents an annular spot that is prone to variations in the power distribution depending on the working distance. Moreover, it mentions the difference in the power profile between this design compared to the Gaussian-like profile typical of models using a central laser beam (Figure 16). Another important difference compared to traditional nozzles is given by the shielding gas supply, which normally is delivered through the external cavity simultaneously with the powder flow, while in this category it flows from the central cavity, significantly reducing the protective effect (Shi et al., 2018).

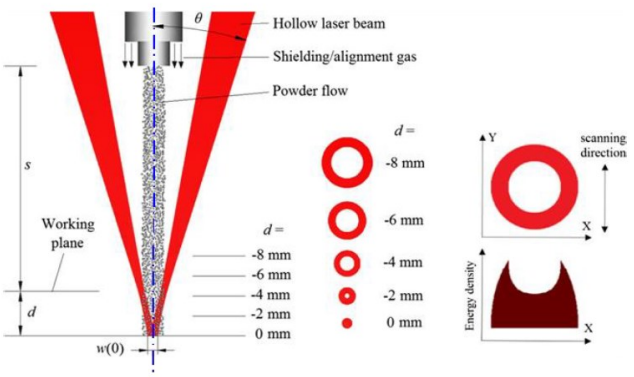

Figure 16 Nozzle with central powder feeding and external laser beam, laser spot at different working distances, with laser power profile (Shi et al., 2018).

2.4.1 Powders flow distribution

During a DMLD process, the laser beam scans the surface of the component, melting the substrate and creating a molten pool, thanks to the high thermal energy supplied. The nozzle injects into the molten pool the metal powder employing a flow of inert gas. The layer that is created is obtained from the interaction between the powder flow and the laser beam. Consequently, the spatial distribution of the powder flow assumes considerable importance, to define the shape of the clad. The distribution of powders is strongly influenced by the geometry of the nozzle, which requires a complex and accurate study using mathematical models and software, to define its characteristics and shape (Arrizubieta et al., 2016). In the analysis carried out on a coaxial nozzle, the models show how the axial-symmetrical flow converges from a toroidal profile, in the area closest to the nozzle, to a Gaussian-like profile on the plane of powder focus. The plane in which the profile assumes a Gaussian trend is of fundamental importance for the process. This plane, called the consolidation plane, must be placed just below the focus plane of the laser beam, to make the focus point of the laser beam coincide with the focus point of the powder flow and with the surface of the substrate. An example of the profile that the flow assumes is shown in Figure 17 from (Tabernero et al., 2010).
The distribution profile of the powders varies on different planes placed between the nozzle outlet and the focal plane parallel to the workpiece. It can be noticed that coming close to the focal plane the flow tends to follow a Gaussian-like distribution profile. Also, the distribution will vary according to the distance from the workpiece surface and the height of the deposition, significantly affecting the powder concentration.

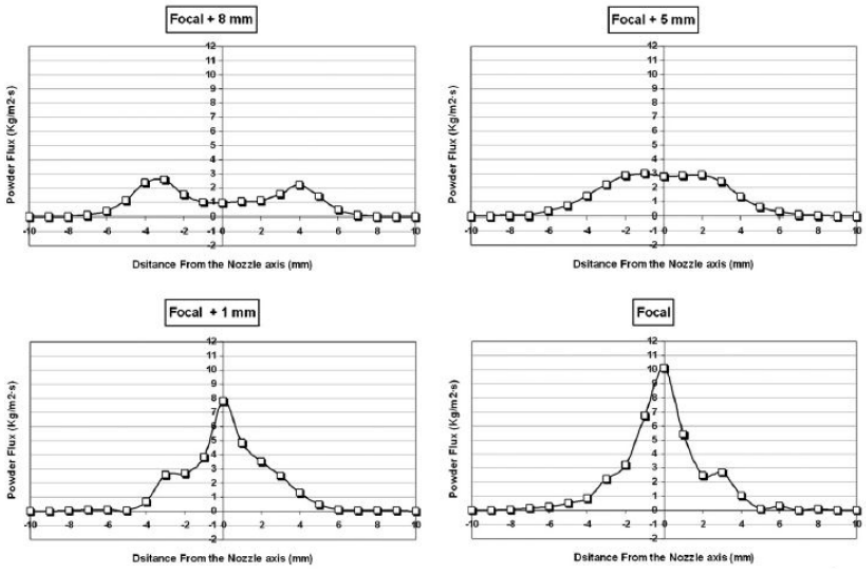

Figure 17 Powder flow distribution, from (Tabernero et al., 2010).

2.5 Laser system

Basically, a laser system is composed of different components. A pump mechanism (optical or electrical) that supplies sufficient energy in the active material and produces a population density inversion. The resonator that through the mirrors selectively reflects some of these photons in the active material. Finally, the active material which under a certain stimulation produces the radiation (Menzel, 2007). Lasers are generally classified according to the material used (active material) that inside the optic cavity can be in a *gaseous, solid, or liquid state.*
The first two of these categories are commonly used in DLMD processes. Consequently, specific ways of managing the energy required for the emission (pumping) are adopted, resulting in different performance and consequently possible uses (Toyserkani et al., 2005). In particular, for mechanical applications, it is possible to distinguish:

- *Gas laser*: the active material consists of a gaseous mixture contained in a tube, generally of quartz, in which the pumping is obtained by an electrical discharge. The wavelength between 9.3 and 10.6 μm. The most important is a CO_2 laser, already used in industrial processes.
- *Solid-state laser*: characterised by an active material consisting of ions of impurities in a solid matrix. The active material has the shape of a cylindrical bar with the end faces flat and parallel. The pumping is an optical type. And the wavelengths of the laser beam are comprised between 0.6 μm and 2.6 μm. These include the *Ruby laser* and N*eodymium-doped Yttrium Aluminium Garnet laser (Nd:YAG)*.
- *Semiconductor laser*: based on the coupling of semiconductor (diode) type P and N obtained by doping the GaAs crystals, in which the pumping is carried out by passing through the P-n junction from high-intensity currents. The laser effect is obtained with the energy generated by the forced displacement of the electrons of the *N* zone and gaps of the *p* zone. The wavelength is usually between 0.44 and 0.95 μm. The yields are very high, but the powers in practice obtainable are rather low.

2.5.1 CO_2 laser system

The CO_2 laser has found a remarkable application in the manufacturing field. It is used, in particular, for marking, drilling, welding, and cutting. The high-power densities that can be reached make it suitable for high precision machining. It is currently the most powerful (up to 1 MW of continuous output power) and one of the most efficient laser sources (between 15 and 20% efficiency, defined as a percentage ratio between optical output power and power input). The wavelength of the CO_2 laser is 10,6 μm. In addition to carbon dioxide, in the cavity are also present N_2 and *He*, in order to improve the efficiency of the process. Nitrogen has a simpler molecule than the CO_2, once energized it is located at an energetic level very close to the upper one of the active materials and thus favours the excitation. The role of helium is, instead, to absorb the excess energy that CO_2 preserves after the emission, bringing them back to the non-energized state and allowing that the N_2 molecules can resume to excite them. The CO_2 laser is very used in continuous working operations (*CW)*. A schematic draw of the system is present in Figure 18 (Ready, 1997; Toyserkani et al., 2005).

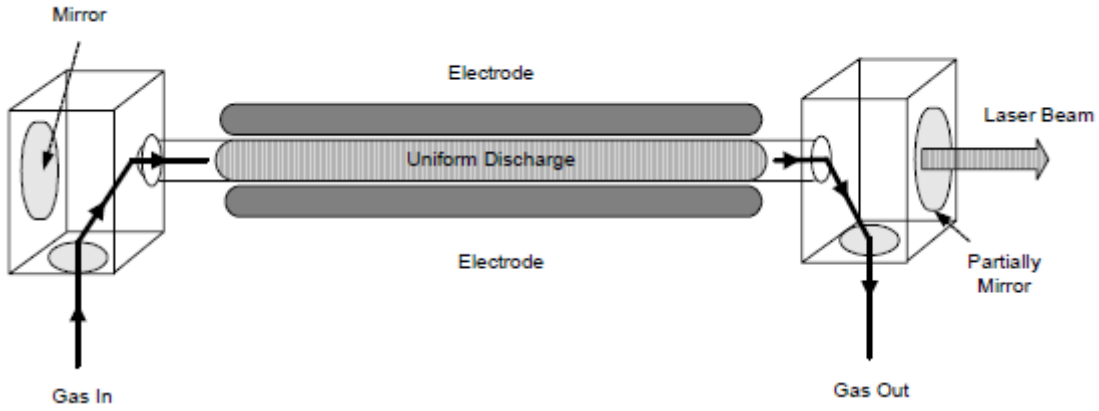

Figure 18 CO_2 laser schematic process (Toyserkani et al., 2005).

2.5.2 Nd:YAG laser system

Neodymium-doped Yttrium Aluminium garnet source (Nd:YAG) is today the most widespread in industrial applications. The Nd: YAG sources can work in both pulsed and continuous mode and with powers that can range

from a few watts to about 6 kW (500 W in pulsed mode and 1 kW in continuous). In *Nd:YAG* the active mean consists of Neodymium ions (Nd^{3+}) which are contained in crystals of *YAG*. This is a synthetic crystal of yttrium and aluminium garfish ($Y_3Al_5O_{12}$). Sources are also developed that use as active means *Nd:Glass*, which compared to YAG has higher thermal conductivity (therefore more resistant to breakage for thermal shock) and is more suitable for generating very short pulses with great peak power. The energetic pumping is an optical type, carried out by means of a light source. The Nd:YAG source has a four-level energy scheme. The permanence time at the third energetic level (metastable level) is about 250 μs and the wavelength of the emitted radiation is equal to 1,064 μm (Menzel, 2007; Ready, 1997). The wavelength of the beam generated by an Nd:YAG source is about ten times smaller than the beam generated by a CO2 source. On the market, there are two different optical pumping systems: *lamps* and *the* most recent *laser diodes.* A schematic draw of the system is shown in Figure 19.

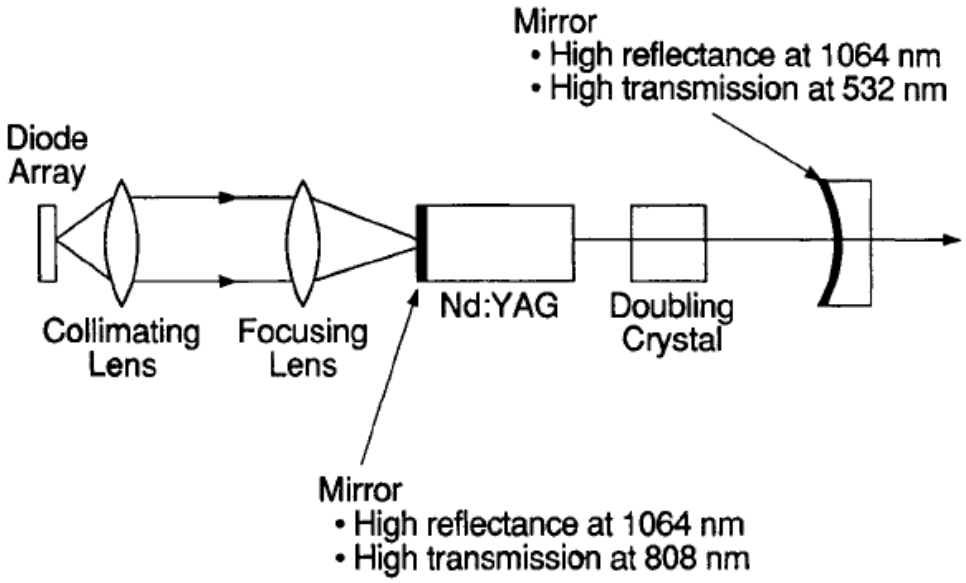

Figure 19 Nd: YAG laser schematic process (Ready, 1997).

2.5.3 Diode laser system

In the laser diode process, the energetic pumping directly takes place and requires a brief analysis of the structure of quantum solids and, in particular, of semiconductors. Passing from the single atom to the crystalline lattice constituting a solid, the energy levels admissible by the solid become energy bands. The energy bands linked to electron mobility are the conduction band and the valence band. The structure shown in Figure 20 is the first type of semiconductor laser structure developed (Toyserkani et al., 2005).

A conductive material has the full valence band while the semiconductors have an intermediate structure with a partially full valence band. For a semiconductor, the Fermi energy level is *Eg/2*, which is the average energy level in which the electrons that continue to move between the two bands are located. Within the structure of a semiconductor can be inserted ions of a different element, which can provide or acquire electrons from the atomic structure of the semiconductor. In this case, the semiconductor is said to be *doped*. The emission wavelength of the laser diodes typically varies between 0.80 μm and 0.95 μm, concerning the operating temperature, and therefore falls in the near-infrared, at the limit of the visible. A P-n junction is obtained by flanking a P-type semiconductor with one N-type. Thanks to the energy pumping carried out directly through the P-n junction, the overall efficiency reaches about 30%. The commercial sources are flanked by multiple joints of type P-N to form a diode stack capable of emitting a "laser emission line" at each junction.

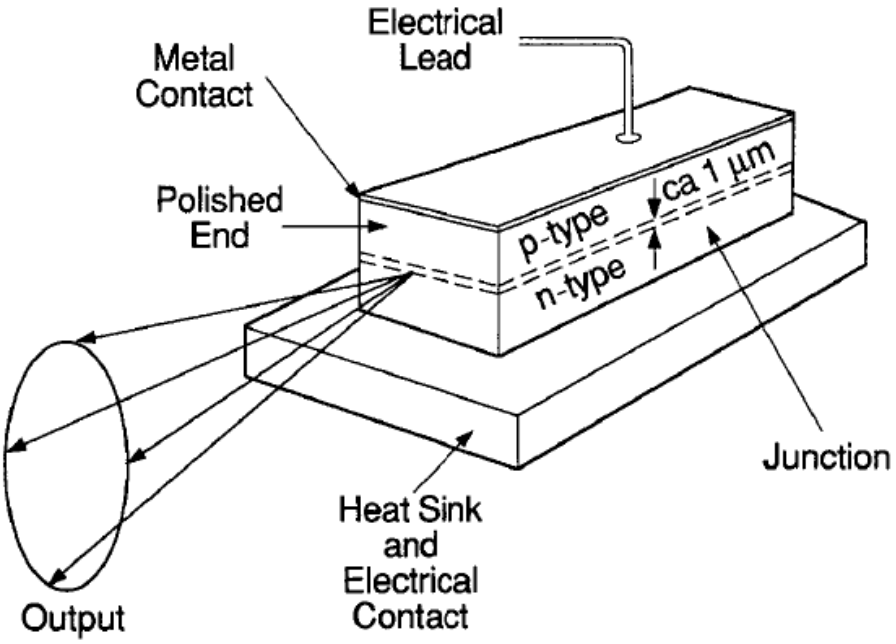

Figure 20 A simple semiconductor laser structure (Ready, 1997).

2.5.4 Laser Beam Characteristics

In the frontier area of the beam, the irradiance does not suffer a discontinuity but the intensity of the bundle decays continuously from the value it possesses within the beam to a null value outside it. It is therefore not possible to give the beam a unique diameter or radius, but a convention should be set. There is a close relationship between the geometry of the resonant cavity (in particular the curvature of the mirrors) and the distribution of the power density. In fact, the cavity geometry directly influences the resonance modes of the waves inside the resonant cavity, causing the energy to concentrate more in some areas of the beam cross-section compared to others (Menzel, 2007). One way to characterise the spatial profile of the beam power density is by the *transverse electromagnetic mode* indicator (*TEM*). The notation uses the TEM_{mn} indicator where m and n represent the number of minimum power densities present in the normal section of the beam axis in the two orthogonal x and y directions, respectively. A source with TEM_{00} indicates a beam with a spatial profile without minimums and with a single maximum, centred on the axis, and corresponds to the *Gaussian distribution*. The TEM_{01} mode indicates a beam with a minimum in the y-direction and none in x, as shown in Figure 21, while the TEM_{11} mode indicates a beam with a minimum in each direction x and y, for a total of four power maxima. A laser source can generate a beam that has more overlapping TEM_{mn} modes. In this case, it talk about a multimode laser, distinguishing it from a single-mode laser. One of the most frequent occurrences is the sum of the mode TEM_{00} with the mode TEM_{01}*, which gives the beam a distribution close to the homogeneous distribution (Toyserkani et al., 2005).

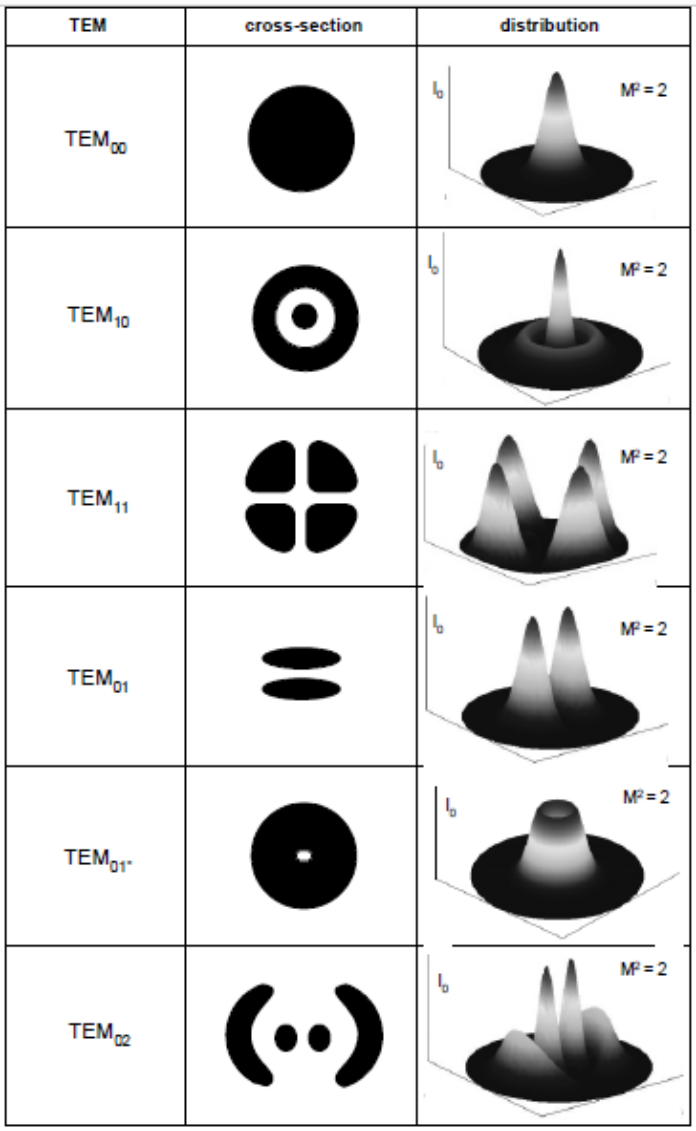

Figure 21 Examples of TEM modes and relative power distribution (Toyserkani et al., 2005).

Distinct types of laser sources show very different behaviours depending on the workpiece material to be processed. The parameter that describes the laser-matter interaction and strongly affects laser processing is the reflectivity (R) of the surface. This feature describes the fraction of the incident light that contributes to heating effects while the other fraction is reflected. Thus, it is defined as the ratio of the radiant power reflected from the surface to the radiant power incident on the surface. However, the absorptivity is the amount of light absorbed by a metallic surface and is proportional to 1 - R. The reflectivity of several metals as a function of wavelength is shown in Figure 22. The actual value of the reflectivity also depends on other variable conditions, such as surface finish and state of oxidation. In general, the reflectivity of all metals becomes high at long infrared wavelengths. The CO_2 laser (wavelength of 10.6 μm) has an R close to 1. Only a small part of the light incident is absorbed from the workpiece surface and is available for processing. For example, copper and silver at long infrared wavelengths (10.6 μm) have 1 - R is about 0.02, whereas for steel it is about 2.5 times higher (0.05). This means that steels absorb much more of the incident light, getting easier to treat using a CO_2 laser than other metals such as aluminium or copper. The wavelength variation is also important. All metals show a lower reflectivity coefficient at shorter wavelengths. The light absorbed from a Nd:YAG laser is 7 times higher than a CO_2 laser for equal irradiance from the two lasers. In summary, the choice of the laser source is highly dependent on the material of the workpiece, although in general laser operations with a shorter wavelength laser demonstrate greater efficiency (Ready, 1997).

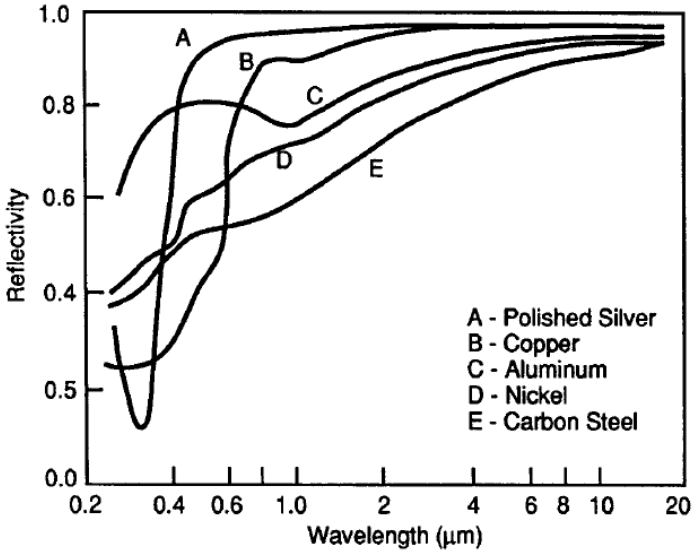

Figure 22 Reflectivity as a function of wavelength for several metals (Ready, 1997).

2.6 Chiller system

Laser sources are systems with remarkably low energy efficiency (10 - 30%). This means that a large amount of the electrical power taken from the grid is converted into heat. If it is not properly disposed, it could lead to overheating of critical components, causing a lowering for optimum beam quality or blocking of the facility. Furthermore, the laser beam overheats the instrumentation with which it comes into contact on its passage toward the workpiece, such as fibre optics, optics, and nozzle. It is of paramount importance that the DLMD includes a chiller system to effectively dissipate heat in the surrounding environment.

Industrial-use chillers remove heat via a compression or absorption refrigeration cycle. Vapor compression chillers are the most common type of chiller. Natural water (or demineralized water) flow is employed in an internal circuit, to capture the heat from the source and convey it to the evaporator, where it is cooled by exchanging the heat with the refrigerant fluid, without coming into contact. A pump sucks from the tank and sends it back to the source. In the external circuit, the mechanical compressor (usually a pump) pushes the refrigerant gas from the evaporator into the condenser. The condensers dissipate the heat through air or water, causing the refrigerant fluid to condense. The air-cooled chiller removes heat using fans that force air through the exposed condenser tubes. It requires more energy than water-cooled chillers and has lower efficiency. Otherwise, the water-cooled chiller uses pumps to send water through a sealed condenser and remove heat from the refrigerant fluid, which is diffusing through a cooling tower by evaporation. The high heat capacity of water compared to that of air makes these models more energy efficient. A schematic representation is depicted in Figure 23.

The chiller is equipped with sensors that recognize the variation of the thermal load only when the water reaches the threshold temperature. Future applications include an integrated systems of laser sources and chillers capable to communicate, planning the thermal load, and manage it more effectively, avoiding the delay of the response and significantly increasing the overall efficiency (Zobler and Mantwill, 2018).

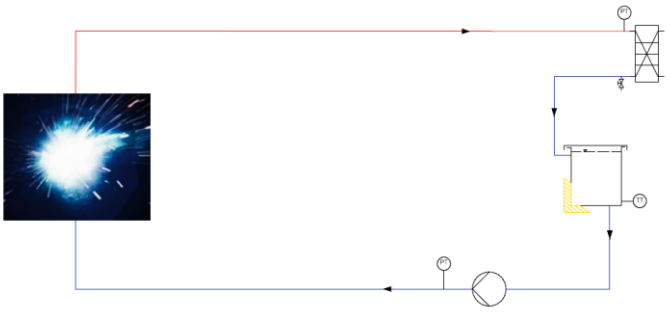

Figure 23 Water cycle with laser (left), plate heat exchanger (top right), tank (right) and pump (bottom) (Zobler and Mantwill, 2018).

2.7 Materials for Additive Manufacturing

As previously illustrated, the additive manufacturing technologies are numerous and consequently, the materials implementable are varied. Initially, the materials used for the AM technology were chosen from those already commercially available for casting processes. These materials were not optimized for such a characteristic technology as AM. Currently, available materials are specifically designed for the physical phenomena related to this technology and therefore, components are more accurate, resistant, and durable, taking advantage of rapid solidification following the passage of the laser. This has allowed its use in thermally stressful contexts, favouring the manufacture of smaller components, and an increase in productivity (Gibson et al., 2015). These can be classified into polymers, ceramics, composites, and metallic materials. Table 2, from (Bourell et al., 2017) provides an overview of the main materials used for AM. Plastics are both thermoplastic polymers and thermosetting polymers. The former is used in powder for SLS or SLM, creating a "bed" of material to be melted. ABS, nylon, or polyamide belong to this category. The second category includes polymers used for photopolymerization, such as acrylic monomers, epoxy resins, or vinyl ester, and the related additives such as inhibitors, antioxidants, and hardening agents. Ceramic materials are poorly processable by AM due to the combination of high melting point and low ductility. The use of composite materials is quite complex due to the dissimilar characteristics of various categories of polymer, metal, and ceramic matrix.
In general, metals with high reflectivity and high thermal conductivity are challenging to process, such as gold and some copper or aluminium alloys. In the other cases, unless processing in an improper atmosphere (which could lead to the formation of oxides with difficulty in the formation of bonds between particles), there are no particular problems, especially when these materials have good weldability.

	Amorphous	Semi-crystalline	Thermoset	Material extrusion	Vat polymerization	Material jetting	Powder bed fusion	Binder jetting	Sheet lamination	Directed energy deposition
ABS [Acryonitrile Butadiene Styrene]	X			X						
Polycarbonate	X			X						
PC/ABS Blend	X			X						
PLA [Polylactic Acid]	X			X						
Polyetherimide (PEI)]	X			X						
Acrylics			X		X	X				
Acrylates			X		X	X				
Epoxies			X		X	X				
Polyamide (Nylon) 11 and 12		X					X			
Neat		X					X			
Glass filled		X					X			
Carbon filled		X					X			
Metal (Al) filled		X					X			
Polymer bound	X	X		X						
Polystyrene	X						X			
Polypropylene		X					X			
Polyester ("Flex")							X			
Polyetheretherkeytone (PEEK)		X		X			X			
Thermoplastic polyurethane (Elastomer)				X			X			
Chocolate		X		X						
Paper									X	
Aluminum alloys							X	X	X	X
Co–Cr alloys							X	X		X
Gold							X			
Nickel alloys							X	X		X
Silver							X			
Stainless steel							X	X	X	X
Titanium, commercial purity							X	X	X	X
Ti–6Al–4V							X	X	X	X
Tool steel							X	X		X

Table 2 *Materials of commerce for AM, from* (Bourell et al., 2017).

It is possible to notice that the Direct Energy Deposition technology (and consequently the DLMD) focuses on the use of metallic materials, of which a general overview is provided in this paragraph. Metallic materials are often used as alloys, which are also mixed in the molten pool to build elements with varying compositions. The most used are:

- Stainless steels
- Maraging steel
- Tool steels
- Nickel-based alloys
- Titanium alloys

- Copper and its alloys
- Tungsten carbides

In the literature there are several studies on specific metal alloys in order to highlight the specifics of the processing and the finished product, a brief mention is provided below.

2.7.1 Steels

Among the various types of steel for Additive Manufacturing, the most used are maraging steel, austenitic steel (AISI 304L; 316L), and tool steel (H13). Maraging steel is aged martensitic steel with prolonged tempering. It allows the manufacturer to easily create high-density parts with appropriate process parameters and mathematical models. As regards the metallurgical defectology of the final component, generally the part is free from cracks and shows a limited amount of pores and voids. It also has a good bond between base and filler material, thanks to the reduced thermally altered zone generated (Campanelli et al., 2017a).

Austenitic stainless steel exhibits higher yield strength, ultimate tensile strength, hardness, and lower ductility in the AM process. Components made by DLMD have a structure similar to a welded joint, also in this case with a complete lack of pores, inclusions, and cracks. Furthermore, a good connection between various layers is guaranteed, as well as a fine microstructure, even if it is significantly influenced by thermal cycles and process parameters.

Depending on the cooling rate, Iron-based alloys give rise to different phase compositions, such as martensite and retained austenite, in precipitation hardening steels, will be sensitive to the selection of AM parameters, which must therefore be carefully chosen and controlled (Herzog et al., 2016).

2.7.2 Nickel-based alloys and superalloys

The nickel-based alloy powders used in AM are formed by particles of an approximately spherical shape, allowing good flowability and uniform melting. Thanks to the reduced thermal input required for melting and to the rapid cooling, a fine microstructure and good mechanical properties can be obtained for the workpiece. However, there may be some porosity caused by the process of gases trapped in the molten pool during solidification (Caiazzo, 2018). Ni-based superalloys show high performance at elevated temperatures which makes them suitable for the aerospace industry. Ni-based superalloys have nickel as a base alloying element, and generally have a microstructure consists of three major phases: the matrix austenite gamma(γ), the precipitation hardening phases gamma prime (γ') and carbide particles that contribute to the mechanical properties (Bian et al., 2017).

Commercially, these alloys and superalloys are available with distinct nomenclature, according to the manufacturer and the different chemical compositions. The best-known alloys are Colmonoy, Inconel, René, Waspaloy (Campbell, 2006). Colmonoy is a nickel-based alloy used for automotive and aeronautical components. It produces pieces characterised by good mechanical characteristics, a fine microstructure, a low level of defects, and with a micro-hardness greater than the conventional processes. This alloy also has a high density and a very low roughness (Angelastro et al., 2017).

The superalloy of the Inconel type is well suited to AM processing thanks to the high energy input required, which defines a final dendritic structure with good mechanical characteristics. Since dendrites reduce the propagation of cracks, making a piece made for DLMD comparable with a forging using the same alloy (Yuan et al., 2018).

2.7.3 Titanium alloys

Titanium and Ti-based alloys are of extreme interest due to their attractiveness for a broad range of industrial applications. Generally, Ti-alloys can be qualitatively classified into three main categories: $\alpha\beta$, $\alpha + \beta$, and β (metastable and stable) alloys. Upon rapid cooling from the β phase field, three potential phases are formed: α' martensite in a lath morphology, α'' martensite distorted hexagonal structure and $\omega_{athermal}$ in a fine nano-sized phase (Bian et al., 2017).

Ti-based alloys are ideal materials for AM technologies since combining high performance with high machining costs in conventional processing. The marked allotropy and great variety of alloy composition make the Ti-based alloy a great challenge for many researcher groups.

Especially Ti-6Al-4V has been extensively investigated and is nowadays widely used in the aviation and aerospace sectors.The resulting thermal history and cooling rates of the produced components strongly determining microstructure and resulting properties. Ti-6Al-4V is an extremely susceptible material and even slight changes in thermal process conditions can influence mechanical properties and microstructure, increased α lath thickness, and prior-β grain size. Ti-6Al-4V also shows a low strain hardening behaviour, thus variations in ductility do not affect strength proprieties (DebRoy et al., 2018).

2.8 Feedstock material

Depends on the additive manufacturing process, feedstock materials are supplied in a compatible form that can be solid (powders, wire, or sheets) or liquid. The use of powders is preferable for some reasons. First, today most of the materials are commercially available in form of powders. Powder feeding also implies no direct contact with the molten pool, making the process more flexible and allowing the thickness or composition of each layer to be varied at any time. Finally, the process efficiency improves because strictly connected to the shadowing effect of the laser beam, which is significantly lower compared to wire feed.
The alloy powders produced through different processes have distinctive shapes and characteristics that strongly affect the deposition quality. Powders produced by the plasma rotating electrode process (PREP) are perfectly spherical in shape with smooth surfaces. In this process, powders are produced by rotation of the end of a metal bar that is melted by means of an electric arc or plasma. In the rotary atomization (RA) process, the molten metal is flowed on a rotating disk producing powder particles with a smooth surface and elongated shape. Powder particles with a coarse surface texture and the presence of the satellite particles are produced by gas atomization (GA) and water atomization (WA) process. Both processes use high-pressure flow to atomize the molten alloy, in GA is a flow of argon and nitrogen gas while in WA process is a water jet. This affects the shape of the particles, which for GA is spherical, while for WA it is highly irregular. The shape and surface finish of the particles influence the geometry and porosity of depositions made under the same processing conditions (DebRoy et al., 2018).
In the DLMD process, the particle size distribution ranges from 20 to 150 μm. In particular, this process prefers particles with good surface finish, particle size distribution, and flow rate. It must be carefully studied to ensure good flowability, compatibility with the molten pool, and a suitable level of laser transmissivity. An incorrect particle flow can excessively absorb laser energy, leading to a low transmission toward the substrate. This would cause a premature melting of particles and no substrate melting, with a consequently poor bond between substrate and clad. For this purpose, a particle size distribution in the range of 40-90 μm and low powder feed rates are preferred, as reported by Wolf et Booth. In fact, this range allows keeping the laser transmission to the substrate approximately constant, compensating for any fluctuations in the powder feed rate (Wolf, 2016).

2.9 DLMD applications

Direct laser metal deposition is an extremely flexible technology that has found application in various industrial sectors, ranging from automotive to aerospace. The capability to operate both from the scratch and on existing components, with an extreme customization of the final product, lays this application at the heart of the research activities of many research groups. Applications that can thus adapt to very different stresses and requests, are also having a strong development. The main applications of DLMD technology present in literature today will be illustrated below.

2.9.1 Manufacturing of 3D components

One of the main DLMD applications is the production of 3D objects with complex geometries. This kind of application is feasible thanks to recent developments in the field of numerical control machines and real-time and adaptive control of AM process parameters. In particular, the development of handling systems with 5-axis configurations or through the use of anthropomorphic robots favour the creation of curved shapes, twisted parts, and thin-wall. Specific studies and algorithms consent the technology to overcome some problems related, for example, to the translation speed of the head in creating complex geometries. This facilitates the trajectories and permits an adequate material deposition, which avoids the presence of unfused areas or significant porosity, or even "gluing" due to failure of the substrate to melt. These objects are made thanks to sufficiently “fluid” patterns and a uniform speed of the head (Boisselier et al., 2014). Thanks to appropriate adjustments of process parameters, it is possible to create hemispherical objects with a reduced thickness, a good geometric tolerance, and a minimum roughness (Milewski et al., 1998). Besides, it is possible to make objects with different thicknesses and ramifications, as in Figure 24. It has been demonstrated that an object made in this way has a reduced porosity and the microstructure is not affected by the variation in thickness in each area of the specimen (Jones et al., 2017).

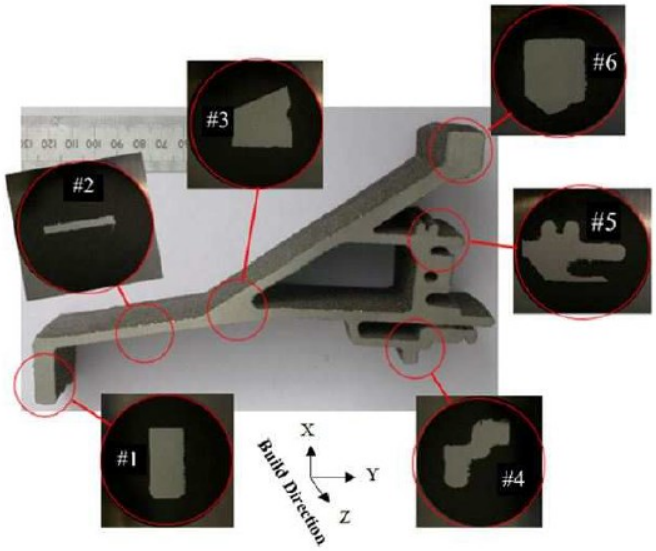

Figure 24 Geometry made by DLMD process (Jones et al., 2017).

2.9.2 Repair of mechanical components

Metal additive manufacturing, depending on whether it is DLMD or SLM, is a process that has a low environmental impact. This value is even more clear in the repair of worn mechanical elements, thus avoiding their disposal and extending their useful life. Currently, this is the most interesting application, because it ensures restoring the original shape of the component with the same metal alloy as base component, thus keeping its mechanical characteristics unaltered. Moreover, it is also economically suitable when applied to elements which production and replacement are excessively expensive, such as turbine or compressor blades. The process is achievable through the integration in a single system of the specific devices for laser cladding, 3D scanning, and subtractive machining, in order to speed up the acquisition of the geometry of the damaged part and repair it (Nowotny et al., 2007; Zhang et al., 2018).

Fundamentally, the processing obtained through additive technology is a functional repair since it allows the complete reuse of the piece which original geometry is restored. This result is also possible thanks to the appropriate choice of process parameters in relation to the metal alloy, which minimizes the occurrence of distortions due to rapid cooling and restores the initial microstructure and mechanical characteristics. Among the examples present in the literature, the repair of excessively worn components, such as large camshafts used in ship propulsion, is of considerable value. Here it appears that the treatment of small surfaces with an accurate distribution of the powders reduces the necessary energy input and decreases distortions. Despite this, the process shows disadvantages related to the high cost of the necessary equipment (Torims, 2013).

The technology achieves its greatest application in the aeronautical sector, especially for the repair of turbomachinery blades, in particular turbines. These objects are exceptional for complex geometry, microstructure, and high operating temperatures, which cause considerable stress, creep, and erosion problems. The types of repair approach are related to the damage magnitude: if the damage is superficial, a simple remelting can be used, or in the case of more significant interventions, laser cladding can even reach up to 0.5 mm in thickness. In the latter case, you can proceed with single-layer depositions or multi-layer depositions, depending on the damage extension. In all cases, the result is remarkable and guarantees the reconstruction of damaged areas with the original microstructure, being able to reuse the piece without being affected by the applied process (Alfred et al., 2018).

The multi-layer deposition strategy with a defined overlap is the most widespread because the multiple fusion of traces permits better adhesion and dilution with the base material. The resulting remelting can be successfully applied to turbine blades, which structure is monocrystalline (Kaierle et al., 2017). Before reaching the deposition phase, a thorough preparation must be carried out. Initially, a notching phase is carried out to regularize its shape, followed by a scanning phase of the piece. The scan is divided into three steps. The first is simply the 3D scanning of the piece. The second is more complex and concerns the identification of the most appropriate modelling by discretizing the piece in adjacent planes. Finally, the deteriorated part is extracted from the scan in order to define the digital model with which to compose adequate patterns for the deposition. The scanning phase is followed by the deposition phase, which realization requires an adequate adjustment and choice of the process parameters. This experiment is performed on specimens that have a

groove with inclined walls, to define a standard strategy on a conventional repair. An example of this sort of repair is shown in Figure 25 (Sun et al., 2019).

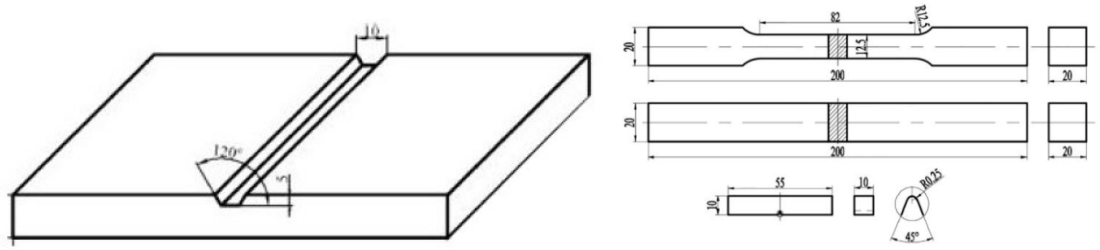

Figure 25 Basis for repair process test (Sun et al., 2019, 2018).

Once the deposition has been carried out with the chosen strategy, the specimen is trimmed by electro-erosion techniques and shaped to obtain the "dogbone" samples used for tensile, hardness, bending, and impact tests. The choice of the optimal parameters is carried out based on the overcomes of microstructure, micro-hardness, and mechanical properties obtained (Sun et al., 2019, 2018).

2.9.3 Deposition of dissimilar materials

One of the most innovative aspects of DLMD technology is the capability to produce complex, high performance multi-metal parts. If properly controlled and optimized, this capacity can have interesting implications in the mechanical manufacturing industry. Above all in the automotive and aerospace industries, dissimilar Fe/Ti materials can play an important role because their outstanding properties when combined into a single product.

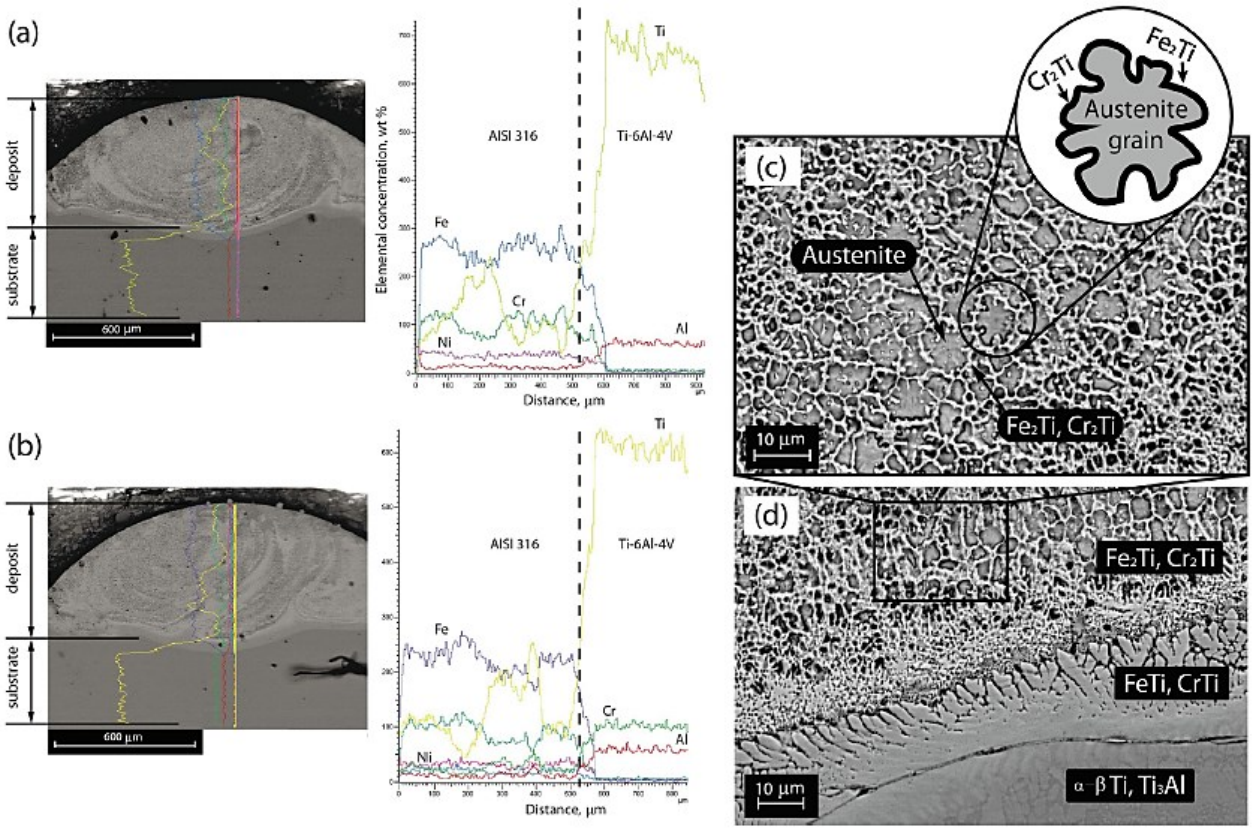

Figure 26 SEM analysis: EDS line scanning element distribution along the metal deposition for samples S1 (a) and S2 (b), microscopic images of diffusion area (d) and meta phases (Rashkovets et al., 2020).

Therefore by joining these metals, weight reduction coupled with high mechanical strength and corrosion resistance can be achieved (Casalino et al., 2018; Mahamood and Akinlabi, 2017). A wide variety of intermetallic compounds (IMCs) such as TiFe, $TiFe_2$ are formed through the fusion of Ti alloy and stainless steel. The excessive formation of brittle

intermetallic phases, however, will decrease the strength of the resulting bond in dissimilar bond metals. Nonetheless, one of the key concerns about the titanium - steel bond is the intermetallic process. To prevent the formation of the intermetallic process, a new filler transition route was built (Cooke et al., 2020; Li et al., 2017).
Rashkovets et al. show the difficulties arise in creating titanium - stainless steel bond, both from the macroscopic point of view with cracks and voids, and from the microscopic point of view with a complex and brittle microstructure. In fact, XRD analysis identified the λ + FeTi brittle phases, which completely wetted the grain boundary matrix, as shown in *Figure 26* (Rashkovets et al., 2020). These troubles could be overcome through the use of functionally graded material.

2.9.4 Functionally graded materials

AM processes are very flexible technologies, and some of them are capable to alter the material composition in different parts of the component to create functionally graded materials and objects. The Functionally Graded Materials (FGMs) also regards a single material object in which void space is purposefully added to create variable porosity within the body. Graded tructures in ordered porosity (Gasars) are a special category of materials with ordered porosity, which can be considered as gas reinforced composites achieved by unidirectional solidification of a gas supersaturated melt. Gasars applications including filters, fuel cells, components of rocket combustion chambers (Sobczak and Drenchev, 2013)
Nevertheless, the most attractive FGM involves the variation of the material composition of metal alloy components, polymers, or variable mixes of binders. Some AM processes can only produce discrete and abrupt variations between the layers while the DLMD process can also produce continuous and smooth variations in a material, as in Figure 27. This feature makes the DLMD the leading technology for producing FGM object (Thompson et al., 2016)

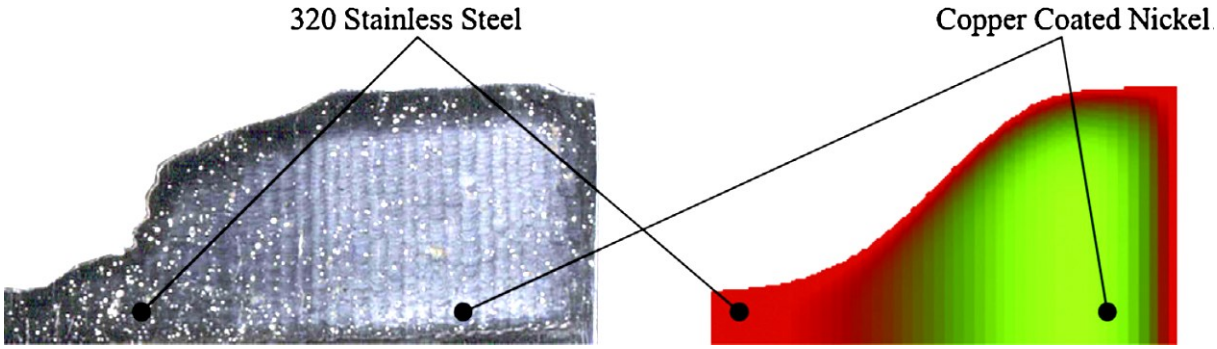

Figure 27 Cross-section of a functionally graded material (Thompson et al., 2016).

The FGM mechanical characteristics depend on several factors, such as modality of variation (smoothly or abruptly), crystal structures, and process parameters. The FGM hardness is heavily influenced by the variation modality. In smoothly graded with the same crystal structure, the hardness of the composite is governed by the mixtures constituting the alloy, varying proportionally from the hardness of the first to the last. In FGMs with different crystal structures, the hardness swings and not follow a rule of mixtures. In abrupt gradient FGMs, the hardness trends are not clearly defined because it usually presents a marked microstructure variation and intermetallic phases formation in the transition zone between the two elements. One of the most important drawbacks of the FGMs is the formation of brittle phases like intermetallic and carbides during manufacturing. It can lead to the development of microcracks and macrocracks covering a layer or the entire sample (DebRoy et al., 2018).
There are several potential applications and challenges in manufacturing functionally graded materials via DLMD, making it a strong research topic. For instance, FGMs may provide possible support in dissimilar metal welds and joints. However, it will require continuous optimization of the DLMD process for the production of functionally graded material. It will concern real-time control of multi-material powder delivery, thermal monitoring of composition materials (the emittance will constantly depend on the mixing), and consequently the process parameter optimization that depends on the concentration gradients of each material (Thompson et al., 2015).

2.10 Experimental DLMD equipment

The experimental tests were carried out using the prototype Direct Laser Metal Deposition system (shown in Figure 28) at the Hybrid Welding laboratory of the TISMA network of laboratories and the Junctions and Laser Technologies laboratory of the Department of Mechanics, Mathematics and Management (DMMM) of the Polytechnic University of Bari. This section describes the plant and the prototype equipment used.

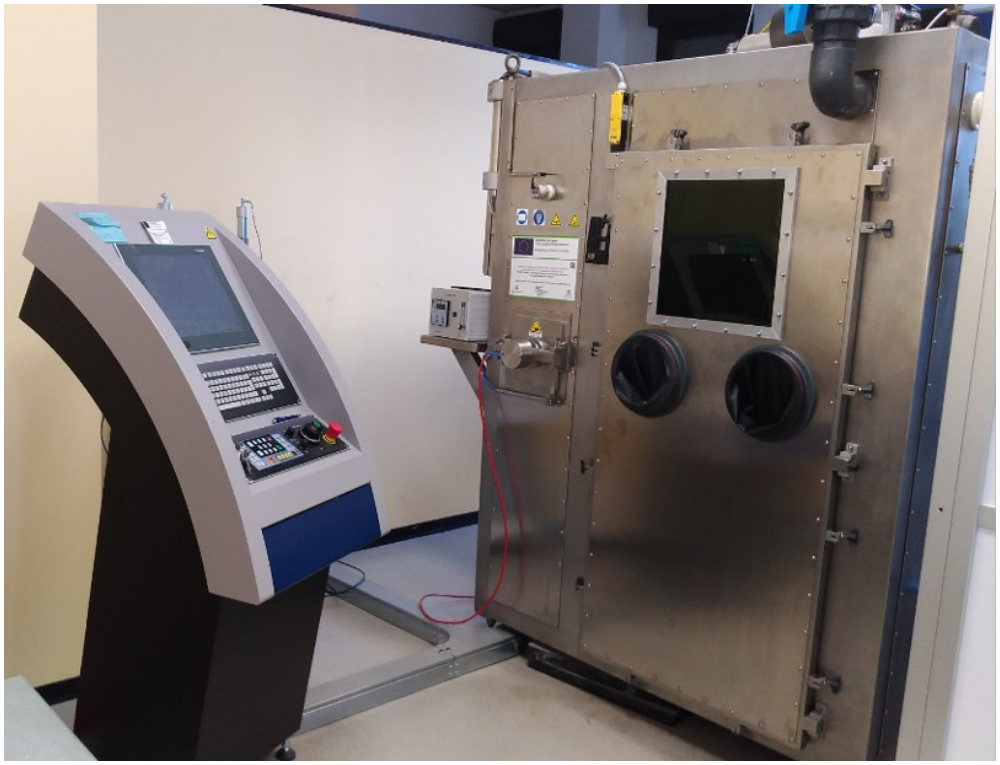

Figure 28 Prototype Direct Laser Metal Deposition system

2.10.1 Glove-Box

The glove-box has a structure made up of square section tubes of AISI 304 stainless steel on which panels of the same material are mounted. The front side is composed of two holes which allow, by means of suitable long-sleeved neoprene gloves installed on the PVC flange, the manual adjustment of the piece on the worktable. Moreover, a shielding glass panel consents the operator to monitor the processing. A double-door pre-chamber is also installed on this side of the box, for the handling of materials during processing with a controlled atmosphere. The hinged door is locked with a pneumatic device with a key opening in order to permit easy access to bulky components or to perform maintenance operations.
The glove-box is also equipped with a control panel that allows the operator to perform some elementary functions, such as activation and management of the movements of the machine axes, and an alphanumeric keyboard for entering commands on the Panel PC.
The glove-box system also includes:

- An automatic system for regulating the operating pressure of the process gas, consisting of pressure switches to regulate the pressure for a correct functioning of the solenoid valves. These are suitable for regulating the flow of gas inlet and the processing fumes outlet. The processing fumes are aspirated from the work chamber utilizing a centrifugal aspirator located on the upper wall of the glove box.
- An oxygen analyser, which probes the air in the cabin and calculates the amount of oxygen inside with a scale from 0 to 100 ppm.
- A dex-point meter, examines the humidity of the air inside the cabin.
- A basic drying system, which consists of a cylindrical containment structure with adjustable rubber anti-vibration supports at the base, equipped with molecular sieves that can be removed and disassembled for regeneration.

2.10.2 Suction system

The suction system, connected to the pipe on the upper side of the Glove Box, is composed of a fan system and a gravimetric dispenser. The ECO series filters capture and filter fumes and powder deriving from welding and depositions processes. The sucked gas flows via the connection pipe towards the filtration chamber, passing through the decantation chamber. As a result of the depression caused by a motor fan, fumes and powders pass through the cartridge filter elements on which the pollutants are deposited. The counter-current compressed air cleaning system allows the cartridges to be

optimally cleaned, without extracting them. The powder, deposited on the external surface of the cartridge, is shaken and collected by gravity in a separate container placed in the lower part of the collector.
The calcium carbonate gravimetric dozer is a machine designed for the release of powders to reduce the risk of explosion deriving from processing using fine powders. The gravimetric dosing system uses a load cell that records the weight variations of the tank group. The electronic boards check that the quantity of material previously set is correctly released.

2.10.3 Hopper powder feeder

The GTV powder feeder is a system for a controlled storage, transport, and dosage of powder. It consists of two hopper for the powders (dosing units) and a lower body on which the drive and control systems are installed. The hopper is constituted by a cylindrical upper part and a lower conical part which guarantees an optimal supply of powder for the dosing disc on which an annular groove is obtained. A scraper avoids the consolidation of stored powders. Through the rotation of the dosing disc, the powder material reaches the outlet hole is conveyed in flexible pipes to the nozzle through a carrier gas.
In this case, the powder mass flow is linearly proportional to the number of revolutions of the set dosing disc, which can be variably adjusted from 0 - 10 rpm in steps of 0.1 units. During operation, the powder feeder is in a state of slight overpressure. Through the variation of gas flow, it is also possible to regulate the output powder speed. Calibration tests were carried out in the laboratory to obtain the mass flow graphs as a function of the input parameters for every material used.
Humidity control is a fundamental factor in powder dynamics. In fact, the tanks are wrapped externally by flexible and heating panels, which guarantee reducing the humidity rate reaching a temperature of 50-60 °C.

2.10.4 Gantry handling system

The movement takes place via three X-Y-Z axes positioned on the upper part of the glove-box and two B-C axes positioned on the worktable (rotary-tilting table). The translation in X takes place thanks to two axes, X and X1, electronically coupled, consisting of a brushless motor, belt transmission, and ball screw. The Y and Z axes are driven by single brushless motors.

2.10.5 Optical system with adjustable collimator

This system consists of a robust metal structure equipped with an adjustable and motorized collimator, optimized for laser cladding and additive manufacturing.
The collimator is mounted in the upper part of the focusing optical system and, above the latter, a connector for the fiber laser system is positioned. Depending on the position of the collimating lens, the laser beam can be convergent, parallel, or divergent type. The lens can be adjusted by a translation in the vertical direction within a path of 15 mm. To protect the collimator from the infiltration of materials resulting from processing, the head is supplied with a continuous gas flow.
A CCD-camera is integrated between the collimator system and the focusing lens, useful for positioning on the working point, focusing, and process monitoring. A lighting unit is also mounted on the optics, which consists of LED elements embedded in a sturdy metal housing. This has the function of illuminating the processing area of the piece, which image can be observed through the CCD-camera, thus allowing to adjust the path of the laser beam.

2.10.6 Coaxial nozzle

The prototype DLMD system used for the experimental tests is equipped with a coaxial nozzle capable of operating on metal alloy powders based on nickel, cobalt, titanium as well as steels. This type of nozzle ensures correct operation with spherical-shaped powder particles with a diameter in the range of 15-45 μm, reaching focal diameters of the powder flow in the range 0.4 - 0.6 mm. The coaxial nozzle consists of a nozzle - optical system interface since it is directly mounted on the optical system as a single unit. The fluids for cooling and protecting the whole unit flow through special internal channels. There are adjustment modules, which consent the alignment between the laser beam and the powder flow delivered by the nozzle, employing systems of translation along the X and Y axes of the nozzle. A three-way plexiglass powder splitter, divides the flux of powders leaving the feeder into three parts, which are directed to as many nozzle inlets.

2.10.7 Ytterbium-doped fiber laser source

The laser source used in the laboratory is an IPG Photonics model YLS-4000. This is a 4kW power ytterbium-doped fiber laser system. In the device, there is a 2-way switch, which permits the source to be used simultaneously in two distinct processes. The system can be controlled through a digital I/O, analog control system or using specific software. The standard active fiber is 50 μm, but fibers with a diameter of 100 or 200 μm are also available.
The IPG lasers of the YLS series work in CW or modulated frequencies up to 20 kHz. These compact models have an overall efficiency of around 30%, i.e. the energy conversion efficiency with which the system converts electrical energy into radiant flux (total optical power). This is due to the better heat dissipation, due to the higher active material surface/volume ratio.
Fiber lasers also have high beam quality and allow the use of lenses with a long focal length to improve depth of field and have less damage to optical components. While conventional lasers can be delicate due to the precise alignment of the mirrors, fiber lasers are more robust and capable to operate in difficult working environments.

2.10.8 DLMD chiller system

The prototype DLMD system is equipped with a chiller system consisting of three distinct chillers, to dissipate the heat of the deposition head, the laser source, and the fiber, respectively. The chillers use R407C as the refrigerant fluid, common for industrial applications. The operation of the chiller is based on a vapor compression cycle, carried out within the refrigeration circuit. This consists of an evaporator that allows the heat exchange between water and refrigerant fluid, a compressor that compresses the values coming from the evaporator to send them at higher pressure to the condenser. The latter is a finned tube exchanger for the heat exchange between refrigerant and air. The condensation of the refrigerant gas is carried out to transfer its condensation heat to the air. Finally, there is a lamination member that reduces the pressure of the liquid refrigerant coming from the condenser and then sends it to the evaporator, restarting the cycle. In the model used, a thermostatic valve modulates the flow of refrigerant to keep the superheating of the gas, in different working conditions.
The cooling circuit components are complemented by the fan, which ensures the cooling of the condenser by forcing the passage of air through the fins. The hydraulic circuit consists mainly of a pump, an evaporator, a tank, a bypass calibrated between the pump delivery and the system return. The water first flows into the evaporator, where it is cooled, then into the tank and is subsequently sucked by the pump which sends it to the system.
There is also an electronic control system to keep the water temperature within the desired values (by activating and deactivating the compressor appropriately) and to prevent and manage danger situations for the integrity of the machine.

2.10.9 Pyrometer

The PA-29 CellaTemp pyrometer, connected to the optics housing, is specific for continuous control of process temperatures of laser applications. The device records analogically and digitally the temperatures in the range of 250 - 2000 °C, operating at a wavelength between 1.8 - 2.2 microns. In order to avoid damage due to the dangerous working environment, the pyrometer has a distance/target ratio of 200:1 with a focus range between 200 - 400 mm.

2.10.10 Experimental materials and setup

In the different sessions of this work, different combinations of materials as powder and substrates were used. The materials treated are described below.
The AISI 304 and AISI 316L stainless steels, designations given by American Iron and Steel Institute, are austenitic stainless steels with a good resistance to corrosion in the presence of chlorides and an excellent fabricability and formability, which chemical compositions are shown in Table 3.
Type 304 stainless steel is a variation of the 18% chromium – 8% nickel austenitic alloy, the most familiar and most frequently used alloy in the stainless steel family. This steel is also known as "18-10 stainless steel", and its combination of properties is the reason for the extensive use of this alloy for pots and cutlery production.
Type 316L stainless steel is a molybdenum-bearing austenitic stainless steels which are more resistant to general corrosion and pitting/crevice corrosion than the conventional chromium-nickel austenitic stainless steels such as AISI 304. This alloy also offer higher creep, stress-to-rupture and tensile strength at elevated temperature.
A Nickel-based superalloy is a precipitation hardening and solid solution strengthening which chemical composition is shown in Table 4. Nickel-based superalloys have an exceptional performance at high temperatures for extended periods (up to 1000 °C) that makes them fit for the high-performance components. These superalloys have a relatively high yield

and ultimate tensile strengths, good creep properties, and outstanding fatigue resistance. While showing good oxidation resistance, the superalloys prove poor hot workability and weldability (Satyanarayana and Eswara Prasad, 2017).

Material	C	Cr	Ni	Mo	Mn	Si	N	P	S	Fe
AISI 304	≤ 0.08	18.00 – 20.00	8.00 – 10.50	–	≤ 2.00	≤ 0.75	≤ 0.10	≤ 0.045	≤ 0.030	Balance
AISI 316L	≤ 0.03	16.00 – 18.00	10.00 – 14.00	2.00 – 3.00	≤ 2.00	≤ 0.75	≤ 0.10	≤ 0.045	≤ 0.030	Balance

Table 3 Chemical composition of stainless steel material (wt.%).

Material	C	Cr	Mo	Co	B	Other	Ni
Nickel-based superalloy	≤ 0.07	14.60	4.20	15.00	0.015 – 0.016	7.60	Balance

Table 4 Chemical composition of Nickel-based superalloy material (wt.%) (Mazzarisi et al., 2020b).

Depending on the test, different combinations of materials were used both as substrates and as powders. The granulometry of the powder is in the range of 15 – 45 μm, compatible with the equipped coaxial nozzle.
The powder was supplied from the external powder feeder using Argon as a carrier gas and was injected through the coaxial nozzle into the melt pool. Argon was also used as shielding gas of the working area, to prevent oxidation phenomena.
The Ytterbium-doped fiber laser source (λ = 1.070 μm) produces a laser beam characterised by a Gaussian-like power distribution. The use of the innovative motorized optical collimator, mounted on the deposition head, allows the variation of the defocusing distance and consequently of the size of the laser spot, in a totally decoupled way with the variation of the standoff distance. Figure 29 shows the circular shape of the laser beam used and the intensity distribution profiles.

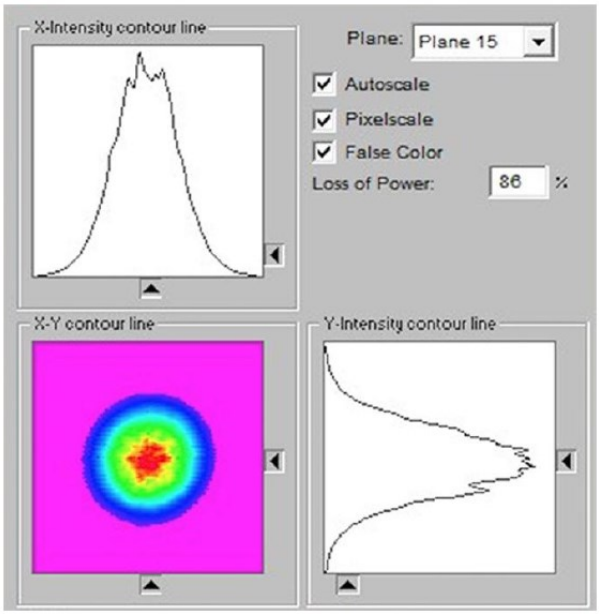

Figure 29 Laser beam and power distribution profiles.

3 MODELLING OF DLMD PROCESS

The laser deposition of metal powders is part of the family of industrial laser processing. Over the course of history, the versatility of this energy source has allowed the development of a long series of applications. According to the level of energy density and time of laser-matter interaction, three processing modalities and numerous applications can be distinguished, as shown in Figure 30 (Dutta Majumdar and Manna, 2011).

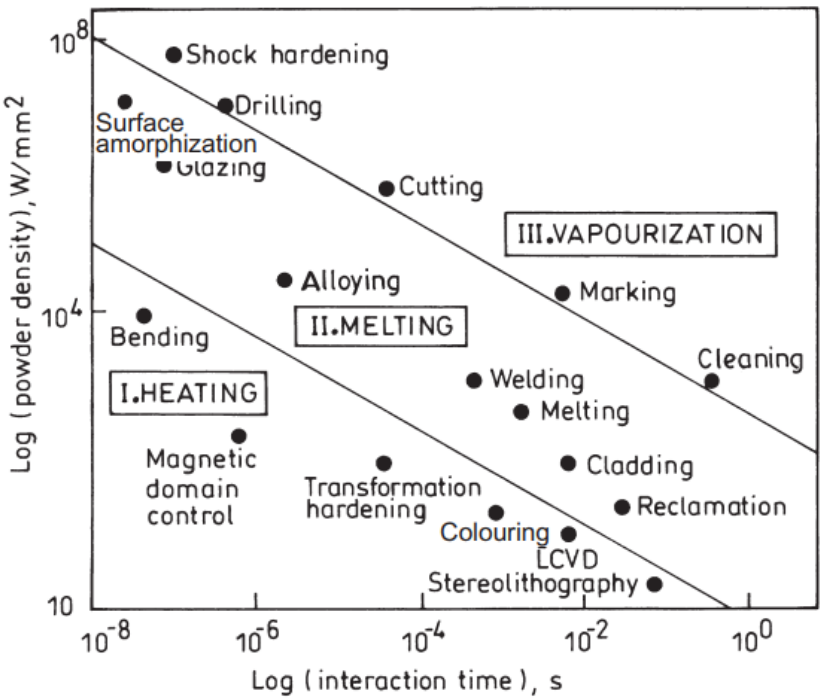

Figure 30 Process map as a function of laser power density and interaction time for several laser processing of the material (Dutta Majumdar and Manna, 2011).

The first mode concerns surface treatments in which the laser beam is essentially used as a means of rapidly and selectively heating the surface area of the metallic or non-metallic material. Given the rapid cooling that characterises this application, the mechanical characteristics of the material can be selectively improved.
On the other hand, a more intensive application is given by laser cutting or drilling, which thanks to the very high energy densities generated by the laser source is capable to instantly vaporize and turn into plasma even metal elements in fractions of seconds.
In the melting mode, one of the most widespread laser applications in the industrial sector is laser welding, a technique useful for joining two or more components, even of different materials. The laser beam interacts with the surfaces of the joint, properly coupled, and determines its autogenous welding by fusion of the edges.
In some cases, filler materials are used to compensate for failings of autogenous processing (joints too far apart) or in order to improve the mechanical characteristics of the joint.
A variant of the laser welding technique with material addition is represented by laser cladding, in which the contribution of material is consistent, in order to produce a surface coating layer. This technique is not used to join elements, but to coat flat or curved surfaces and restore or improve the original performance of worn components.
The evolution of laser cladding finally gave rise to the additive technique (or laser manufacturing) of which DLMD is part. As previously described, technological advances in the field of robotics, laser, and computerized simulation contributed to the birth of a cladding technology extremely flexible and adaptable, significantly raising its performance.
In this way, the combination of single tracks allowed the creation of 3D components with complex geometries or the repair of worn components.

3.1 Process parameters

All these laser applications are based on the same energy source, which induces different reactions in the treated material depending on the intensity and modality with which it is employed.
Therefore, it is of paramount importance the definition, optimization, and combination of process parameters that determine the processes performance.
Technological processes such as DLMD, laser cladding, and laser welding, are governed by the same process parameters that affect the quality of the process and final product.
The main process parameters considered are:

- **Laser power**. It is a parameter correlated to the type of laser used. The required intensity level must be sufficient to melt the base material. This parameter has a direct influence on power and energy density. A significant increase in power density can causes convective phenomena in the molten pool by modifying the thickness of the molten pool or generating defects.
- **Translation speed**. Also known as process speed, it directly affects the size of the treated area, since its increase results in a reduction in the interaction time between laser and matter, reducing the heat input on the component. As a result, the molten pool and the deposited layer decreases in thickness.
- **Laser spot size**. This parameter is a function of optical devices that converges the laser beam on the component and the standoff distance. An increase in the size of the laser spot results in a lower power density, therefore in a lower amount of thermal energy useful for melting the metal. This causes a reduction in the size of the molten pool.
- **Powder flow rate**. As already described, the metal powder is supplied to the molten pool via a coaxial or lateral nozzle and is conducted by means of an inert carrier gas. Its range, speed, and spatial distribution substantially influence the final shape of the clad.
- **Carrier gas flow rate**. The translation of powders from the feeder to the processing area takes place by means of an inert gas flow. This strongly influences the speed with which the particles are transported, which determines times and interaction modes of the particles with the laser and the molten material.
- **Shielding gas flow rate**. The molten material is subject to oxidation phenomena due to the reaction with the oxygen present in the air. These degrading phenomena are greatly reduced by protecting the process area by means of an inert gas. This gas is also useful for the protection of instruments (optics).
- **Standoff distance**. Also known as working distance, it is the distance between the nozzle and the surface of the workpiece. A variation in distance during the process affects the amount and distribution of powder that reaches the melt pool. Its decrease typically causes a reduction in the thickness of the layer due to the lower flow rate that reaches the molten pool. On the other hand, an increase in distance beyond the focus point can reduces the clad thickness since the concentration of the powder is reduced.
- **Tilt angle**. The laser beam is generally inclined at a certain angle concerning the normal surface of the workpiece, in order to prevent the reflection of the laser on the metal surface from returning to the optics and damaging it. Usually, the tilt angle has a value of 4÷5°.

3.2 Material characteristics

The increase in temperature resulting from the laser-matter interaction on the surface of the material, however, is not merely related to the process parameters previously described. Once the laser energy is absorbed by the material and was converted into heat, this temperature increase is also a function of the thermal properties of the material (Steen and Mazumder, 2010).
In metallic materials, for example, parameters of interest are:

- **Characteristic temperatures.** Each material is characterised by specific temperatures that define the states of matter. In metallurgy, the fundamental temperatures are the melting temperatures, which refers to solidus and liquidus. Solidus is the temperature below which a material is completely solid or crystallized. It is usually defined as the temperature at which a substrate begins to melt, but not necessarily when it is completely melted. On the contrary, liquidus temperature, indicates the temperature above which a material is completely liquid. Between these temperatures, crystals co-exist with the melt material in thermodynamic equilibrium. Moreover, the vaporization temperature refers to the temperature at which the material turns into a gas.

- **Thermal conductivity**. It describes the property of the material to conduct heat away from the interaction zone. It is proportional to the electrical conductivity of the metal, so a good electrical conductor also has a high thermal conductivity.
- **Specific heat**. It determines the amount of energy needed to increase the temperature of a given mass of material by one degree.
- **Density**. It measures the mass per unit volume of material.
- **Latent heat**. It is the amount of energy exchanged in the form of heat during a phase transition.
- **Thermal diffusivity**. It is a combination of the previous characteristics. It assesses how the amount of energy is transferred to the surrounding material by increasing the temperature of the whole workpiece. Materials with high values of thermal diffusivity are prone to transfer the heat received and therefore will require greater energy to create and sustain a melting pool.

In DLMD technique, process parameters and material characteristics are strictly related. The quantity of energy needed to reach the melting or vaporization temperature point and allow the transition of the state of matter is a function of process parameters that refers to the laser beam and material characteristics such as specific heat and latent heat. The relationships between the different parameters are often very complex. For this reason, an attempt is made to define process models that can be both simple and effective.

3.3 Geometrical characteristics of the clad

In the DLMD process, the quality of the product are strictly related to the geometry of the clad. The component is constituted of a series of single tracks side by side or overlapping with each other. Therefore, the hemispherical shape and geometrical characteristics of the solidified single track play a fundamental role in defining the quality of the process. These geometric characteristics can be clearly analysed by optical microscope, as a result of the metallographic preparation, which involves trimming of the products, hot mounted in resin and etching by means of special chemical compounds. *Figure 31* shows the geometrical characteristics taken into account in this work:

- **Clad height.** This represents the maximum height of the deposited track.
- **Penetration depth of molten pool.** It is the maximum depth reached by the molten pool inside the substrate.
- **Clad width.** This describes the attachment size between the deposited track and the substrate.
- **Area of the clad.** It evaluates the cladding amount that was generated during the deposition. It is conventionally defined as the area above the substrate boundary, and it is a function of clad height and width.
- **Area of the molten substrate.** It describes the size of the substrate affected by each individual laser pass. It is conventionally defined as the area below the substrate boundary, and it is a function of clad width and the penetration depth.
- **Dilution.** It is the ratio between the molten pool area and the total clad area or the ratio between the penetration depth and the total height of the clad. Both methods provide comparable results, but for the study of clads with marked asymmetry, the relationship between regions is more appropriate.
- **Aspect ratio.** This is calculated as the ratio between the width and height of the clad. It is useful for evaluating the outcome shape of the track.

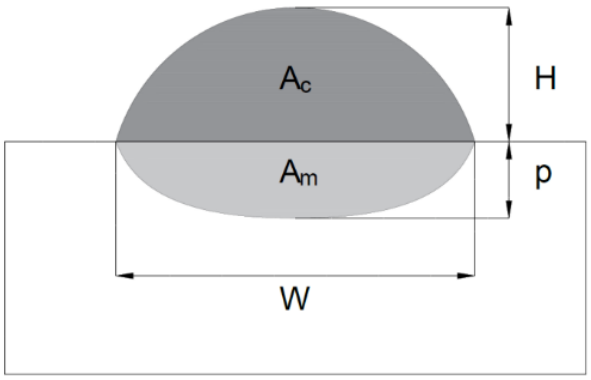

Figure 31 Cross-section drawing and geometrical characteristics of the clad (Mazzarisi et al., 2020a).

3.4 Welding process with filler material

As mentioned above, laser welding with filler material shares many aspects with the DLMD process.
As shown for the depositions of dissimilar materials, the addition of filler material can change the composition of the welded joint, improving the microstructure and mechanical properties of the weld bead by changing the chemical composition. In the literature, most of the investigations on powder-fed laser welding processes focus on the effects of the filler material on the microstructure and mechanical properties of the weld (Z. Lei et al., 2018; Zhang et al., 2017).
As shown in *Figure 30*, the process conditions characterizing the welding process with material supply, cladding, and additive manufacturing are very similar. Slight variations in the energy parameters of the process may lead to incorrect deposition or welding process.
For this reason, researchers investigated the effects of process parameters on the quality of the welding process with and without the addition of powder, also considering the transition from conduction mode to keyhole mode (Long et al., 2018; Lu et al., 2019).
Errico et al. examined the feasibility of laser welding of AISI 304 stainless steel with metal powder as filler material. The study focuses on defining the best range of the main process parameters and their effect on the characteristics of the weld bead. Besides, the transition between the welding mode of conduction and keyhole was detected, both with and without the addition of powder, as shown in *Figure 32*.

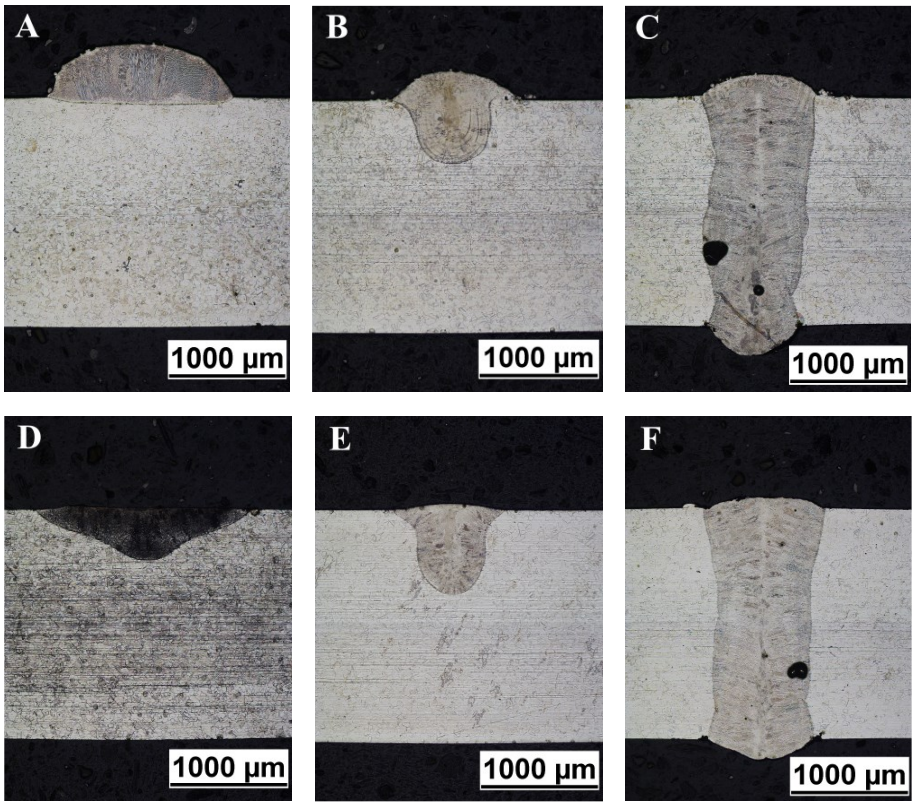

Figure 32 Macrographic cross-section of the bead-on-plate with powder (A, B, C) and without powder (D, E, F) (Errico et al., 2020).

This work was useful for identifying the energy ranges of the conduction mode and evaluating the effect of powder flow on welding. The DLMD operates under conduction regime and has found a useful comparison in the development of subsequent work.

3.5 Phenomenological modelling of Direct Laser Metal Deposition for single tracks

So far, several attempts have been proposed in the literature to explain the physics behind DLMD technology. Several elements are involved in the process such as lasers, powders, gases, and substrate, and interactions take place between them in a very short time scale, increasing the complexity of the analysis and prediction.
Thompson et al. summarized and categorized the prevailing physical phenomena according to energy and momentum transfer, as shown in Figure 33. The main events include laser and powder delivery and interactions, melt pool initiation and morphology, and the solidification process (Thompson et al., 2015).

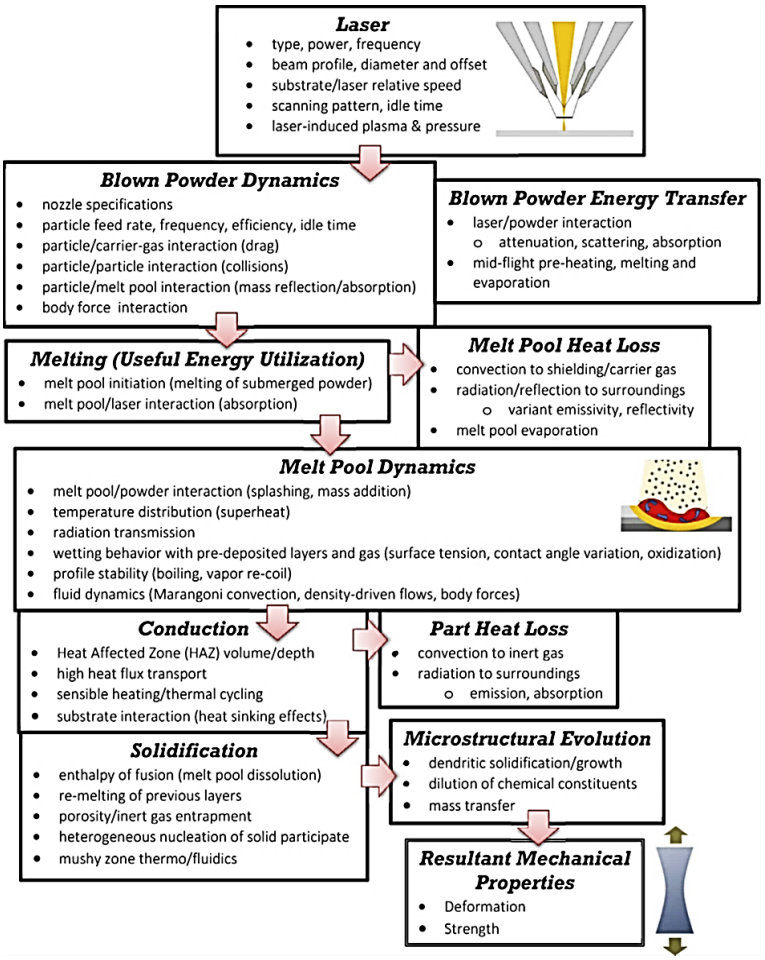

Figure 33 Physical events occurring during DLMD (Thompson et al., 2015).

Correct forecasting of process parameters, mainly using appropriate process models, is a viable alternative to shorten the setup phase of the process avoiding waste in terms of time and material. In the literature, three main approaches and related types of models are available to pursue this goal.

3.5.1 Physical process-models

The first one pertains to sophisticated models explaining in detail the physics behind the process: this first class refers to the physical process models.
Numerical models have turned out to be the best performing in this class for the analysis of the powder-laser interaction, melt-pool behaviour, and residual stress, but at the same time the most complex to be used in industrial applications. Computational fluid dynamics (CFD) techniques such as the Finite Volume Method (FVM) or finite difference method (FDM) are usually used to solve the conservation equations of mass and momentum for the flow of gas in the powder stream. Whereas the finite element method (FEM) is preferred for solving the heat loss through the substrate by means of inactive element method, various numerical part-level models, and hybrid element method (Guan and Zhao, 2020; Zhang et al., 2020). Figure 34 shows a typical part-level model whit active and inactive mesh elements.

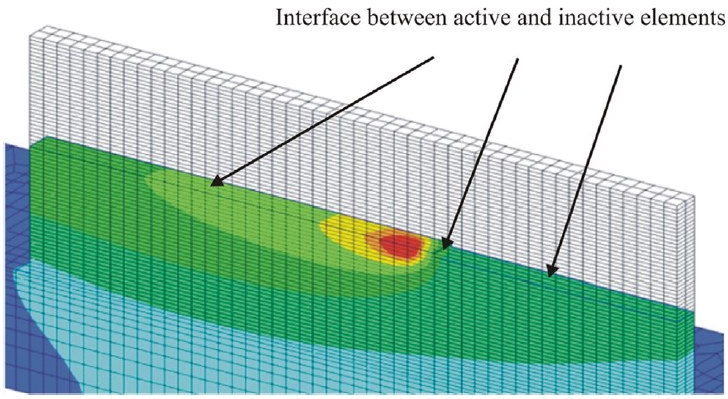

Figure 34 Part-level model: active and inactive elements (Guan and Zhao, 2020)

Analytical models propose a basis for estimating geometrical features such as dilution rate, process efficiencies, and defectiveness in laser cladding and repair applications. Models focus on the mathematical analysis of the process and establish mass and energy balances based on one-dimensional heat conduction to the substrate (Andrew J Pinkerton and Li, 2004; Xi et al., 2019).
Mathematical models were developed to forecast the microstructure evolution, inclusions growth, and parameters of the hardening phase (Alekseev et al., 2020).

3.5.2 Heuristic process-models

A major part of models in the literature makes an empirical resume of experimental evidence. These kinds of models do not let deriving generalised inferences amongst the parameters of the analysed process. It will call this class heuristic process-models.
These statistical models are typically developed through factorial experiments and analysis of variance (ANOVA) (Caiazzo et al., 2017). This technique is used to compare the means and variances of two or more groups, and to evaluate whether these differences are statistically significant.
Several methodologies are related to the ANOVA, such as Taguchi's orthogonal design (Verdi et al., 2017), which ensures that all levels of all factors are considered equally and avoids incorrect assessments due to the imbalance of the data.
Response surface methodology (RSM) (Sun and Hao, 2012) uses data from a series of experiments for adequate predictions of response or fitting empirical models, an example is shown in Figure 35. The central composite design (CCD) (Yu et al., 2018) helps develop a second-order model for the response variable without the need to use a full three-level factorial experiment.

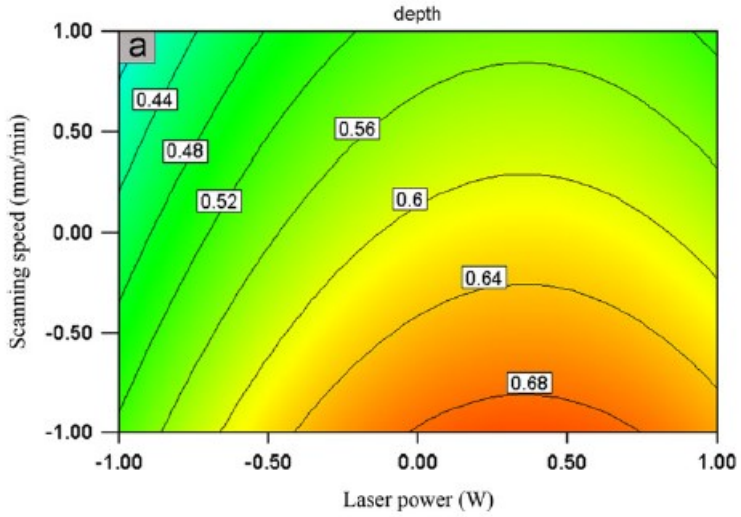

Figure 35 Contour plot of effects from RSM (Sun and Hao, 2012).

3.5.3 Phenomenological models

On the other hand, through a mathematical relationship, most of the models found in the literature relate the most significant controllable parameters of the process to geometric characteristics. This class of models will be called phenomenological models since they are generally based on multivariable statistical analysis. The phenomenological models represent the best compromise between predictive accuracy and computational efforts among the three classes.
In the literature, several models are proposed that relate to the fundamental process parameters of laser power (P), powder feed rate (F), and scanning speed (V), using various materials and machine configurations. Using a few factors, the combination of these process parameters was initially identified and qualitatively related. In Table 5 an overall summary of the aforementioned studies is presented, sorted by machine setup and materials used.

N	Ref.	AUTHORS	YEAR	LASER/NOZZLE CHARACTERISTICS	POWDER MATERIAL	BASE MATERIAL
1	(Costa et al., 2003)	L. Costa et al.	2003	CO_2 laser system – 5 kW lateral powder nozzle	Stellite 6	DIN Ck45 steel plate 100x200x10 mm
2	(de Oliveira et al., 2005)	U. de Oliveira et al.	2005	Nd:YAG laser system – 2 kW coaxial powder nozzle	19E Ni-Cr-based alloy	C45 low-alloyed steel plate 60 mm bar diameter
3	(Ocelík et al., 2007)	V. Ocelik et al.	2006	Nd:YAG laser system - 2 kW (top hat)	Eutroloy 16006 (Stellite 6)	Gray cast iron and CGI plates 400×140×16 mm
4	(El Cheikh et al., 2012)	H. El Cheikh et al.	2011	Nd:YAG laser system - 0.7 kW coaxial powder nozzle	SS 316L	SS AISI 316L plate 50×100×10 mm
5	(Nenadl et al., 2016)	O. Nenadl et al.	2016	Fiber laser IPG - 3.3 kW lateral/coaxial powder nozzle	SS Höganäs 3533	SS AISI 304 40 mm bar diameter
6	(Barekat et al., 2016)	M. Barekat et al.	2016	Nd:YAG laser system - 0.7 kW multi-jet powder nozzle	Metcocladd21	γ-TiAl plate 100x100x40 mm
7	(Ansari et al., 2016)	M. Ansari et al.	2016	Nd:YAG laser system - 0.7 kW multi-jet powder nozzle	NiCrAlY super-alloy	Inconel 738 plate 100×100×5 mm
8	(Erfanmanesh et al., 2017)	M. Erfanmanesh et al.	2017	Nd:YAG laser system - 0.7 kW coaxial powder nozzle	WC-12Co alloy	SS AISI 321 plate 200x200x10 mm
9	(Nabhani et al., 2018)	M. Nabhani et al.	2018	Nd:YAG laser system - 0.7 kW coaxial powder nozzle	Ti-6Al-4V	Ti-6Al-4V plate 100×100×10 mm
10	(Bax et al., 2018)	B. Bax et al.	2018	Diode laser system - 2.5 kW (top hat) coaxial powder nozzle	Inconel 718	Mild steel (S235JR) plate 100×100×10 mm

Table 5 Summary of the analysed works according to the experimental setup (Mazzarisi et al., 2020a).

The present work focuses on the implementation of a *general phenomenological model* to explain DLMD's behaviours by evading complex minor physical details from being modelled while providing a precise explanation of the relationships between the process's controllable variables. Considering the formulations and experimental setups suggested by a number of works present in the literature, the process model proposed was derived.
The study goes beyond the simple review of previous works, demonstrating a reasonable approach by correlating the main physical characteristics of the materials processed with the process parameters involved in the model to enhance and generalize it. Thus, a set of experiments proved the feasibility of applying the proposed process-model. The objective of the model is to rapidly set and optimize process parameters in order to improve the sustainability of manufacturing processes in terms of energy consumption, waste reduction, efficiency improvement in resource use, which is crucial in the vision of Industry 4.0.

3.5.4 General phenomenological model of DLMD process

As a result of the bibliographic analysis carried out, it can be noted that heuristic process models lack in generality and are therefore strictly linked to the specific application conditions tested, whereas physical process models are too elaborate to provide adequate forecasting capacity due to the level of detail involved, particularly in industrial applications. Otherwise, in phenomenological models, there is a lack of soundness which does not allow researchers or producers to

correctly predict the performance results of laser deposition processes, expressed in terms of output quality, economic feasibility, and sustainability of production.
The proposed phenomenological model includes the most important factors to be considered in the evaluation of the key performance parameters of the DLMD process, generalized considering the properties of the materials to be processed. Also making it affordable in most production situations. It would then be possible to set the key parameters of the model with a limited number of field tests and provide an efficient forecasting tool, saving an enormous amount of time and money to achieve optimal operating conditions.
A sketch of the DLMD process, mapping its main factors and essential parameters, is provided in Figure 36.

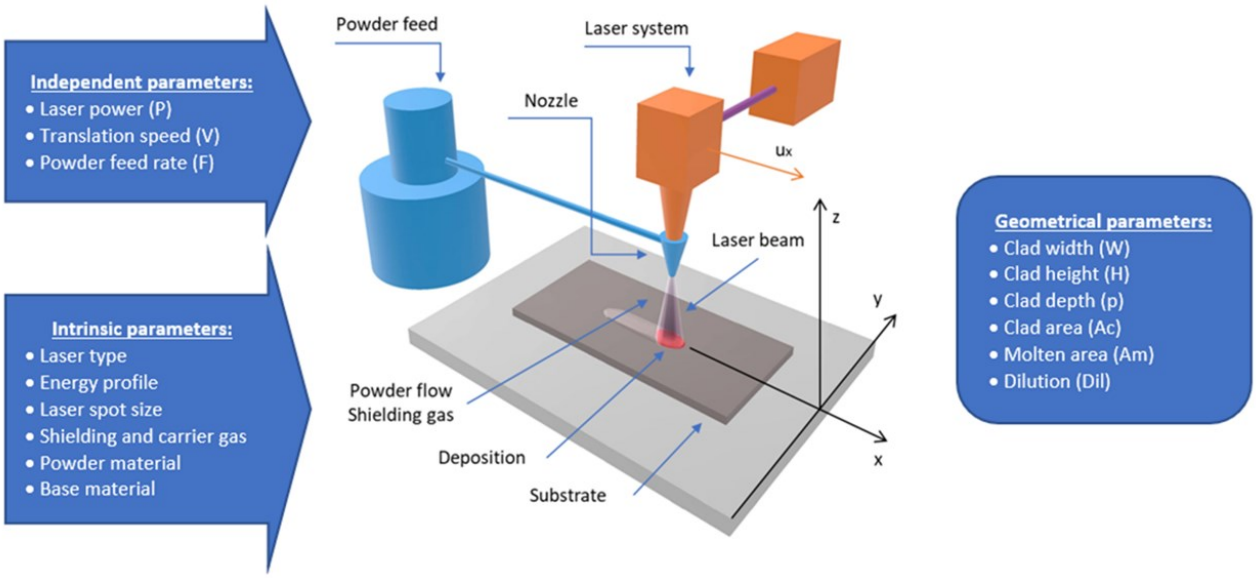

Figure 36 Schematic drawing of the DLMD process (Mazzarisi et al., 2020a).

The methodology used to generate the combined relationship of process parameters is a variant of conventional linear regression analysis, widely used to derive a model that explains the output parameters as a function of various independent inputs. These simple models are an easy but good explanation of the complex physical phenomena in additive processes that underlie the deposition of metal powder. Several relationships have been provided in the literature to relate the process parameters and the clad geometric characteristics. These are usually expressed in the multiplicative terms of the main process parameters with several variables as exponents. The combination of parameters in the model makes it easier the best fit, eliminating the issues associated with the use of multiple units of measurement that are peculiar to linear models. The standard formulation is here defined as follows:

$$Y \cong P^{\alpha} F^{\beta} V^{\gamma} \quad (1)$$

In Eq. (1), Y is the process performance (dependent variable) that is being pursued. The geometrical characteristics of the clad shown in cross-section, as previously described in Section 3.3, are:

- clad height (H)
- depth of molten pool (p)
- width of the clad (W)
- area of the molten substrate (A_m)
- area of the clad (A_c)
- dilution (Dil)

Eq. (1) simplifies the physical equations that underlie the direct deposition process. Only the key parameters are considered, assuming as constants the intrinsic parameters involved, as summarised in Figure 36.
Laser power (P), powder feed rate (F), and translation speed (V) are the key parameters considered herein. Typically, the process parameter exponents (a, β, γ, respectively) can be obtained via a design of experiments approach. Several authors proposed their relation and comparing all of them, it is easy to recognize the wideness of the range of their values. The

size of the range is related to the intrinsic properties of materials used for the deposition as well as other specific process conditions: working distance, powder distribution, and gas flow.
In the present research, a comparative review was carried out among all the formulations available in the considered literature, in order to define these associations and to set the general phenomenological model.

PROCESS PERFORMANCE	LITERATURE FORMULATIONS									
Y	**1**	**2**	**3**	**4**	**5**	**6**	**7**	**8**	**9**	**10**
W	-	$P\,V^{-1/2}$	$P\,V^{-1/2}$	$P^{3/4}\,V^{-1/4}$	$P\,V^{-1/2}$	$P\,V^{-2/3}$	$P^{3/2}\,V^{-1/3}$	$P\,V^{-1/2}$	$P\,V^{-1/3}$	$P\,V^{-1}$
H	$P^{1/2}\,V^{-1}\,F^{1/2}$	$V^{-1}\,F$	$V^{-1}\,F$	$P^{1/4}\,F^{3/4}\,V^{-1}$	$F\,V^{-1}$	$F\,V^{-5/4}$	$P^{2}\,F\,V^{-3/2}$	$P^{2}\,F^{1/4}\,V^{-2}$	$P\,F^{1/4}\,V^{-1}$	$F\,V^{-1}$
p	-	-	-	$\mathrm{Ln}\,(P^{2}\,F^{-1/4}\,V^{1/4})$	-	$P^{2}\,F^{-1/4}\,V^{-1/4}$	$P\,F^{-2/3}\,V^{2/3}$	$P^{2}\,F^{-1/4}\,V^{1/4}$	$P\,F^{-1/8}\,V$	-
A_c	-	$P^{1/2}\,F\,V^{-1}$	$P^{1/2}\,F\,V^{-1}$	$P\,F\,V^{-2/3}$	-	-	-	-	-	$P^{1/2}\,F\,V^{-1}$
A_m	-	$P\,F^{-1/3}\,V^{-1/3}$	$P^{2}\,V^{-1/2}$	$\mathrm{Ln}\,(P^{4/5}\,F^{-1/4})$	-	-	-	-	-	$P\,F^{-1/3}\,V^{-1/3}$
Dil	$P\,F^{-1}\,V$	$P^{1/2}\,F^{-1/2}\,V^{1/2}$	$\mathrm{Ln}\,(P\,F^{-1}\,V^{1/2})$	-	-	$P^{2/3}\,F^{-1/2}\,V^{1/2}$	$F^{-1}\,V$	$P^{1/2}\,F^{-1}\,V^{2}$	$F^{-1/2}\,V$	$\mathrm{Ln}\,(P\,F^{-1/2}\,V^{1/2})$

Table 6 Summary of the literature formulations examined (Mazzarisi et al., 2020a).

PROCESS PERFORMANCE	LITERATURE FORMULATIONS NORMALIZED									
Y	**1**	**2**	**3**	**4**	**5**	**6**	**7**	**8**	**9**	**10**
W	-	$P^{2}\,V^{-1}$	$P^{2}\,V^{-1}$	$P^{3}\,V^{-1}$	$P^{2}\,V^{-1}$	$P^{3/2}\,V^{-1}$	$P^{9/2}\,V^{-1}$	$P^{2}\,V^{-1}$	$P^{3}\,V^{-1}$	$P\,V^{-1}$
H	$P^{1/2}\,F^{1/2}\,V^{-1}$	$F\,V^{-1}$	$F\,V^{-1}$	$P^{1/4}\,F^{3/4}\,V^{-1}$	$F\,V^{-1}$	$F^{4/5}\,V^{-1}$	$P^{4/3}\,F^{2/3}\,V^{-1}$	$P\,F^{1/8}\,V^{-1}$	$P\,F^{1/4}\,V^{-1}$	$F\,V^{-1}$
p	-	-	-	$\mathrm{Ln}\,(P^{8}\,F^{-1}\,V)$	-	$P^{8}\,F^{-1}\,V^{-1}$	$P^{3/2}\,F^{-1}\,V$	$P^{8}\,F^{-1}\,V$	$P\,F^{-1/8}\,V$	-
A_c	-	$P^{1/2}\,F\,V^{-1}$	$P^{1/2}\,F\,V^{-1}$	$P^{3/2}\,F^{3/2}\,V^{-1}$	-	-	-	-	-	$P^{1/2}\,F\,V^{-1}$
A_m	-	$P^{3}\,F^{-1}\,V^{-1}$	$P^{4}\,V^{-1}$	$\mathrm{Ln}\,(P^{4/5}\,F^{-1/4})$	-	-	-	-	-	$P^{3}\,F^{-1}\,V^{-1}$
Dil	$P\,F^{-1}\,V$	$P\,F^{-1}\,V$	$\mathrm{Ln}\,(P^{2}\,F^{-2}\,V)$	-	-	$P^{4/3}\,F^{-1}\,V$	$F^{-1}\,V$	$P^{1/4}\,F^{-1/2}\,V$	$F^{-1/2}\,V$	$\mathrm{Ln}\,(P^{2}\,F^{-1}\,V)$

Table 7 Literature formulations normalized with respect to the translation speed (V) (Mazzarisi et al., 2020a).

Table 6 are shown the examined literature formulation as were presented in the relative references, while Table 7 are listed the normalization of those formulations, performed to the translation speed (V). Unlike P and F, all mentioned formulations contain the V parameter, making it a common point of reference. Also, the weakest intrinsic correlation to the material properties was found to this process parameter. Since the forecasting model examines the best correlations between process parameters and material properties, by neglecting its influence, the models have been revised. All equations were reported in power-law forms to define the laser power (α) and powder feed rate (β) coefficient ranges, shown in Table 8.
In Table 8, it is pointed out that the β coefficient varies over a restricted interval. The maximum Δ occurs in Am and Dil parameters, in which values between 1,00 and 1,50 are reached. The α exponent shows much wider ranges of variation with the broadest intervals for W, p, and Am.

PROCESS PERFORMANCE	α			β		
Y	**max**	**min**	**Δ**	**max**	**min**	**Δ**
W	9/2	1	3.50	0	0	0.00
H	4/3	0	1.33	1	1/8	0.88
p	8	1	7.00	-1/8	-1	0.88
A_c	3/2	1/2	1.00	3/2	1	0.50
A_m	4	4/5	3.20	0	-1	1.00
Dil	2	0	2.00	-1/2	-2	1.50

Table 8 Ranges of variation of laser power (α) and powder feed rate (β) coefficients

The width of the range of process parameters was influenced by the material properties of the samples produced. This is confirmed by several physical models, as summarized in Reddy et al. (Reddy et al., 2018), in which thermal and mass properties are proved to impact process efficiencies and geometric characteristics of the clad.
To provide a coherent general phenomenological model, relationships between exponents and properties of materials were established in the present work. In Table 9 are summarized the physical parameters of thermal conductivity, density, specific heat, and thermal diffusivity of the base materials used in the analysed works while the density of the powder materials is recapped in Table 10.

SUBSTRATE MATERIAL	DIN Ck45 steel [1]	C45 low-alloyed steel [2]	Grey cast iron [3]	SS AISI 316L [4]	SS AISI 304 [5]	γ-TiAl [6]	Inconel 738 [7]	SS AISI 321 [8]	Ti-6Al-4V [9]	S235JR [10]
Thermal Conductivity (W/m K)	50	48	53.3	16.3	16.2	22	11.8	16.1	6.7	49
Substrate Density (kg/m^3)	7800	7800	7060	8000	8000	3900	8100	7900	4430	7800
Specific heat (J/kg K)	470	470	490	500	500	500	420	500	530	470
Thermal Diffusivity (mm^2/s)	13.64	13.09	15.41	4.08	4.05	11.28	3.47	4.08	2.85	13.37

Table 9 Physical properties of base materials of the literature formulations examined (Mazzarisi et al., 2020a).

POWDER MATERIAL	Stellite 6 [1]	19E Sulzer-Metco Ni-Cr [2]	Eutroloy 16006 [3]	SS 316L [4]	Höganäs 3533-00 [5]	Metcoclad21 [6]	NiCrAlY [7]	WC-12Co [8]	Ti-6Al-4V [9]	Inconel 718 [10]
Powder Density (kg/m^3)	8400	8000	8900	8000	-	8400	7000	4600	4430	8200

Table 10 Density of powder materials of the literature formulations examined (Mazzarisi et al., 2020a).

3.5.5 Influence of α-exponent

Any general phenomenological interpretations of the DLMD can be taken from the scientific literature checked and used to suggest the proposed model. The α coefficient of the laser power factor is strictly related to the base material's thermal characteristics and the characteristics of the laser source and beam. In most of the cases examined, Nd:YAG laser sources were used, while CO_2 and diode laser sources were adopted only in a few works, making the analysis of source effects undetermined for the failure in comparing. Eq. (2) shows the significance of the thermal parameters of the base material in determining the molten area. the substrate melting efficiency (η_{melt}) and the absorbance of the powder (α) depends on the materials and has constant values, as stated by Reddy et al. (Reddy et al., 2018). Similarly, independent powder efficiency (η_i) in Eq. (3), is considered as a constant under certain hypotheses on the powder distribution. Consequently, the molten area is strongly affected by the thermal characteristics of base and powder materials.

$$A_m = \frac{\eta_{melt}\left(\alpha\frac{P}{V} - \frac{\eta_i F\left(C_{(p)}\Delta T_{(p)} + L_{f(p)}\right)}{V}\right)}{\rho_{(s)}\left(C_{(s)}\Delta T_{(s)} + L_{f(s)}\right)} \quad (2)$$

$$\eta_i = \frac{A_c V \rho_{(p)}}{F} \quad (3)$$

The thermal diffusivity (Dt), which is a function of thermal conductivity, specific heat, and density, is used to classify the substrate materials. This property summarizes different attributes, making it the most suitable thermal parameter for the characterization of the materials. The thickness of the substrate characterises, in theory, the mode and speed of heat diffusion, but there is minimal knowledge on this aspect in the literature. Most of the considered authors have implemented substrates of 10 mm thick or more and large diameter round bars.

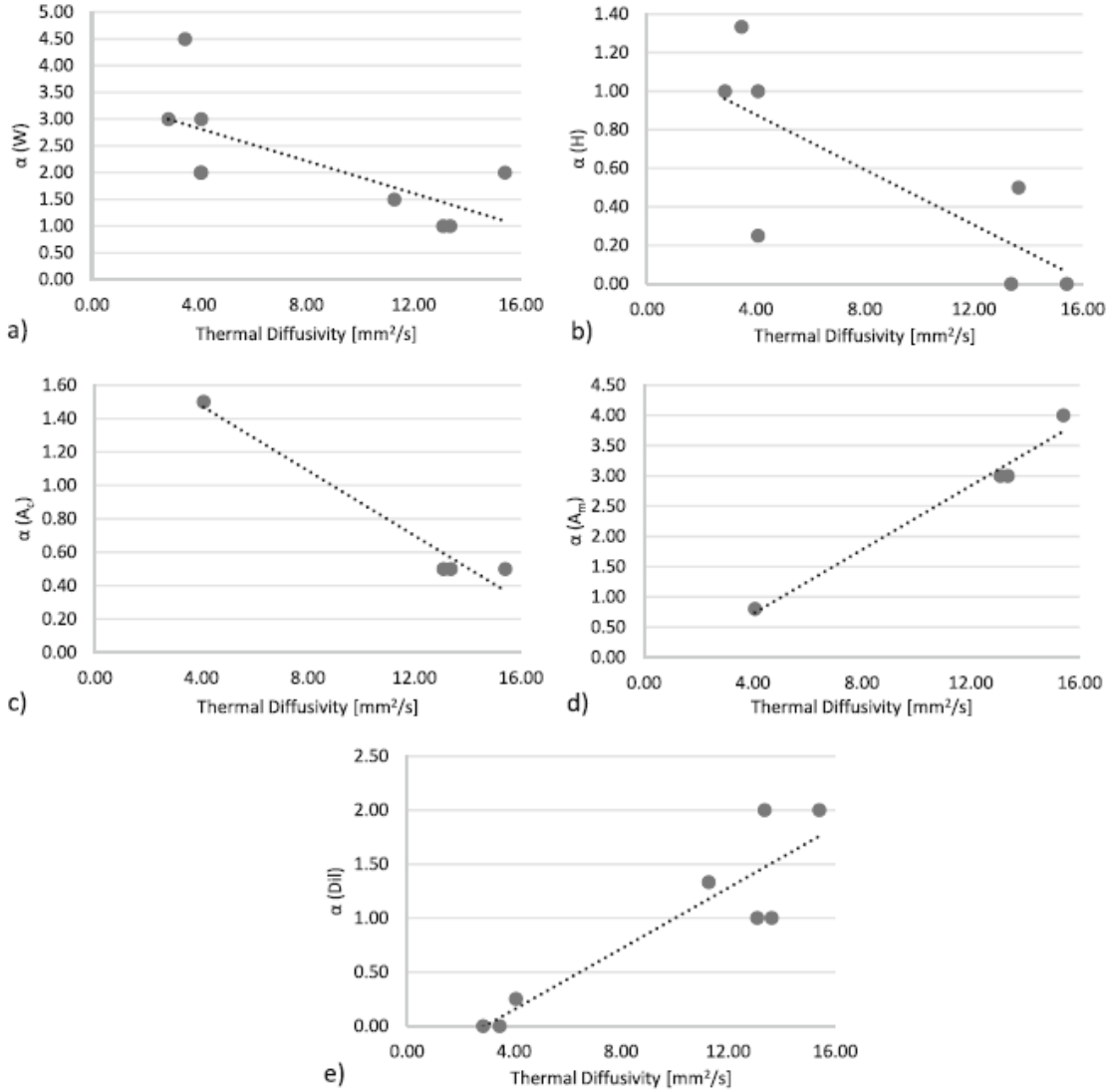

Figure 37 Trends of α coefficient of a) width, b) height, c) clad area, d) molten area and e) dilution vs thermal diffusivity of the base material (Mazzarisi et al., 2020a).

The thermal properties of the base materials implemented in the models analysed in the literature were summarized in Table 9. Data were used to discern the relationship between the α exponents and thermal diffusivity. The graphs plotted in Figure 37 demonstrate the negative correlation for W, H, and A_c while for the A_m and Dil a positive correlation is highlighted. In both cases, it is clear from Figure 37 that α coefficient values are grouped into two clusters, for low and high thermal diffusivity.

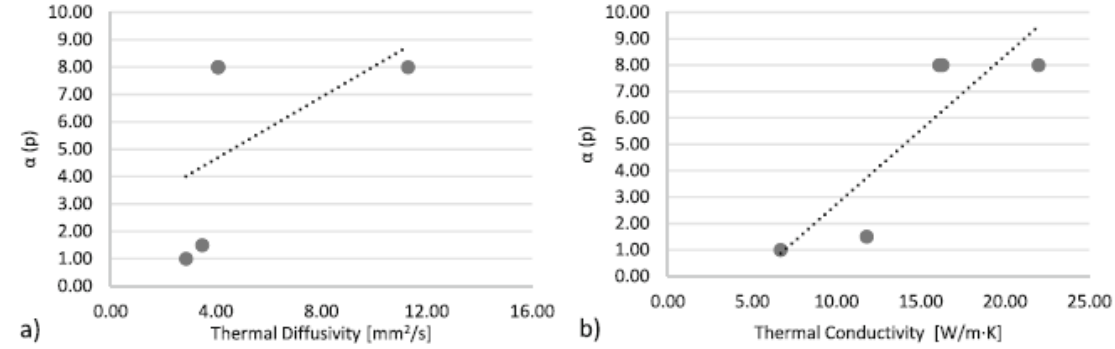

Figure 38 Trends of α coefficient of penetration depth vs a) thermal diffusivity and b) thermal conductivity of the base material (Mazzarisi et al., 2020a).

In the literature, the relationship between the α coefficient with the penetration depth is less obvious (see Figure 38(a)). To establish a correlation, the analysis was refined employing the α(p) graph plotted against the thermal conductivity, as shown in Figure 38(b). In this graph, it is feasible to reassign data points to two different clusters.

3.5.6 Influence of β-exponent

A strong relationship between the powder feed rate (F), the height of the clad (H), and the clad area (A_c) are found. Taking up the Eq. (4) from (Reddy et al., 2018), the clad area (and consequently the height) is a function of F, V, and $\rho_{(p)}$:

$$A_c = \frac{F}{V\,\rho_{(p)}}\eta_d\,\eta_i \tag{4}$$

$$\eta_d = \ln\left(\sqrt{\frac{P}{F\left(C_{(p)}\Delta T_{(p)} + L_{f(p)}\right)}}\right) \tag{5}$$

The laser power-dependent deposition efficiency (η_d) in Eq. (5), represents the efficiency in melting an incoming powder of the laser beam with a Gaussian distribution of power. The thermal properties of the powder materials involve only the η_d and have a low influence on β. A regression analysis was performed between the β coefficients found in the models and the density of the powders $\rho_{(p)}$ adopted by the authors and summarized in Table 10. Values are plotted in Figure 39. Two intervals are therefore described in the proposed model, where the β coefficients vary as a function of the deposited material density. It should be noted that the details on the powder properties used in some of the considered works are not available, making the β coefficients in some cases less precise depending on the properties of the materials and the chemical composition.

Resuming the analysis of literature models, as in Table 8, the F is not mentioned in any formulation relating to the width of cladding, revealing a negligible impact on this characteristic. Consequently, in our general phenomenological model, a value of 0 for the β coefficient is assumed for any density of powder.

A good correlation between β(H) and the powder density is shown in Figure 5a. For the high and low density of powder, the graph clearly indicates the existence of two different clusters. The satisfactory number of data allows the establishment of a regression function in order to simplify the determination of the infra-cluster value. The low number of values regarding the penetration depth makes it difficult to ascertain the β exponent behaviour.

Since a few values are available in the literature regarding the molten area and the clad area, it was unfeasible to infer any specific information for this model, as indicated the Figure 39(c) and (d). Nonetheless, for comparable densities of powder similar coefficients were found in the literature and a single value for $\beta(A_c)$ is provided. Similarly, the molten area formulations with a β coefficient variable between 0.00 and 1.00 were estimated in the same powder density range. Due to the unclear effect on the molten field, which is expressed in a very blurry interval estimation, there is still an ambiguity in the determination of this value.

The review of literature models designed for the dilution (Dil) displays a moderate correlation between β coefficient and ρ(p). Besides, it should be noted that most of the formulations in the literature were constructed using the process of "trial and error" and are therefore often influenced by considerable uncertainty.

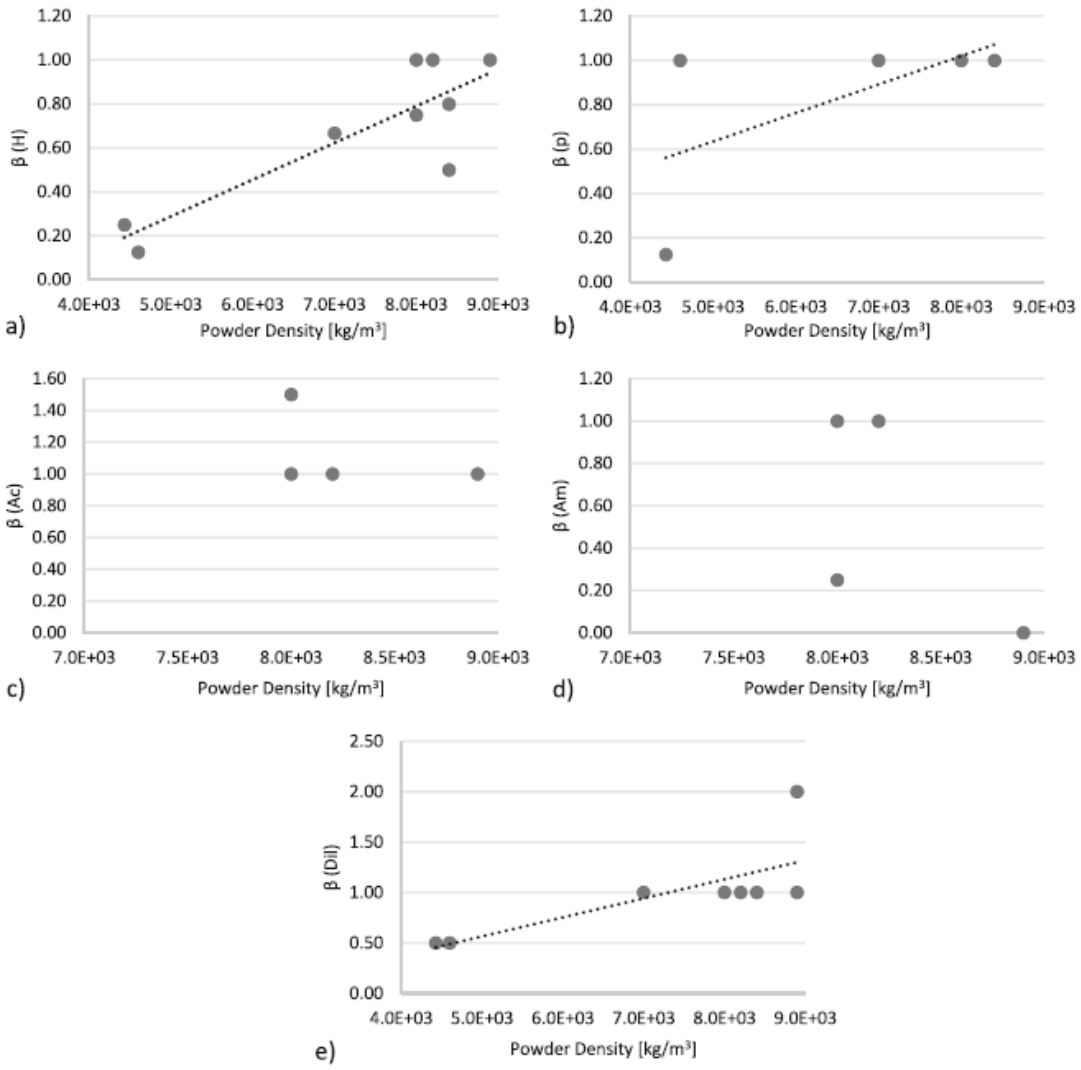

Figure 39 Trend of β coefficient of a height, b penetration depth, c clad area, d molten area and e dilution vs density of the powder material (Mazzarisi et al., 2020a).

3.5.7 Phenomenological model

Finally, the investigations performed on process parameters were incorporated in the proposed general phenomenological model. Two clusters were formed for the characterization of thermal diffusivity of base material and density of powder material. For each cluster and every geometrical characteristic, the optimal ranges of α and β coefficients were established (see Table 11).

PROCESS PERFORMANCE	**α Thermal Diffusivity [mm²/s]**		**β Powder Density [kg/m³]**	
Y	**0 - 8**	**8 - 16**	**0 - 6000**	**6000 - 10000**
W	2.00 - 4.50	1.00 - 2.00	0.00	0.00
H	0.00 - 1.50	0.00 - 0.50	0.00 - 0.50	0.50 - 1.00
p	0.00 - 8.00	8.00 +	0.00 – 1.00	1.00 +
A_c	0.50 - 1.50	0.00 - 0.50	0.00 - 1.50	1.00 - 1.50
A_m	0.00 - 2.00	2.00 - 4.00	0.00 - 1.00	0.00 - 1.00
Dil	0.00 – 1.00	1.00 - 2.00	0.00 - 0.50	0.50 - 2.00

Table 11 General phenomenological model with α and β coefficient ranges

3.5.8 Machine setup and materials

A basic industrial test case was chosen as a benchmark to demonstrate the viability of the phenomenological model as a decision-making method. The prototype DLMD system extensively described in Section 2.10 was used.
The Nickel-based superalloy is the powder material explored in this work. A 6 mm thick AISI 304 plate was used as a substrate. Chemical compositions of the materials consumed are displayed in Table 3 and Table 4. Argon, with a flow rate of 3 l/min, was used as shielding gas to achieve adequate processing results and obtain oxide-free depositions. From a preliminary study, to obtain a good surface finish and low porosity, the value of 3 l/min was considered the optimal flow rate of the shielding gas.

3.5.9 Experimental plan

A fractional factorial plan of experiments was carried out in order to correctly validate the phenomenological-model application, where three variables were modified at different levels, as shown in Table 12.

Parameter	**Unit**	**Notation**	**Factor Levels**			
			1	**2**	**3**	**4**
Laser power	W	P	400	600	-	-
Translation speed	mm/min	V	500	750	1000	-
Powder feed rate	g/min	F	1.5	2.5	5.0	10.0

Table 12 Experimental plan (Mazzarisi et al., 2020a).

The outcome was a total of 24 combinations of parameters and depositions. Other process parameters were kept constant. To achieve a reliable operation, the design of the experiment was chosen based on the efficiency and limitations of the equipment. Each track was deposited on a single substrate in order to prevent mutual heating and to maintain stable boundary conditions. To be examined using an optical microscope, the single-track depositions were trimmed, hot mounted in resin, polished, and chemically etched. Cross-sections were captured for each deposited track, as well as geometrical characteristics were measured.

3.5.10 Metallographic inspection

In the DLMD process, predicting the geometry of individual tracks is crucial. This makes it possible to correctly set process parameter values for the subsequent layer by generating layers, either for repair or 3D manufacturing purposes. The geometry of single tracks changes depending on the process parameters combination, as shown in Figure 40 and Figure 41, which report micrographs of transversal cross-sections of built samples after etching with glyceregia, respectively for power levels of 400 W and 600 W. This procedure is used to reveal the geometry of single clads, etching only the substrate and leaving the molten area intact. This approach makes it possible to expose the existence of dendritic grain defects (cracks or pores) that are typical of a molten and quickly re-solidified clad region.

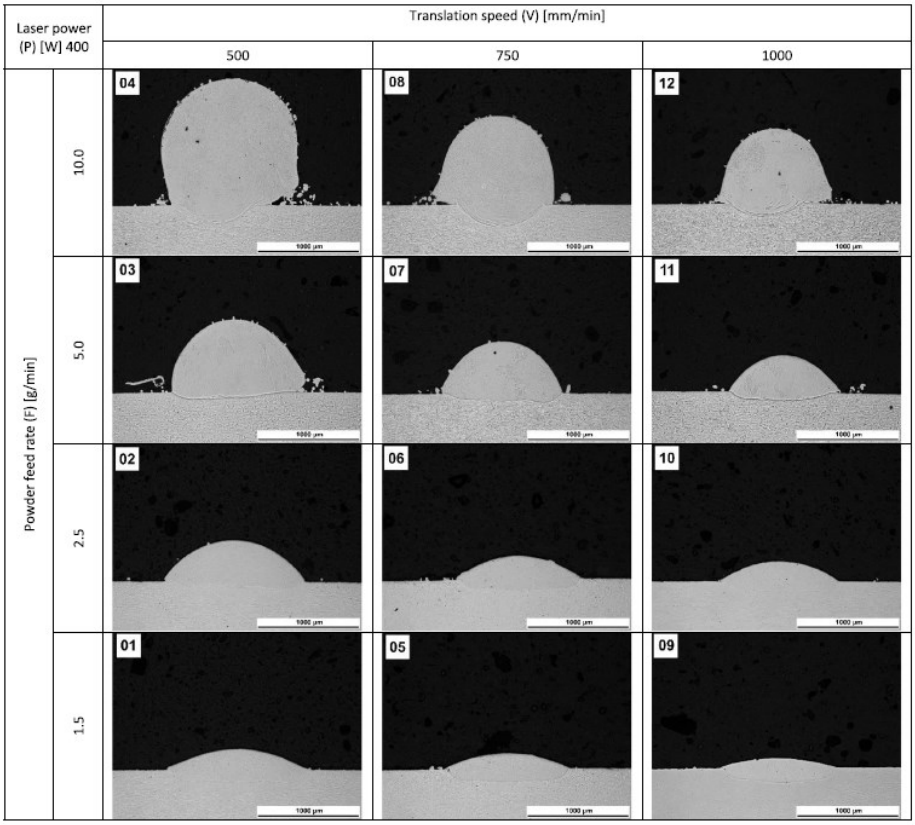

Figure 40 Cross-section morphology of single-track samples realised using 400 W laser power (Mazzarisi et al., 2020a).

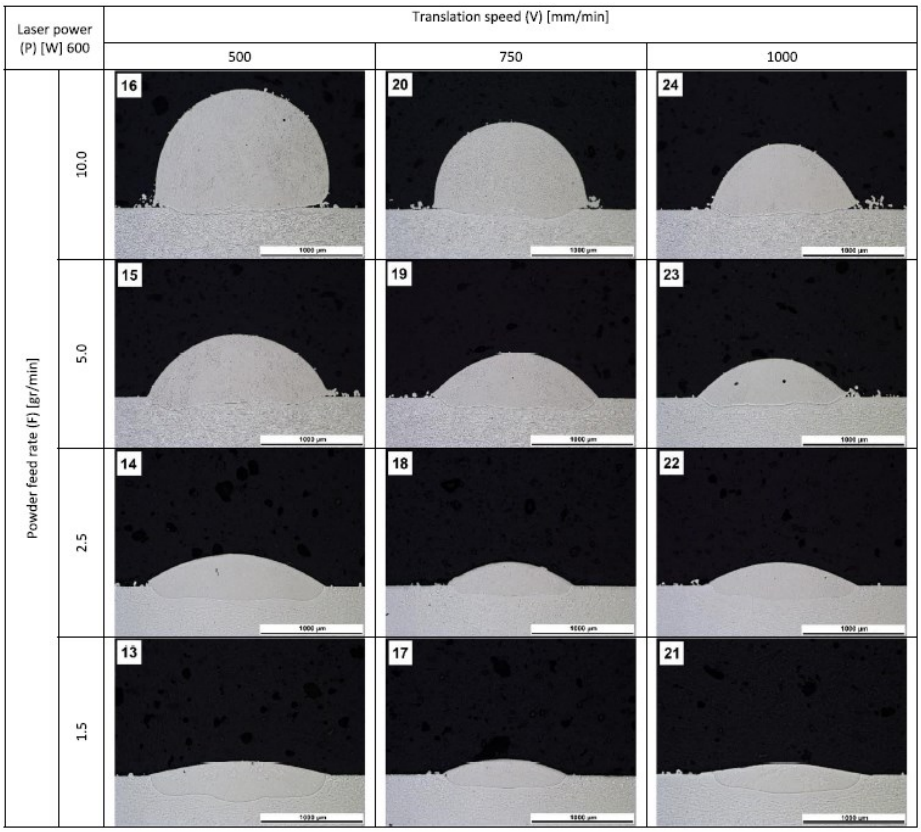

Figure 41 Cross-section morphology of single-track samples realised using 600 W laser power (Mazzarisi et al., 2020a).

3.5.11 Benchmarking the phenomenological model

ANOVA outcomes derived from the test case (see summary in Table 13) were used to assess the proposed phenomenological-model predictions. The effect of the key parameters of the process on the different geometric features of the deposition has been chosen as benchmarks. As a feature of the signal-to-noise ratio, the F-value (0.05) quantifies the influence of a given parameter and thus provides a sound reference to determine the phenomenological model's forecasting capabilities. The P-value suggests that second-level interactions are of poor statistical significance.
Provided the general model formulated in Eq. (1), in order to illustrate the use of the proposed phenomenological model, here it is first derived the exponential coefficients of Eq. (1) out of the ANOVA analysis used as a learning test. Therefore, to predict other operating conditions accordingly, the model and its combined parameters will be exploited.

			W			***H***			***p***	
Source	DoF	Main influence	F-value	P-value	Main influence	F-value	P-value	Main influence	F-value	P-value
Model	17		289.04	0.000		203.29	0.000		5.67	0.020
Linear	6		780.03	0.000		547.07	0.000		7.97	0.012
Laser power (P)	1	↑	**3391.64**	**0.000**	↑	**21.26**	**0.016**	↑	**7.49**	**0.038**
Translation speed (V)	2	↓	**226.87**	**0.000**	↓	**187.58**	**0.000**	↓	**1.08**	**0.399**
Powder flow (F)	3	↓	**278.26**	**0.004**	↑	**961.99**	**0.000**	↓	**13.40**	**0.005**
2-way interactions	11		21.23	0.001		15.77	0.001		4.41	0.041
P * V	2		6.91	0.028		5.41	0.045		0.79	0.498
P * F	3		6.17	0.029		1.04	0.441		14.22	0.004
V * F	6		33.53	0.000		26.59	0.000		0.71	0.658
Error	6									
Total	23									
R-sq (adj)			99.53%			99.34%			77.52%	

			A_c			A_m			***Dil***	
Source	DoF	Main influence	F-value	P-value	Main influence	F-value	P-value	Main influence	F-value	P-value
Model	17		123.06	0.000		12.22	0.003		36.66	0.000
Linear	6		313.55	0.000		25.72	0.000		97.58	0.000
Laser power (P)	1	↑	**10.11**	**0.019**	↑	**49.64**	**0.000**	↑	**23.64**	**0.003**
Translation speed (V)	2	↓	**177.52**	**0.000**	↓	**5.74**	**0.048**	↑	**13.53**	**0.006**
Powder flow (F)	3	↑	**505.37**	**0.000**	↓	**31.74**	**0.000**	↓	**178.26**	**0.000**
2-way interactions	11		19.15	0.001		4.86	0.032		3.42	0.072
P * V	2		0.02	0.984		2.24	0.188		3.15	0.116
P * F	3		2.73	0.136		14.01	0.004		6.72	0.024
V * F	6		33.74	0.000		1.16	0.432		1.87	0.234
Error	6									
Total	23									
R-sq (adj)			98.90%			89.24%			96.34%	

Table 13 Summary of results of the analysis of variance (ANOVA) and main influences (Mazzarisi et al., 2020a).

A strong correlation between width (W) and laser power (P) and a weak correlation between the same geometrical characteristic and the translation speed (V) is shown by the main influences resulting from ANOVA. Therefore, a high value was chosen in the range of α coefficient proposed in the model, while for the β coefficient the model prescribes a value equal to 0, according to the formulation in the literature.
The height is positively related to F and V. On the contrary, there was a low correlation between H and P, corresponding in the model range to a low value of α coefficient. The β was taken as the maximum value proposed in Table 11.
On the other hand, because of the complexity of the phenomena involved, the penetration depth (p) registered a low significance with $R^2 = 0.7752$. The largest negative impact of F was revealed by ANOVA. The statistical significance of the P was strong, while the V had a very low correlation. That corresponds to the phenomenological model's high value of the alpha and beta coefficients.

The clad area (A_c) had a strong correlation with H. In reality, F and V, which describe the amount of added content, were the most influential parameters, as seen for height. This relationship in the model was expressed through a moderate β coefficient value. In the creation of the clad field, the P assumed a secondary function, which determined a low alpha coefficient.
The molten area (A_m) showed a higher coefficient of determination concerning the penetration depth ($R^2 = 0.892$), which demonstrated the greater relevance of the analysis. The P and F independent parameters remain the most relevant. For this reason, in the model were chosen the higher values in the range for α (0.00 – 2.00) and a β = 1.00.
In comparison to the penetration depth, the molten region (A_m) showed a higher coefficient of determination ($R^2 = 0.892$), which showed the greater importance of the analysis. The most important is still the P and F independent parameters. For this reason, the higher values in the range of α (0.00 - 2.00) and a β = 1.00 were chosen in the model.
A fundamental feature of laser cladding and 3D processing is dilution. The P, F, and V parameters had statistical relevance in the analysis (P-value < 0,05). This justifies the selection of high values of the α and β coefficients in respective ranges in Table 14.

PROCESS PERFORMANCE	**COMBINED PARAMETERS**				
Y	**α**	**β**	**α : β : γ**	**X**	**X_{Adj}**
W	3.00	0.00	3 : 0 : 1	$P^3 V$	$P V^{-1/3}$
H	0.00	1.00	0 : 1 : 1	$F V^{-1}$	$F V^{-1}$
p	4.00	1.00	4 : 1 : 1	$P^4 F^{-1} V^{-1}$	$P^4 F^{-1} V^{-1}$
A_c	0.50	1.00	1/2 : 1 : 1	$P^{1/2} F V^{-1}$	$P^{1/2} F V^{-1}$
A_m	2.00	1.00	2 : 1 : 1	$P^2 F^{-1} V^{-1}$	$P^2 F^{-1} V^{-1}$
Dil	1.00	2.00	1 : 2 : 1	$P F^{-2} V^{-1}$	$P^{1/2} F^{-1} V^{-1/2}$

Table 14 Combined parameters from the experimental plan performed in the test case *(Mazzarisi et al., 2020a)*.

The combined parameter formulations generate by the model in Table 14 were achieved using the ANOVA data (adequately reviewed for a simpler formulation) in order to identify the contributions of each input variable. The proportions between the α, β, γ were compared with the ranges identified in the general model.
By evaluating the main influences, the sign of each output variable was evaluated. This approach led to a linear relationship between the Y characteristics of the clad and the combined process parameters. The combined parameters can easily predict the effects of the DLMD process with a great simplification compared to the approaches that employ physical equations, given only the key parameters are considered. In fact, parameters such as working distance, gas flow, and particle size of the powders are missing in the model.
The comparison between the formulation proposed in Table 14 of the present work and those analysed in the literature (see Table 5) led to the corroboration of H and A_c behaviours, while others forecasting formulations proposed differ from those of the literature.

COEFFICIENT OF DETERMINATION	**LITERATURE FORMULATIONS**										**GENERATED FORMULATIONS**
R^2	**1**	**2**	**3**	**4**	**5**	**6**	**7**	**8**	**9**	**10**	**-**
W	-	0.7214	0.7214	0.7753	0.7214	0.6517	0.7805	0.7214	0.7747	0.5134	0.8880
H	0.7989	0.9778	0.9778	0.9378	0.9778	0.9570	0.6146	0.1886	0.3811	0.9778	0.9778
p	-	-	-	0.1108		0.2144	0.2375	0.1829	0.0324	-	0.4676
A_c	-	0.9848	0.9848	0.8991	-	-	-	-	-	0.9848	0.9848
A_m	-	0.7649	0.2595	0.6259	-	-	-	-	-	0.7649	0.8413
Dil	0.8343	0.8792	0.8652	-	-	0.8656	0.8027	0.6246	0.6647	0.7825	0.9208

Table 15 Coefficients of determination of literature formulations and formulation generated by the model on the test case experimental data *(Mazzarisi et al., 2020a)*.

The quality of the phenomenological model and literature formulations were evaluated by referring to the coefficients of determination R^2 in Table 15, to consider the deviations of the actual Y values of the test case from the values predicted by the models. The predictive phenomenological model demonstrates a substantially better output for each characteristic by comparing the R^2 coefficient values of different formulations. Except for the penetration depth ($R^2 = 0.4676$), it seems to be efficient. Literature formulations also describe the above outcome, which suggests a significant uncertainty in the

forecast. Based on the formulations in Table 14, it is worth providing a physical explanation coming out from the proposed phenomenological model.For the definition of W, the equation ($P\ V^{-1/3}$) is plotted in Figure 42a. In the prediction of W, laser power plays a major role: this sounds physically rational as an increase in laser power produces an increase in the energy density available for melting powders and substrates. as well explained in Barekat et al. (2016). The buoyancy and Marangoni forces control the geometry of the melted pool: the buoyancy forces are produced by the liquid material density variation, which is therefore a temperature and input energy function. A temperature rise moves the hotter material outwards, expanding the pool. The translation speed has an opposite effect on the width of the track. Both the volume of powder injected per unit of length and the energy density used for melting are involved in it.

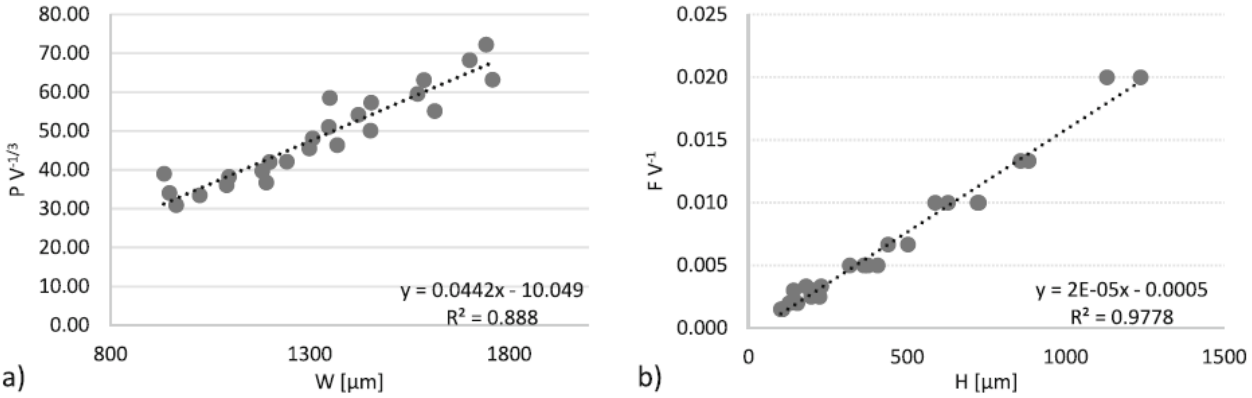

Figure 42 Plot of combined parameters against actual characteristics of a width and b height (Mazzarisi et al., 2020a).

Laser power (P) plays a marginal function in the proposed H forecasting formulation, similar to those found in the literature. The quantity of powder deposited per unit of length is determined by the translation speed (V) combined with the powder feed rate (F). In fact, the relation ($F\ V^{-1}$) reveals a noticeable coefficient of determination (see Figure 42b). As reported in De Oliveira et al. (de Oliveira et al., 2005) when the translation speed increases there is a reduction of laser-material interaction time. Therefore, the fraction of powder that exceeds the temperature of melting decreases, producing a lower height cladding. Besides, the increase in the translation speed results in a decrease in the amount of powder supplied per unit of length, which also causes a decrease in height.

Figure 43(a) underlines the complexity in the determination of p by the model (low R^2). The effect of parameter V in the literature is also discordant, resulting in some formulations being positive (Ansari et al., 2016; El Cheikh et al., 2012; Erfanmanesh et al., 2017) and negative in others (Barekat et al., 2016; Nabhani et al., 2018). Usually, at the central point of the deposition, the maximum penetration depth is determined. Areas with irregular shapes can result from laser processing issues, such as the irregular distribution of powders or a tilt angle between lasers, powders, and substrates. Barekat et al. (Barekat et al., 2016) pay great attention to the parameter P, which defines the energy density: there are higher temperatures with the increase in laser power, causing higher turbulence in the pool. The increase in penetration into the base material results from these turbulences. As it subtracts part of the input energy, the powder feed rate has a negative effect on p, which therefore does not reach the substratum.

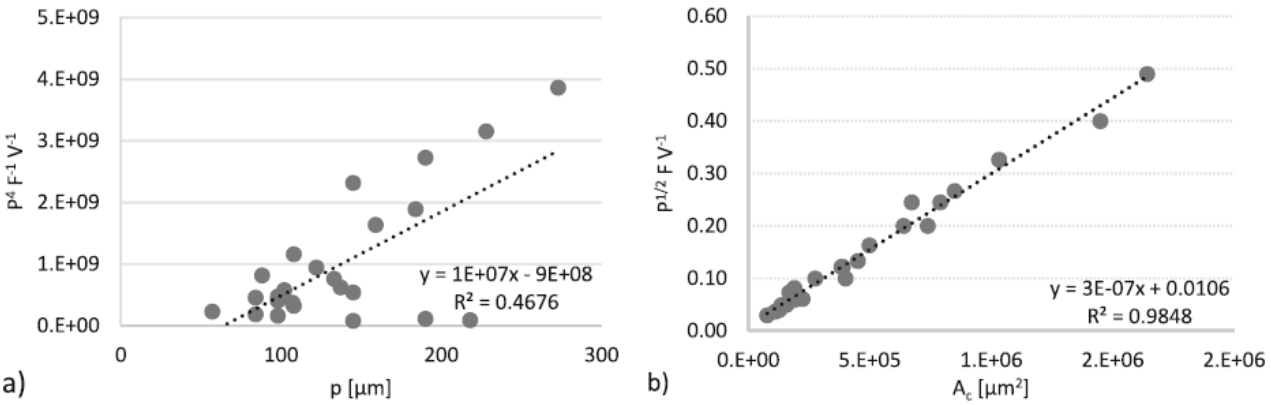

Figure 43 Plot of combined parameters against actual characteristics of a penetration depth and b clad area (Mazzarisi et al., 2020a).

For the prediction of A_c, the formulation ($P^{1/2}$ F V^{-1}) shown in Table 14 is plotted in Figure 43(b). The fundamental parameter, as already stated for H, is the powder mass per unit of length F V^{-1}. The laser power takes greater importance, as it is fundamental in determining the width of the clad. As P increases, a wider track with constant height is obtained, increasing the clad area.
Similarly, the outcomes of the A_m formulation are shown in Figure 44(a), having an intermediate behaviour between W and p. Laser power remains the fundamental parameter, considering the Marangoni and buoyancy forces. The model has a higher R^2 than p, as it avoids the aforementioned asymmetry problems.

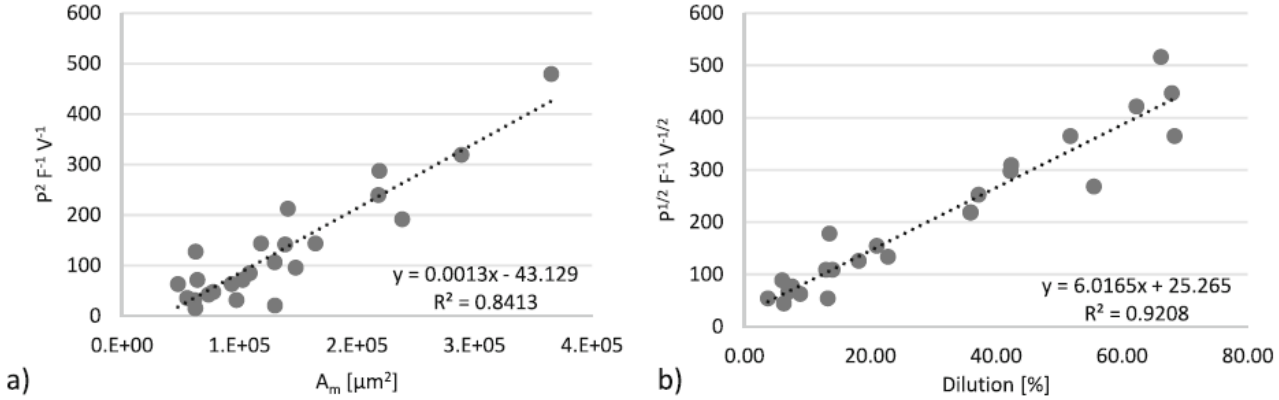

Figure 44 Plot of combined parameters against actual characteristics of a) molten area and b) dilution (Mazzarisi et al., 2020a).

The dilution is governed by parameters that have opposite effects on the areas. A rise in F has a positive impact on A_c and a negative effect on A_m. There is a superposition of effects in Dil that makes the powder feed rate the most significant parameter as shown in the formulation ($P^{1/2}$ F^{-1} $V^{-1/2}$) plotted in Figure 44(b). P and V have the same weight but have the opposite effect on the dilution predicted. A slow deposition allows a significant amount of energy to be released per unit of clad length, but the volume of powder supplied per unit of clad length increases at the same time. Both areas are increased by such phenomena, keeping the ratio constant.

3.5.12 Conclusions

The proposed combined parameters created by the phenomenological model on a general test case show excellent performance compared to the classic models present in the literature.
It can be stated, as a general conclusion, that the predictive phenomenological model proved to be worth predicting the geometrical outcome of components generated by DLMD. The possibility of training the model to capture the real phenomenological relationships between process parameters through a few learning tests makes it sustainable for the process of this Additive Manufacturing technology to be quickly set up.
The generalization of the model concerning different materials can also improve the design of dissimilar materials deposition in order to create Functionally Graded Materials (FGMs). In future applications, it is possible to further assess the forecasting capabilities of the phenomenological model by adjusting the number of depositions and materials.

3.6 Influence of Standoff Distance and Spot Diameter on Direct Laser Metal Deposition of a Nickel-based superalloy

The quality of the final parts produced by DLMD, in terms of dimensional accuracy and surface regularity, is strongly affected by many process parameters. Plenty of studies were carried out so far in the literature, to explore the best combination of process parameters and deposition strategies in order to optimize the process and maximize the final quality of the workpiece (Dubourg and St-Georges, 2006; Ludovico et al., 2010). Most of all, the production of thin-walled parts is achieved by the overlap of many single-tracks, in which the former acts as a base for the subsequent layer. Therefore, the occurrence of localized deposition defects (for instability of the powder flow or the laser power) may have a cascade effect on the overall quality of the workpiece. These inaccuracies affect the flatness of the deposition surface, modifying the nozzle standoff distance (or working distance).
The standoff distance between the nozzle and the substrate is a critical process parameter. In fact, by varying this parameter it is possible to modify the spot dimensions of the laser beam and the powder stream imprint on the workpiece surface. Moreover, in case the system is equipped with a non-adjustable laser beam collimator, changing the standoff distance is the only way to focus the laser beam. The study of the effects of these parameters on the process and the investigation of the best strategies to mitigate them are essential.
In the literature, studies have shown that the standoff distance affects the deposition efficiency and the surface quality in direct laser metal deposition. Zhu et al. produced thin-walled metal components that have different conditions for powder and laser defocusing distances. The results showed that when the powder focuses below and the laser focuses above the top surface of the substrate, a high surface quality can be obtained (Zhu et al., 2012).

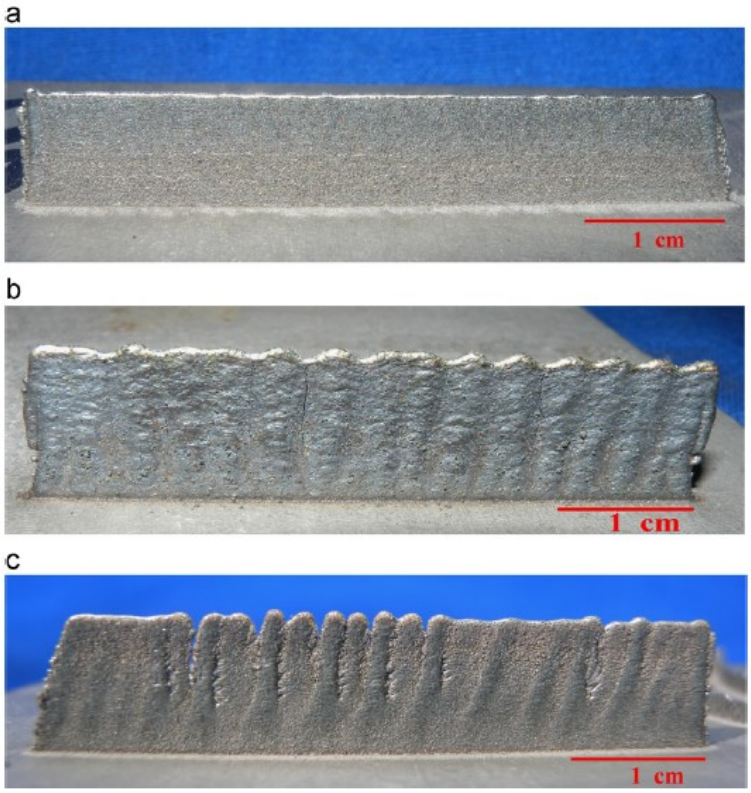

Figure 45 Front view of the thin-walled parts with different powder defocusing distances:(a) Zp -1 mm;(b) Zp 0 mm;(c) Zp +1 mm (Zhu et al., 2012).

The influence of the standoff distance on the final component quality was similarly examined by Pinkerton and Li. Three alternative approaches were analysed to change the standoff distance between a track deposition and the subsequent one. Experimental results showed that good layer consistency can be achieved under tested conditions without relative movement between nozzle and substrate for walled parts up to 10 mm thick, and mediocre results were obtained through normal movement. Finally, a model was developed to analyse the distribution of temperature and estimate the size of the molten pool as a function of the standoff distance (Andrew J. Pinkerton and Li, 2004).
Tan et al. performed a study on the effect on the height of the single deposited clad of the standoff distance. The work documented that with the increase of the standoff size, the height of the single deposited clad rapidly increases and then

decreases slowly. The authors compared this pattern with the trend of the concentration of powder mass along the powder flow vertical symmetry axis (Tan et al., 2012).

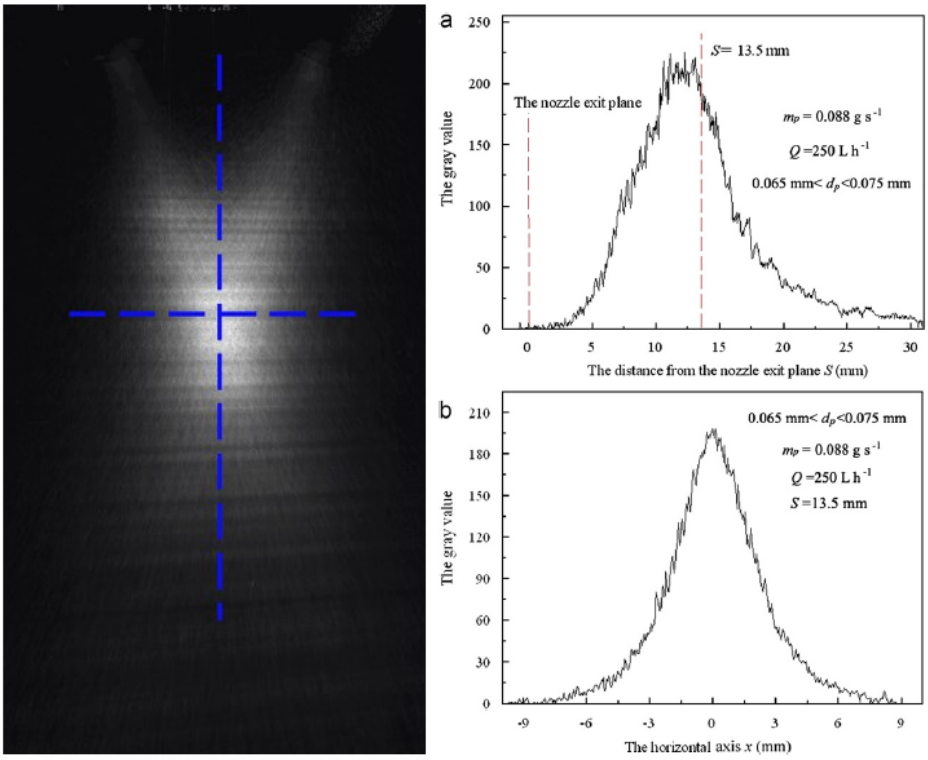

Figure 46 Powder flow image and variation of grey values along (a) vertical axis of symmetry and (b) horizontal axis (Tan et al., 2012).

The effects of certain process parameters, such as translation speed, powder feed rate, and laser power, on the characteristics of deposition are clear in the literature. On the other hand, it is vague and describes findings that are still not very robust in terms of the impacts on the single-clad dimensions of laser spot diameter and standoff distance.
This research aims to investigate the effects on the geometrical characteristics of the single deposited clad of two important process parameters, laser spot size and standoff distance. During the development of thin walls, the variations of the standoff distance and laser spot will simulate the possible changes in the regularity of the deposition.

3.6.1 Experimental conditions and procedure

A series of single clad deposition were performed on a 6 mm thick AISI 304 stainless steel plates, sized 100 × 160 mm, which chemical composition is shown in Table 3. The Nickel-based superalloy powder, which composition is shown in Table 4, was used as deposition metal.
The prototype DLMD system adopted for experimental testing, is meticulously described in Section 2.10. The laser beam was measured using a rotating pin-hole beam profiler (Primes Focus Monitor). The beam and intensity distribution profiles are shown in Figure 29.
Tests carried out were characterised through a geometrical analysis of the cross-sections of the clads, which were obtained by cutting them in transversal direction by means of the AbrasiMet 250 metallographic cut-off machine. A polishing process was performed, aiming to make the surface of the cross-section highly reflective and free of scratches and deformations. The samples thus prepared were observed through Nikon Eclipse MA200 inverted optical microscope for micrographic analysis.

3.6.2 Experimental plan

A full factorial experimental plan with five levels of standoff distance and three levels of laser spot diameter was carried out. Table 16 shows the values chosen for the two varied process parameters (independent variables). The other process parameters are kept constant, based on previous tests, as listed in Table 17.

Parameter	Unit	Notation	Factor Levels				
			1	2	3	4	5
Laser spot diameter	mm	d	1.0	1.5	2.0	-	-
Standoff distance	mm	hs	-3.0	-1.5	0.0	1.5	3.0

Table 16 Experimental plan.

Parameter	Unit	Notation	Value
Laser power	W	P	600
Translation speed	mm/min	V	500
Powder feed rate	g/min	Q	5.0
Carrier gas flow rate	l/min	G	3.0

Table 17 Constant process parameters.

A total of 15 combinations of process parameters were tested. Three replications were performed for each combination of process parameters. Figure 47 displays a schematic representation of the experimental work carried out according to the investigated process parameter variations. This study focused on the variation of geometrical characteristics of the deposited clad by changing each of the two investigated process parameters.

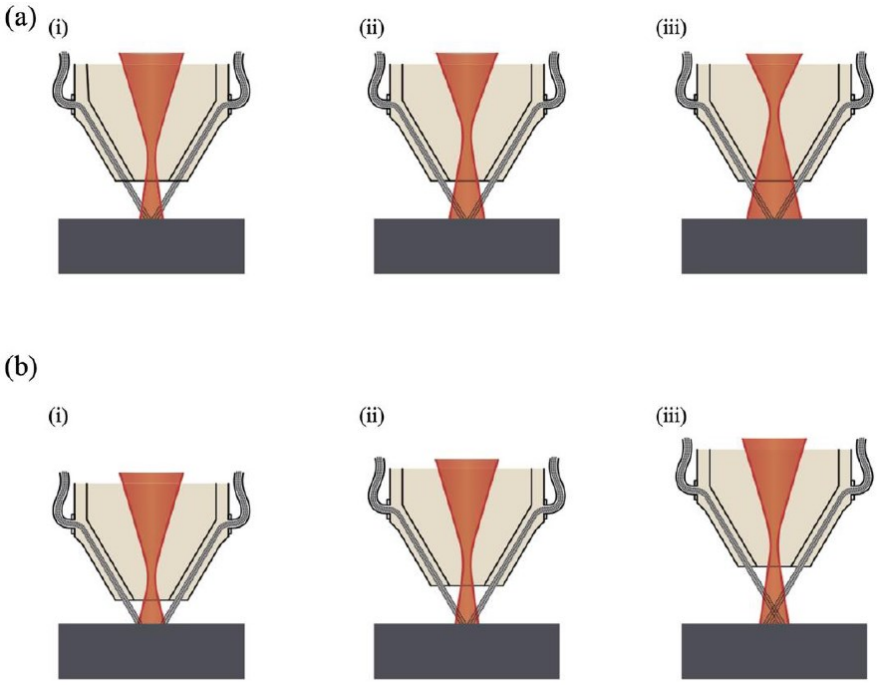

Figure 47 Schematic representation of the process in some employed configurations: a) varying the laser spot diameter b) varying the standoff distance.

Each clad was cross-sectioned, as shown in Figure 48, and analysed by means of an optical microscope. In order to investigate the statistical significance of the effects of the two analysed process parameters on the quality of the deposited clad, the analysis of variance (ANOVA) with a general linear model was used. The analysed data set included the same number of observations for each combination of factor levels. The ANOVA procedure involved the use of *P*-value, defined as the maximum level of significance, which in this case was considered equal to 0.05 (Marzban et al., 2015).
The geometrical characteristics of the clad considered were:

- Clad width (*W*)
- Clad height (*H*)
- Penetration depth (*p*)

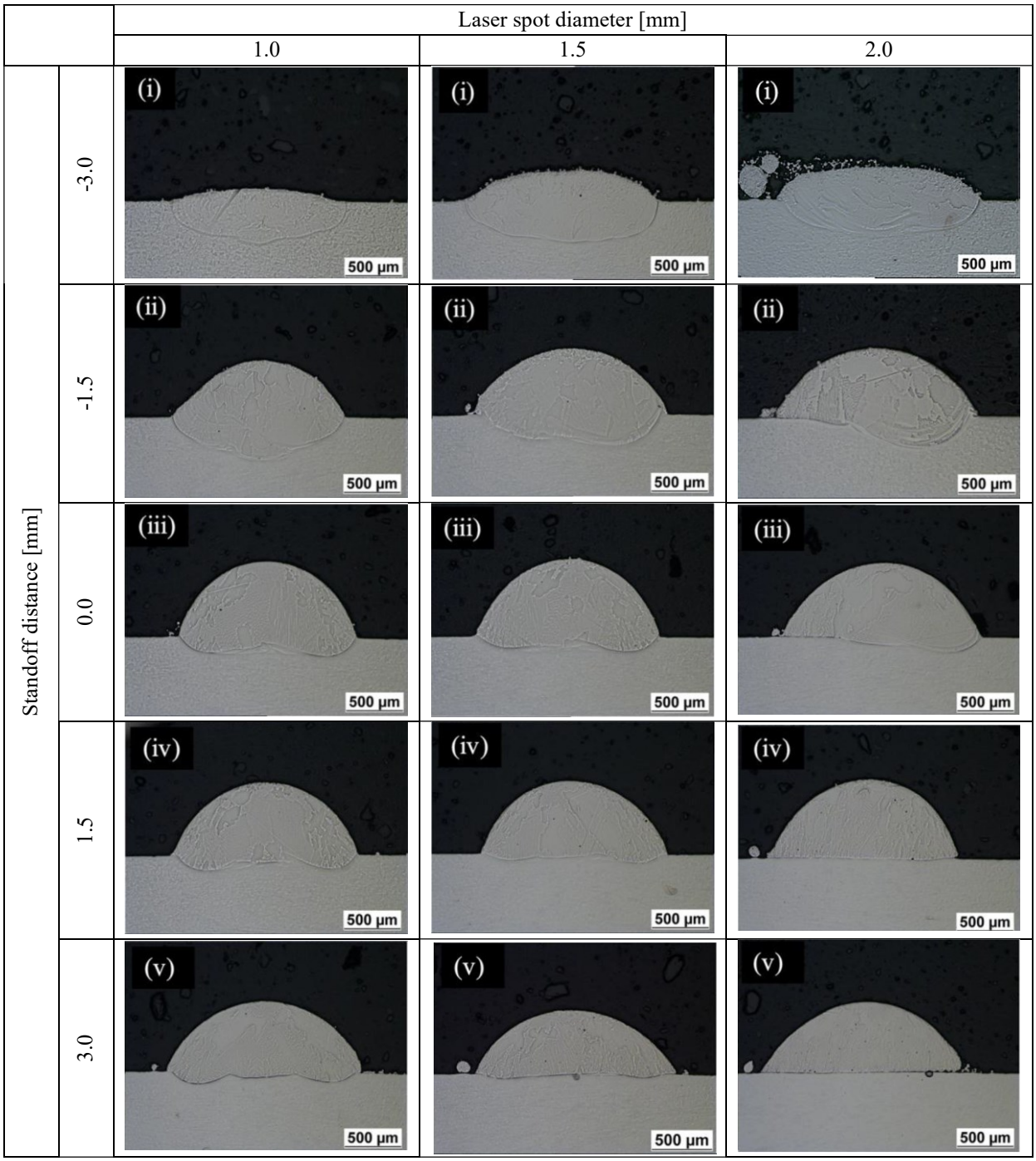

Figure 48 Cross-section macrographs of deposition tests.

3.6.3 Effect on the clad width

In laser cladding and 3D manufacturing applications, an important variable for the DLMD technology is the clad width, which mainly dependent on the molten pool size (Ocylok et al., 2014). Figure 49 shows the effects of the laser spot diameter (d) and standoff distance (hs) variations on clad width (W). Each plotted value is the average of measures taken on three replications performed using the same set of process parameters.

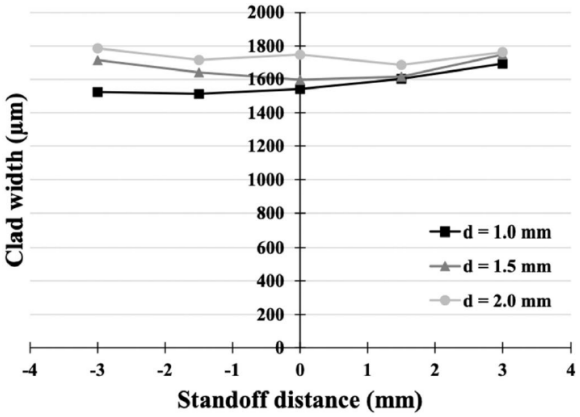

Figure 49 Influence of standoff distance and laser spot diameter on the clad width

Figure 48 shows cross-section macrographs in which the clad width increased with the laser spot diameter. Similar effects were also deduced from the study of Tan et al. and Zhang et al. (Tan et al., 2012). The explanation for this result stems from the fact that the laser focus upwards in order to increase the spot size on the deposition surface, as it can be seen in Figure 47(a). Therefore, the laser irradiation area expands and the interaction time between laser beam and substrate increased, creating a larger molten pool and increasing the width of the single clad deposited. The powder focus was located on the surface of the substrate when the standoff distance was on standard position (0 mm). It can be observed that the standoff distance variance had a slight impact on the clad width for any value of d. Similar effects were also stated in the width model of a single track established by Zhu et al. (Zhu et al., 2012). The width model of a single deposited clad, modified from Liu and Li (Liu and Li, 2005) is the following:

$$W = 2\left(\frac{PA(1-r_p)d^{1/2}}{2(T_m-T_0)\sqrt{\pi\lambda v\rho c_p}}\right)^{1/2} \quad (6)$$

where P (W) is the laser power, A is the laser absorptivity, r_p is the reflectivity factor of powder (from Pinkerton and Li (2004b)), d (mm) is the laser spot diameter, Tm (K) is the melting temperature, T_0 (K) is the initial temperature, λ (W/m K) is the coefficient of thermal conductivity, v (mm/s) is the laser translation speed, ρ (kg/m^3) is the density and c_p (J/kg K) is the specific heat.

However, results found through this experimental work differed from outcomes obtained through the model shown in Eq. (6) for a calibration coefficient k equal to 0.667. This coefficient can be traced back to the use of a nickel based superalloy powder, which is different from the material of the substrate. Furthermore, it must be said that accurate values of the physical properties of this particular superalloy were not known because covered by copyright. Hence, the values of the physical properties of the AISI 304 stainless steel at 1000 °C, as listed in Table 18, were used in the model.

Parameter	Unit	Notation	Value
Absorptivity	-	*A*	0.35
Reflectivity factor of power	-	*rp*	0.09
Melting temperature	K	*Tm*	1650
Ambient temperature	K	*T0*	290
Thermal conductivity	W/m K	λ	28.12
Density	Kg/m^3	ρ	8000
Specific heat	J/Kg K	*cp*	500

Table 18 Physical properties of AISI 304 stainless steel.

Other process parameters kept constant in the model are listed in Table 17. Therefore, the width model can be modified as follows:

$$W = 2k\left(\frac{PA(1-r_p)d^{1/2}}{2(T_m-T_0)\sqrt{\pi\lambda v\rho c_p}}\right)^{1/2} \quad (7)$$

As can be seen from the model shown in Eq. (6) and (7), the standoff distance did not affect the clad width. Figure 50 shows the comparison between experimental and calculated values of clad width. It was therefore possible to notice an excellent correlation between experimental and model outcomes, which make it a useful tool for a careful forecasting of the clad width.

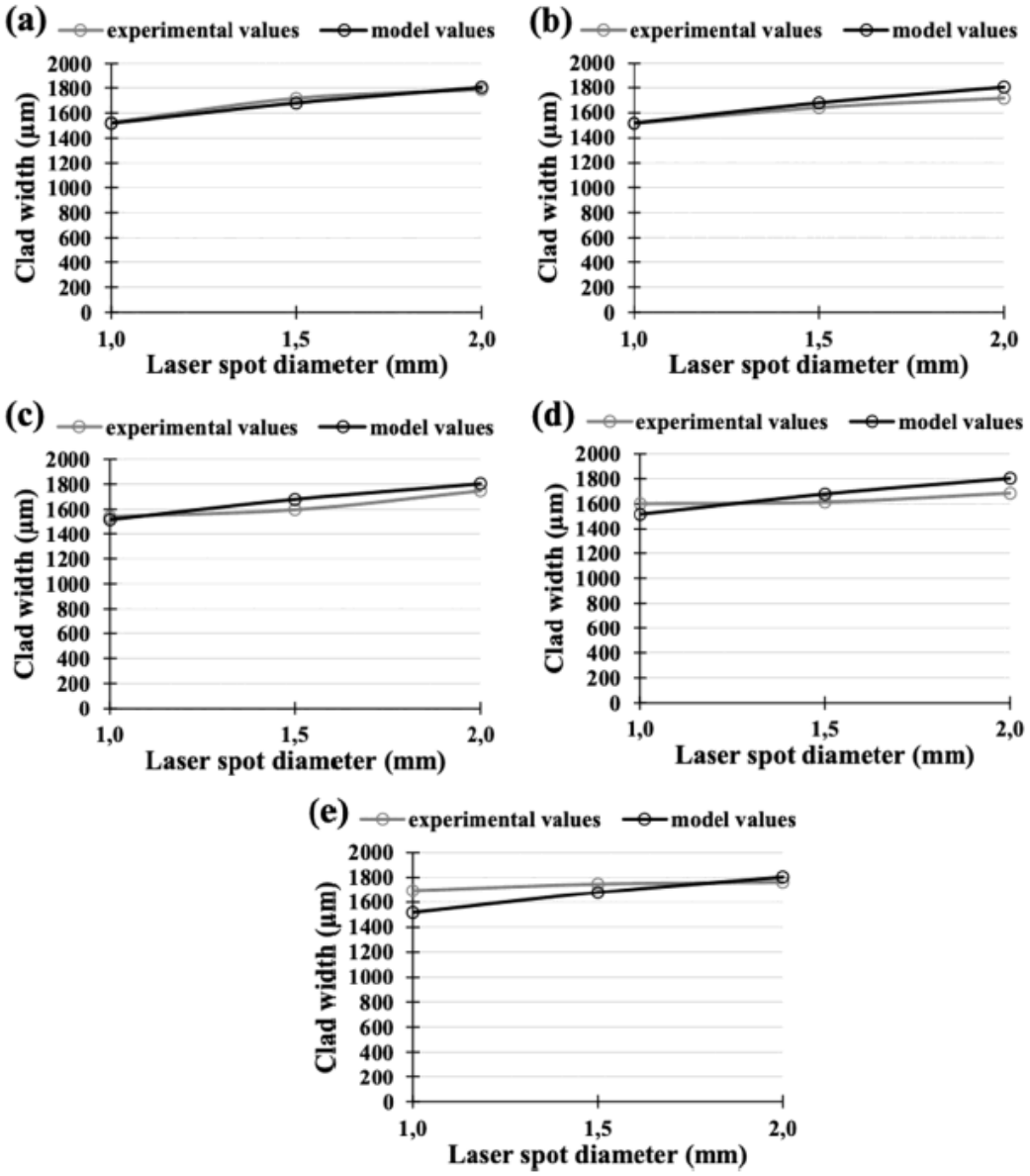

Figure 50 Comparison between experimental and calculated values of clad width versus spot diameter at different standoff distances: (a) H = -3.0 mm; (b) H = -1.5 mm; (c) H = 0 mm; (d) H = 1.5 mm; (e) H = 3.0 mm.

3.6.4 Effect on the clad height

The clad height is another very crucial geometrical feature of the laser deposition. This geometrical characteristic is important for the control of the production accuracy in vertical direction (Zhang et al., 2007). In Figure 51 are shown the effects of the laser spot diameter and standoff distance variations on the clad height (*hs*).

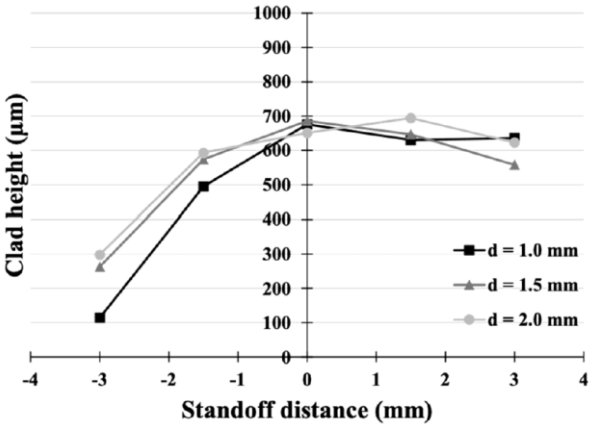

Figure 51 Influence of standoff distance and laser spot diameter on the clad height

The effect of laser spot diameter on clad height is not clearly evident. In Figure 51 it is noticed that the spot size had no influence on the clad heigh, while was detected a strong relationship with the standoff distance. Figure 48 shows that the clad height increased very quickly in the transition of *hs* from a value equal to -3 mm to -1.5 mm, with respect to the standard position. In fact, at such a low standoff distance, the powder stream meets the substrate before focusing, and the altered powder distribution on the substrate results wider. During the toolpath, the laser beam intercept a low number of powder particles and released almost all its energy on the substrate, creating deposition with a lower clad height and greater penetration depth. The powder flow was better defined when the standoff distance is equal or larger than the standard position, in which the powder focus move above the surface of the substrate and the laser can interact with more powder. Besides, the shadowing effect produced by the powder stream originates a more uniform distribution of the laser energy on the substrate.
Further increases in *hs* caused the change of powder focus, and after an initial phase in which the clad height increase with the standoff distance, a slight decrease was observed. The maximum track height was detected at standoff distance of standard position (0 mm), when was equal to the powder focus length, as also stated by Zhu et al. and Tan et al. (Tan et al., 2012; Zhu et al., 2012).

3.6.5 Effect on the penetration depth

As previously mentioned, the variation of laser spot diameter and standoff distance affects the molten pool, thus influencing the penetration depth of the single clad deposition.

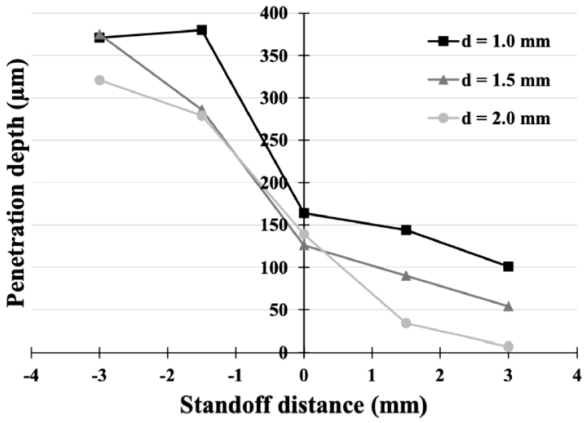

Figure 52 Influence of standoff distance and laser spot diameter on the penetration depth

Figure 52 shows that the penetration depth decreased while the laser spot diameter increased. This trend is clear in Figure 48, especially in clad cross-sections obtained using *hs* equal to 3.0 mm. The laser power density was analysed to explain this effect. Eq. (8) shows the formulation of laser power density (*D*).

$$D = \frac{4P}{\pi d^2} \quad (8)$$

From the Eq. (8), the increase in laser spot diameter resulted in a decrease in the average density of laser power and thus a lower incidence on melting the substrate. This effect caused a decrease in the penetration depth of the molten pool.
The penetration depth decreased almost linearly with the increase of the standoff distance in Figure 52. At the same energy density, operating at closer standoff distances, a reduced amount of energy is captured by the powder to create the clad. The remaining fraction is released onto the substrate, enlarging the molten area. Instead, increasing the hs a huge quantity of energy is captured by the powder flow led to a rapid increase in the clad area and a decrease of p, which practically became zero at too high hs values. Hence, the clad appeared to be glued or simply lied on the substrate. Essentially, the standoff distance governs the fraction of laser energy captured by the powder or released towards the substrate. The standoff distance is also the distance travelled by the particles before reaching the substrate, which also indicates the interaction time with the laser beam, if the powder flow velocity is considered constant.

3.6.6 Statistical Analysis

In order to statistically examine the effects of the two process parameters on the geometric characteristics of the single deposited clad, Analysis of Variance (ANOVA) with a general linear model was used. Five levels for the standoff distance and three levels for the laser spot diameter were evaluated. Three replications were performed for each combination of factorial levels. The main effect of the investigated factors were analysed: it represents the average effect of an independent variable (*d* and hs) on the dependent variable (*W*, *H*, and *p*). The threshold for the *P*-value is set equal to 0.05, below which the effects of each factor on the output were statistically significant. If the effect of the factor was statistically significant, it means that its variance was not equal to zero. Table 19 summarised the results of the ANOVA, which confirmed previous analyses and considerations concerning the clad width. It is found that only the laser spot diameter had a statistically significant influence on the clad width (*P*-value = 0.002), while for the standoff distance a *P*-value equal to 0.106 was obtained. Otherwise, the standoff distance has a statistically significant influence on the clad height, with a *P*-value equal to 0.000, while for the laser spot diameter a *P*-value equal to 0.227 was taken. Results confirmed that both *d* and *hs* are statistically significant for the penetration depth.

Factor	Notation	P-Value (W)	P-Value (H)	P-Value (p)
Standoff distance	hs	0.106	0.000	0.000
Laser spot diameter	d	0.002	0.227	0.004

Table 19 Analysis of variance for clad width (w), clad height (hs) and penetration depth (hi).

3.6.7 Conclusions

In this work, the effects of laser spot diameter and standoff distance variations on the geometrical characteristics of the single deposited clad was analysed. The clad width behaviour was studied through an analytical model and experimental measurements.
The variation of the standoff distance is a simulation of defects that can arise during the manufacture of multilayer components. It has thoroughly analysed how this affects the geometry of the clad and which strategy should be chosen to stem them. The use of a variable size laser spot is a solution which, by modifying the density and distribution of laser energy, could be used above all for the control of the width and penetration depth.
This research was a preliminary study that will be useful for monitoring the quality and accuracy of the future multilayer deposition carried out via a laser head fitted with the aforementioned advanced motorized optics device that enables the modification of laser spot size on the deposition surface, independently of the standoff distance.

4 MONITORING OF DLMD PROCESS

The direct laser metal deposition is a multifaceted process that involves, as explained in previous chapters, the contribution, and optimization of numerous parameters, including laser power, scanning speed, and powder flow. Furthermore, the deposition is affected by several boundary conditions that can drastically vary during production, for example, the substrate temperature that affects the dilution between clad and base material. Therefore, in order to achieve components with high-quality standards, required by some industrial sectors, it is unavoidable to perform an extremely accurate design of the main process parameters involved (Angelastro et al., 2011).
To be effective, the design of the process must be supported by a system that can record what happens during production, which can often last several hours. It is therefore essential to monitor this large amount of data to report the onset of production defects and, if necessary, apply strategies that can stem or repair these errors. Researchers are currently studying new devices and integrated adaptive approaches to monitor the process thus ensuring the final product quality.
Generally, the aim of the monitoring process is the improvement of the quality of the final product and process within a production cycle. However, quality assurance and process optimization are not the only relevant aspects. This also allows the observation of the process status during the manufacturing, the systematic collection of information, and the development of a series of automated process control actions (Purtonen et al., 2014).
As is known, process monitoring and control are essential methods for reducing the amount of waste, improving the reproducibility of the process, and saving costs. These methods differ in the capability to find the relationship between the process parameters and the good quality of the workpiece.
Process control is also generally divided into two categories: open-loop and closed-loop. What essentially differ is the feedback signal from the system. An open-loop control system performs completely based on input and the output does not affect the control action. A closed-loop control system looks at the current output of the process and adjusts it to reach the desired condition.
The lack of robustness and the uncertainty of final quality for parts manufactured using Additive Manufacturing is the relevant technological barrier limiting its industrial diffusion. The quality requirements in manufacturing environments and the high costs of additive manufacturing encourage the development of these feedback systems for adaptive control of process parameters (Everton et al., 2016).
Non-destructive testing (NDT) for AM metal parts is not a standardized procedure yet but the main agenda of ASTM and the International Standards Organization (ISO) has recently adopted (Gisario et al., 2019).

4.1 Metal Additive Manufacturing Defects

The monitoring systems have as their main purpose the identification of defects in the laser deposition process. These flaws can originate from fluctuations in the flow of gas, powder, or instability of the laser beam. Many studies have found that these compromise the mechanical performance of components up to the failure, when they are present in large quantities. Therefore, first of all, their timely identification and the application of protocols to prevent them is essential (Colosimo and Grasso, n.d.; Everton et al., 2016; Kim and Moylan, 2018).
DLMD and laser welding share the same defect categories (see Figure 53):

- **Porosity**. Two types of porosity can occur in AM processes. Porosity due to a lack of fusion between layers, which is caused by inadequate energy density in the melt pool. It has a jagged shape and usually manifests itself in the interface between layers or tracks. Gas porosity arises for the high powder flow rate, causing gasses to be trapped into the melt pool. It has a rounded shape and can develop along the entire clad.
- **Crack**. This is the result of differences in the coefficients of material thermal expansion or due to powder contamination.
- **Lack of fusion**. It usually occurs between cladding and substrate. The dilution between materials is essential to ensure a good bond. When this is limited or completely missing, a gluing between the two elements occurs, with extremely low bonding forces.
- **Residual stresses**. These are usually generated by inappropriate process design. The dimensional accuracy and performance of the component can be affected by residual stresses. Especially in large components, thermal stresses can result in the delamination of the part from the substrate.
  -

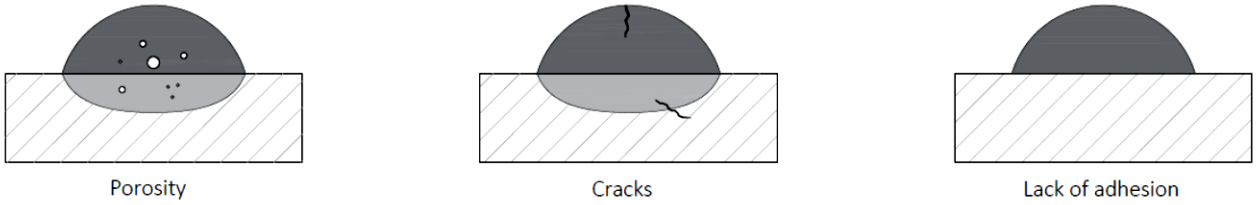

Figure 53 Main defects in DLMD process

4.2 Monitoring methods and sensors

The monitoring and control methods exploiting various physical phenomena that occur during the process. DLMD technology involves thermal, mechanical, and fluid dynamics events that require specific methods to be analysed. The approaches are also combined to enhance the efficiency of the monitoring (Purtonen et al., 2014; Tapia and Elwany, 2014). The main monitoring methods are:

- **Thermal methods**. These are the most utilized in the metal AM field, and are carried out using contact sensors such as thermocouples or contactless sensors such as pyrometers (single, double, or multiple bands) and thermal cameras. In measurements realised by pyrometers and thermal imagers, the workpiece temperature is determined based on the emitted radiation power. These are considered more inaccurate because they are related to the emissivity of the components. For an accurate temperature measurement, the emissivity must be known or estimated. Estimating emissivity is complex as it is a function of the part temperature. Moreover, thermal imaging cameras showed advantages over pyrometers, being the first a full-thermal field technique and not a point-to-point technique (Liu et al., 2017).
- **Optical methods.** These are frequently used for their versatility due to the contactless device and availability of a large amount of information. Optical methods provide limited information regard the shape of the treated area on the component surface or the powder flux. Lighting is essential in this method. Achieved through narrow-spectrum lamps or lasers, it aims to reduce the contrast. Charge-coupled device (CCD) and complementary metal-oxide semiconductor (CMOS) image sensors with related filters are currently the most widely used sensor types for optical monitoring particles (Wirth et al., 2018).
- **Acoustic methods.** These are usually applied to processes involving melting or vaporization of metal. When these are applied in-process, they are useful for monitoring rapid phase changes and crack propagation. The techniques are also employed in post-process activities for quality control of final components, indicating the occurrence of porosity and cracks. Acoustic emissions are detected with piezoelectric sensors connected to the workpiece. Non-contact acoustic detection is faster but inaccurate because the acoustic emission in the air can be subject to disturbances (Gaja and Liou, 2018).

4.3 In-situ monitoring of Direct Laser Metal Deposition of a Nickel-based superalloy using infrared thermography

The temperature field is the core feature to track in the DLMD process. It can be measured using contact sensors (thermocouples) or contactless sensors (pyrometers and thermal imaging systems). There are some measurement uncertainty caused by high contact temperatures in commercial thermocouples, so contactless sensors represent an acceptable option for this form of operation. The thermographic analysis carried out by means of an IR thermal camera seems the most appropriate solution to detect the thermal behaviour of the process. The temperature of metallic powder depositions was investigated by several research groups, showing the most impacting process parameters and implications.

In order to record the melt pool temperature field, Farshidianfar et al. used a thermal camera and measured the cooling rate, which is considered the paramount factor affecting the microstructure and the overall quality of the clad. The instantaneous heat flux, which depends on several variables such as scan speed, laser power, and laser beam size, was exploited to describe the thermal parameters. Thus, authors defined some combined indices to determine the clad consistency (Farshidianfar et al., 2016a, 2016b).

Campanelli et al. stated that deposition defects depend heavily on peak temperature and cooling rate. They tracked the thermal field in the DLMD processes by employing an IR thermal camera, for the deposition of a nickel based superalloy powder on a stainless steel substrates. The effects of thermal cycles on clad geometry and dilution were examined, taking into account the effects of preheating due to previous depositions on the same sample (Campanelli et al., 2017b).

A monitoring framework constituted of a high-resolution IR camera (see Figure 54), permitted to Liu et al. to perform a real-time temperature detection of the Inconel 718 deposition by LENS process. The impacts on the molten pool temperature and cooling rate of deposition variables have been studied. A positive association between molten pool temperature and dendrite arm spacing (DAS) was also found by authors (Liu et al., 2019).

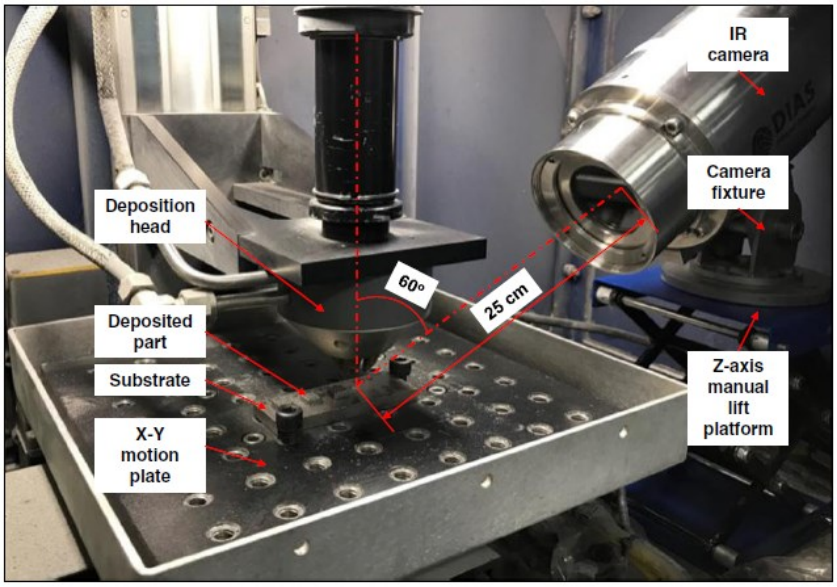

Figure 54 The IR camera apparatus (Liu et al., 2019).

Thermal analyses are often assisted by numerical simulation. Several simulation categories have been developed to investigate different features of the deposition process such as Finite Element Models (FEM) for the analysis of thermal field and thermal-induced stress (Mirkoohi et al., 2018; Zhan et al., 2018) and Computational Fluid Dynamics (CFD) models to highlight the internal dynamics of the melting pool (Song et al., 2019; Wolff et al., 2019).

The numerical results are useful for investigating the relationship between thermal history and deposition microstructure. The combination of the thermal gradient (G) and the solidification growth rate (R) processed by numerical simulation of additive processes enables the final microstructure and mechanical characteristics to be predicted. (Du et al., 2018; Gan et al., 2017). In solidification maps, appropriate for the prediction of deposition microstructure variations produced by changes in process conditions, values calculated for different alloys were summarized. (Blecher et al., 2014; DebRoy et al., 2018).

A thermal analysis was carried out in the present research to understand the relationship between the key process parameters, the thermal fields produced during the treatment, and the effect on the characteristics of the cladding. Single-track depositions of a nickel-based superalloy that has only recently been studied in the literature by a few authors have been thoroughly tracked. (Liu et al., 2019; Wolff et al., 2019). The solidification maps technique were applied via a ground-breaking approach directly to the experimental data collected by the IR camera. Using this approach, predicting the microstructure lays the groundwork for more refined process monitoring and the generation procedure of relevant process conditions and parameter settings.

4.3.1 Machine setup and materials

In this work, thermographic data detected, by IR thermal camera, during DLMD process were subsequently elaborated off-line with specific suitable algorithms implemented in MATLAB to identify some thermal features.

4.3.2 DLMD setup

The nickel-based superalloy powder was deposited on a substrate of the same composition having a thickness of about 6 mm by the prototype DLMD system presented in Section 2.10. The granulometry of the powder used is in the range 15-45 μm and the chemical composition is shown in Table 4. Argon was employed as a carrier gas for the powder coming from an external powder feeder. The same gas is used as a shielding gas to prevent clad oxidation. Figure 29 shows the laser beam shape and the intensity distribution profiles adopted.

4.3.3 Thermographic setup

For the monitoring of the thermal behaviour of the cladding process, a system equipped with a FLIR MWIR SC7000 thermal imaging camera featuring a Focal Plane Array cooled detector with a high acquisition speed and 20 mK NETD (temperature difference corresponding to the background noise) was used. For remote data collection and analysis, Altair® software was used. Characteristic of a thermal imaging camera that mounts filtering lenses to measure various wavelengths, the capability to detect temperatures up to 2500 °C is to automatically set the correct lens based on the examined processes. There may be damage to the thermal imaging camera caused by critical environmental conditions. Noteworthy in this regard, an IR window in sapphire crystal, transparent to IR radiation, were realized and endowed with a Plexiglas safety system. Certain thermographic parameters were set accordingly. The acquisition interval was set at 250 seconds for every deposition. An image acquisition rate of 50 Hz was set, but the frequency for image elaboration was downgraded to 5 Hz with an integration time of 12 μs. This decision allowed a temperature range between 483 °C and 2117 °C to be observed. One of the greatest issues related to the use of thermographic analysis is the emissivity value of the nickel-based superalloy at high temperatures. The substrate was warmed up to 800 °C in an oven for the experimental assessment of the material emissivity. The value corresponding to the highest temperature considered was chosen and was assumed to be a constant in the molten pool. The emissivity variation at high temperature is considered negligible by Gan et al (Gan et al., 2017), while during the whole process monitoring, Farshidianfar et al. assume a constant value and consider the emissivity referred to powder material (Farshidianfar et al., 2016a).
To avoid the dangerous atmosphere produced by the laser, the IR thermal camera was located around 500 mm from the deposition area. By comparing the measurements in the thermal images and in the macrography, a dimensional calibration was carried out. Considering the resolution of the sensor, each pixel corresponded to an area of 0.25 mm^2 (0.5 mm length and width), in which the temperature signal was averaged by the sensor.

4.3.4 Experimental plan

Based on previous studies, the experimental plan included 8 treatments obtained by varying three process parameters: laser power (P), translation speed (V), and powder feed rate (F). The spot diameter (D) and the carrier gas flow were kept constant with values of 1.00 mm and 3 l/min, respectively. The parameters used for the current work were designed to prevent defects such as porosity and cracks. The experimental plan adopted is summarized in Table 20. For each of them, the amount of powder per unit of length (F/V), which is the ratio between the powder flow rate and the translation speed, and the energy density (E_d) was calculated as stated by Campanelli et al. (Campanelli et al., 2017b), and defined as shown in Eq. (9):

$$E_d = \frac{P}{V\,D} \quad (9)$$

Treatment #	P [W]	V [mm·min^{-1}]	F [g·min^{-1}]	E_d [J·mm^{-2}]	F/V [mg·mm^{-1}]
1	400	500	1.50	48	3.00
2	600	1000	1.50	36	1.50
3	400	500	2.50	48	5.00
4	600	1000	2.50	36	2.50
5	400	500	5.00	48	10.00
6	600	1000	5.00	36	5.00
7	400	500	10.00	48	20.00
8	600	1000	10.00	36	10.00

Table 20 Experimental plan (Mazzarisi et al., 2020b).

Parallel and spaced 10 mm apart from each other, the single tracks were deposited. To allow the cooling of the substrate and prevent the pre-heating effect from affecting the subsequent depositions, an idle time between every deposition was defined in 180 seconds, as described by Angelastro et al. (Angelastro et al., 2018).
The tracks were trimmed, polished, and chemically etched at the end of the deposition process. A metallurgical microscope, the Nikon Eclipse MA200, was used with a digital camera to analyse geometry and microstructure.

4.3.5 Thermographic analysis and maximum temperatures

A suitable algorithm was implemented in order to plot global thermal information about the DLMD process over time These thermograms referred to a single image reporting the maximum temperatures reached in every timestep. In the thermal maps of each deposition (Figure 55) can be distinguished the dimensions of the thermally affected zone, in which the temperature goes above the lower limit (483 °C). Additionally, in thermographic maps, it is simple to classify depositions with different translation speeds (500 and 1000 mm/min) that are marked by a different number of acquisition frames.

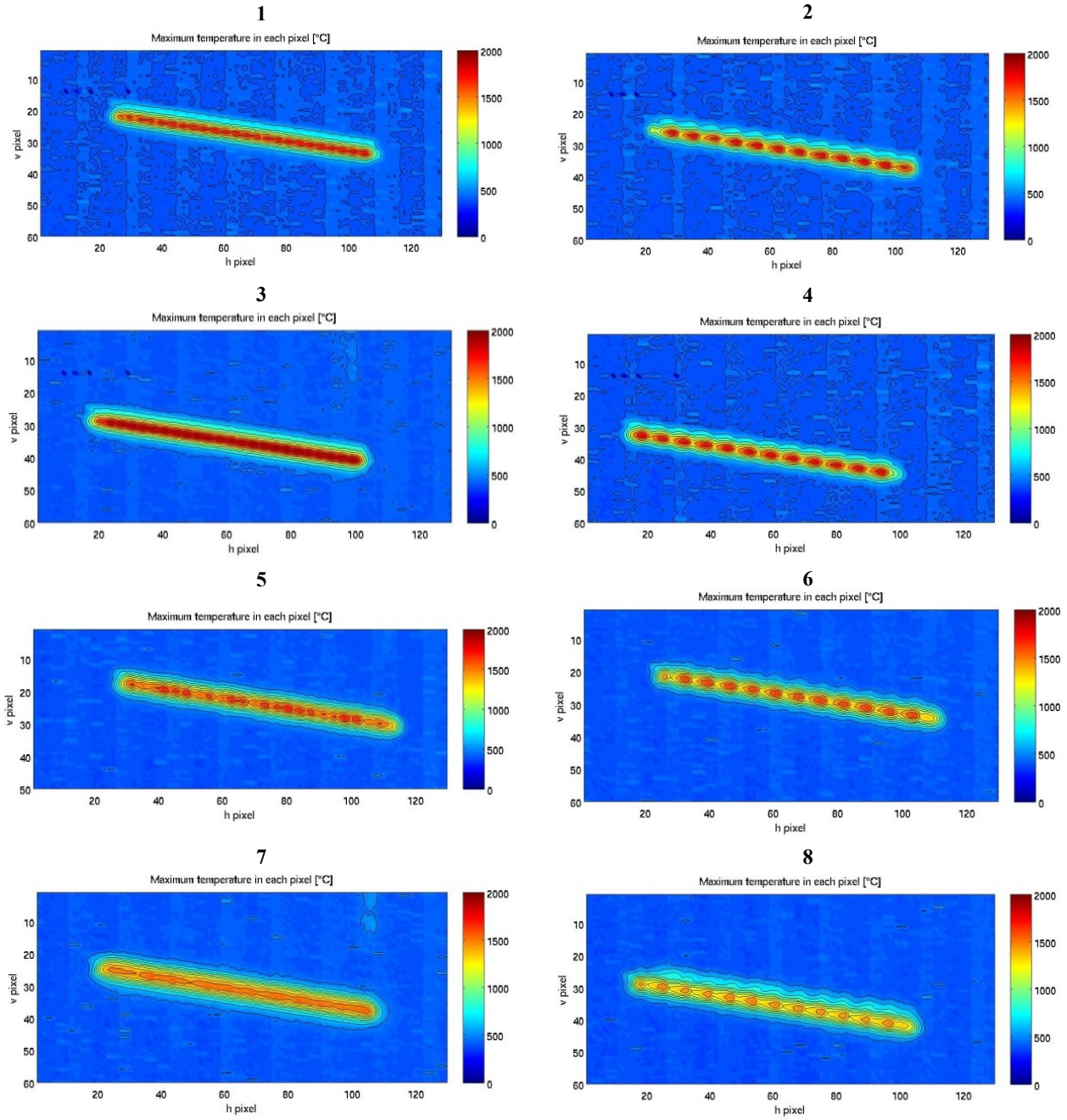

Figure 55 Thermograms with isotherms indicating the maximum temperature reached in every point of the deposition path for each treatment (ref. Table 20) (Mazzarisi et al., 2020b).

Maximum temperatures of each deposition versus time are plotted in Figure 56. Treatments at translation speed of 500 mm/min are represented with longer peak lines while those realize with 1000 mm/min are characterised by shorter lines. The alloy melting temperature (T_m) equal to 1350 °C is also marked in the dotted line plot: this helps to immediately observe that all depositions have reached a full melting as long as temperatures greater than T_m are reached.

Besides, the higher average maximum temperatures are achieved by depositions carried out at a lower powder feed rate (deposition 1, 2, 3, and 4). In these situations, the laser beam is partly shielded by a very small amount of powder. As the powder flow rate increases, temperatures drop significantly.

The deposition thermal behaviour is explained in the literature by taking into account only an intermediate point, representative of the entire phase (Arrizubieta et al., 2017; Emamian et al., 2017; Farshidianfar et al., 2016b; Muvvala et al., 2017). In this work, maximum temperatures and thermal behaviours were evaluated at three points chosen to describe the process and verify the homogeneity of temperatures in order to better compare the eight depositions: starting point, middle point, ending point.

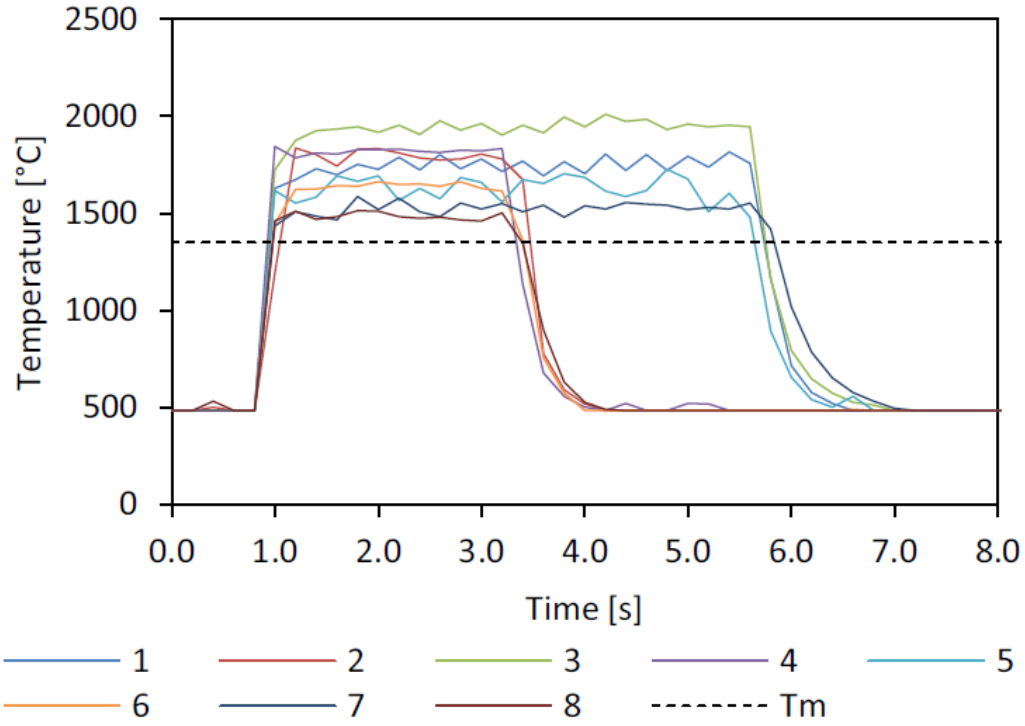

Figure 56 Maximum temperatures of each deposition and melting temperature versus time for each treatment (ref. Table 20) (Mazzarisi et al., 2020b).

The thermal cycle is shown in Figure 57 at the three key points of each treatment. Phases and microstructure of a metal alloy depend essentially on the maximum temperature and the cooling rate as a result of a thermal cycle (Arrizubieta et al., 2017; Everton et al., 2016; Luigi De Filippis et al., 2017). These thermal attributes were acquired from the thermal cycles.

The distance between the thermal cycles is strongly related to the translation speed of the heat source. The maximum temperature reached in the key points are recapped in Figure 58(a), where can observed the variation during the process and the influence of process parameters.

The average maximum temperatures are summarised in Table 21 and the results are plotted in Figure 58(b) as a function of F/V.

To appreciate the slope of the functions and the angular coefficients, a linear regression function is applied to the scattering points of *Figure 58*(b) grouping with respect to energy density, reflecting the energy extracted by the powder from the pool. The clear impact of the powder flow rate on the parameters characterizing the thermal field is evident when comparing the plots in *Figure 58*(b).

The slope of linear regression function of maximum temperature pass from -41.567 °C·mm/mg to -18.187 °C·mm/mg increasing the energy density of the process. As a consequence, the influence on the maximum temperature was 2.28 times higher in the deposition using less energy.

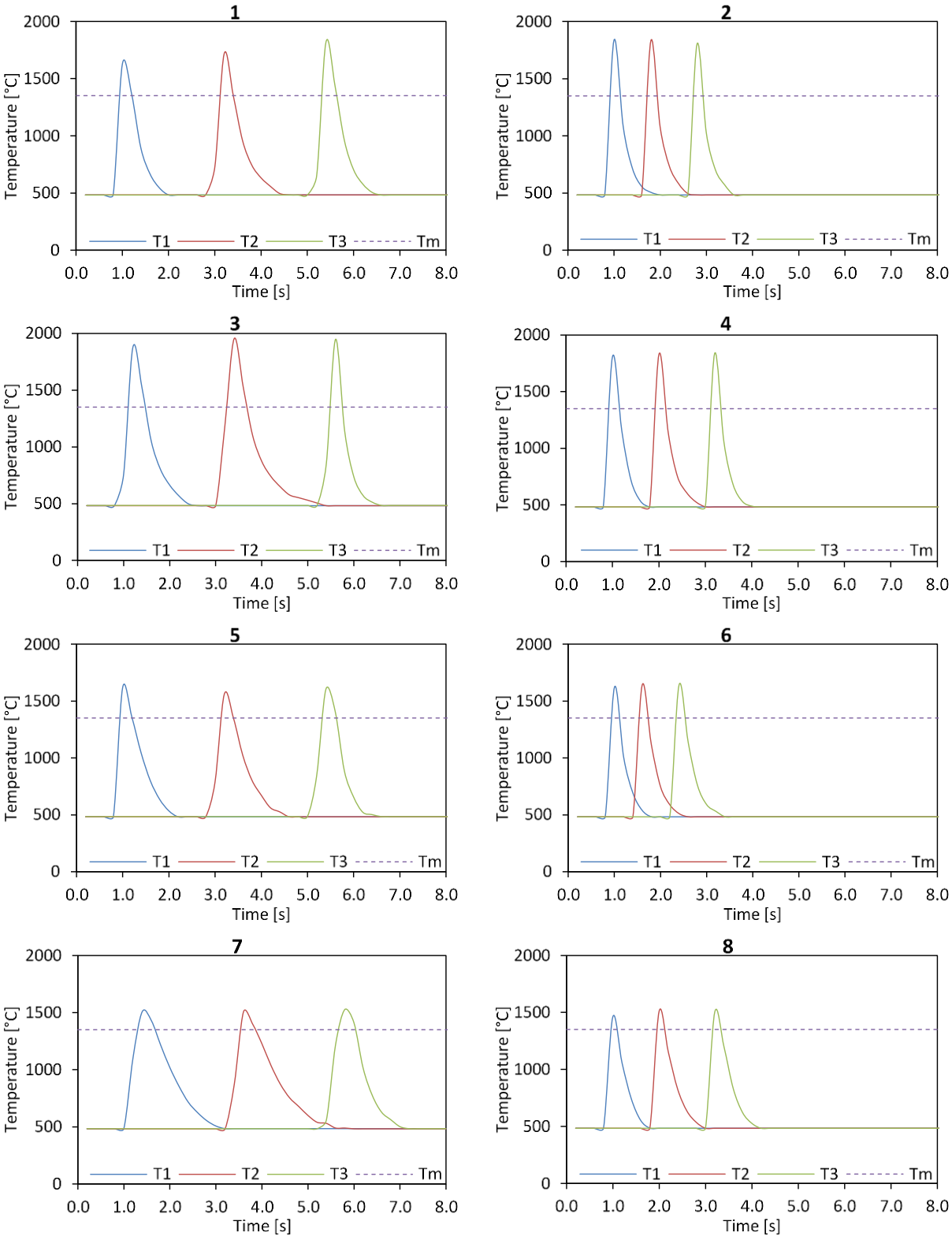

Figure 57 Comparison between thermal cycles of starting points (T_1), middle points (T_2), ending points (T_3), and the melting temperature (Tm) for each deposition (ref. Table 20) (Mazzarisi et al., 2020b).

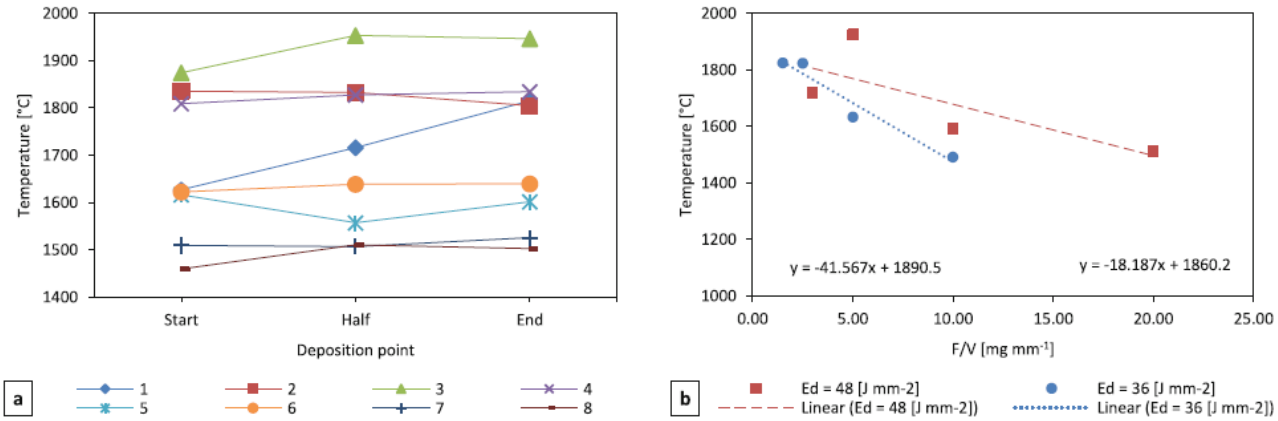

Figure 58 (a) Trend of maximum temperatures of the characteristic points for each deposition (ref. Table 20) and (b) influence of F/V and Ed (Mazzarisi et al., 2020b).

The robustness of the process was assessed by evaluating the average values of the maximum temperature and the relative deviations as in Table 21. The maximum temperatures had slight deviations with respect to the average value, in the order of 1.3%. It should also be noticed that in the faster deposition images, the lower deviations were captured, where the heat diffusion has less effect on the process's development. The use of the maximum temperatures as representative of the temperatures of the entire deposition is justified by the exceptionally low deviations.

Treatment #	**$T_{max,avg}$ [°C]**	**$T_{max,deviation}$ [°C]**	**$T_{max,deviation}$ [%]**
1	1719	64	3.7
2	1824	13	0.7
3	1925	34	1.8
4	1824	10	0.5
5	1592	23	1.5
6	1633	7	0.5
7	1514	8	0.5
8	1491	21	1.4

Table 21 Averaged maximum temperature, deviation, and percentage deviation from characteristic points for each deposition (Mazzarisi et al., 2020b).

4.3.6 Cooling rates

The cooling phase of the thermal cycle governs the microstructure and the associated mechanical properties. The cooling rate (C) is the slope of the cooling curve and was calculated at the key points of the tracks, according to Eq. (10).

$$C = \frac{\Delta T}{\Delta t} = \frac{T_{max} - T_{it}}{t(T_{it}) - t(T_{\max})} \quad (10)$$

Where:

- T_{max} is the maximum temperature reached at the point.
- T_{it} is the interaction temperature equal to 483 °C.

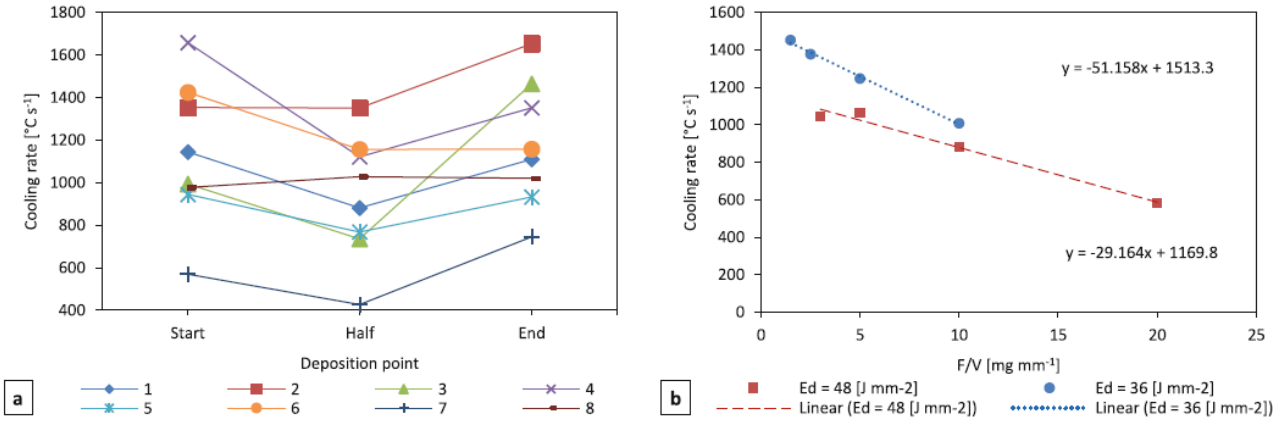

Figure 59 (a) Trend of cooling rate of the characteristic points for each deposition (ref. Table 20) and (b) influence of F/V and Ed (Mazzarisi et al., 2020b).

The trend of cooling rates in the characteristic points of each track is shown in Figure 59(a). Values significantly lower than the starting points (T_1) and ending points (T_3) were reported in the points at half of each deposition (T_2). The cooling rates were found to vary in the 400 - 1800 °C/s range, which largely corresponds to the values suggested by Muvvala et al., which also analysed a superalloy based on nickel. (Muvvala et al., 2017). The effects of boundary conditions on the study of starting and ending points are the causes of this phenomenon. The energy flow shifts here, causing an increase in the diffusion of heat and thus an increase in the cooling rate. In Table 22, examining the $C_{deviations}$, it is clear how the powder feed rate often affects the cooling rate.

In comparison to the maximum temperatures, there is a clear negative correlation between Ed and C, which decreases dramatically as the energy supplied to the substrate rises, as shown in Figure 59(b). Comparing the equations of the linear regression functions, the intercept has a 23% lower value as the energy density increases while the slope decreases by 43%.

As seen before, effects of varying energy density and powder feed rate have the same result in the cooling rate. Therefore, a superposition of effects occurs during the depositions, amplifying the whole trend.

Treatment #	**C_{avg} [°C·s^{-1}]**	**$C_{deviation}$ [°C·s^{-1}]**	**$C_{deviation}$ [%]**
1	1045	109	10.5
2	1452	134	9.2
3	1064	266	25.0
4	1376	187	13.6
5	881	76	8.6
6	1245	119	9.6
7	580	110	18.9
8	1008	21	2.1

Table 22 Averaged cooling rate, deviation and percentage deviation from characteristic points for each deposition (Mazzarisi et al., 2020b).

4.3.7 Thermal gradients

Generally, the thermal gradient (or temperature gradient) gives the rate of temperature variation, expressed with respect to the distance between the reference points. The thermal gradients (G) of the DLMD deposition were determined for each characteristic point using a spatial analysis performed by the IR thermal camera. For each deposition, the translation speed vector (Vs) and the normal vector direction (N) for the thermal gradient (see Figure 60(a)) were calculated.

The thermal gradient was calculated by means of Eq. (11):

$$G_y = \frac{\Delta T}{\Delta Y} = \frac{T_{yi} - T_{yi+1}}{Y_i - Y_{i+1}} \qquad (11)$$

The slightly tear-dropped form produced by the heat source in motion above the substrate and the considered vectors is shown in Figure 60(b).

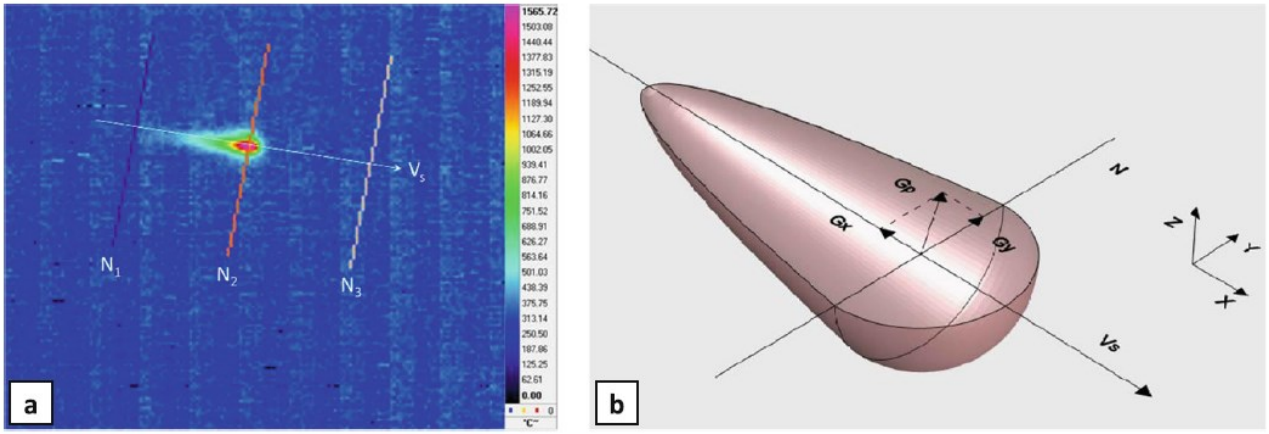

Figure 60 (a) Thermal map and (b) schematic representation of the melt pool with translation speed vector (Vs) and the normal direction (N) (Mazzarisi et al., 2020b).

Considering the camera resolution and the distance of the thermal camera from the treated area, the length ΔY was calculated. It was verified that each pixel has a dimension of 0.5 mm per side by comparing the dimensions of the heat zone from thermograms (measured in pixels) and the cross-section of the cladding examined by the microscope. A comparison between the temperature profile and the gradient profile, in the Y-direction, for the various main deposition points as shown in Figure 61.

The superposition of the plots shows the regularity of the key points in the temperature and gradient profiles. Due to image distortion induced by the inclination of the thermal camera with respect to the deposition process of approximately 30°, the temperature profile is slightly asymmetrical.

The thermal gradient calculated by numerical simulation was investigated in the literature only at the middle point of the deposition in which the conditions of the stationary process are defined (Gan et al., 2017; Lee et al., 2014). Thus, no evidence is provided of the thermal gradient trend along with the single track deposition. Besides, the experimental thermal gradient G observed in this study assumes values (100 - 900 °C/mm) that comply with the Lee et al. prediction of the numerical model for a Ni-based superalloy (Lee et al., 2014).

Table 23 shows the average thermal gradient on the Y-direction that represents the highest slope of the temperature trend, which usually appears outside of the molten pool. The $G_{y,avg}$ decreases with the increase of the powder feed rate. Hoverer, the $G_{y,deviation}$ does not show a significant correlation with the amount of powder intake in the molten pool. In Table 5, except for deposition 5, the average deviations assume not substantial values. During the procedures, the normal thermal gradient is kept substantially stable.

Figure 62(a) shows the trend of the thermal gradient for each deposition, where the strong impact of F/V on the thermal gradient G_y is clear. In Figure 62(b) the $G_{y,avg}$'s are plotted as a function of F/V, and a linear regression function is thus computed to quantifying the influences. The equation intercepts have comparable values, which suggest a minimal effect of E_d on the thermal characteristics of the maximum temperature.

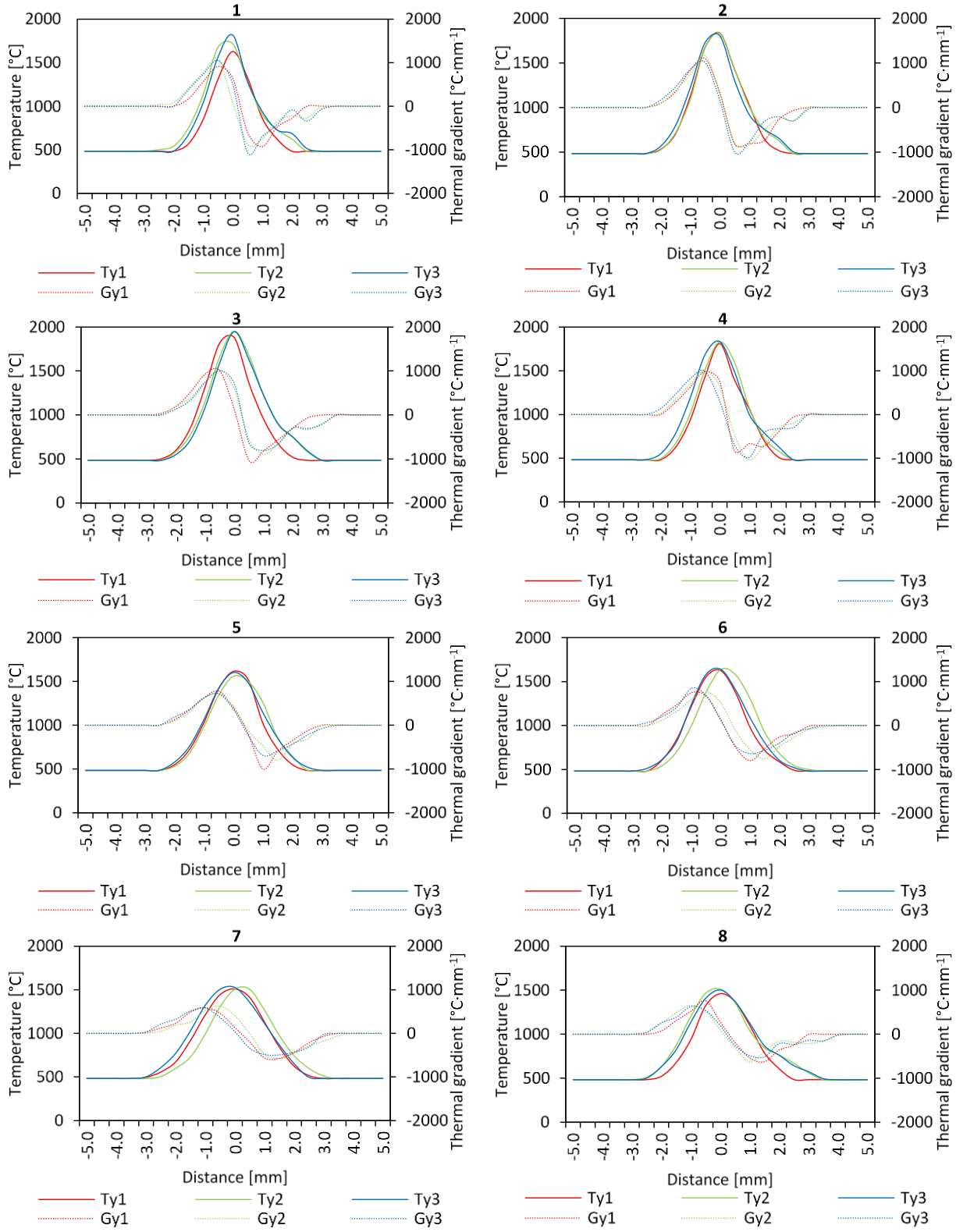

Figure 61 Comparison between the thermal gradients of key points for each deposition with Ty1, Ty2 and Ty3 temperature profile and Gy1, Gy2, Gy3 thermal gradient profile, on the Y-direction (ref. Table 20) (Mazzarisi et al., 2020b).

As the lateral zone is the largest region for the dispersion of heat during the process, the boundary effect present at the beginning and end of the deposition is slightly affected. Anyway, the G_y trend is mainly influenced by the translation speed that the powder feed rate in the first four depositions, in which there is reduced values of F (1.5 and 2.5 g/min). Generally, at the beginning and the end, the translation speed is always lower than the central point due to the acceleration

and deceleration ramp. The G_y values are therefore slightly lower than those of the central point, as the released energy is less localized. At the highest powder flow rates, the effect of acceleration and deceleration ramp on G_y is amplified by the shadowing effect on the laser. Therefore, moving on with the deposition, it is observed that the G_y, undergoes a slight decrease compared to the initial stage.

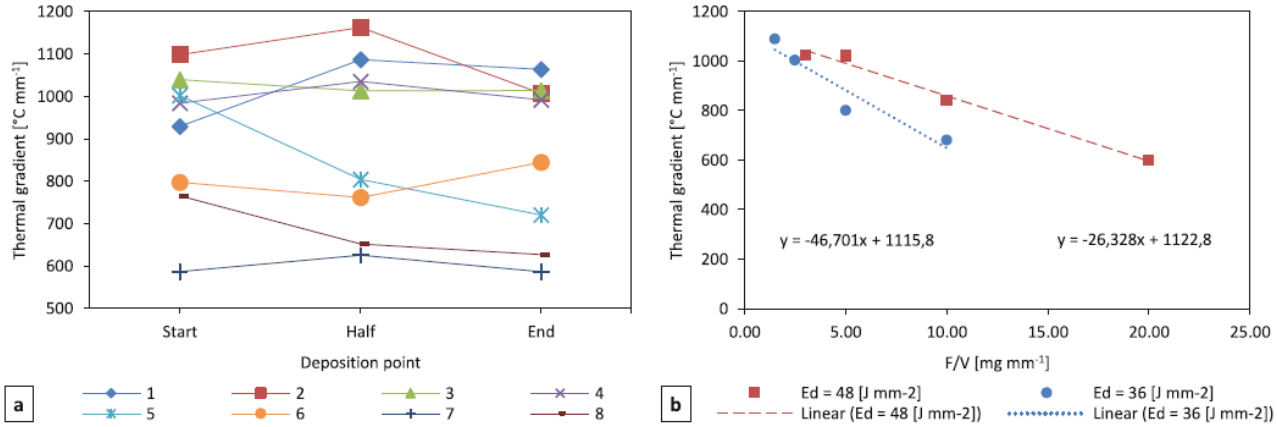

Figure 62 (a) trend of thermal gradients of the characteristic points for each deposition (ref. Table 20) and (b) influence of F/V and Ed (Mazzarisi et al., 2020b).

The slope of the G_y trend calculated with $E_d = 36$ J/mm^2 has values of 1.77 times greater than those using the $E_d = 48$ J/mm^2. The values obtained were normalized with respect to the corresponding peak values in order to compare the effect of the powder flow on various thermal characteristics. It should be noted that there is a greater effect on the thermal gradient than on the maximum temperature. For the monitoring of the DLMD process, this is crucial to understand, as a significant change in the gradient can cause a change in the deposition microstructure and the associated mechanical properties.

Treatment #	**$G_{y,avg}$ [°C·mm^{-1}]**	**$G_{y,deviation}$ [°C·mm^{-1}]**	**$G_{y,deviation}$ [%]**
1	1027	65	6.3
2	1089	55	5.0
3	1022	11	1.1
4	1004	21	2.1
5	842	107	12.7
6	801	29	3.6
7	600	17	2.9
8	682	56	8.2

Table 23 Average normal thermal gradient, deviation and percentage deviation from characteristic points for each deposition (Mazzarisi et al., 2020b).

4.3.8 Planar thermal gradient

The planar thermal gradient (Gp) that characterises the heat diffusion of the deposition track on the surface is obtained by combining the parallel (Gx) and normal (Gy) thermal gradients with respect to the translation speed vector (Vs), as shown in Figure 60(b). The vertical component of the thermal gradient (G_z) was tough to analyse by means of non-destructive thermographic techniques. The thermal gradient is directly connected with the base material volume. Therefore, the vertical component assumes lower values relative to the planar components for reduced substrate thickness. This makes the study of planar components appropriate to thermally describe the depositions. A common temperature range was chosen to define the planar gradient G_p of the deposition. The temperature range between the maximum temperature reached at the key point and the melting temperature (solidus), equal to 1350 °C, was set in order to analyse the molten pool dynamics. The thermal gradient along the axis of the laser spot translation can be defined through the cooling rate C_m, which is calculated in the temperature range between the maximum and the melting limit by means of linear interpolation of values. The cooling rate is the temperature variation in a point as a function of time. The variation is

produced by the heat source that moves at a given translation speed above the point. Hence the thermal variation between two points at a given distance is obtained by relating the cooling rate C_m to the translation speed. The G_x was calculated using Eq. (12) and the results are shown in *Table 24*.

$$G_x = \frac{\Delta T}{\Delta t}\left(\frac{\Delta X}{\Delta t}\right)^{-1} = \frac{\Delta T}{\Delta X} = \frac{T_{xi} - T_{xi+1}}{X_i - X_{i+1}} \quad (12)$$

Treatment #	$C_{m,start}$ [°C·s^{-1}]	$C_{m,half}$ [°C·s^{-1}]	$C_{m,end}$ [°C·s^{-1}]	$C_{m,avg}$ [°C·s^{-1}]	V [mm·s^{-1}]	G_x [°C·mm^{-1}]
1	1311	1845	1983	1713	8.33	206
2	3765	3771	3885	3807	16.67	228
3	1953	2139	4049	2714	8.33	326
4	3273	3441	3884	3533	16.67	212
5	1570	1042	1362	1325	8.33	159
6	3082	2604	2528	2738	16.67	164
7	730	637	1061	809	8.33	97
8	2010	1801	1524	1778	16.67	107

Table 24 Cooling rate Cm between the maximum and melting temperature of characteristic points for each deposition, average value, translation speed, and parallel thermal gradient (Mazzarisi et al., 2020b).

The thermal gradient G_y along the normal plan at the translation speed vector (V_s) was also estimated in the temperature range between the maximum and the solidus. The temperature was averaged on both sides of the molten pool to overcome the asymmetry of the thermal area. The parallel, normal, and planar thermal gradients are summarized in Table 25. The latter was estimated using Eq. (13):

$$G_p = ||\nabla T|| = \sqrt{G_x^2 + G_y^2} \quad (13)$$

The angle of the local heat flow direction (α) with respect to the normal plan, which is a function of the thermal gradients G_x and G_y (ref. Figure 60(b)) is reported in Table 7. As shown before, the powder flow rate affects the thermal gradients, and consequently also the angle of the planar thermal flow. In substance, G_y decreases as powder flow rate increases, and consequently, the angle α tends to grow.
As explained by DebRoy et al. (DebRoy et al., 2018), this angle is closely associated with the deposition microstructure, where the thermal flux determines the principal dendrite growth directions. Moreover, the undercooling can be quantified by comparing the dendrite growth angle and the local heat flow angle.

Treatment #	G_x [°C·mm^{-1}]	G_y [°C·mm^{-1}]	G_p [°C·mm^{-1}]	α [deg]
1	206	819	844	14.1
2	228	873	903	14.7
3	326	840	901	21.2
4	212	778	807	15.2
5	159	494	519	17.9
6	164	522	547	17.5
7	97	358	371	15.2
8	107	309	327	19.0

Table 25 Normal, parallel and planar thermal gradient and angle of local heat flow (Mazzarisi et al., 2020b).

4.3.9 Evaluation of geometrical characteristics and quality

The cross-section images of the deposited tracks were used to calculate width (W), height (H), depth (p), substrate melted area (A_{melt}), and clad area (A_{clad}) in the geometric shape analysis of solidified clads performed by means of the optical microscope, as shown in *Figure 31* in Section 3.3.
In order to quantify geometric factors and to define the consistency of the deposition, such as dilution and aspect ratio, these measurements were required. The volumetric mixing between the clad material and the substrate is indicated by the

dilution, following Eq. (14). To ensure bonding between the clad and the substrate while retaining the microstructure's homogeneity, the ideal value of this parameter should be about 10-30 percent.
The aspect ratio (AR) is calculated as the ratio between the width and height of the clad section (Eq. (15)). It is useful for evaluating the outcome shape of the track. In order to avoid tracks with small amounts of material added or clads too high to cause interclad porosities, an ideal AR range is usually set between 3 and 5.

$$Dilution\ (area) = \frac{A_{melt}}{A_{melt} + A_{clad}} \quad (14)$$

$$AR = \frac{W}{H} \quad (15)$$

Treatment #	W [µm]	H [µm]	p [µm]	AR [-]	A_{clad} [µm^2]	A_{melt} [µm^2]	Dilution [%]
1	1485	194	461	7.65	187872	519773	73.5
2	1630	47	410	34.68	39284	588488	93.7
3	1958	188	479	10.41	235583	615187	72.3
4	1521	29	471	52.45	30048	561964	94.9
5	1430	642	320	2.23	689263	320291	31.7
6	1505	343	314	4.39	353612	337763	48.9
7	1393	1217	377	1.14	1419124	327579	18.8
8	1440	650	216	2.22	699012	230994	24.8

Table 26 Geometrical characteristics of depositions (Mazzarisi et al., 2020b).

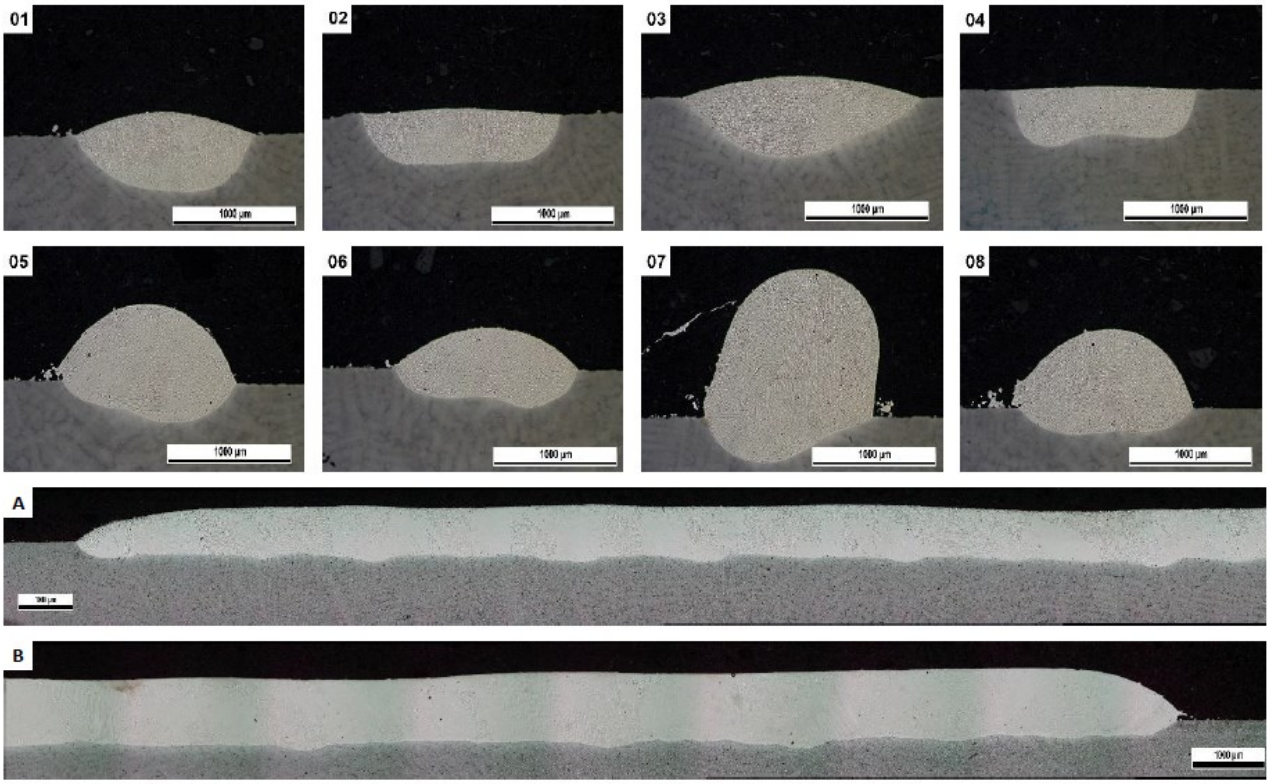

Figure 63 Transversal cross-section morphology per each deposition (ref. Table 20) and longitudinal cross-sections (A and B) (Mazzarisi et al., 2020b).

The macrographs of the transversal cross-section of clads obtained per each treatment and the longitudinal cross-section of treatment 5 are shown in Figure 63. The latter demonstrates that, over its entire length, the deposition microstructure is fine and homogeneous, with no noticeable welding defects, such as porosity due to trapped gas, lack of fusion, and cracks. Table 26 summarizes all the measured values per each track. The low powder flow rates and an excessive heat

transfer to the substrate produced an excessive dilution (sample 1, 2, 3, 4). These latter correspond to powder flow rates ranging from 1.5 g/min to 2.5 g/min, considered too low for the laser energy density tested. Even the aspect ratio provides some out-of-range values for the considered F range. Thus, at high powder flow rates, the best configurations from the geometrical characteristic point of view appeared.

4.3.10 Effects of thermal parameters on geometrical characteristics

The molten and clad area values versus the fundamental thermal parameters are plotted in Figure 64. A significant correlation exists between the maximum temperature and the melted area extension (see Figure 64(a)). This is likely related to the thermal energy input that induced a change in surface temperature, as observed by the IR camera. As previously shown the surface temperature varies strongly as a function of the powder income and its shadowing effect when it crosses the laser beam before touching the substrate. As the temperature in the region below the laser spot increases, the material melts and the dilution increase gradually. Therefore, the slope of the regression line was related to the thermal characteristics of base material and powder. Similarly, due to heat accumulation in the clad zone, the cooling rate and the clad area were strictly linked, as shown in Figure 64(b). As widely proved in the literature, F/V is the parameter which deeply influences the growth of the clad. Thermal energy allows the powder to melt, accumulating heat in the top region of the cladding. As the cladding increases in height, the region in which the heat can disperse is reduced, thus slowing down cooling times. The superimposition of the results of an increase in energy density reinforces this pattern. Consequently, tracks with a low AR (i.e. deposition 7) are characterised by cooling rates lower than those with an exponentially higher AR, thus also affecting the clad microstructure. In thin-wall manufacturing, this effect is intensified. The reduced wall-substrate interface and the preheating induced by previous layers are superimposed on these pieces, which greatly slow down the heat diffusion and change the thermal cycles. (Angelastro et al., 2018).

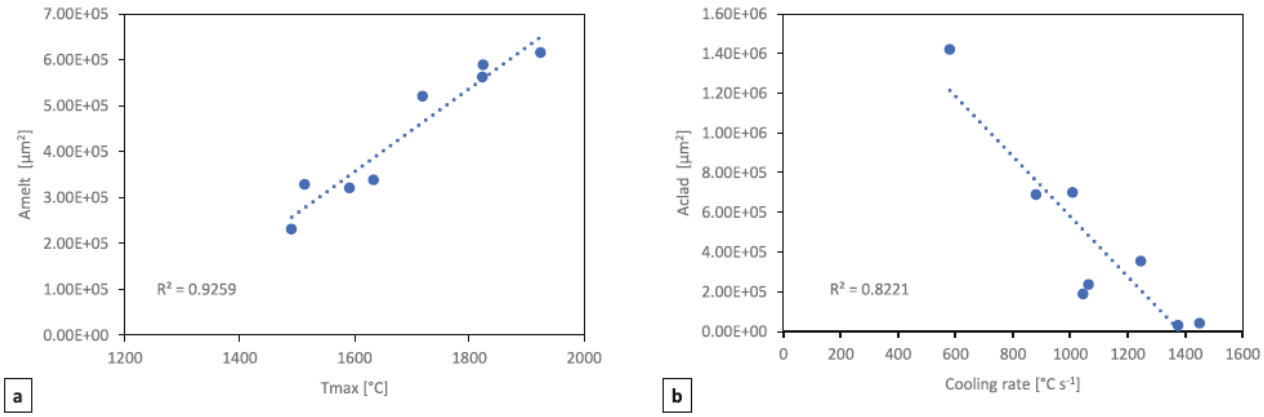

Figure 64 (a) Melt area vs maximum temperature and (b) clad area vs cooling rate (Mazzarisi et al., 2020b).

The study of the geometric factors was carried out in order to accurately track the deposition quality. Figure 65(a) shows the relations between dilution and thermal parameters. The dilution exhibits a strong correlation with the maximum temperatures exactly like the molten area. A good R^2 value is returned by the trendline and the regression function has been used to describe a temperature range useful for optimum dilution. The range adopted for the process conditions considered was between 1450 °C and 1560 °C. Monitoring the dilution through the measurement of the cooling rates was less detailed. A low coefficient of determination (R^2 = 0.6777) resulted from the regression function, with moderate uncertainty in the predictive model.

The second quality assessment regards the aspect ratio (AR). The plot in Figure 65(b) relates the AR (on a logarithmic scale) with the thermal characteristics. AR relates to linear dimensions, which are more difficult to predict to areas. The logarithmic regression function shows an adequate correlation with the cooling rate. Indeed, the AR is the proportion of the clad area of which, as previously proven, there was a strong correlation with the same thermal parameter. The optimum range is thus between 940 °C/s and 1030 °C/s for the experiments presented.

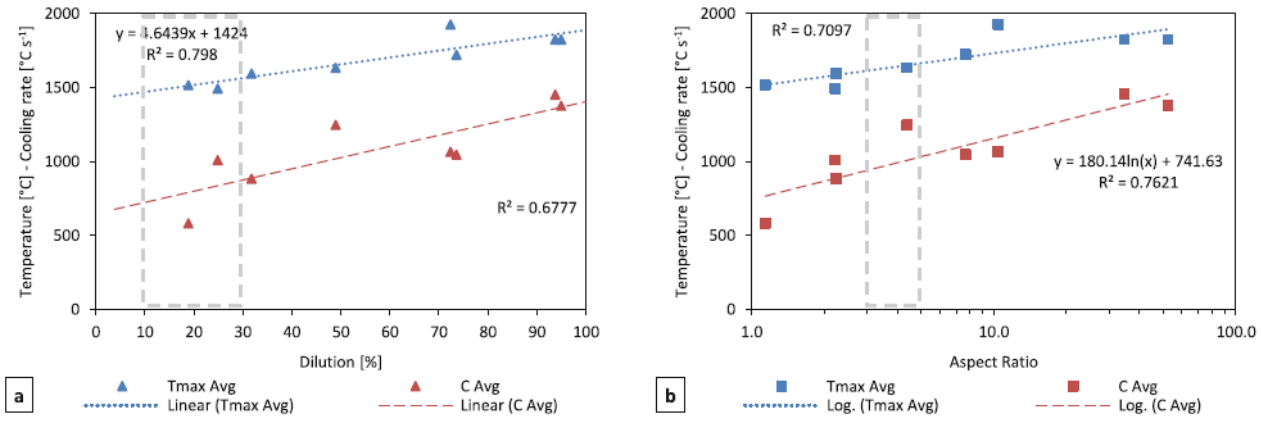

Figure 65 (a) Dilution and (b) aspect ratio vs maximum temperatures and cooling rates with the optimum range (Mazzarisi et al., 2020b).

A combination of the above parameters can be used to accurately predict dilution and aspect ratio, as defined by Wolff et al. (Wolff et al., 2019). The energy density on powder mass (E_f) is the ratio between the energy density and the F/V, as shown in Eq. (16).

$$E_f = \frac{E_d}{\frac{F}{V}} = \frac{P}{D \cdot F} \tag{16}$$

Therefore, the E_f summarized the effect on thermal parameters and geometric characteristics, previously defined. In Figure 66, the dilution correlation (logarithmic trendline) is very high ($R^2 = 0.9174$). The aspect ratio, on the other hand, is lower and the R-squared is lower. Output increases considerably in the AR range [3-5].

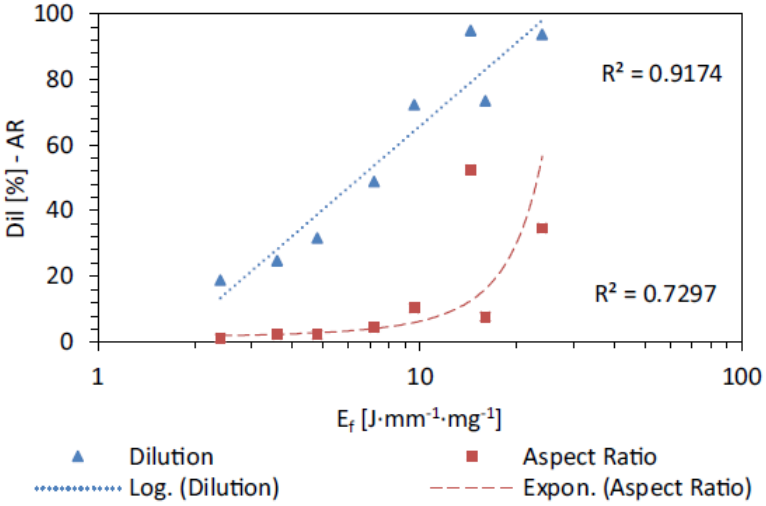

Figure 66 Dilution and aspect ratio vs energy density on powder mass (Mazzarisi et al., 2020b).

4.3.11 Solidification maps and microstructure

Generally, the thermal gradient (G) and the solidification growth rate (R) strongly influence the microstructure of the metal depositions constructed using AM technologies, as stated by Flemings et al. (Flemings, 2006). The solidification map method greatly summarized the effects of these parameters, introducing the G/R coefficient that describes the modality of solidification while the G·R coefficient that explains the scale of the solidified microstructure, as explained by DebRoy et al. (DebRoy et al., 2018). Usually applied using numerical simulations, the solidification map method was compared with thermal data obtained from experimental measurement. To overcome the lack of details obtained from the thermal analysis, several changes were introduced. In this work, the vertical component (G_z) was considered negligible, and the planar thermal gradient (G_p) was used for the study of the microstructure. Compared to the scanning speed in powder bed fusion processes, the deposition rate of DLMD applications is relatively low, and R was approximated with the translation speed of the laser. The solidification rate is a function of normal component (G_y) and vertical component

(G_z) of the thermal gradient, as described by Debroy et al (DebRoy et al., 2018). As previously stated, the influence of the latter was neglected for the specific boundary conditions of the test case, which corroborate the approximation. Furthermore, it was confirmed by the works of Gan et al. and Lee et al., in which the solidification growth rate of the superficial layer is considered close to the translation speed used for the deposition simulation (Gan et al., 2017; Lee et al., 2014).

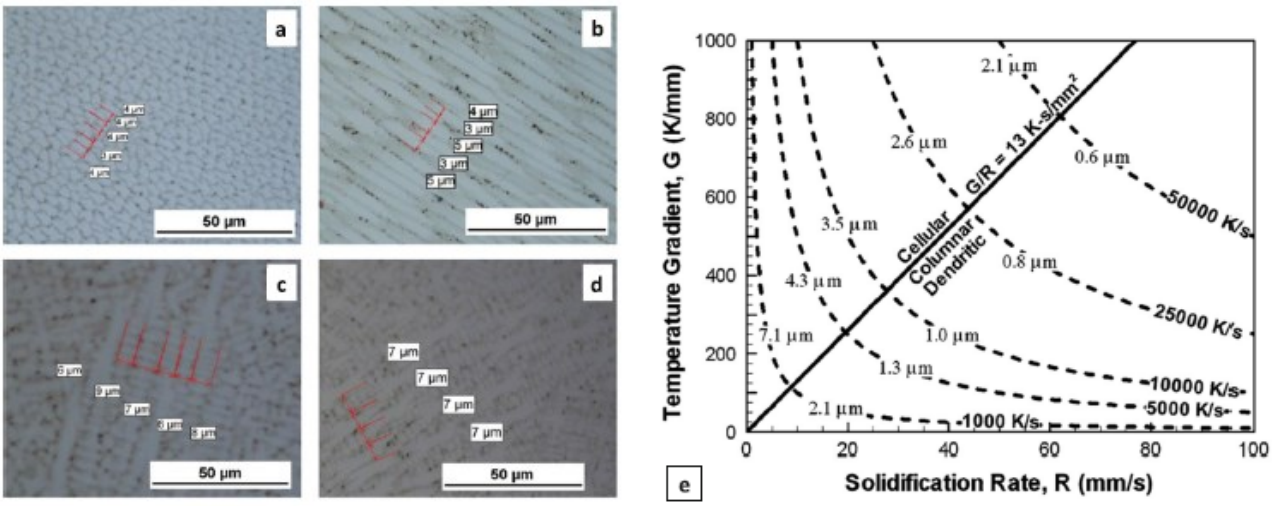

Figure 67 Microstructure morphology and grain size inside the clad: a) treatment 2, b) treatment 3, c) treatment 7, d) treatment 8, and e) solidification map of Blecher et al. (2014) for IN 690 (Mazzarisi et al., 2020b).

Figure 67 show the grain sizes measured in a different point of each deposition. The outcomes are recapped in Table 27. The deposition with a low powder flow rate (treatment 1, 2, 3, and 4) have an average grain size in the range between 3.8 µm and 4.2 µm, which greatly match with the values proposed by Blecher et al. (Blecher et al., 2014) for IN 690 in Figure 67(e). On the other hand, the average grain size increased for depositions from 5 to 8, distinguished by lower cooling rates, varying from 4.6 µm to 7.2 µm.

Treatment #	**G [°C·mm^{-1}]**	**R [mm·s^{-1}]**	**G·R [°C·s^{-1}]**	**G/R [°C·s·mm^{-2}]**	**Average Grain Size [µm]**
1	844	8.33	7031	101	4.2
2	903	16.66	15044	54	3.8
3	901	8.33	7505	108	4.0
4	807	16.66	13445	48	3.8
5	519	8.33	4323	62	6.8
6	547	16.66	9113	33	4.6
7	371	8.33	3090	45	7.2
8	327	16.66	5448	20	7.0

Table 27 Thermal parameters related to the microstructure morphology and grain size of some clad (Mazzarisi et al., 2020b).

The results presented in Table 27 demonstrated the great impact of the powder flow rate on thermal properties and average grain size. This also suggests that depositions have a better microstructure with a smaller clad area and hence with a higher aspect ratio. In deposition 7, which was distinguished by the lowest AR (1.14), the largest grain was detected by comparing the results of the average grain size and AR (in Table 26), while deposition 4, which had an AR of 52.45, also had a finer microstructure.

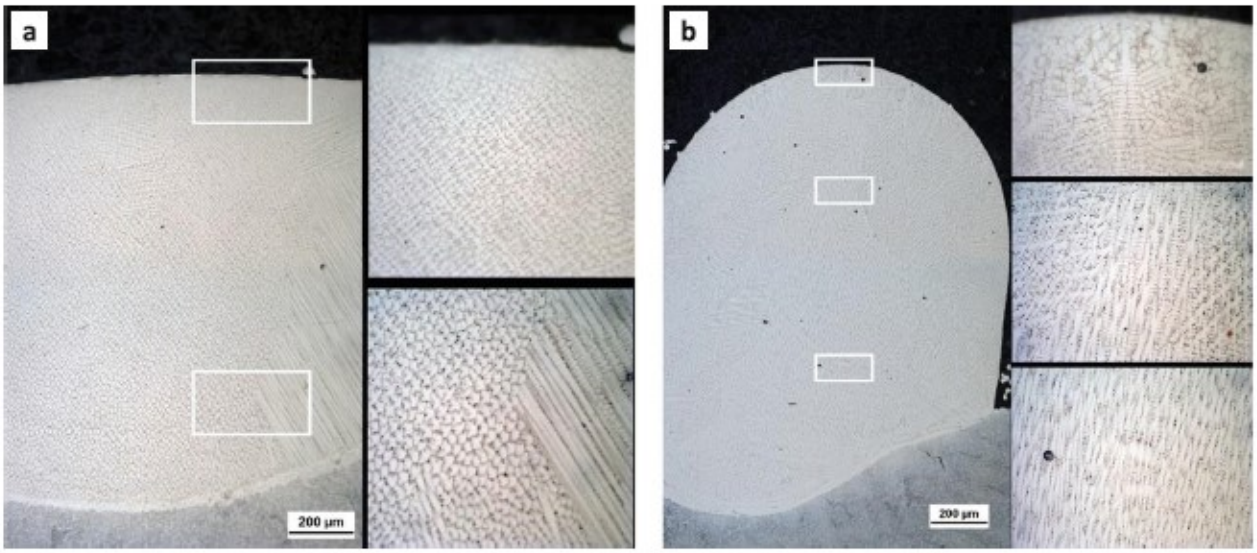

Figure 68 Microstructure morphology of the clad: (a) treatment 3 and (b) treatment 7 (Mazzarisi et al., 2020b).

Process parameters, mainly the powder feed rate, strongly affected the morphology of the clad microstructure. The main structure that characterises the depositions is dendritic, which assumes columnar, cellular, or equiaxial tendencies depending on the thermal history identified per each treatment. Concerning elevated and low powder flow, treatments may be divided into two categories. The structures of treatments 3 and 7, which have the same solidification growth rate and different thermal gradients, were examined to illustrate the microstructure differences.
Treatment 3 is characterised by a high G/R value and a very high G·R value, which indicates in the solidification map in Figure 67(e) a columnar dendritic structure tending to cellular and very fine grain size, as shown in Figure 68(a). The deposition has a homogeneous microstructure probably due to the low amount of powder intake.
Conversely, treatment 7 is characterised by the highest F/V value that causes a planar thermal gradient three times smaller than treatment 3. Examining Figure 68(b), there is a wholly different microstructure that changes along with the vertical development of the clad, as stated by Gan et al. (Gan et al., 2017). There is a dendritic grain, with a slight equiaxial trend, in the upper part of the clad. Low thermal gradients that characterise the region below the laser beam originate this microstructure, as shown by Lee et al. (Lee et al., 2014). In the central area the structure appears dendritic, with distinct primary and secondary arms. In the lower area, however, the structure appears dendritic columnar, showing smaller secondary arms and a more marked directionality of growth.

4.3.12 Conclusion

The monitoring of the DLMD process temperature field employing an IR thermal camera produced noticeable results. The thermal parameters representing the temperature distribution on the samples were affected by a set of process parameters and the best way to predict them is by analysing the energy density (E_d) and the powder flow rate per unit of length (F/V). As regards the clad geometry, the clad area is strongly correlated to the cooling rate, while the dilution can be adequately monitored by detecting the maximum temperatures and can be widely predicted using the energy density on powder mass (E_f).
The microstructure was examined by coupling the growth rate (R) and the planar thermal gradient (G_p) in the solidification map method. The experimental data are in good agreement with the solidification map created for a similar Nickel-based superalloy and has proven effective in predicting the size and morphology. It was strongly affected by the powder feed rate.
Multilayer depositions with various strategies and a method to determine the magnitude and impact of the vertical thermal gradient on thin walls will be considered for further applications of this research.

4.4 Thermal analysis of built-up strategies using DLMD

Nowadays, Additive manufacturing using DLMD technology makes it possible to carry out claddings and build three-dimensional components with extremely complex geometries. The deposition strategies (or patterns) therefore assume a role of primary importance in the design of the process. These strongly influence the heat diffusion generated during the process and consequently the microstructure and mechanical characteristics of the part, as well as the distortions of the base component. In the literature there are some works that investigate the most common deposition strategies and, in some cases, propose innovative ones.

Yu et al. studied the classic deposition patterns (raster and offset) and evaluated a new pattern, called fractal, in the Laser Solid Fabrication (LSF) process. Influences of the different deposition patterns on the deformation of the fabricated parts, internal quality and mechanical properties were investigated. The results of the simulations with the finite element method (FEM) indicate that the offset-out (deposition from the outside inwards) and fractal deposition patterns generate a circular symmetrical and eccentric temperature distribution respectively at the end of the deposition process, as shown in *Figure 69*. There are small temperature gradients using these two types of deposition compared to raster and offset-in (from the inside out) deposition patterns. It is also found that the intensity of the temperature gradient has a critical effect on the distortion of the component during the LSF process. The fractal deposition pattern generates smaller deformations, followed by offset-out, while the raster pattern shows very high thermal gradients and residual deformations (Yu et al., 2011).

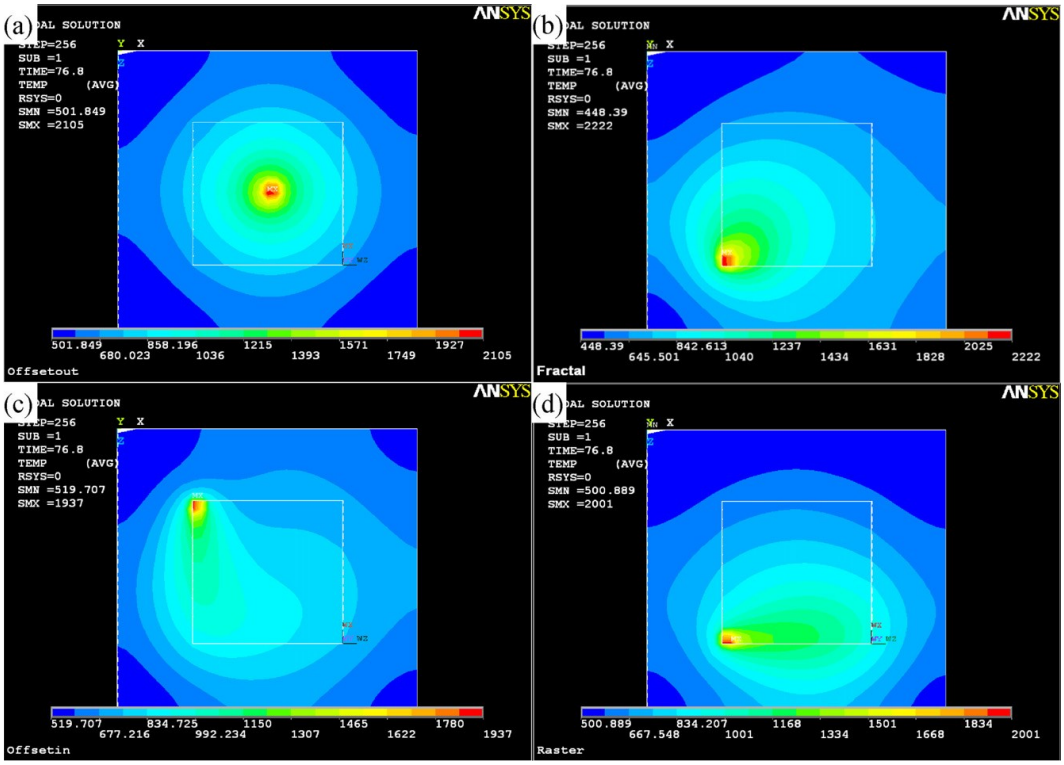

Figure 69 Temperature distributions of the different deposition patterns at the end of the deposition process (a) offset, (b) fractal, (c) offset and (d) raster (Yu et al., 2011).

Ri-sheng et al. to improve the quality of thin-walled metal components fabricated by Laser Direct Deposition Shaping (LDDS), developed a 3-D multitrack and multilayer thin-walled model with the "birth and death" method. Various scanning methods were investigated, such as alternating parallel to long side scanning (LPRS), alternating parallel to short side scanning (SPRS) and alternating parallel to orthogonal interlayer scanning (IOPRS). The equivalent Von Mises stress, and the principal stresses along the X-Y-Z directions, were analysed in detail. Under the same conditions used in the simulations, the deposition experiments were conducted, and the influence of different scanning methods on the fracture behaviour of thin-walled metal parts was compared. Therefore, reasonable planning of the scan path based on the analysis of the mechanical characteristics of the parts has a strong influence on the fracture behaviour of the metal parts (Ri-sheng et al., 2016).

Spranger et al. investigated deposition of 3D titanium alloy Ti-6Al-4V components by Laser Metal Deposition (LMD). The cylindrical specimens are made by means of standard shell-core construction strategies and pendulum compensation layers. Mechanical properties and fracture mechanisms were determined. For the analysis, slender cylinders consisting of more than 240 layers with a height of more than 120 mm and a constant diameter of 19 mm were manufactured. Based on results of tests with traditional strategies, which highlighted a non-homogeneity of the layer deposited in the central area, experiments were conducted to improve the deposition strategy and have a more regular deposition. This strategy incorporates overlap ratios of varying tracks in the core to achieve constant growth from the periphery of the shell to the core. The samples were analysed by X-ray inspection in order to find defects in the material. Fractured surfaces were observed by scanning electron microscopy and the composition of the surfaces was determined by energy dispersion X-ray spectroscopy (Spranger et al., 2018).
Although research on thermal process monitoring has grown in recent years, there is still little work that focuses on using thermal camera monitoring on different construction strategies. In strategies consisting of numerous layers, thermal monitoring plays a fundamental role, because it is able to detect deposition defects that could lead to manufacturing failure. This monitoring is also capable to evaluate components from a mechanical point of view, analysing the thermal factors related to the microstructure.
This research provides fundamental results for increasing the quality of components produced or repaired by DLMD through the optimization of the deposition path.

4.4.1 Experimental setup and material

The prototype DLMD system shown in Section 2.10, is used to carry out the experimental tests. The Ni-based superalloy was employed as powder material and supplied to a coaxial nozzle via an external powder feeder using Argon as carrier gas and shielding gas. The substrate material consisted of a 6 mm thick AISI 304 steel plate. The chemical compositions of materials used are shown in Table 3 and Table 4.
The equipment adopted for the thermographic process monitoring, as previously exposed in Section 4.3.3, is composed of FLIR NIR thermal camera SC7200M characterised by Focal Plane Array cooled detector, high acquisition rate and 20mK NETD (Noise Equivalent Temperature Difference), a personal computer laptop and the remote control acquisition and data elaboration software Altair (see Figure 70). The thermal camera was capable of detecting a temperature range between 483 °C and 2117 °C, thanks to filter lens capable to measure various wave lengths of interest.

Figure 70 Machine setup and thermal camera device.

4.4.2 Experimental tests

Experimental tests were performed using a set of process parameters shown in Table 28, which were kept constant throughout the process. Previous experimental tests showed that this combination of process parameters produces porosity

and crack-free cladding, with strong metallurgical bonding and adequate dilution with the substrate. A square-shaped monolayer deposition of 25 x 25 mm was chosen as the object of the analysis.

Parameter	Unit	Notation	Value
Laser power	W	P	400
Translation speed	mm/min	V	1000
Laser spot diameter	mm	D	1.00
Powder feed rate	g/min	F	10.00
Carrier gas flow rate	l/min	G	3.00

Table 28 Process parameter for multiclad depositions

As illustrated in Figure 71, two deposition strategies were considered for the experimental test:

a) unidirectional contouring
b) bidirectional contouring

Both strategies are based on concentric square depositions, as a spiral that moves from the edge to the centre of the area. The starting point of each square deposition is placed on the same diagonal, which brings to drastically reduce the idle time between subsequent depositions. During the depositions, the laser works in continuous mode.
Strategies differ in direction of the deposition: in the unidirectional strategy the laser follows the clockwise direction for the whole process, while in the bidirectional strategy the deposition reverses its direction after each square path.

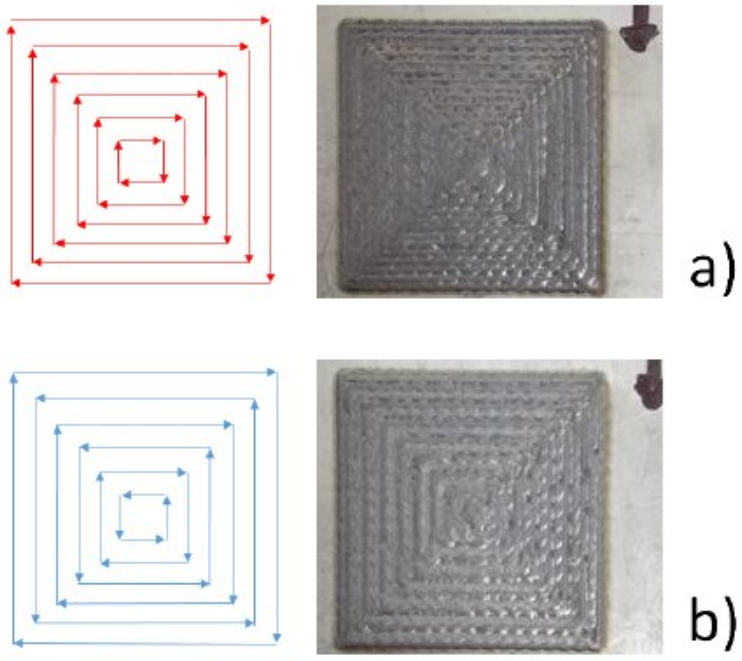

Figure 71 Representation of the scanning strategies: a) unidirectional contouring; b) bidirectional contouring.

4.4.3 Thermographic monitoring

The thermal assessment of deposition strategies was carried out through the data collected by the IR camera during the thermographic monitoring of the process. Algorithms were implemented on MATLAB® software to elaborate the thermographic data and investigate the most appropriate thermal features. In particular, the following were analysed:

- Maximum temperatures
- Thermal cycles

Based on the temperature range of the IR filter used, MATLAB® routines are developed and calibrated. The custom routines developed for this study are standardised and also applicable to other DLMD process thermographic studies. The purpose is to establish a unified approach for the treatment of thermographic post-process data.
Single thermograms do not provide an overview of the process and the maximum temperatures that are reached at each deposition stage. An algorithm was implemented, capable of producing a global thermogram obtained as an overlapping

of single thermograms into a single picture. It reflects the maximum temperatures reached in every single pixel during the deposition.
Figure 72 reports the thermographic maps of the maximum temperatures reached in each pixel of the image (which can also be represented with isotherms) give a comprehensive vision of the geometry and temperature distribution of the deposition.
Both thermographic maps highlight the temperature peaks in the centre of the deposition that coincide with the end of the deposition. The squares are getting smaller and closer, the heat accumulates and quickly increasing the temperature.

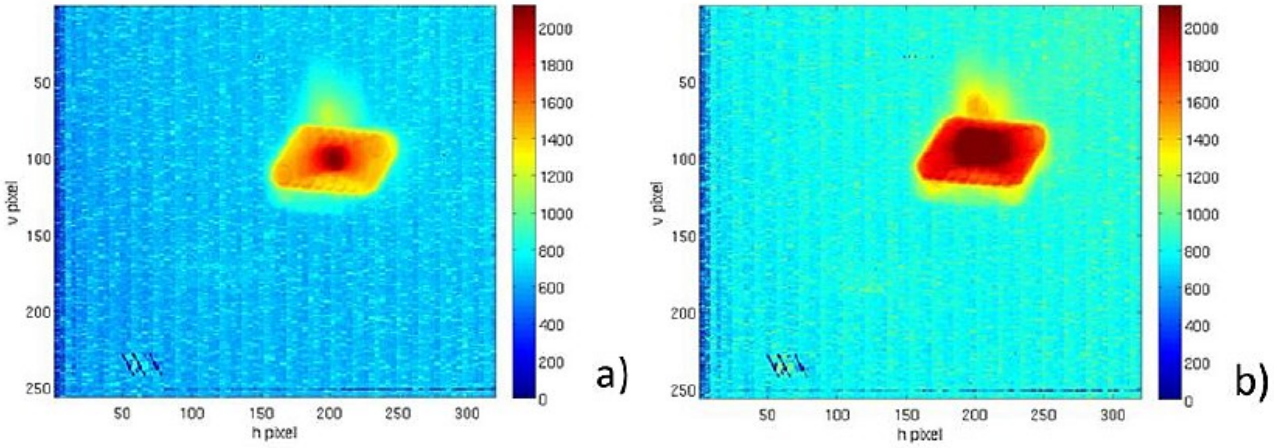

Figure 72 Thermographic maps of the maximum temperature: a) unidirectional contouring; b) bidirectional contouring.

4.4.4 Analysis of maximum temperatures

The temperature trends obtained during the depositions is the first step in the thermographic analysis. The routines allowed the tracking of the average temperature trend and the visualizing of the thermogram for each frame. The average temperature trend reached during depositions is useful for verifying the temperature distribution surrounding the melting pool. This activity shows the overall thermal behaviour of the area.
The thermogram graphically reports the information relating to the beginning and the final frame of each square deposition with respect to the total data acquisition. This provides information on the laser on and off periods and consequently it is possible to calculate exactly the duration of the whole deposition and individual traces. These data are often unclear in multiclad depositions and are indispensable for subsequent analyses.
The maximum temperature trend is defined according to two different methods:

- Punctual approach
- Average melting pool approach

The punctual method analyses the value of the pixel reaching the maximum temperature in every single frame (Emamian et al., 2014). As shown in Figure 73(a), the maximum temperature trend of the unidirectional contouring strategy shows a rapid growth. The peaks represent the corner points, where the laser source changes direction by 90°.
In these points the heat diffusion is limited in the internal part of the deposition, generating a temperature peak with a regular trend. Subsequently, the maximum temperature is reduced due to the re-establishing of stationary conditions of the straight section.
This trend leans to become shorter during the deposition due to the decrease in size of the deposited squares.
The negative temperature peaks can be explained by the interaction of the nickel-based superalloy powder with the molten pool. It produces a multi-phasic mixture characterised by a floating emissivity. In addition, the radiation emitted by the molten pool and read by the sensor is altered by particles passing through the laser beam before reaching the substrate. This creates the background noise readable on the graph.
The bidirectional contouring strategy shows a more confused trend, owing to the reversal of direction that occurs at the end of each square, which significantly modifies the conventional heat dissipation. Extremely high temperatures were reached in a shorter time respect to the unidirectional strategy, exceeding the limit imposed by the filter of 2117 °C.

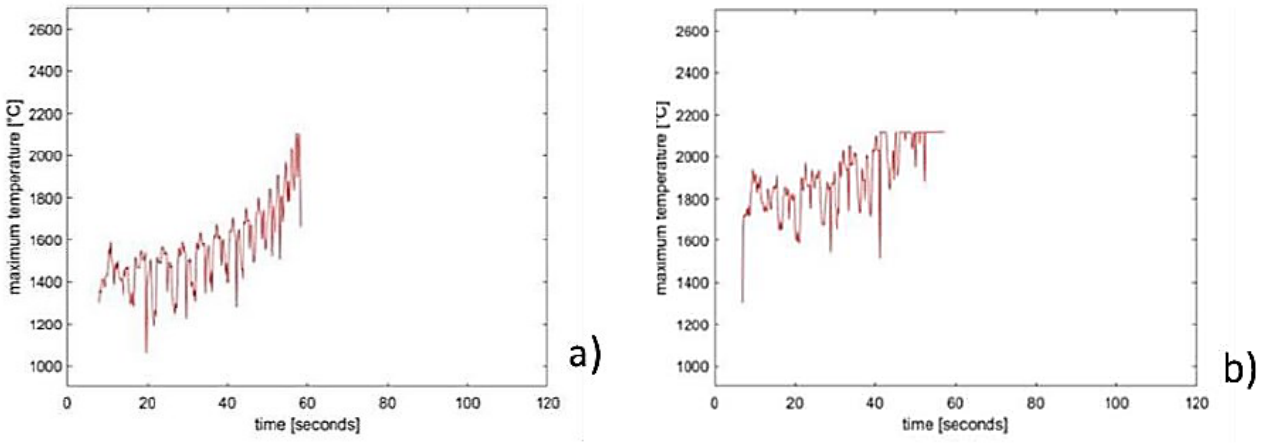

Figure 73 Maximum temperature trend: a) unidirectional contouring; b) bidirectional contouring.

Nevertheless, the punctual approach is measurement error-prone. The trend was built considering only one point (pixel) of the sensor for each frame, which may be malfunctioning thus detecting an altered temperature.
In order to overcome problems deriving from considering a single pixel in the computation of the maximum temperature, a second approach was used to define the temperature trend. The average melting pool approach defines for each frame a molten pool temperature (T_{pool}) as the average of the values above the setting melting temperature (T_m), as described by Marshall et al. (G Marshall et al., 2015) in Eq. (17).

$$T_{pool} = \sum \frac{(T > T_m)}{n_p} \qquad (17)$$

- T_m is the melting temperature
- n_p is the number of pixels considered

In this work, the melting temperature was set at 1400 °C considering the materials involved in the process, the Nickel-based superalloy powder and AISI 304 substrate.
The maximum temperature as defined is averaged over several points that definitely reach the melting temperature and are easily visible on the thermogram. Therefore, it can be considered as a more accurate temperature of the melting pool. This kind of methodology reduces the measurement errors because it avoids the problem of saturated pixels. Through this second approach, temperatures are generally lower than those of T_{max} built with the first routine.
The strategies are characterised by increasing trends in the temperature of the molten pool, as shown in *Figure 74*. The laser source works in continuous mode, resulting in faster depositions, slower cooling and higher temperatures.

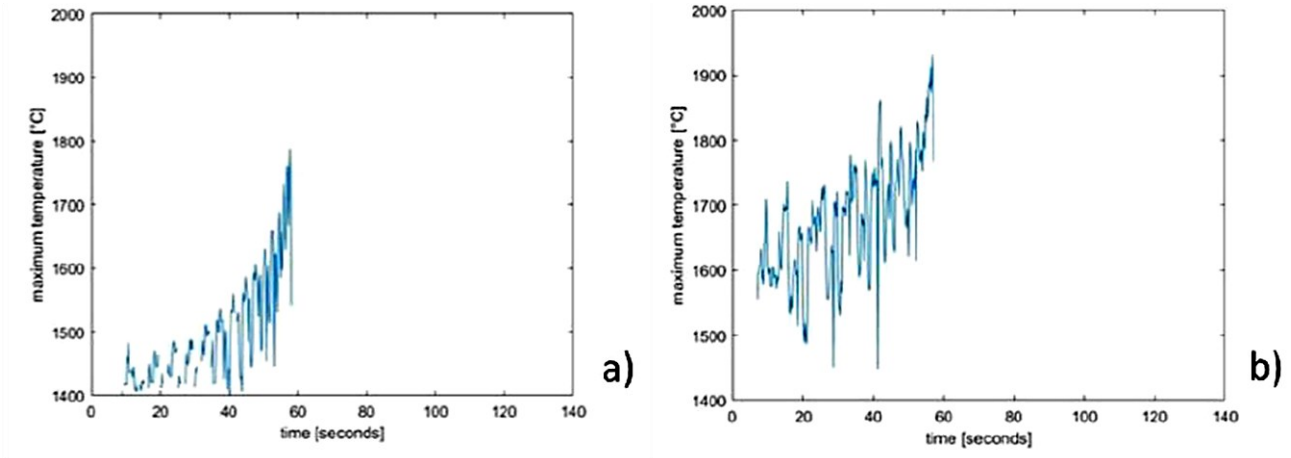

Figure 74 Molten pool temperature trend a) unidirectional contouring; b) bidirectional contouring.

The molten pool temperature plot shows a discontinuous trend for the unidirectional contouring strategy, mainly in the early part of the process. As noticed before, the reason come from the radiation distortion of the molten pool caused by

the powder flow. The temperature considerably drops down especially in the first depositions, going below the threshold set in the routine. In this way, some sections are missing in the T_{pool} curve and can be correlated to the negative peaks of the T_{max}.
The pre-heating of the substrate in the first deposition phases of the bidirectional strategy covers this kind of phenomenon. A greater temperature variability due to the stationing of the laser source on the direction reversal points can be observed. In these areas the heat dissipation is altered, causing a local pre-heating. Therefore, the graph of the maximum temperatures of the bidirectional strategy shows higher peaks related to the aforementioned zones, followed by considerably lower temperature values, when the heat source moves away from the zone.

4.4.5 Analysis of thermal cycles

For the study of the thermal cycles of the contouring strategies, four characteristic points were chosen:

1. start of deposition
2. end of deposition
3. half of total deposition
4. point that reaches the T_{max}

In both contouring strategies, the end point of the deposition corresponds to the geometrical centre of the square. The point of half deposition is calculated with respect to the deposition time.

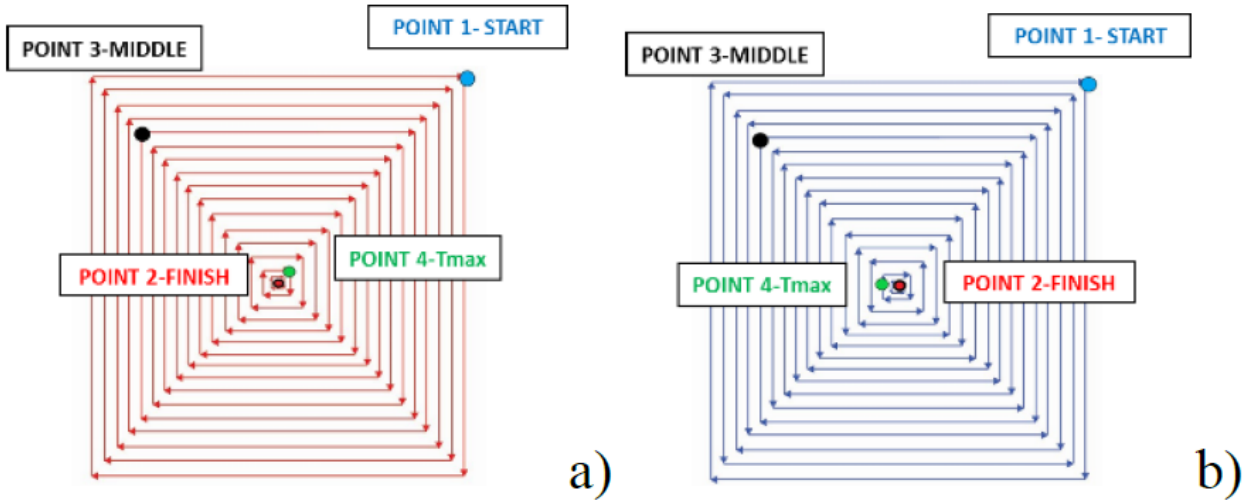

Figure 75 Characteristic points on the deposition a) unidirectional contouring; b) bidirectional contouring.

The Figure 75 shows the characteristic points on the deposition square of the unidirectional and bidirectional contouring strategies used for processing the thermal cycles relative to each point.
The aim is the evaluation of the temperature trend and thermal cycle during the entire deposition for each of these points. A custom routine was implemented to define the area and coordinates of characteristic points on which the thermal cycle was calculated. The coordinates refer to the geometry chosen for the deposition, but also considers the asymmetry due to the positioning of the camera. For each key point, temperature is measured in a rectangular area inscribed in the spot visible in the thermograms as shown in Figure 76.
A reference value of this area was calculated as the average of the areas defined for all the points of the strategies in terms of pixels involved. The estimation was carried out considering the distance of the thermal camera to the plates during the acquisition of the thermographic data, obtaining a resolution of 1 pixel ≈ 0.1 mm. The calculated average area used to determine the thermal cycles is approximately 1.50 mm^2, which is close to the area of spot laser. The calibration curves of the camera filter must be taken into account to understand the related integration time.

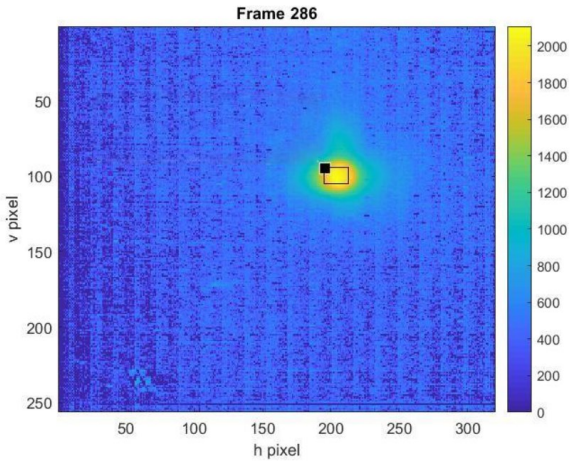

Figure 76 Rectangular area consider for the thermal cycle.

The temperature trend of the unidirectional strategy is regular, with constant heating and cooling cycles, which gradually become shorter (Figure 77(a)). The displacement of the laser source on the characteristic points is easily readable on the graph by the displacement of the temperature peaks as a function of time.
In Figure 77(b), thermal cycles of the bidirectional strategy are more complex to interpret, with a series of coupled peaks representing the inversion of direction of the heat source. As mentioned before, the trend grows very quickly and exceed the filter range in the final part of deposition on points 2 and 4.

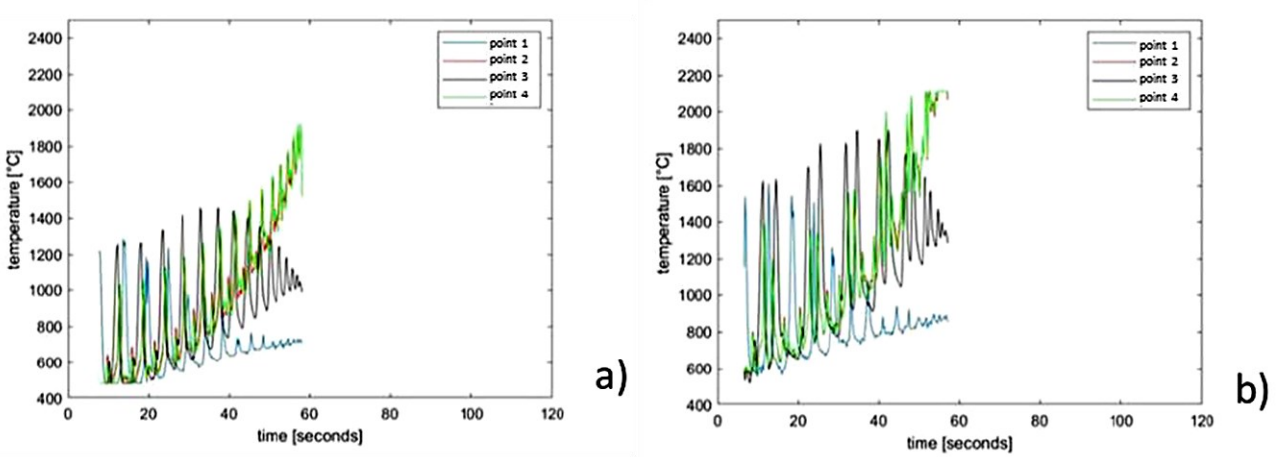

Figure 77 Thermal cycles: a) unidirectional contouring and b) bidirectional contouring.

4.4.6 Analysis of cooling rates

Researchers are facing several challenges in the development of real-time efficient cooling rate monitoring systems, due to the high speed of the process (Emamian et al., 2014).
The cooling rate is one of the thermal aspect that most influences the final microstructure of the deposition, because modality and time of solidification depends on it. In general, the faster the cooling, the finer will be the microstructure of the deposition (Farshidianfar et al., 2016b).
The cooling rate was estimated from the maximum temperature trend. This is a global approach because it considers the trend of the maximum temperature on the whole deposition area.
The cooling rate was calculated using two different methods:

- Incremental ratio (point by point)
- Linear interpolation

The concept behind both methods is that the cooling rate is the slope of the temperature curve over time. The selection of points to consider for the estimation is of primary importance.
The first routine estimates the slope of the curve as an incremental ratio, point by point, of the maximum temperature plot. The time period used is connected to the acquisition frequency of the IR camera, equal to 0.2 sec (Figure 78).

It is important to point out that all computations were carried out on the maximum temperature trends taking into account the calibration range of the IR camera filter. It is evident that the cooling rate is zero when the temperature peaks overcome the limit, in particular at the end of the bidirectional contouring strategy, where the maximum temperature trend flattens due to the calibration.

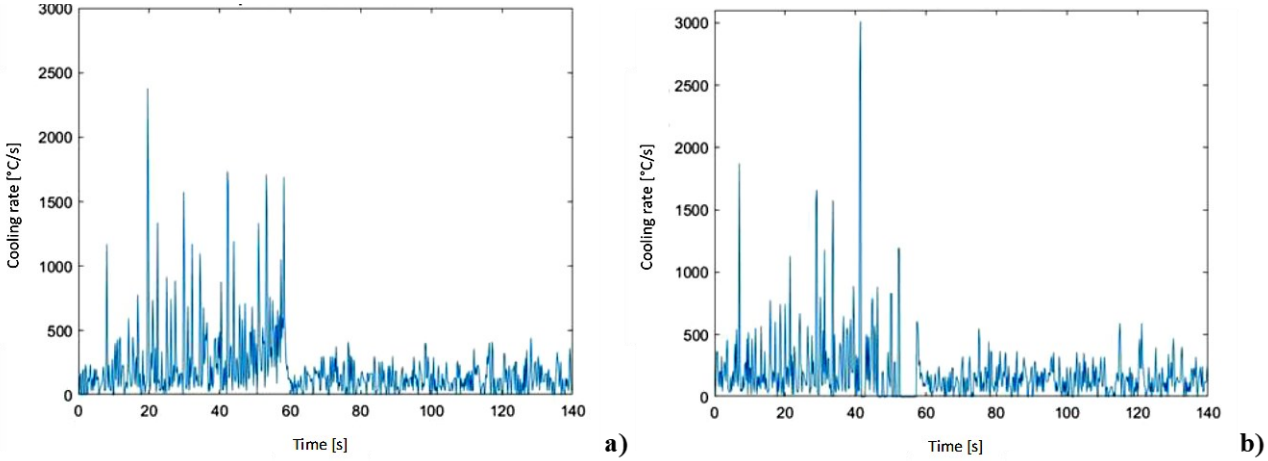

Figure 78 Cooling rate trend according to incremental ratio method: a) unidirectional contouring; b) bidirectional contouring.

On the other hand, the second routine implemented in MATLAB® for the calculation of the cooling rate analyses the slope of the trend of the maximum temperature by linear interpolation on each linear section following the temperature peaks. Unlike single-track depositions, in the case of deposition strategies, the temperature patterns have numerous peaks. As seen in the plot of thermal cycles, each clad is characterised by at least one temperature peak. Usually, the squares that constitute the contouring strategies have two main peaks.
In the routine, an additional cycle was inserted. It allows defining the number of deposited lines and choosing the temperature peak and the consecutive frames on which to interpolate. In this case, a least squares linear interpolation is considered.

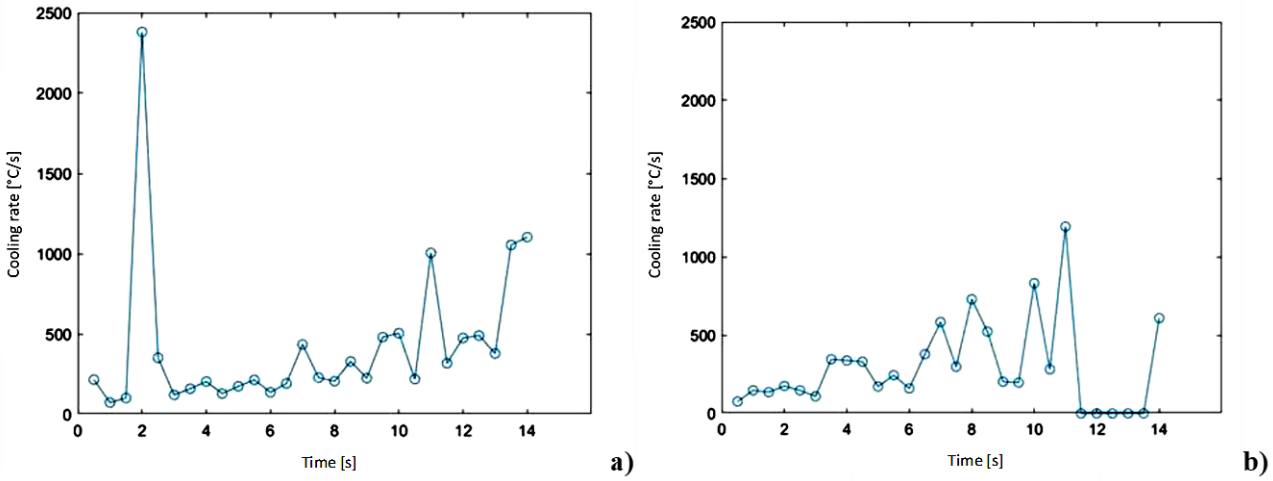

Figure 79 Cooling rate trend according to linear interpolation: a) unidirectional contouring; b) bidirectional contouring.

This second method of evaluation of the cooling rate (slope of the T_{max} curve) consequently provides a more in-depth and accurate study of the strategies.
Figure 79 shows that in both contouring strategies the cooling rate increases with the deposition progress because of the increasing of maximum temperatures reached.
In the first clads there are rates of about 200 °C/s while they increase to about 1000 °C/s in the last depositions of the unidirectional strategy. In the bidirectional strategy, rates exceeding 1200 °C/s are reached.

In the plot of the unidirectional strategy there is an anomalous peak during the deposition of the second square. It originates from an incorrect estimation of the maximum temperature.

4.4.7 Macrostructural analysis

In order to understand the relationship that the thermal parameters have on the qualitative characteristics of the deposition, it was considered as important to correlate the thermal data with the metallographic analysis. The specimens were trimmed using a metallographic cutting machine, hot mounted in resin and finally polished.
In the macrograph of the unidirectional contouring strategy there is a planar and regular shape of the deposition with several cracks and porosity, as shown in Figure 80(a). In Figure 80(b) the bidirectional contouring strategy shows a much more irregular deposition in which couples of single clads can be seen. There are no cracks but some inter-clad porosity. It is worth mentioning that the presence of crack could be due to incorrect preparation of the specimen in complex trimming phase , especially in the presence of materials such as nickel-based superalloy.

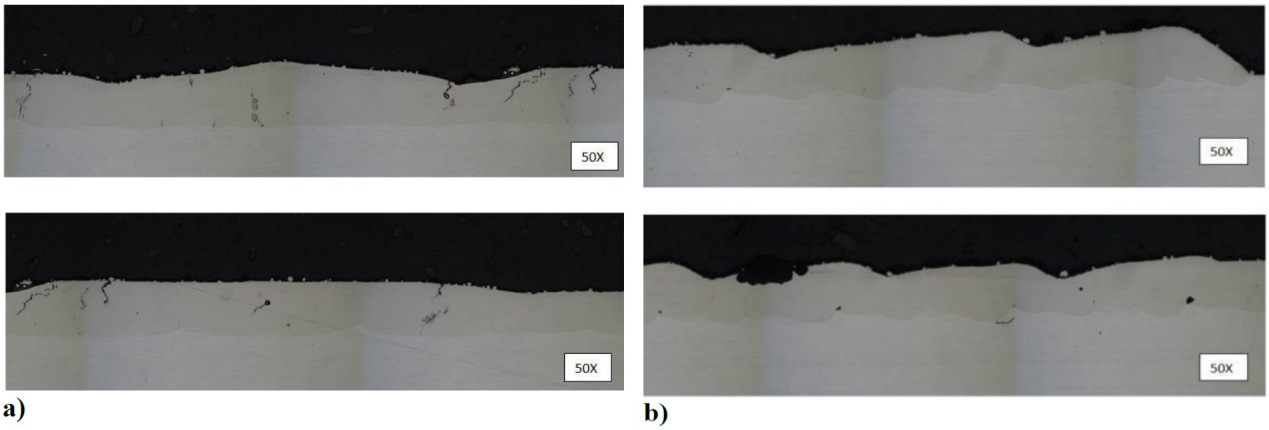

Figure 80 Cross section: a) unidirectional contouring; b) bidirectional contouring.

4.4.8 Conclusion

The thermographic analysis carried out on some deposition strategies has shown remarkable results. As can be seen in maximum temperature trends and thermographic maps, unidirectional strategies shown lower temperatures, evenly distributed. While the bidirectional strategies are generally characterised by higher and irregular peaks due to the persistence of the laser beam in the direction reversal area.
The unidirectional strategy has regular thermal cycles that shorten as the process progresses. Otherwise, in bidirectional deposition the thermal cycles are more noise-affected.
Both deposition strategies are characterised by increasing of cooling rates as the process progresses.
The metallographic analysis showed that the unidirectional strategy leads to a greater number of cracks due to the thermal cycles. On the other hand, the bidirectional strategy has much inter-clad porosity due to the deposition of clad pairs.
The investigation of the thermal behaviour of different deposition strategies is of considerable importance for the development of AM in the industrial sector. In future applications, other deposition strategies will be evaluated, also modifying the boundary conditions, which strongly impact on thermal factors such as the cooling rate.

4.5 Coaxial monitoring of 316L thin walls fabricated by Direct Metal Laser Deposition

Optical systems and methods are the most widely used among the monitoring methods for AM processes, because of their many advantages: possibility of real-time and multipurpose acquisitions, intuitiveness and flexibility (He et al., 2019). For instance, geometrical features can be measured from the acquired images after a processing phase. Several aspects of the manufacturing process can be observed by CMOS, CCD, and IR cameras.

The relationship between melt pool geometry and key process parameters during the laser metal deposition process was investigated by Ocylok et al., by means of a coaxial process control. The melt pool back reflections were recorded by CMOS camera. The melt pool size was estimated and the influence of thresholding on acquired image binarization was established. The same threshold value was applied to all the images examined and the results showed a constant deviation between the deposited track width and the width measured in the images. The widening of the track is caused by the heat diffusion and the viscosity of the melt pool, but also by the presence of sparks. The effects of glares on the width and length of the melt pool were reported to be less than 0.5%. Results showed that the laser power had a positive proportional effect on the size of the melt pool, while the relationship between the translation speed and the melt pool size was negative. The thickness of the single track is increased almost linearly by increasing the powder mass flow and the penetration depth decreases continuously, leading to a slight decrease in the size of the melt pool . The effect of preheating the substrate was also evaluated, hence that up to 300 °C increases the melt pool size by more than 20% at all studied laser power values (Ocylok et al., 2014).

A combined systems was used by Ding et al. that performed experiments using CCD camera and IR camera. They performed the calibration of the CCD camera by comparing the acquisitions of the IR camera, as shown in Figure 81. To remove acquisition disruptions due to the presence of powder above the melt pool, an IR filter was added to the CCD camera. Since the melting temperature of the material determined the edge of the melt pool, the emissivity was constant along the entire contour and the edge temperature was represented by an isotherm. The images derived from the videos of the two separate cameras were superimposed to determine this isotherm. The greyscale threshold value for the IR images was found by overlapping the images with the IR background. The value was confirmed by experiments performed without powder at various scanning speeds and the findings were equal to the size of the tracks deposited within the ±0.1 mm range (Ding et al., 2016).

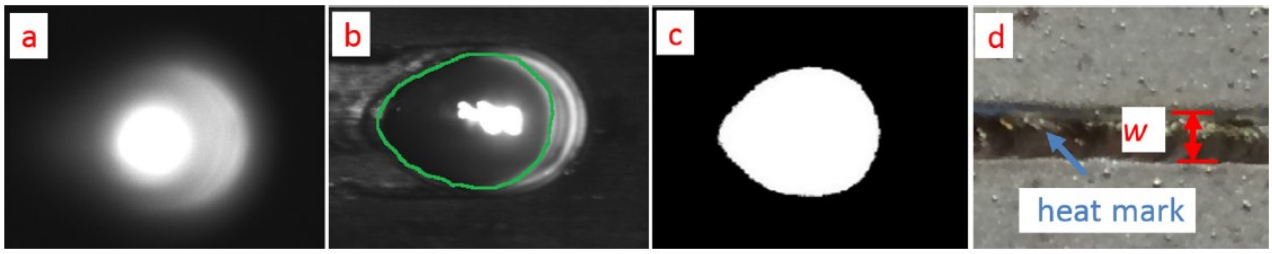

Figure 81 Captured images: (a) infrared image, (b) video image, (c) the contour of the molten pool on infrared image, (d) heatmark on the substrate (Ding et al., 2016).

Off-axis optical systems are also employed to monitor geometrical characteristics of the clad. Hsu et al suggested an inspection method focused on three digital cameras to measure the height of cladding. The three cameras were located at the same distance from the middle of the platform, and from each other and rotated about 15 degrees from the vertical direction, as shown in Figure 82. In order to compensate the field of view and perspective effects of the trinocular system, a calibration bar was used in this system. An image processing technique was previously used to isolate the nozzle and the melt pool. The findings showed how, based on the distance between two reference points located at the nozzle tip and the centroid of the melt pool, the clad height was determined. It was compared with 3D scan models to assess the accuracy of the device, giving an error of 4.2% (Hsu et al., 2019).

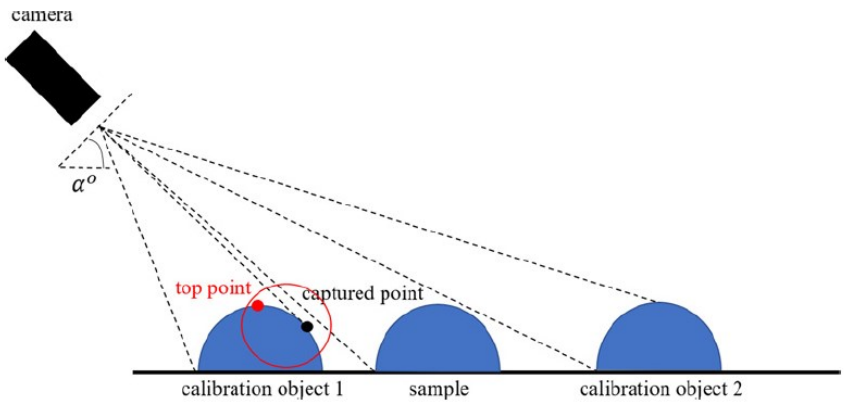

Figure 82 Schematic illustration for DED cladding height measurement process (Hsu et al., 2019).

As previously described, optical systems can be extremely useful for guaranteeing an adequate quality of AM processes. The possibility of combining different systems and being capable to monitor a wide range of deposition strategies requires further studies. The purpose of the following work was the coaxial monitoring of the melt pool during the fabrication of thin walls by DLMD, using different strategies of deposition. In order to detect and analyse the melt pool geometry and the influence of the strategy, an algorithm based on the active contour methodology was used. This monitoring methodology can help to design and implement the best building strategy for the fabrication of 3D components.

4.5.1 Experimental setup

Three thin-walled depositions were performed. The experimental work was carried out using the prototype DLMD system, described in Section 2.10. The laser beam and power distribution profiles are shown in Figure 29.
The substrate used in this work was an AISI 304 stainless steel with a size of 100 x 80 x 2 mm, which chemical composition is shown in Table 3. The powder material used was AISI 316L stainless steel, a commercial powder presenting spherical particles produced by gas atomization, which composition is also shown in Table 3. A coaxial Argon flow with equal to 10 l/min was used to shield the working area. Argon is also used as a carrier gas of the powder.
Depositions were carried out by using the same process parameters, which were obtained from previous studies and assessed as suitable for multilayer depositions. Table 29 lists the process parameters, which were kept constant throughout the process.

Parameters	**Unit**	**Notation**	**Value**
Laser power	W	*P*	400
Translation speed	mm/min	*v*	1000
Powder feed rate	g/min	*Q*	10
Carrier gas flow rate	l/min	*G*	10
Laser spot diameter	mm	*d*	1.5

Table 29 Experimental process parameters.

The thin walls consist of 15 overlapping layers, built adopting the following deposition strategies (see Figure 83):

- S1: two-way continuous, without dwelling time
- S2: two-way with 10 seconds of dwelling time between two consequent paths
- S3: one-way with 10 seconds of dwelling time between two consequent paths

Patterns differ in the direction of deposition and for the implementation of an idle time between passes, in order to favour the heat diffusion. The dwelling time is the waiting time between two consequent paths in which the laser is off. Two replications were performed for each deposition strategy.

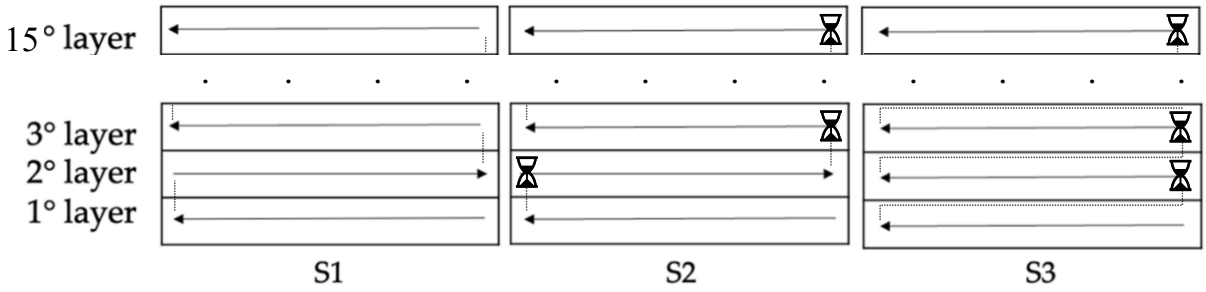

Figure 83 Schematic representation of three different deposition strategies.

During the thin wall fabrication, a coaxial CCD camera, integrated into the deposition head, was employed to monitor the melt pool. The camera was a Mono CCD sensor, with an acquisition frequency of 40 frames per second, and an optimal resolution of 1024 x 768 pixels. A series of frames were extracted from videos, which were then processed by means of algorithms implemented in the MATLAB® software, to extract the melt pool geometry.
In order to investigate the effects of the three proposed deposition strategies on the final quality of the thin walls, a geometrical analysis of the cross-sections of the samples was carried out. Samples were trimmed using an AbrasiMet 250 metallographic cut-off machine. A polishing process was carried out to make the cross-section surface flat, highly reflective, and free of scratches.
In order to characterise the samples in terms of microstructure, geometry, and defectiveness, they were etched by the Glyceregia reagent (5ml HNO_3, 10ml glycerol, 15ml HCl). The samples were observed by a Nikon Eclipse MA200 inverted optical microscope suitable for micrographic analysis.

4.5.2 Analysis and characterization of the melt pool

The video of the molten pool evolution was acquired from each deposition test using a coaxial CCD camera with an acquisition rate of 40 Hz. The configuration of the CCD camera on the deposition head is shown in Figure 84.

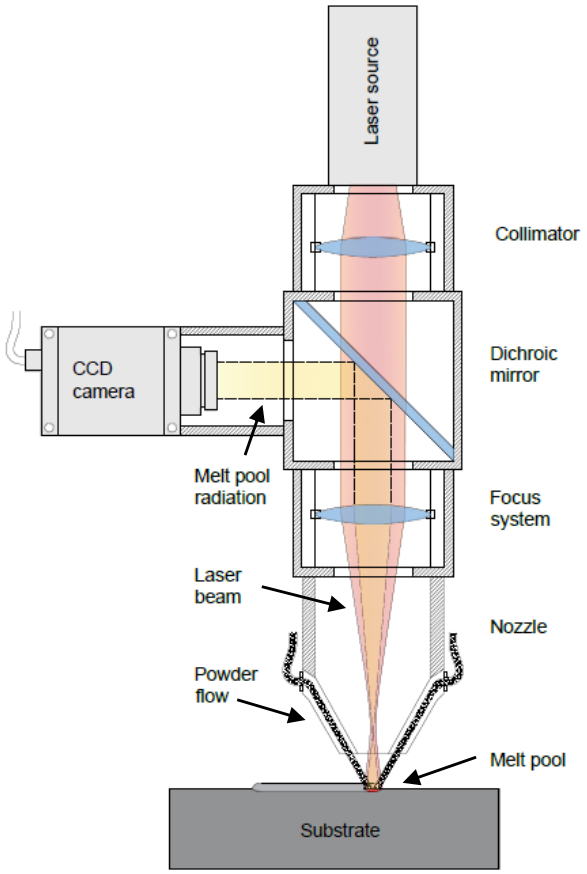

Figure 84 Coaxial CCD camera configuration.

The coaxial configuration is particularly suitable for the DLMD process monitoring as it is not affected by field of view occlusions and perspective distortion (Vandone et al., 2018). Image sequences were extracted from the acquired videos and subsequently processed and analysed using dedicated algorithms developed in MATLAB® environment. For each deposited layer, video frames were extracted and evaluated at three different moments:

- at the beginning of the layer
- at the middle of the layer
- at the end of the layer

The melt pool shape monitoring was performed by extracting its geometrical characteristics using advanced image processing techniques. The assessment focused on the analysis of the melt pool area identified by an algorithm based on the active contour method. This technique, also used by Lei et al. (K. Lei et al., 2018), consists in the implementation of an iterative method starting from a first definition of the zero-level contour in the form of a closed curve known as mask. Through the minimization of an energy function, the mask iteratively evolves and adapts by applying shrinking/expanding operations called "contour evolution" (Chunming Li et al., 2008).
The active contour method gives better results than classical image segmentation methods (edge detection/thresholding, and region growth) such as "Canny Edge" that operate finding discontinuities in the brightness intensity of the image. Therefore, since these methods are based on a locally-derived analysis, they are not very effective in the presence of weak object boundaries or noisy patterns as in the images obtained from the DLMD monitoring (Caltanissetta et al., 2018).

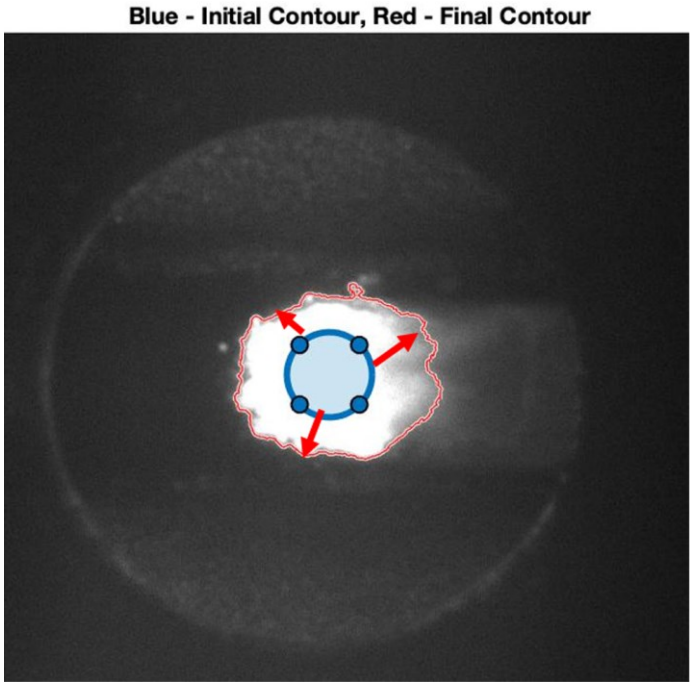

Figure 85 Automated detection of a melt pool edge from a video frame by means of the active contour algorithm.

The region-based algorithm seeks to identify each region of interest (ROI) using a region descriptor that guides the evolution of the active contour. The algorithm works by segmenting the image in order to find regions with homogeneous properties. A circular shape was chosen as mask level, as it is similar to the incident laser spot diameter. Figure 85 shows an example of active contour where both the zero-level contour (blue) and the extracted melt pool contour (red) are represented. As a result of heat dissipation through the substrate, the brightness gradient at the top of the molten pool is steep. On both sides of the melt pool, the high luminosity regions may be a function of the high emissivity of the non-molten particles and oxides. (K. Lei et al., 2018). Doubenskaia et al. considered the high thermal emission in the peripheral region of the melt pool owing to oxides and other non-metallic inclusions that are normally concentrated in that field. The weak brightness gradient detected in the trailing part of the melt pool is describing low temperatures associated to the cooling and solidification of the material in that area (Doubenskaia et al., 2013).

4.5.3 Analysis of melt pool geometry

The melt pool size is an important feature for the characterization of DLMD manufacturing. The effect on the melt pool size of the two-way deposition strategy without dwelling time is shown in Figure 86(a). Each value plotted is the average of the measurements taken with the same deposition strategy on two replications carried out.

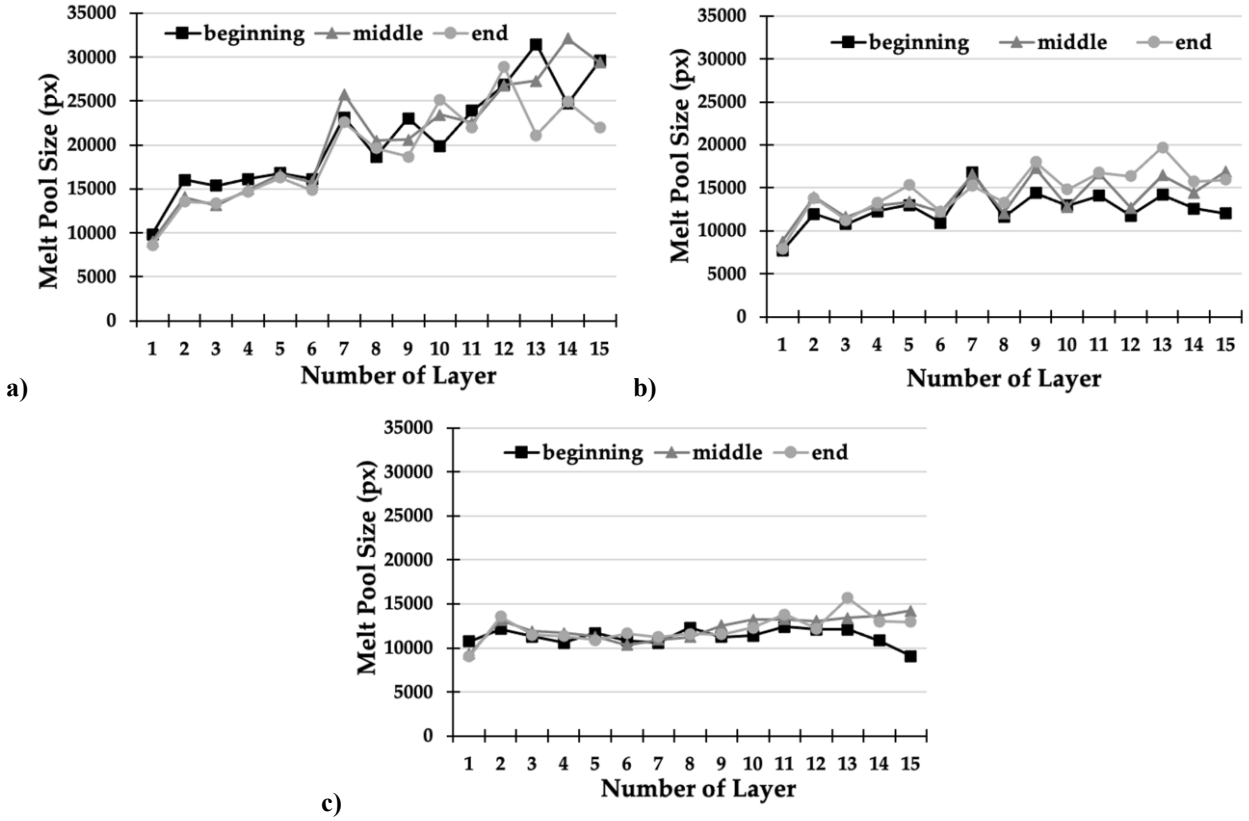

Figure 86 Melt pool size for each deposited layer with a) strategy S1, b) strategy S2, and c) strategy S3.

The results show an increasing trend in the size of the melt pool as layers deposited increase. In fact, two-way laser scanning generates an excessive heat accumulation in the area, which does not have enough time to be dissipate in the workpiece, rapidly widening the size of the melt pool, as stated by Yang et al. (Yang et al., 2020). Besides, there is no dwelling time in the deposition under examination, therefore this effect is amplified.

Figure 86(b) shows the trend of the extracted and measured melt pool areas, in the two-way deposition strategy with 10 seconds dwelling time and evaluated at three different moments of the deposition along with the layer, i.e. at the beginning, at the middle, and the end of the sample. The results show that there is a growing trend in the melt pool area, even for two-way deposition with dwelling time. However, the growing pattern is less sharp than the previous one as the heat accumulation is attenuated by the idle time between depositions applied in this case.

Finally, Figure 86(c) plots the trend of one-way deposition strategy with 10 seconds dwelling time. In this case, outcomes show that the trend of the melt pool size is approximately constant during the series of deposited layers. In fact, during the period in which the laser is turned off, there is enough time to substantially cool down the deposited track and to not accumulate the heat generated into the previous run, thus restoring the initial thermal conditions.

Comparing the results obtained by the three analysed strategies (see Figure 87) it is even more evident how the dwelling time between consecutive layers is a key variable for the final results of the analysed strategies. In the graph, the areas of the melt pool have been converted from pixels to square millimetres, with a surface conversion: 10x10 [px] = 1 [mm^2]. This relationship was found through a calibration process, using a millimetre-sized sample. The aggregate trend of each deposition strategy in Figure 87 were obtained averaging areas at the beginning, at the middle, and the end of each layer of samples.

The average areas for the three deposition strategies were compared and it was found that the strategy S1 increased the average melt pool area from 0.917 mm^2 to 2.698 mm^2, with a variation between the first and last layer of 1.781 mm^2. For the strategy S2, an increase in the average melt pool area was recorded from 0.815 mm^2 to 1.497 mm^2, with a difference

of 0.682 mm^2. For the strategy S3, the melt pool area varied from 0.97 to 1.208 mm^2 from the first to the last layer, recording an increase of 0.238 mm^2.

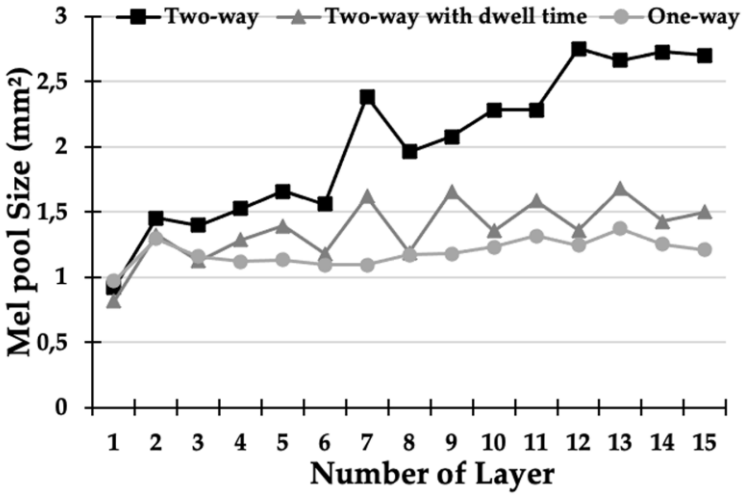

Figure 87 Comparison of melt pool sizes for each deposited layer for the three different strategies.

4.5.4 Analysis of macrography cross-sections

Finally, the analysis of the macrography cross-sections was carried out to corroborate data obtained from the analysis of the melt pool. Figure 88(a) shows the cross section of the thin wall obtained using the deposition strategy S1. This macrography revealed that the width of the deposited thin wall increased as the deposited layers increased, confirming the trend determined in the melt pool assessment. On the other hand, Figure 88(b) shows the cross section of the thin wall obtained using the deposition strategy S2. This revealed a clad width increasing as the layers deposited with this deposition strategy increased. However, the increase in width is much less pronounced.

Figure 88(c) shows the cross section of the thin wall obtained with the strategy S3. This macrography confirms the outcomes of the melt pool monitoring, since the width of the deposited thin wall remains almost constant as the deposited layers increase.

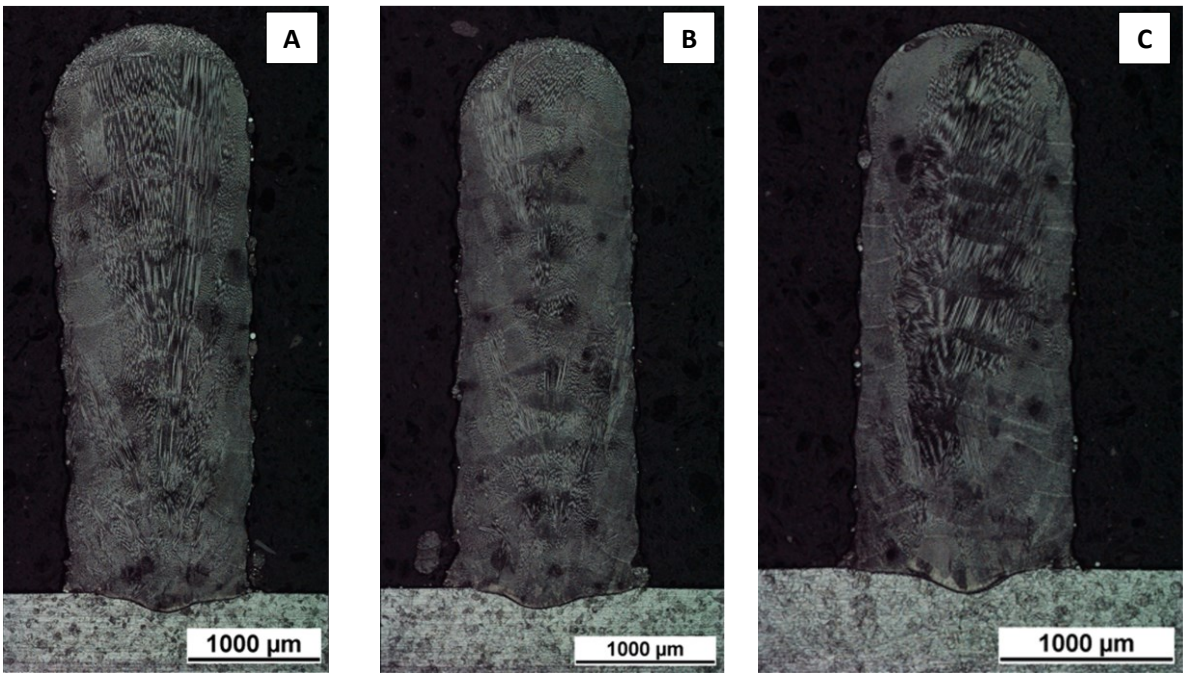

Figure 88 Macrography cross-section of the thin wall obtained using a) strategy S1, b) strategy S2,and c) strategy S3.

4.5.5 Conclusions

In this work a coaxial monitoring of AISI 316L thin wall deposition fabricated by Direct Metal Laser Deposition using different deposition strategies was carried out and outcomes were compared to macrography cross-sections. For the two-way continuous (no dwelling) deposition strategy, as the deposited layers increased, an increase in the melt pool area was observed. Dwelling time between layers had a significant impact on the amplitude of the melt pool, allowing a more effective diffusion of the accumulated heat and the restore of the initial workpiece temperature. The boundary conditions of the process for depositions with strategy S2 and S3 were similar, which in fact showed a more contained variation in relative melt pool.

Finally, the unidirectional deposition strategy revealed a more uniform process, avoiding heat accumulations in the peripheral areas of the thin wall, due to the reversal of direction.

This work is a preliminary study that might be useful for improving the accuracy and quality of depositions performed employing complex deposition strategies and complex geometries. Outcomes demonstrated that a fast and stable image processing implementation is a successful methodology for real-time applications and for eventually closed-loop monitoring.

4.6 Ultrasonic Characterization of Components Manufactured by Direct Laser Metal Deposition

As previously stated, a key problem in the AM manufacturing is the assessment of component quality both during the process and post-process. Numerous approaches were suggested in the literature to afford this challenge. Among these methods, researchers have recently investigated the capabilities of ultrasonic testing, in order to establish effective procedures for process monitoring and quality control of AM components.

Although these are rarely used during the process, due to the difficult environmental conditions (especially for contact probes) and the high background noise that often makes the signal unclear. These techniques are finding increasing interest as non-destructive post-process inspections, thus leaving components undamaged. Various methods for ultrasonic analysis were developed in the literature, depending on the medium used and the objective pursued.

The pulse-echo ultrasonic method was performed in order to investigate the mechanical behaviour of selective laser melting additively manufactured AlSi10Mg. By means of ultrasonic tests, a slight elastic anisotropy with symmetry along the construction direction was found. The anisotropy was correlated to the attenuation of the experimental data in terms of ultrasonic wave velocity and frequency (Sol et al., 2018).

Using the ultrasonic immersion C-scan method, the ultrasonic backscattering data produced by the microstructure of the AM material generated by the selective laser melting (SLM) process was evaluated. The structural noise in the ultrasonic waveforms, which interferes with the wave reflections caused by defects, is a crucial problem which compromises the interpretation of ultrasonic data. The structural noise is known as the backscattering ultrasonic signal and provides meaningful details on the material microstructure, geometrical and mechanical properties (Siva Shashidhara Reddy et al., 2005).

Another non-contact ultrasonic method consisting of the innovative laser ultrasonic technique was proposed by Cerniglia et al., which was employed for the inspection of laser powder deposition (LPD) components in order to detect near-surface and surface defects. A prototype laser device mounted on the LPD robot was suggested by the authors, which enables detailed inspections of the LPD parts during AM manufacturing (Cerniglia et al., 2015). The inspection of each reference sample consisted of the A-scan signal collected along the single-layer deposition. The B-scan image is constructed after that ultrasonic signals are obtained, displaying the magnitude of normal displacement in a colour map to demonstrate the presence of wave irregularities due to defects, as shown in Figure 89.

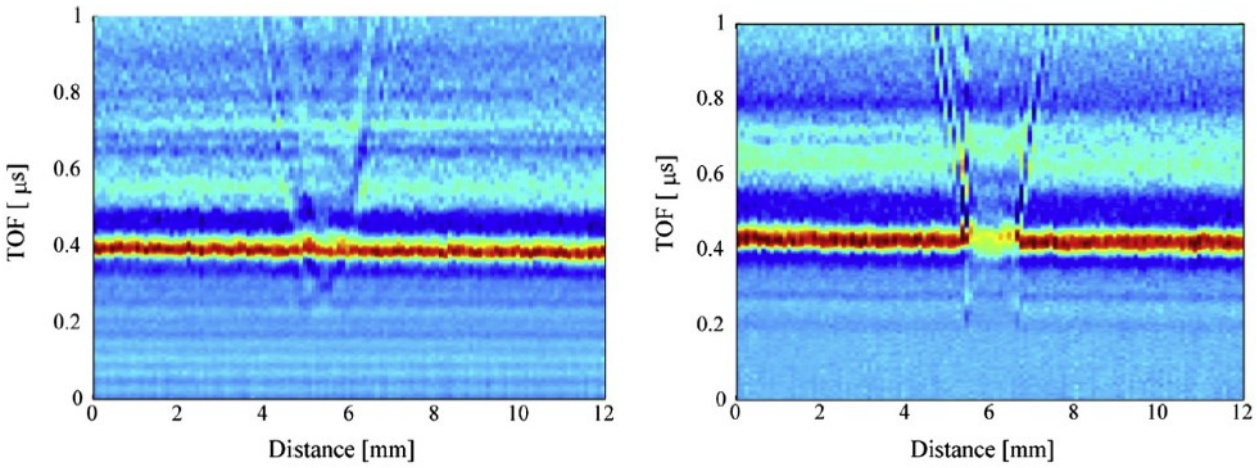

Figure 89 Experimental B-scan of the reference samples (Cerniglia et al., 2015).

Despite the several advantages provided by ultrasonic techniques for the mechanical characterization of AM components, there are still few literature studies that propose theoretical and experimental procedures to solve this problem.

A new experimental approach to the mechanical characterisation of these kind of components is here proposed, based on the results obtained by goniometric ultrasonic immersion tests. The objective is to apply the proposed experimental method to examine the whole part, both of the substrate and of the new material obtained by the AM process.

4.6.1 Materials and DLMD machine setup

In the present work, several specimens were produced using the prototype DLMD system described in Section 2.10.
A 6 mm thickness AISI 304 substrate is employed, which chemical composition is shown in Table 3. The Nickel-based superalloys is used as powder material with a granulometry in the range 15 - 45 µm, and chemical composition shown in Table 4. It is carried from an external powder feeder by means of Argon gas with a flow rate of 3 l/min and conveyed inside the melt pool to build the trace. The Argon gas was also employed as shielding element to prevent clad oxidation. The specimens were built applying different sets of process parameters identified in previous studies as feasible for a deposition with good characteristics as shown in Table 30.

Deposition	P [W]	D [mm]	V [mm/min]	F [g/min]
1	600	1.00	750	5.00
2	400	1.50	750	2.50
3	600	1.00	500	5.00

Table 30 Process parameters (Castellano et al., 2020).

For the multiclad deposition, a unidirectional 'raster' strategy was selected, in which 5 single tracks with a length of 40 mm were deposited side by side. Clad overlap (OV%) describes the percentage of intersection of adjacent tracks (Angelastro et al., 2011). Overlaps of 10% (S1), 20% (S2), 30% (S3), 40% (S4) and 50% (S5), were employed in the experiment. In addition, in order to assess the capability of the proposed experimental method to characterise such deposition irregularities a moderate turbulence of the powder flow in strategy S2 and S4 was induced. In this way, different substrate penetration and problems with interlayer porosity were obtained. For each set of parameters, two replications were performed.
Subsequently, specimens were trimmed using a SiC cut-off wheel in position A and B (see Figure 90(a)), hot mounted in phenolic resin, polished and chemically etched. A metallurgical microscope with a digital camera, designed for digital imaging, was used to analyse the cross-section geometry and ensure the occurrence of defects.

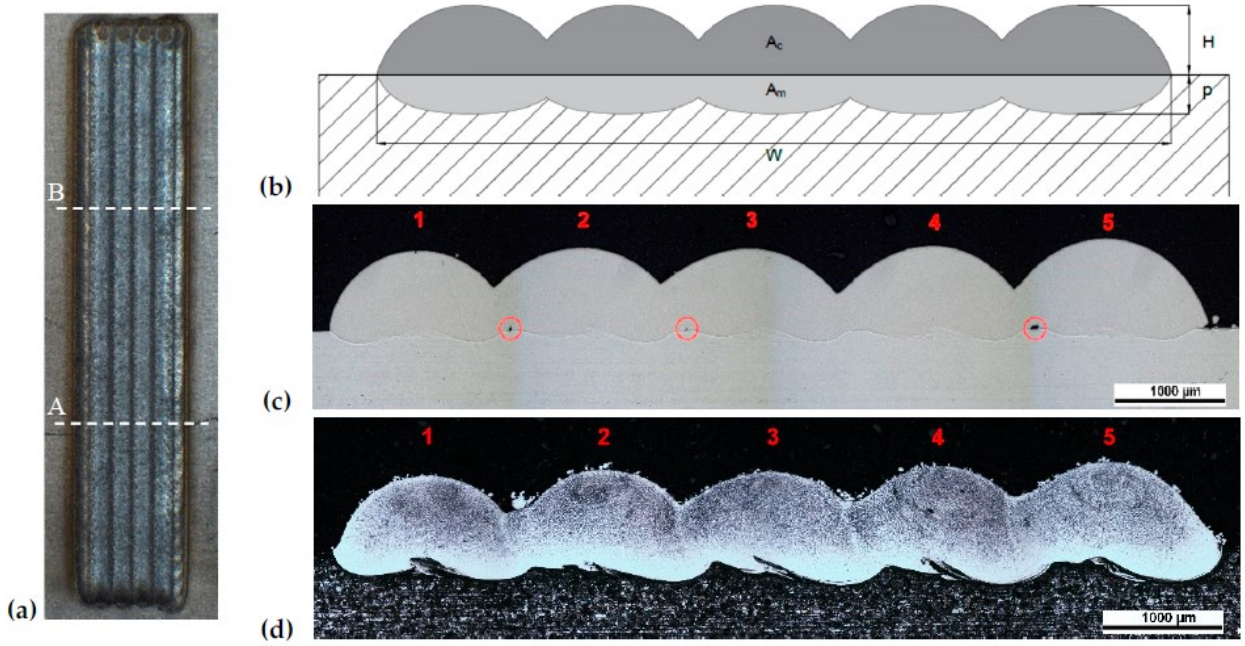

Figure 90 Front view of deposition 3.2 with cross-section positions (a); schematic representation of a deposition with geometrical characteristics (b); macrographic cross-section of deposition 1.3 (c); macrographic cross-section after chemical etching of deposition 2.3 (d) (Castellano et al., 2020).

In the schematic representation of the deposition in Figure 90(b), the geometric features considered in the study are shown. The scheme is compared with a cross-sectional macrographic deposition image, shown in Figure 90(c), indicating the

presence of defects at the interface between the deposition and the substrate. The cross-sectional macrographic images of the depositions after etching (Figure 90(d)) are useful to emphasize the penetration in the substrate. This parameter is of utmost significance since the bond between the base material and the cladding increases as it rises. The mixing between the two materials, however, is also growing, changing the same metallurgical and mechanical characteristics. The cladding detachment may be caused by low penetration, whereas a value too high would compromise the mechanical properties.

Specimen Overlap [%]	Deposition	W [µm]	Ac [µm²]	Am [µm²]	H_{avg} [µm]	p_{avg} [µm]	Dil [%]
S1 - OV10%	**1.1**	7358	2819623	522432	383	71	15.6
	1.2	5185	1641342	80638	317	16	4.7
	1.3	7901	4816624	541832	610	69	10.1
S2 - OV20%	**2.1**	6836	2508826	1210793	367	177	32.6
	2.2	4973	1344553	696406	270	140	34.1
	2.3	7463	3979401	1489496	533	200	27.2
S3 - OV30%	**3.1**	6055	2963106	416358	489	69	12.3
	3.2	4250	1599721	49534	376	12	3.0
	3.3	6396	4968972	390807	777	61	7.3
S4 - OV40%	**4.1**	5449	2593035	959149	476	176	27.0
	4.2	4083	1348843	474142	330	116	26.0
	4.3	6043	4240390	1121606	702	186	20.9
S5 - OV50%	**5.1**	4655	2963106	299270	600	64	9.7
	5.2	3429	1599721	4227	518	1	0.2
	5.3	4978	4968972	113891	965	23	2.3

Table 31 Specimens: denomination and geometrical characteristics of each deposition (Castellano et al., 2020).

The AM specimens tested are listed in Table 31, including the overlap percentage (OV%), and the geometrical characteristics of width (W), clad area (A_c) and substrate molten area (A_m) of each deposition. Moreover, the average clad height (H_{avg}) and the average substrate penetration (p_{avg}) were calculated as a ratio between relative areas and the width. Ultimately, the dilution (Dil) computed as ratio between the average substrate penetration and the height of the deposition (H_{avg} + p_{avg}). The H_{avg} and p_{avg} are plotted with respect the overlap percentage of each specimen in Figure 91(a). The increasingly closer depositions cause the average clad height to increase. There are strong variations of p_{avg} in the depositions with an overlap ratio of 20% and 40% which derived from the imposed perturbation of the powders flow (Figure 91(b)).

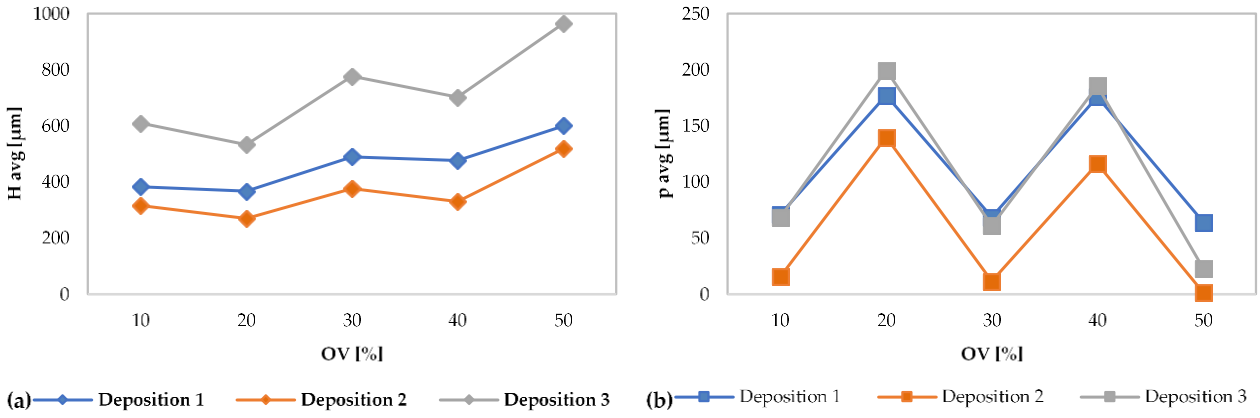

Figure 91 Geometric characteristics of average clad height (a) and average substrate penetration (b) for each deposition vs overlap percentage (Castellano et al., 2020).

4.6.2 Theoretical model of the ultrasonic goniometric immersion tests

The wave phenomena involved in the ultrasonic test should, from a theoretical point of view, be considered as a slight perturbation of the initial state of the body. The propagation of ultrasonic waves can therefore be studied by applying the linear theory of elastodynamics (Castellano et al., 2014).
In particular, the propagation of plane progressive elastic waves may be describing by assuming a displacement field

$$\boldsymbol{u}(\boldsymbol{x},t) = \mathbf{a}\,\varphi(\boldsymbol{x}\cdot\boldsymbol{n} - v\,t) \tag{18}$$

where **x** is a point of referential configuration of the body at the time t, **a** is the direction of motion, **n** is the direction of wave propagation, v is the velocity of propagation and φ is a real valued smooth function.
Without body forces, the wave propagation is ruled by the equation of the motion

$$\mathrm{Div}(\mathbb{C}[\nabla\boldsymbol{u}]) = \rho\ddot{\mathbf{u}} \tag{19}$$

where $\rho = \rho(\boldsymbol{x})$ is the mass density and $\mathbb{C} = \mathbb{C}(\boldsymbol{x})$ is the incremental fourth order elasticity tensor referred to the initial state of the body. From Eq. (19), it is possible to write the condition for wave propagation (the classical Fresnel-Hadamard's propagation condition) in the form of the Christoffel equation

$$[\boldsymbol{\Gamma}(\boldsymbol{n}) - \rho v^2 \boldsymbol{I}]\,\boldsymbol{a} = \mathbf{o} \tag{20}$$

where $\boldsymbol{\Gamma}(\boldsymbol{n})$ is the second order Kelvin-Christoffel propagation tensor for the direction **n**, given by

$$\boldsymbol{\Gamma}(\boldsymbol{n}) = \mathbb{C}^t[\boldsymbol{n} \otimes \boldsymbol{n}], \tag{21}$$

where the superscript "t" represents the minor transposition for fourth order tensors.
Eq. (21) shows that the Christoffel tensor $\boldsymbol{\Gamma}(\boldsymbol{n})$is related only to the elasticity tensor $\mathbb{C}$ and to the direction of propagation **n**.
Moreover, if an elastic wave propagates in a certain direction **n**, the Christoffel equation in Eq. (20) shows that the square of the wave velocity v is an eigenvalue of the Christoffel tensor for the direction of propagation **n**, while the direction of motion **a** is the related eigenvector. Consequently, the symmetry properties of the material strongly influence the features of progressive elastic waves. Consequently, by Eq. (20) and (21), the elastic constants are linked to the velocity of propagation along a fixed direction **n**.
The Federov-Stippes theorem demonstrates that if the elasticity tensor $\mathbb{C}$ is symmetric and strongly elliptic, then at a point **x** there exist longitudinal (**a** and **n** parallel) and transverse (**a** and **n** perpendicular) elastic waves. If the material is isotropic, for each possible direction of propagation **n** only *pure* propagation modes like longitudinal waves and transverse waves may propagate. On the contrary, elastic waves will propagate in non-pure propagation modes for anisotropic materials in the generic direction of propagation **n**, different from the axis of material symmetry (as quasi-longitudinal waves or as quasi-transverse waves).
A non-destructive ultrasonic experimental characterisation of the materials is implied by this theoretical framework. The findings of ultrasonic experiments can then be used to address two big issues in elastic material mechanics. :

1) *the classification problem*, that is the determination of the class of symmetry and the description of the axes of material symmetry
2) the *representation problem*, that is the determination of the elastic tensor components that define the elastic response of the material once the symmetry class is established.

In the research case, using the theoretical model of the isotropic material to explain the mechanical response of the AM components, the elastic moduli could be calculated from experimental measurements of ultrasonic wave velocities.
To this aim, the inversion of the Christoffel equation in Eq. (17) has yielded the well-known relations in Eq. (22)

$$E = \rho V_T^2 \frac{3V_L^2 - 4V_T^2}{V_L^2 - V_T^2}, \qquad G = \rho V_T^2, \qquad \nu = \frac{\left(\frac{V_L}{V_T}\right)^2 - 2}{2\left[\left(\frac{V_L}{V_T}\right)^2 - 1\right]}, \tag{22}$$

between the engineering elastic moduli (the Young's modulus E, the shear modulus G and the Poisson's ratio ν), the velocity of longitudinal waves V_L and of longitudinal waves V_T and the density ρ.

4.6.3 Ultrasonic tests setup

The ultrasonic tests were performed by *Laboratorio Ufficiale Prove Materiali "M. Salvati*" of Polytechnic University of Bari, a laboratory equipped with advanced facilities for non-destructive testing (Castellano et al., 2014). The experimental setup shown in Figure 92 consists of:

- An ultrasonic immersion focused transducer (central frequency equal to 5 MHz) connected to a platform which allow a 3-DOF motion and a rotation of the probe according to fixed angles.
- An Olympus ultrasonic pulser/receiver 5072PR for generating and receiving the ultrasonic waves.
- A digital oscilloscope Agilent MSU-X-4054A (500 MHz, 4 channels) for monitoring the ultrasonic signals.
- A water tank.
- A workstation with ad-hoc developed software in Labview for each phase of tests: the management of the ultrasonic probe and the reprocessing of the experimental data.

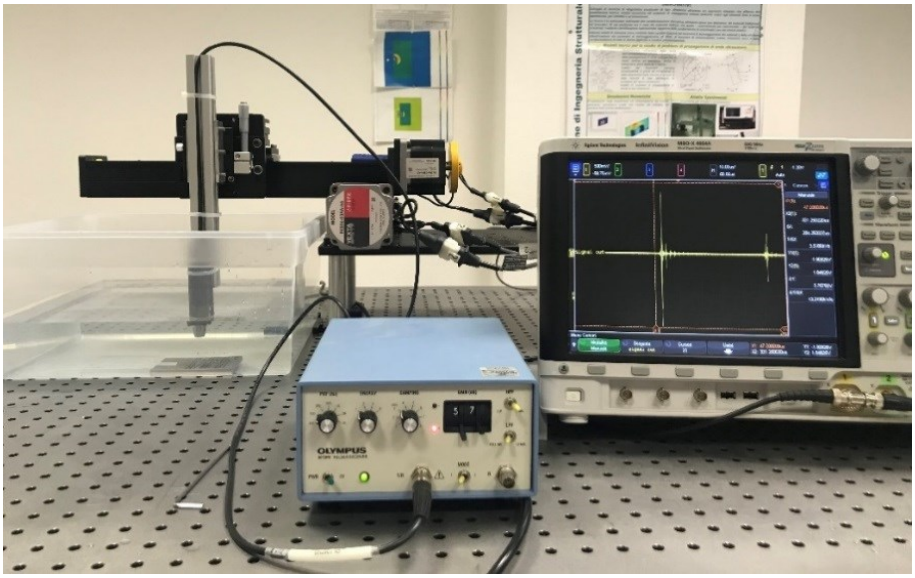

Figure 92 Ultrasonic immersion tests setup: main components (Castellano et al., 2020).

Unlike contact tests, the sample and the transducers are immersed in a water tank without any contact during ultrasonic immersion tests. The water acts as a coupler in this situation, enabling optimum acoustic coupling. In addition, the movement of the probe is not manual, but automatic.

The above two features make the experimental measurements of ultrasonic velocities more precise. Thanks to the rotation of the ultrasonic probe (or the sample), it is possible to investigate the acoustic reaction of the material at various inclination angles of the ultrasonic beam relative to the surface of the sample (Figure 93). This makes ultrasonic goniometric immersion experiment the best experimental non-destructive approach for mechanical characterization.

Longitudinal waves are enabled by water, but the transverse waves can be produced in the sample by adjusting the polarization of the acoustic wave crossing the interface between the various media, i.e. by converting the mode according to the Snell law in Eq. (23).

$$\frac{\sin\theta_i}{v_w} = \frac{\sin\theta_r}{v_p}, \tag{23}$$

where $\theta_i$is the angle of incidence on the surface of the sample of the ultrasonic beam travelling in the water, v_w is the ultrasonic velocity in the water, v_p is the phase velocity of the refracted beam into the sample and θ_r is the refraction angle of the ultrasonic beam into the sample.

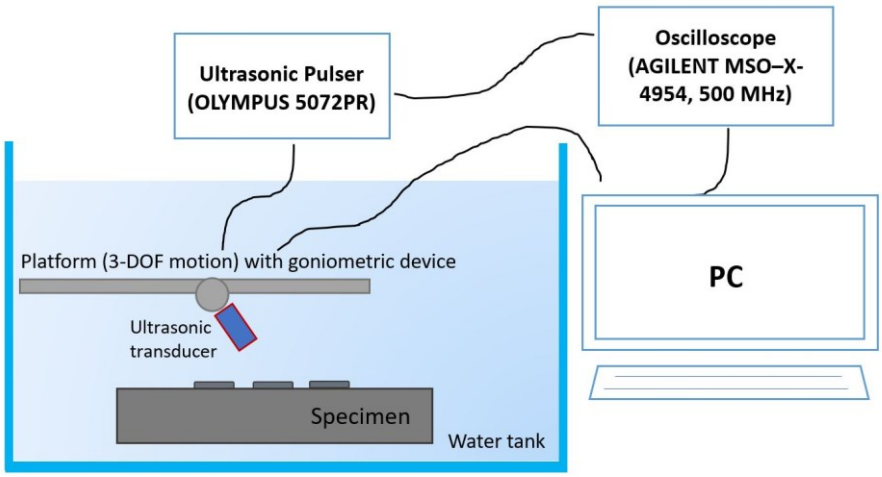

Figure 93 Ultrasonic immersion tests setup: a schematic drawing showing the rotation of the ultrasonic transducer by means of the goniometric device (Castellano et al., 2020).

Using the pulse-eco technique (or back reflection technique), the experiments were carried out. The time of flight (TOF) of the ultrasonic waves propagating in the sample by rotating the probe according to specified angles was calculated during the tests (Figure 94). The TOF of the ultrasonic waves propagating into the substrate and the TOF of the ultrasonic waves propagating into the new material resulting from the AM process consisting of the substrate and the deposition, were calculated for each specimen, respectively.
The TOF measurements were carried out by means of an averaging method of the acquired and also normalised ultrasonic signals for each region of the AM samples tested by the Labview program developed.
The measurements of the TOF of the longitudinal waves were carried out with a probe rotation angle equal to 0°, while for transversal waves, the probe rotation angles range was 15.00°– 16.00°.
Starting from the TOF of the ultrasonic waves, know the thickness of substrate and of the new material (substrate + deposition), the ultrasonic velocities of the longitudinal waves and of the transversal waves were determined. Finally, known the density of the substrate and the resulting AM material (substrate + deposition), the elastic moduli were determined through Eq. (22).

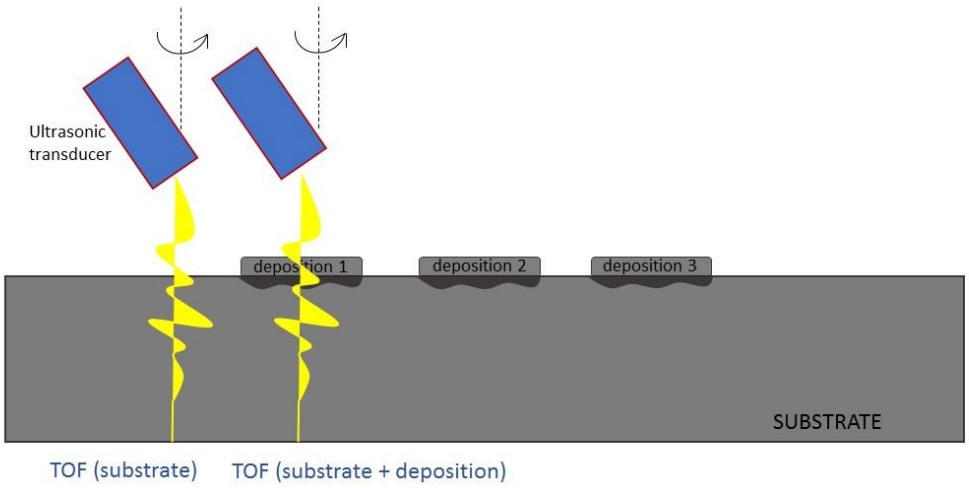

Figure 94 Experimental procedure for measuring TOF of the ultrasonic waves in substrate and in resulting AM material (substrate + deposition) for each specimen (Castellano et al., 2020).

4.6.4 Ultrasonic test results

The experiments carried out on each specimen made it possible to determine the time of flight of the longitudinal and transversal ultrasonic waves, respectively.

The TOF values of the ultrasonic longitudinal waves propagating in the substrate and in the new material produced by the AM process (substrate + deposition) are shown in Figure 95 for each sample compared to the percentage of deposition overlap (OV). In specimens S2 and S4, due to the perturbation of the powder flow induced in these treatments, a strong deviation from the predicted pattern can be observed.

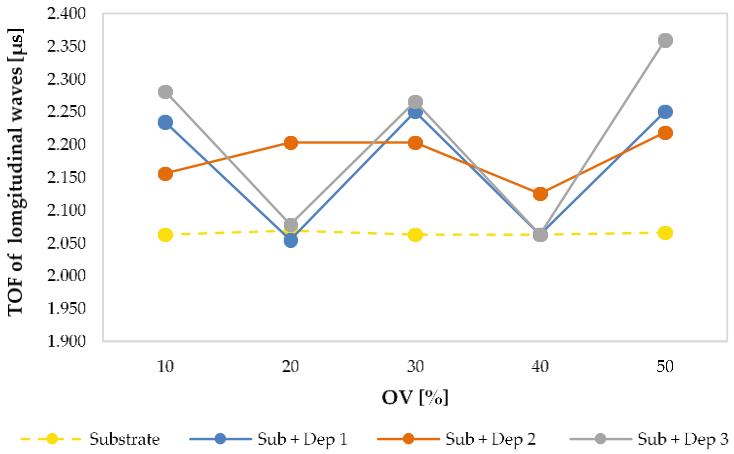

Figure 95 The TOF of the ultrasonic longitudinal waves propagating into the substrate and into the new material resulting by AM process (Sub + Depi, for i=1,2,3) measured for each specimen, i.e. as a function of the overlap percentage (Castellano et al., 2020).

The TOF values of the ultrasonic transversal waves are plotted in Figure 96 with respect to the percentage of deposition overlaps (OV) and grouped for each set of process parameters, showing a more stable pattern with slight growth as OV increases.

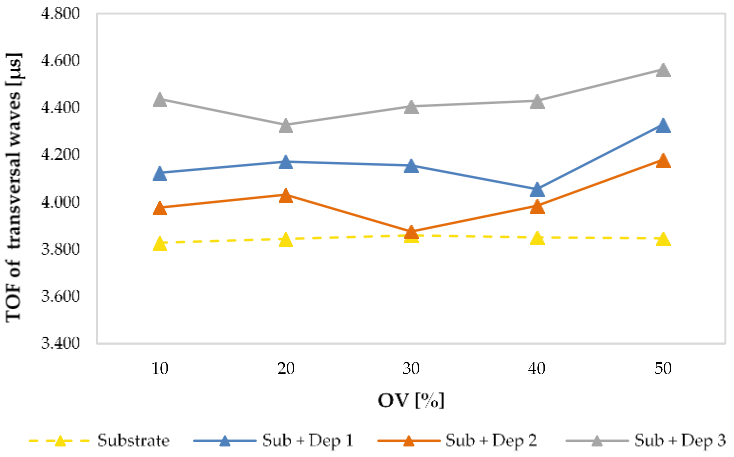

Figure 96 Comparison between the TOF of the ultrasonic transversal waves propagating into the substrate and into the new material resulting by AM process (Sub + Depi, for i=1,2,3) measured for each specimen, i.e. as a function of the overlap percentage (Castellano et al., 2020).

The comparisons between the ultrasonic test results obtained in specimens without deposition anomalies (S1, S3 and S5) and those obtained in all specimens, including those with anomalies (S2 and S4), are discussed below in order to investigate the ability of the proposed ultrasonic method to classify deposition anomalies in specimens.
Figure 97 indicates, in particular, the longitudinal wave TOFs versus the average clad height obtained in specimens without deposition anomalies.

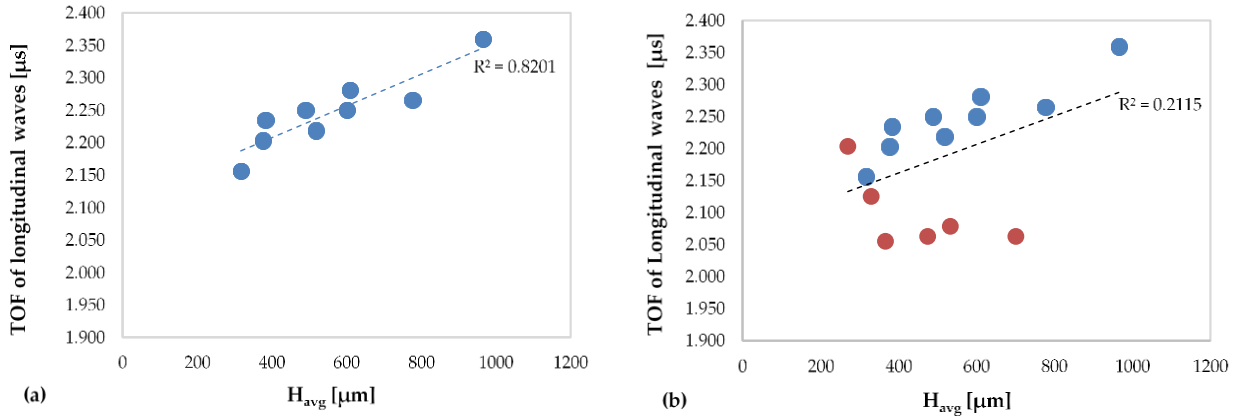

Figure 97 TOFs of the longitudinal waves versus Havg: (a) related to the specimens without deposition anomalies and (b) related to all specimens (including specimens with deposition anomalies in red colour) (Castellano et al., 2020).

An excellent correlation between the longitudinal wave time of flight values and the average multi-clad height (R^2 = 0.8201) is observed in Figure 97(a): as the average clad height increases, the TOF value increases.
Otherwise the presence of a cluster of values altering the reliability of the linear regression function should be noted in Figure 97(b). Indeed the close association between the TOF and the average multiclad height is lost, even considering the TOF of the longitudinal waves obtained in the specimens with deposition anomalies (R^2=0.2115).
The TOFs of the transverse waves versus the average clad height obtained in specimens without deposition anomalies (a) and obtained in all specimens (b) are shown in Figure 98.

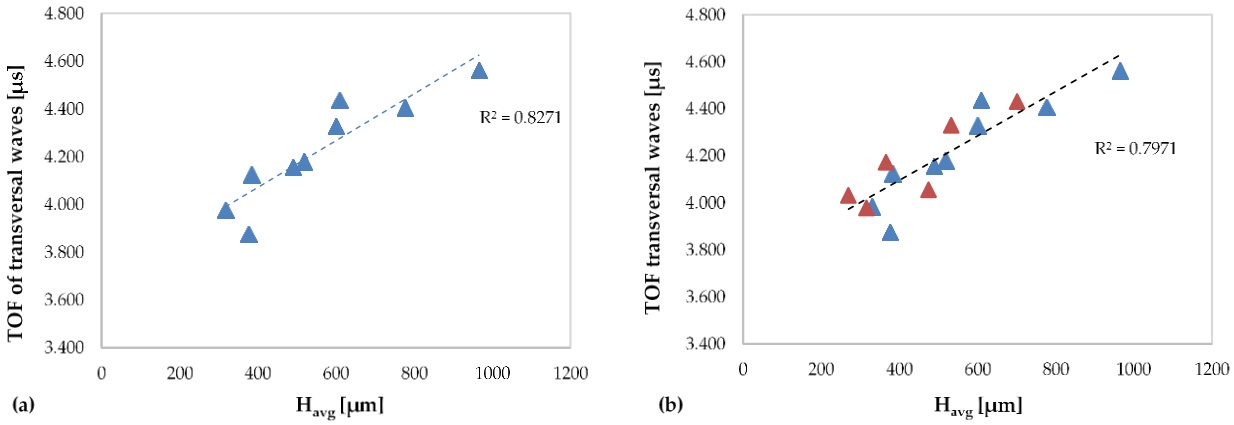

Figure 98 TOFs of the transversal waves versus Havg: (a) related to the specimens without deposition anomalies and (b) related to all specimens (including specimens with deposition anomalies in red colour) (Castellano et al., 2020)

Figure 98(a) and Figure 98(b) display a strong correlation between the time of flight of the transverse waves and the average cladding height, but slightly more marked in the graph with respect to non-defect specimens only (R^2 = 0.8271). The TOF values of the transverse waves are found to increase with the increase in the average clad height in both graphs. The ultrasonic results obtained in terms of longitudinal wave TOFs are capable to better classify the deposition defects in the specimens than those obtained in terms of transverse wave TOFs.
Dil parameter, which describes the dilution of the substrate material in the deposited cladding, analysed the effect of the material mixing on TOFs of ultrasonic waves.
As a function of the dilution percentage, Figure 99(a) shows the trend of the TOF of the longitudinal waves. Two separate clusters are formed with a decreasing propensity to raise. On the contrary, as shown in the previous study, this phenomenon has no effect on the TOF of the transverse waves plotted in Figure 99(b).

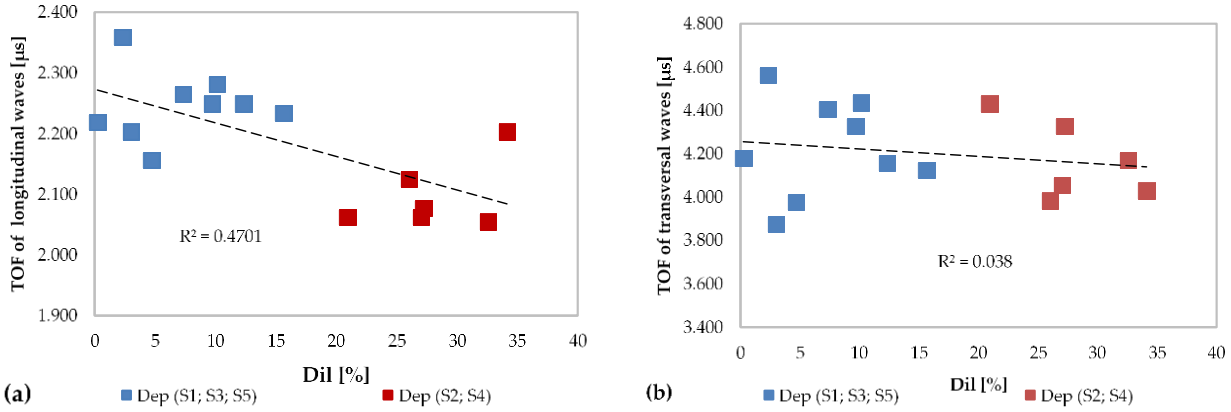

Figure 99 (a) TOFs of the ultrasonic longitudinal waves and (b) TOFs of the ultrasonic transversal waves versus dilution Dil grouped by deposition without anomalies (in blue colour) and deposition with anomalies (in red colour) (Castellano et al., 2020).

The values of the ultrasonic velocities of the longitudinal waves and transversal waves, respectively, were calculated by the measurement of the TOFs of the ultrasonic waves in the substrate and in the new material. Values of ultrasonic velocities of the longitudinal waves (Figure 100) and of the transversal waves (Figure 101) were measured in the substrate and in the new resulting material consisting of the substrate and the deposition (Sub + Dep_i, for i=1,2,3) for each specimen, as a function of the overlap (OV) percentage of the multiclad depositions.

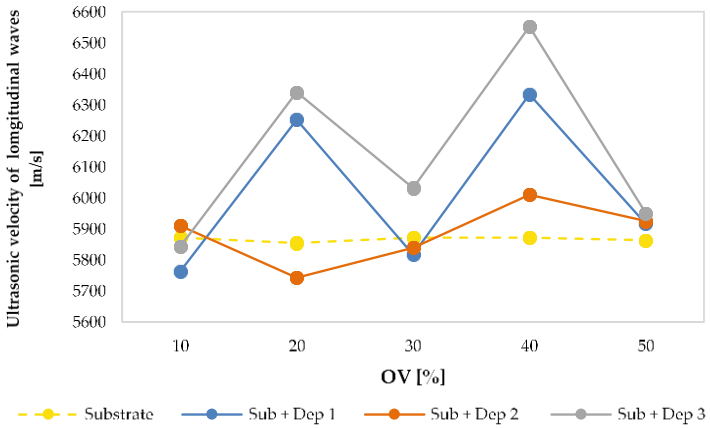

Figure 100 Ultrasonic velocities of the longitudinal waves of the substrate and of the new resulting material (Sub + Depi, for i=1,2,3) measured for each specimen, i.e. as a function of the overlap percentage (Castellano et al., 2020).

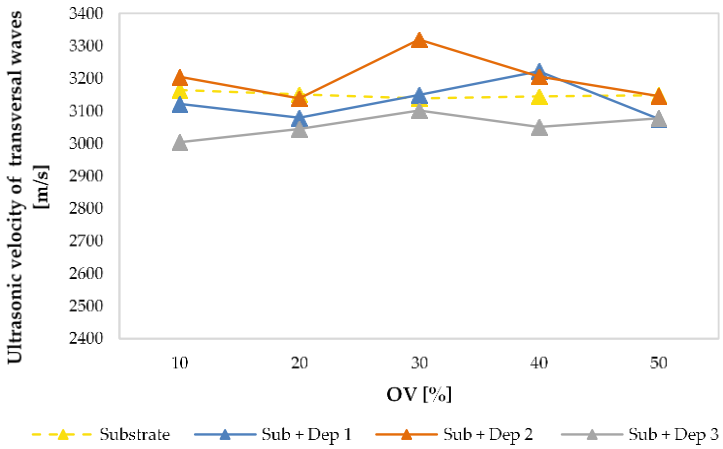

Figure 101 Ultrasonic velocities of the transversal waves of the substrate and of the new resulting material (Sub + Depi, for i=1,2,3) measured for each specimen, i.e. as a function of the overlap percentage (Castellano et al., 2020).

An average values of the ultrasonic velocities equal to 5866 m/s for the longitudinal waves and 3149 m/s for the transversal waves are measured for the substrates. Values are comparable with those reported in the literature concerning a stainless steel AISI 304.

The ultrasonic velocity values obtained by propagating the ultrasonic waves in the new resulting material do not indicate any reliance on the percentage of overlap. As already observed in Figure 6, it should be noted that the S2 and S4 specimens in Figure 100 display a strong deviation from the predicted trend, which was definitely due to the perturbation of the powder flow in these treatments.

The ultrasonic velocity values of the longitudinal waves versus the average height of the clad obtained in specimens without a deposition defect are shown in Figure 102(a) and obtained in all specimens in Figure 102(b). However, Figure 103 shows the same relation with respect to transversal waves.

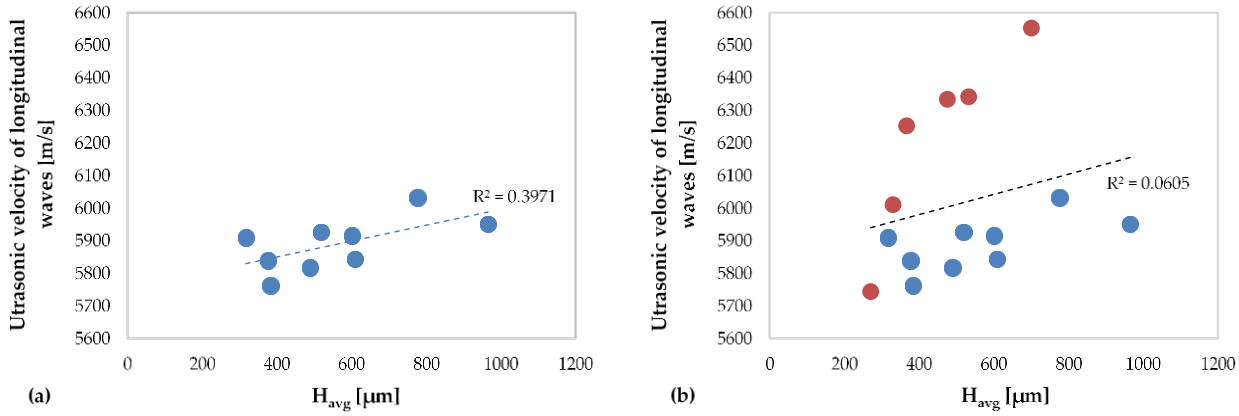

Figure 102 The ultrasonic velocity of the longitudinal waves versus average clad height Havg: (a) related to the specimens without deposition anomalies and (b) related to all specimens (including specimens with deposition anomalies in red color) (Castellano et al., 2020).

Figure 102(a) and Figure 103(a) show a moderate correlation between the ultrasonic velocity of the longitudinal waves ($R^2 = 0.3971$) and of the transversal waves ($R^2 = 0.3585$), respectively, and the average clad height. In particular, as the clad height increases, the ultrasonic velocity of the longitudinal waves increases, while a contrary behaviour is observed for the transverse waves. This is due to the different propagation properties of the longitudinal and transverse ultrasonic waves.

As shown in Figure 97 and Figure 98, the deposition irregularities induced by the interference of the powder flow produced a variation of the ultrasonic velocity trend of both the longitudinal ($R^2 = 0.0605$) and transverse waves ($R^2 = 0.2769$) with respect to the TOFs of the ultrasonic waves. In the graph relating to the ultrasonic velocity of the longitudinal waves, this difference is clearer.

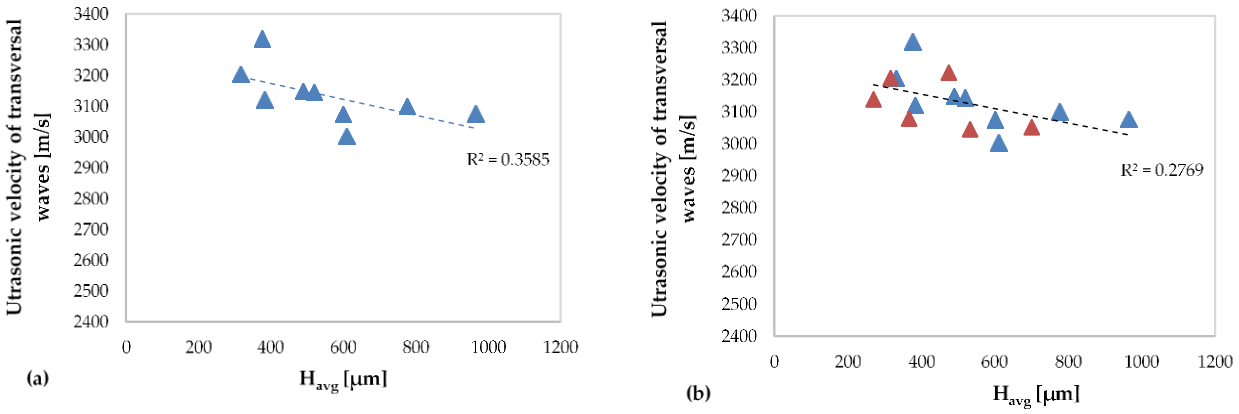

Figure 103 The ultrasonic velocity of the transversal waves versus average clad height Havg: (a) related to the specimens without deposition anomalies and (b) related to all specimens (including specimens with deposition anomalies in red colour) (Castellano et al., 2020).

4.6.5 Determination of the mechanical elastic moduli

The velocity of the longitudinal waves is able to better define the deposition anomalies of the specimens compared to the velocity of the transversal waves, as already emphasised in the results obtained in terms of TOF. The wave propagation properties of longitudinal waves derive from this promising capability, as the direction of motion coincides with the direction of wave propagation, while these two directions are orthogonal in transversal waves.

The propagation features of the longitudinal waves allow the variability of the mechanical behaviour along the thickness of the new resulting material due to the properties of the deposition process to be more accurately investigated. Therefore, with the rise in average clad height in the absence of defects, the pattern of the ultrasonic velocities of the longitudinal waves increases, but in the presence of deposition defects, it is strongly modified.

Nevertheless, the results obtained in terms of longitudinal wave TOF showed an even more obvious correlation with the average clad height relate to those obtained in terms of longitudinal wave velocity because the time of flights are closely related to the ultrasonic wave propagation path length.

Finally, it can be noted that the TOF results of the longitudinal waves can better explain the geometrical variations of the deposition of the AM components, while the ultrasonic velocity results of the longitudinal waves can also show some initial details about the mechanical characteristics of the new materials obtained from the AM process.

Below is the examination of the mechanical behaviour of the AM components in terms of elastic moduli defined by the results of the ultrasonic immersion tests.

Based on the experimental values of the ultrasonic velocities and know of the substrate mass density (approximately 7900 kg/m3) and the mass density of the new materials obtained by the AM process (see Table 32), the engineering elastic moduli were calculated using Eq. (22): Young's modulus, shear modulus and Poisson's ratio for the substrate and the new resulting material for each sample.

Mass density [kg/m^3]	**OV10%**	**OV20%**	**OV30%**	**OV40%**	**OV50%**
Sub + Dep 1	7753.68	8436.28	7826.88	8420.81	7971.26
Sub + Dep 2	7951.35	7749.64	7855.18	8085.94	7984.08
Sub + Dep 3	7861.33	8457.15	8014.45	8515.42	8018.48

Table 32 Mass density [kg/m^3] of the new material (substrate + deposition) obtained by AM process (Castellano et al., 2020).

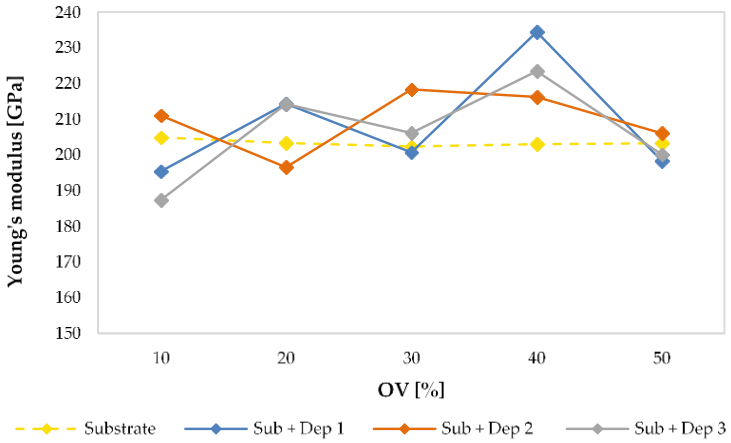

Figure 104 Young's modulus values of the substrate and of the new material (Sub + Depi, for i=1,2,3) measured for each specimen, i.e. as a function of the overlap percentage of the multiclad depositions (Castellano et al., 2020).

The values of the Young modulus (Figure 104), the shear modulus (Figure 105) and the Poisson ratio (Figure 106) assessed for the substrate and the new material (Sub + Depi, for i=1,2,3) for each specimen are shown in the following graphs, as a function of the overlap (OV) percentage of the multiclad depositions.

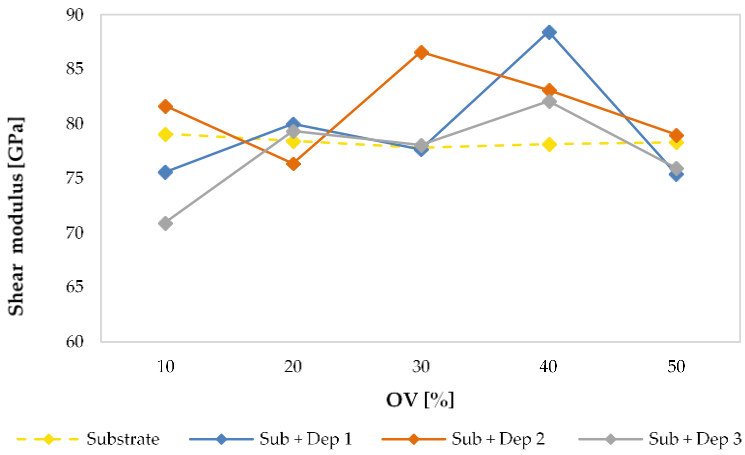

Figure 105 Shear modulus values of the substrate and of the new material (Sub + Depi, for i=1,2,3) measured for each specimen, i.e. as a function of the overlap percentage of the multiclad depositions (Castellano et al., 2020).

As previously indicated, there were very minor differences between specimens with regard to the values of the velocities of the ultrasonic waves, and also with regard to the values of the elastic moduli of the specimen substrate. The average value of the Young modulus (203.33 GPa), of the shear modulus (78.35 GPa) and of the Poisson ratio (0.298) are similar to those stated in the AISI 304 stainless steel literature.

On the contrary, the material produced by the AM process showed a strong discrepancy between the specimens' elastic moduli. Furthermore, as observed in the acoustic response, there is no dependence on the overlap (OV) percentage of the multiclad deposition in the mechanical response in terms of elastic moduli.

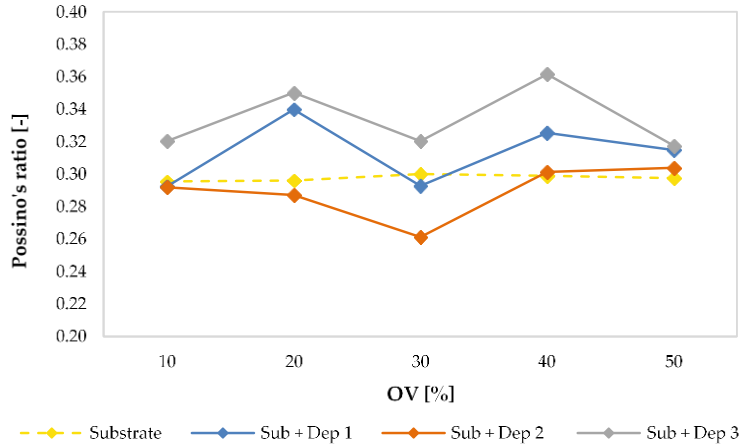

Figure 106 Poisson's ratio values of the substrate and of the new resulting material (Sub + Depi, for i=1,2,3) measured for each specimen, i.e., as a function of the overlap percentage of the multiclad depositions (Castellano et al., 2020).

Finally, by evaluating the mechanical behaviour observed both in specimens without deposition anomalies (S1, S3 and S5) and those observed in all specimens (including specimens with deposition anomalies), and the average height of the clads, the ability of the proposed ultrasonic approach to test deposition anomalies is investigated.

The trend of the Young modulus as a function of the average height of the cladding in specimens without deposition anomalies is shown in Figure 107(a) and in all specimens, including those with deposition anomalies, in Figure 107(b).

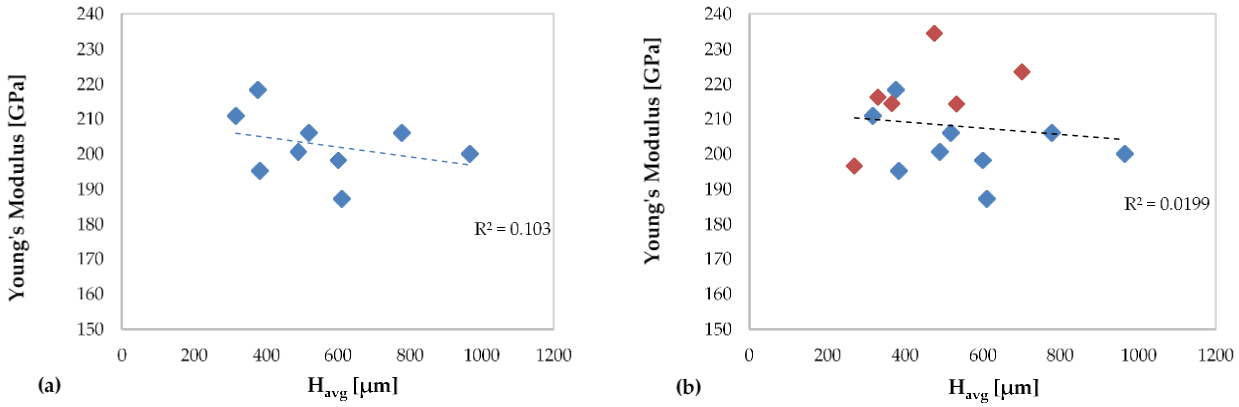

Figure 107 Young's modulus values of the new resulting material versus Havg: (a) specimens without deposition anomalies and (b) all specimens (including specimens with deposition anomalies in red colour) (Castellano et al., 2020).

A low correlation (R^2= 0.103) is observed in Figure 107(a) between the mechanical behaviour of AM specimens in terms of Young's modulus and the average multiclad height.
In Figure 107(b) related to all specimens, including the specimen with anomalies of deposition, the trend of Young's modulus considerably varies, and the correlation observed in specimens without defect completely vanishes (R^2= 0.0199).
Figure 108 shows the association between the shear modulus and the average height of cladding in specimens without deposition anomalies and in all specimens.

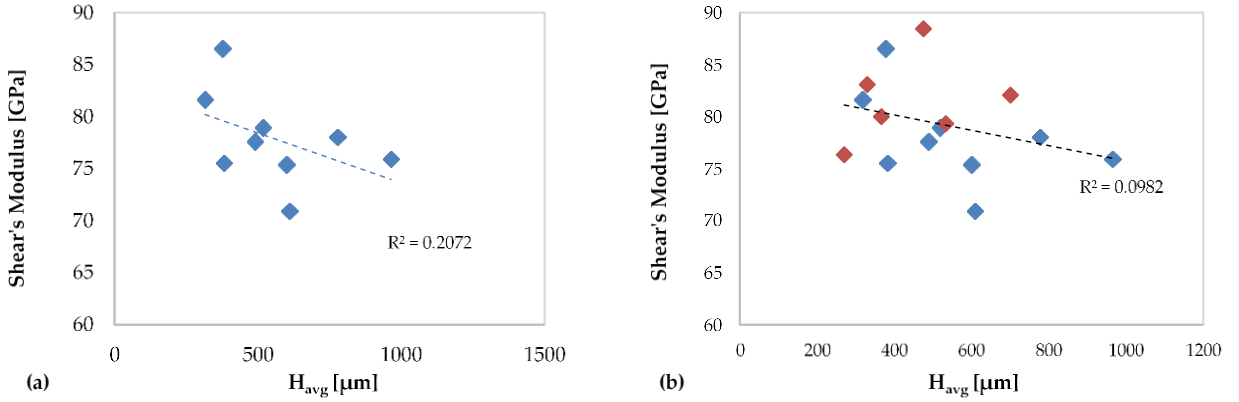

Figure 108 Shear's modulus values of the new resulting material versus average clad height: (a) specimens without deposition anomalies and (b) all specimens (including specimens with deposition anomalies in red colour) (Castellano et al., 2020).

In this case, the strongest correlation is found between the mechanical behaviour of AM specimens with regard to the shear modulus and the average clad height of non-defect specimens (R^2= 0.2072), which is also lost with regard to defect specimens (R^2= 0.0982). Both graphs show that the values of the elastic moduli decrease as the average height of the multiclad increases.
Figure 109 show the correlation between the Poisson's ratio and the average height of the clad in specimens without deposition anomalies and in all specimens.
There is a closer correlation between the mechanical behaviour of the AM specimens with respect to the Poisson ratio and the average height of the multiclad compared to the previous cases especially in Figure 109(a) concerning specimens the without anomalies (R^2 = 0.5462).
A decrease in this correlation is observed in Figure 109(b) (R^2 = 0.2218) due to the values obtained in specimens with trend-altering deposition anomalies.
In comparison to the Young's modulus and the shear modulus plots, it is noticed that the Poisson ratio values increase as the average height is increased.
The results obtained in terms of elastic moduli show a lower correlation from the average clad height of the mechanical response of the new material resulting from the AM process, except for those obtained in terms of Poisson ratio. Predicted

trends for moduli often differ significantly, taking account of the findings obtained in specimens with deposition anomalies.

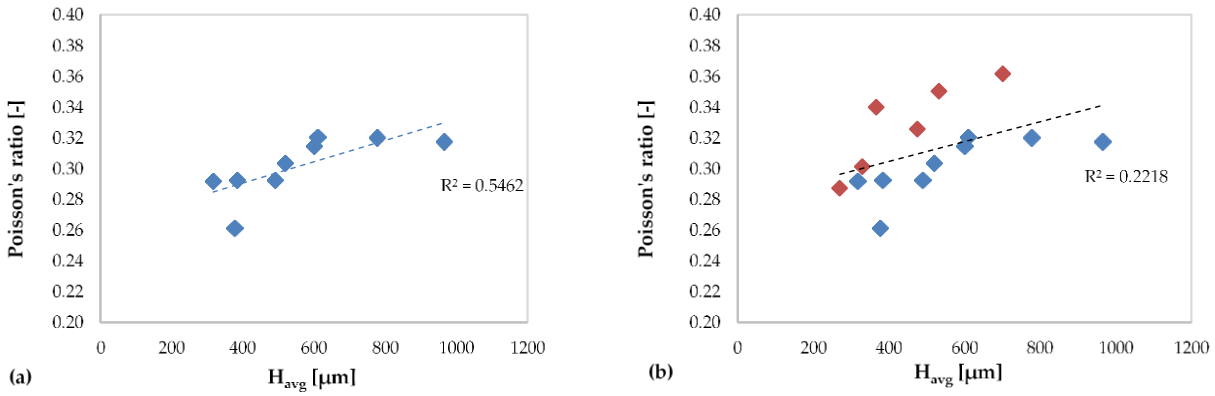

Figure 109 Poisson's ratio values of the new resulting material versus average clad height: (a) specimens without deposition anomalies and (b) all specimens (including specimens with deposition anomalies in red color) (Castellano et al., 2020).

4.6.6 Conclusions

The purpose of the work was to investigate the capability of the proposed ultrasonic approach to characterise the components produced by additive manufacturing. An effective mechanical characterization of the substrate and new material consisting of the substrate and the deposition obtained by the AM process has been carried out by ultrasonic goniometric immersion tests.

It can be asserted that there is a very close relationship between the acoustic and mechanical properties of the AM components and the average height of the clads, according to the results obtained. The effectiveness of the proposed ultrasonic approach for the characterization of deposition anomalies, expressly produced in two specimens, was investigated, leveraging this important correlation. Indeed, the ultrasonic findings related to the specimens with deposition anomalies showed that both the acoustic and mechanical parameters of the AM components altered the predicted pattern. In particular, the results obtained in terms of TOF, and velocity of the longitudinal ultrasonic waves have better explained the alteration of the AM components predicted acoustic and mechanical behaviour.

On the contrary, in all samples, including those with defects, ultrasonic transversal waves were less influenced by deposition irregularities, indicating a robust evaluation method and more reliable values of the average clad height. These waves did not involve any details on irregularities in depositions.

The outcomes shown are the first results obtained by using the proposed non-destructive experimental approach. Further experimental campaigns are ongoing in order to mechanical characterise the AM components that exhibit anisotropic mechanical behaviour.

5 SUSTAINABILITY OF DLMD PROCESS

The World Commission on Environment and Development first introduced the concept of sustainability in the Brundtland Report in 1987. In that year, the commission defined sustainable development as *"…development that meets the needs of the present without compromising the ability of future generations to meet their own needs…"* (Mebratu, 1998).
The report underlined the need to moderate economic development (increasing with the advent of industries and capitalism) and make it sustainable for the environment and the society. This represents the process of change in which the exploitation of resources, the orientation of technological development, institutional and financial changes are all in tune for enhancing the current potential in order to meet both current needs and preserving that of future generations. The guiding principle of sustainability is the sustainable development, which concerns in an interconnected way the environmental, economic, and social sectors to achieve a socio-ecological process characterised by the desire to pursue a common ideal.
In fact, once the main development sectors have been defined, it is clear their indivisible connection and the importance of maintaining this balance so that the growth of one does not compromise others, causing its decline and decay.
Therefore, the sustainability is a multidimensional concept that includes environmental, economic, and social dimensions. These dimensions form the Triple Bottom Line (TBL) or Triple-P (People, Planet, Profit) vision of sustainability (Alhaddi, 2015; Dalibozhko and Krakovetskaya, 2018). The pillars of sustainability are strictly interconnected and can graphically be represented as in Figure 110. The TBL line are:

- **Environmental TBL line**. It is the capability to preserve over time the three functions of the environment which are: providing resources, being a recipient of waste, and being a direct source of utility. In a territorial system, environmental sustainability means the capability to enhance the environment as a distinctive element of the territory itself, while ensuring the protection and renewal of natural resources and heritage.
- **Economic TBL line**. This represents the capability to ensure lasting income, work, and economic growth by achieving eco-efficiency, understood as the rational use of available resources and as a reduction in the exploitation of non-renewable resources.
- **Social TBL line.** Its primary objective is the pursuit of equity. This means that it tends towards the elimination of poverty, the inequality of benefits, the development, and the creation of conditions of dignity for the life of every man. The purpose of social sustainability implies the satisfaction of needs of the individual, established in the general principles of international human rights treaties. In particular, it involves taking useful actions to affirm economic, political, cultural rights, gender, and race equity between people. The idea is that these practices provide value to the community.

Figure 110 Triple bottom line (Dalibozhko and Krakovetskaya, 2018)

These three dimensions interact, overlap, and sometimes conflict. For instance, environmental sustainability could be detrimental to economic sustainability due to the additional investments required for less polluting production processes.

However, organizations must act together to pursue them all. Each dimension alone represents a necessary, but not sufficient, condition to achieve sustainability.
Throughout history, there has always been a heated debate between visions of sustainability that placed the focus on the economy and "manufactured capital", or environment and "natural capital" (Ayres et al., 2001). The concept of social sustainability thus defined can also be divided into two varieties:

- weak sustainability in which natural capital to be handed down can be replaced by manufactured capital, thus created by man.
- strong sustainability in which the capital to be given to future generations can only be "natural", deriving exclusively from natural resources.

5.1 Sustainable Manufacturing

The manufacturing sector, as the main pillar of the civilized lifestyle, is strongly influenced by the problems of sustainability, being today still based on old production paradigms arise during the third industrial revolution. The concept of sustainability was recognized in the manufacturing sector about 100 years after industrialization. Although, after several decades, there is still no common definition among researchers and consequently there are not generally accepted or universal definitions for sustainable manufacturing. Even today, however, the explanation widely used in academic articles is provided by the US Department of Commerce. The concept behind sustainable manufacturing is the creation of products manufactured through non-polluting processes, intending to conserve energy and natural resources, and at the same time can be considered economically advantageous and safe for employees, communities, and consumers. Figure 111 shows a brief timeline of key events in sustainable manufacturing development.

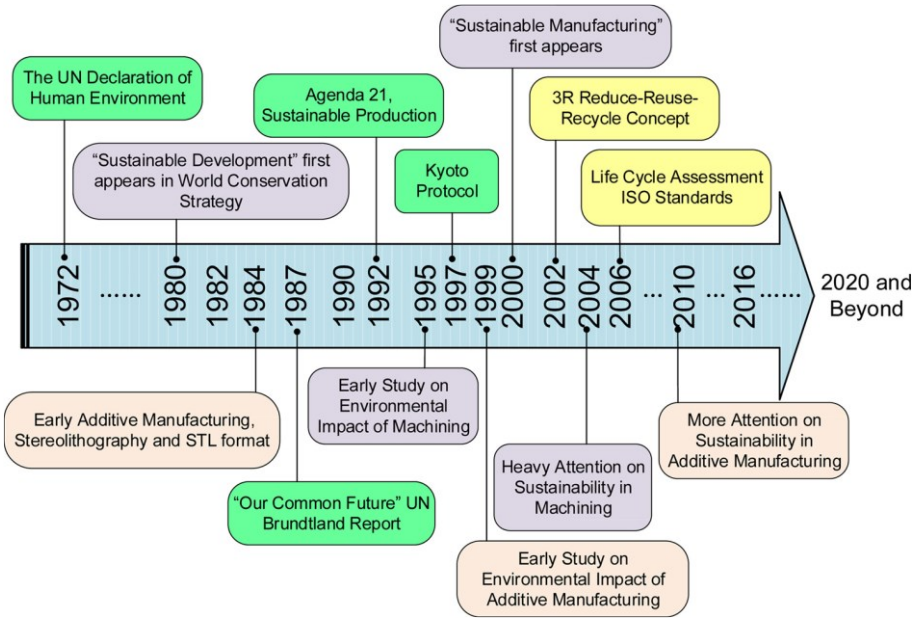

Figure 111 A timeline of sustainable manufacturing milestones (Peng et al., 2018).

Jovane et al. provide a schematic of sustainable manufacturing processes in Figure 112. The major global challenges that humanity must face today need to be addressed in the multifaceted context of the economy, society, environment, and technology (ESET). In recent years, a consensus for sustainable development and its implementation has emerged connected to a belief based on knowledge and competitive sustainable production. The only useful tool to pursue these common goals becomes education, research, and technological development and innovation (E&RTD&I) (Jovane et al., 2009).

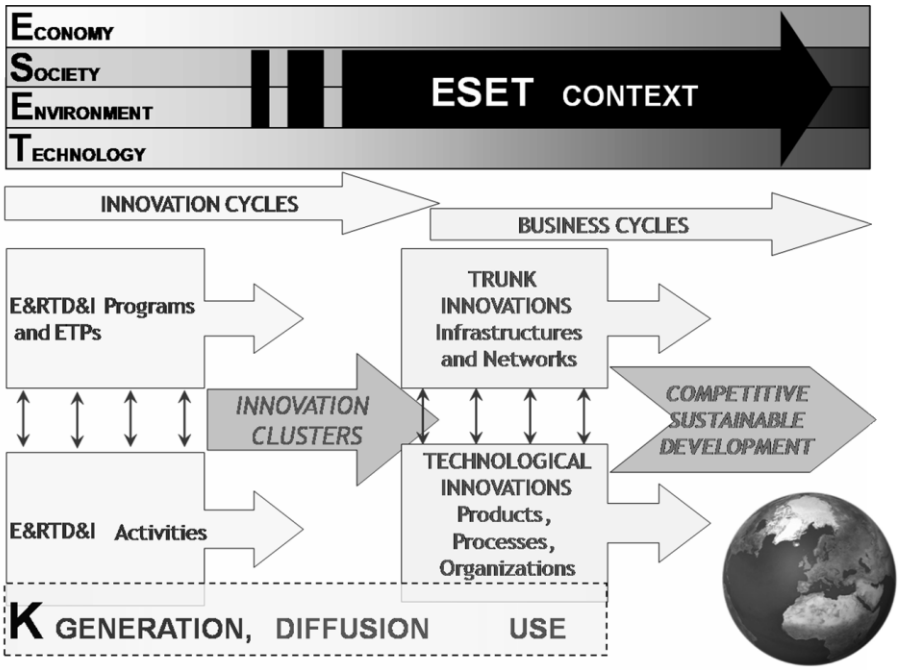

Figure 112 Reference Model: from Innovation Cycles to Business Cycles and Sustainable Development (Jovane et al., 2009)

The approach to be revolutionised is the precautionary principle towards technological innovation. Technological development and innovation are the only ideas capable of countering the current assumption that natural resources are infinite, and that the regenerative capacity of the environment is able to compensate for all human actions. Human actions must begin to be based on the sustainability paradigm. Therefore, the sustainable approach must be related to a policy of change, in order to achieve this goal with a continuous effort in a reasonable time frame for present and future generations. This change towards new linear thinking can be reached with the 6R methodology: Reduce, Reuse, Recycle, Redesign (or Rethinking), Recover, Remanufacture.

Reduce specifically refers to the production phase, where the amount of energy, material, and waste should be minimized. This is connected with the reuse of components after their first life cycle, in order to reduce the consumption of raw resources. Another way to decrease the use of raw materials is achieved by recycling waste materials. Recover is a way to extend the life cycle of a product, which could be extended by remanufacturing, in other words to process the product to restore the original structure. All this can be achieved only by redesigning the product and the life cycle through a vision aimed at sustainability (Jayal et al., 2010).

Although intense studies are being conducted to minimize the impacts of current manufacturing practices, many effects are difficult to both assess and measure. Therefore, sustainability research efforts have found in additive manufacturing the keystone that could guide the industry towards better adoption and actualization of manufacturing sustainability principles.

Sustainability is mainly based on three elements: environmental protection, economic prosperity, and creation of social value. These elements are identifiable in the AM, and it is essential to identify and understand its main impacts in order to grasp its contribution to more sustainable production processes. AM offers various benefits in terms of efficiency in the use of resources, which, added to some peculiarities in the design and production of objects with high performance, generate environmental, economic, and social benefits.

There are three main factors to consider in analysing the sustainable aspects of AM:

- **The product**. AM offers a wide advantage in defining the design. The capability to create more complex products with integrated functions, fewer parts or reduced weight, can reduce the production stages and the flows of materials used, reducing the environmental and economic impact of the products. The use of AM for repair processing improves the environmental impact of products by extending their life cycle and decreasing the energy and resources needed to create a new product.
- **The production process**. The majority of polymers can be recycled, while it is estimated that 90-95% of the metal powders discarded during a process can be reused in subsequent processes. The current state of research suggests a possible better energy performance of AM compared to other production processes, which would have an impact from both an economic and environmental point of view.

- **The supply chain**. Associated with the benefits of the "on-demand" production model allowed by technology and its impact on logistics and the entire value chain. Just as the design and production process change, so changes the way products are distributed. For this reason, the major contribution that AM brings is the decentralization of production.

5.2 Social Impacts of Additive Manufacturing

The social impacts generated by the technology is a relevant and interesting part of its sustainability assessment. The AM is disrupting the manufacturing sector and the conventional conception of work, becoming one of the pillars of the Industry 4.0 paradigm. However, knowledge about the social impacts of this technology is scarce and very limited in some areas.

Designers represent the artisans of our time. In order for a truly comprehensive approach to sustainability, it is necessary to reduce the dominance of mass production to balance the world's models of life that are attentive and responsible while maintaining the ideals of craftsmanship and supporting the work of the individual designer-maker for socio-cultural sustainability reasons.

Digital manufacturing and Web 2.0 have had a significant impact on designer-makers, shifting the entire production cycle into their hands. This brings back the craft sector, which was overtaken by the industrial revolution and mass production, before the systematization of production and the subsequent separation between production and retail. AM now offers the possibility for a reconnection between manufacturers and users that was not possible in the last century, as it enables the designer to exercise control over the entire product lifecycle. Consumers are no longer “passive”, since being able to participate in the production process, they become more and more important, producing for themselves and becoming “active” (Muthu and Savalani, 2016).

AM encourages innovative design and allows for on-demand production. This technology has led to a simplified supply chain, increasing efficiency, and responsiveness. The need for storage, transport, and packaging can be significantly reduced. With the advent of the personal AM machine, customers become manufacturers and can obtain desired products, affordably when they want and without leaving their homes.

The extreme personalization permitted by the AM can also bring positive implications in human health. The technology is used to produce custom surgical implants and custom-made healthcare devices. Researchers are now investigating the use of AM to produce scaffolds for tissue engineering applications and drug delivery devices (Huang et al., 2013).

However, in the literature, there is still unsatisfactory knowledge of social impact assessment. Matos et al. analysed the social impact of AM technology, applying some of Vanclay's categories. In particular, four categories of social impacts were considered relevant: (1) health and social well-being, (2) institutional, legal, political, and equity, (3) quality of the living environment (liveability), and (4) economic well-being and material.

The study appears to corroborate a multitude of positive social impacts of AM technology. These systems can work in autonomy in separate environments from the workers, thus limiting the possibility of injury or illness. Nevertheless, researchers have identified a worrying impact of AM technologies related to the health and safety of workers linked to the risks of exposure to dangerous substances (Matos et al., 2019).

It has been observed that in DLMD, SLS, BJ processes, or similar technologies that use powders or synthetic materials, particles with even nanometric particle size are emitted, which are highly harmful to health. The possibility of using these technologies in places without properly designed ventilation mechanisms, such as an office, home, or garage, it is of great concern (Rejeski et al., 2018).

5.3 Economic impact of Additive Manufacturing

In order to understand the economic trend of AM, or more generally of the Direct Digital Manufacturing (DDM), it is necessary to distinguish the production paradigms and their classification, as shown in Figure 113 and reported by Chen et al (Chen et al., 2015):

1. Craft production is performed by experts through their very specific skills and knowledge, obtained by "learn by doing" for a specialised task. These artisans targeted a close circle of consumers, mainly their local communities. Customer requirements were marginally incorporated into products.
2. Mass production leads to a standardization of products manufactured in a large plant, according to specific designs that maximize the economic aspect and maintain a good quality of manufacture. Consumers are large passive groups with little or no influence on product design.

3. Customized or modularized mass products for specific product end-user segments converge the demand for user groups with design and manufacturing.
4. In the production through Direct Digital Manufacturing (DDM) the design is entrusted to a large number of different people (designers), who create and catalogue the products. These can then be manufactured directly, improved, or modified according to the customer's desire, who in turn becomes designers, or better known as prosumers. The continuous interaction of the prosumers leads to a constant improvement of products over time.

Therefore, it becomes more understandable how the production through DDM can give rise to market democratization, in which individual (or small groups) independent buyers and sellers proliferate, thanks to the possibility of a complete customization of products. DDM's economic potential lies in the enhancement of the design for the various AM systems managed by a global community of users, reducing the development and purchasing times of raw materials.

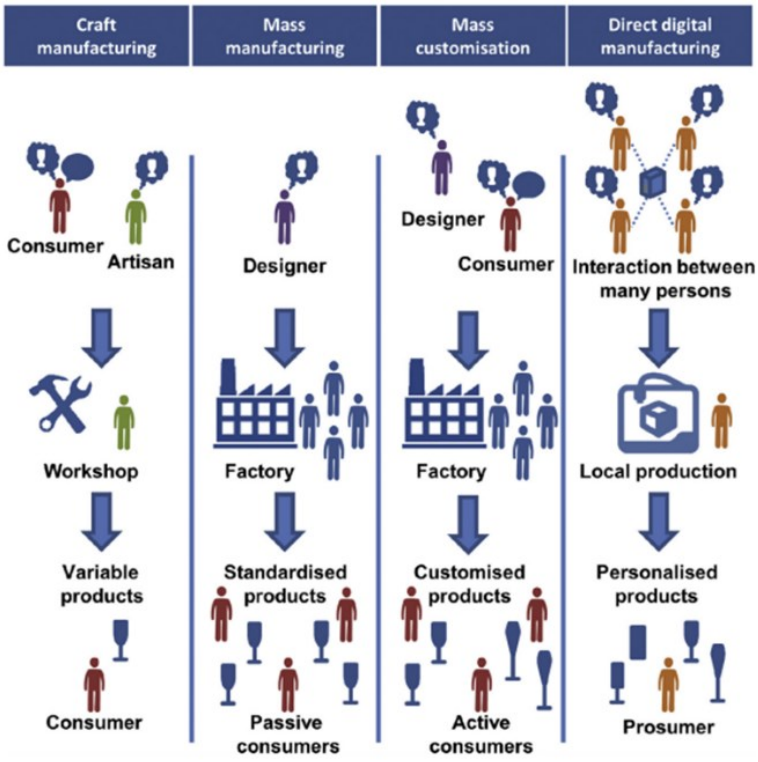

Figure 113 A comparison of manufacturing paradigms and their main actors (Chen et al., 2015)

By changing the business model, it is necessary to rethink a new form of the supply chain to better manage the complexities of AM. Its main purpose is to make the company more effective, efficient, and ready to respond to the needs of customers and suppliers. Thanks to AM, and therefore thanks to decentralization, it is possible to eliminate some phases and to shorten the supply chain. This reduces the transportation cost, the number of intermediaries, improves control along the supply chain, and reduces the time to reach the market. When considering the design of the product, it is important to notice that it is a cost-free phase as it is a file that can be easily transmitted via internet. Therefore, the transportation costs, in this case, are simply those of transferring the raw materials to the place of production, as long as they are not already available in the latter. In fact, this type of cost would be almost eliminated if raw materials are offered in the place of production. Logistics is another positive aspect of the economic sustainability of DDM models throughout the life cycle, with a reduction in delivery times and logistics costs through the distribution of production systems in the geographical areas of greatest interest and this entails a significant reduction of generalized transport costs. The company is no longer the fulcrum of this system. The new business models based on AM have one of the main strength in personalization and a significant role is reserved for the final consumer. The latter provides a lot of information to the company and collaborates in defining the shape and functionality of the product. In AM-based supply chains, the relationship between customer and manufacturer is even closer. In fact, manufacturers can create customized products on different customer indications (Khajavi et al., 2014).

3D printing is more economically advantageous than the traditional process, thanks to a lower production cost at the same production volume as shown in the 2013 Report by Wittbrodt et al. (Wittbrodt et al., 2013). Considering the entire production life cycle with the use of an open code 3D printer, the cost of the material and production was calculated.

Assuming a small volume of production (20 products per year with 25 hours per product), they found that the return on investment exceeds the traditional manufacturing practice by about 200%. This is equivalent to a payback period of 4 months versus 2 years of traditional manufacturing. Waste management is also another good economic indicator. One of the benefits of 3D printing is the fact that the printer can handle the waste produced by bad non-compliant prints, allowing the user to recycle and convert them into re-printable materials to effectively reduce scrap and processing waste.
Another economic indicator is the profitability indicator which was studied by Hopkinson and Dickens in 2003 (Hopkinson and Dicknes, 2003). The costs of machines, materials, and labour were compared for two complex parts with different geometries made by stereo-lithography (SLA), selective laser sintering (SLS), and fused deposition modelling (FDM) and traditional injection moulding parts. At low production volumes, AM technologies can compete with injection moulding, as they are marginally affected by cost variations due to economies of scale.
Regarding the economic criticalities, unsolved problems are evident such as certification rules when production becomes more democratised, a quality problem due to reduced tolerances, as well as material and processing capabilities must also be improved.

5.3.1 AM market

For the study of the market, it is necessary to introduce the trend of additive manufacturing. In fact, various AM technologies are available on the market which varies according to the energy required, materials processed, volume achieved in the unit of time, and accuracy obtainable. To date, AM is a thoughtful innovation capable of intensely modifying the current economy, as it acts on the overall cost structure. The sale of AM technologies has grown exponentially over the last decade. In 2012 a turnover of approximately 2.2 billion dollars was estimated, of which one billion for materials and systems, 1.2 billion for services. Turnover is expected to exceed 10 billion in 2021. In 2012, there were 33 manufacturers of 3D printers for industrial use worldwide: 16 in Europe, 7 in China, 5 in the United States, and 2 in Japan (Wohlers and Campbell, 2017).
All of this makes us understand how the sale trend of new digital technologies is developing within a market revolutionised by the 4th industrial revolution that will lead to fully automated and interconnected industrial production. According to a 2018 analysis on the Industry 4.0 realized by the Italian Ministry of Economic Development, in Italy there is a significantly greater diffusion in the largest companies, assisted by a very high presence also in SMEs (over 20% of companies are involved from 10 employees upwards and almost 50% of the adults). In the following two years, the expected diffusion will be exceptionally high among SMEs (even in the South, which is currently not very interested). At the level of enabling technological components on traditional production assets and related services, the market touched 2.3 billion euros, recording a growth of 30% over the previous year and doubling in the last two years. From these data it can be inferred that at an economic level the AM sector is in continuous sustainable development.

5.3.2 Production cost

Quinlan et al (Quinlan et al., 2017) examined the production costs as a function of the complexity of the piece to be produced, to verify the economic opportunity of the SLM. The complexity of the piece to be made is calculated considering various parameters relating to volumes produced. In the case of conventional techniques, as the complexity of the prototype increases, the costs increase more than proportional. Conversely, with additive manufacturing, the cost per part decreases as complexity increases. The decreasing trend of AM is due to the smaller amount of material used and the relatively low construction time even for complex objects. For instance, low complexity products have a relatively high production cost per part in Selective Laser Melting, which decreases with increasing complexity. Furthermore, since there is freedom in terms of achievable geometries, the number of pieces to be assembled is reduced and, in most cases, it is not necessary to carry out welding or gluing, so the assembly cost is reduced and at the same time better mechanical properties are obtained as joint areas represent points of fragility. Consequently, in the case of unique pieces or small batches of complex pieces, it is preferable to adopt additive manufacturing.
Hopkinson and Dicknes investigated the influence of the production volume on the price for parts of components produced by injection moulding, SLA, FDM, and SLS. As shown in Figure 114, rapid manufacturing techniques are generally convenient for small production batches, while as the volume of production increases, traditional production techniques turn to be advantageous. Only the Selective Laser Sintering maintains an affordability even as the components produced increase, for a more efficient packing (Hopkinson and Dicknes, 2003).

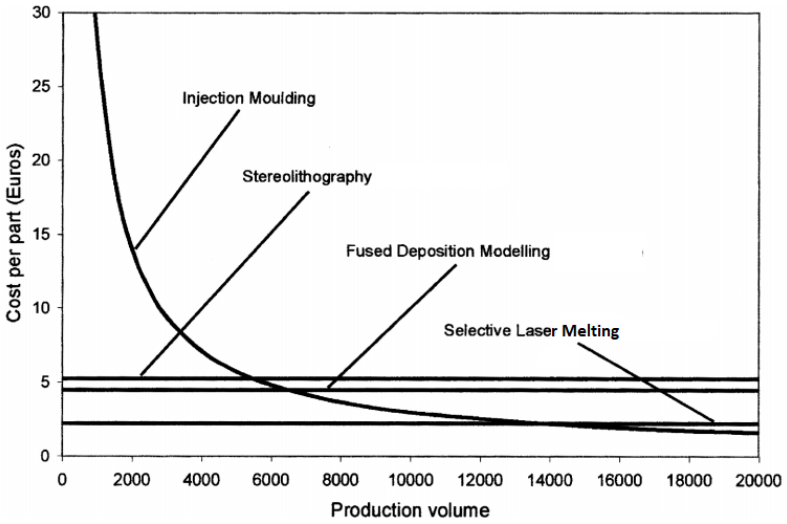

Figure 114 Cost comparison for the lever by different processes (Hopkinson and Dicknes, 2003).

Furthermore, Atzeni et al. (Atzeni and Salmi, 2012) compared SLS with the high-pressure die casting (HPDC) process. The results of this study demonstrate that AM is a suitable alternative to the traditional manufacturing process for small to medium batch productions even end-usable metal products. The cost analysis highlights how the machine cost per piece is the main cost term, while other contributions only marginally affect the total cost. AM is a technology that allows production without the aid of secondary tools and requires a smaller production line, thus reducing potential operating costs. This reduction derives from several factors such as the reduction of inventory costs and the amount of material used. AM can offer a better investment opportunity than traditional production mainly for high-value pieces.

5.4 Environmental impact of Additive Manufacturing

AM technologies, like any other manufacturing activity, impact on the surrounding environment. The main questions related to the environmental impact to be kept under control are greenhouse gas emissions and the receipt of energy sources. Consequences that these environmental impacts have on human health, the quality of the ecosystem, and the incorrect use of natural resources must be considered. Peng et al (Peng et al., 2018) classified the environmental impact of AM technologies in three aspects: Resource Consumption, Waste Management, Pollution Control.

The resources used in the production sector vary according to the manufacturing systems analysed. Many AM technologies implement intensive energy sources (laser, electron beam, etc) thus energy represents the main consumption resource. Furthermore, the energy consumed by the auxiliary equipment must also be considered, which in the case of chillers can also be considerable. Energy consumption can be higher due to relatively low productivity and indispensable idle times, especially for those AM processes that involve long processing and high-energy sources (Yosofi et al., 2018). On the other hand, the consumption of materials includes primary materials (polymers, metal powders), secondary materials (support structures), shielding gases, and cooling fluids. AM technologies have a theoretical efficiency of 97% on the consumption of materials, even if the real efficiency of many systems is lower (Allwood et al., 2013).

One of the strengths of AM is certainly the very low amount of waste produced which can reach 90% less than traditional manufacturing techniques. Some examples of waste deriving from AM can be powders from materials that are no longer recyclable, waste due to defects, and support structures for the protruding parts produced. In the literature, several works study the best orientation of the component in the production phase and how this factor can drastically change the amount of waste produced (Jiang et al., 2019). There are still insufficient data on the recyclability of waste materials from the first processes and their influence on the quality of the products obtained by using them as secondary raw materials.

The forms of pollution produced by AM include gases, liquids, sounds, and solids. Among these, the most worrying ones undoubtedly concern the formation of extremely small particles during the process and the explosive risk of metal powders. The repercussions on the environment and human health can sometimes be very high. For example, FDM mainly uses thermoplastic materials such as PLA or ABS which are non-toxic and have a low melting point, thus requiring less energy for work. However, ultra-fine particle (UFP) emissions have often been reported, suggesting caution when operating in an enclosed, unventilated, or unfiltered environment (Stephens et al., 2013).

5.5 Life Cycle and evaluation methods

According to sustainability principles, an entity can be considered sustainable if it does not compromise the possibilities of future generations. This vision poses challenges from the point of view of the assessment, since the only evaluation of the production phase of a product may not highlight the criticalities that could arise for example in the phase of disposal. Starting from these proposals, the Life Cycle Assessment (LCA) was born. A method approved internationally in the 90s to systematically assess the environmental impact of processes and products. The peculiarity of this method lies in the fact that the environmental analysis is carried out over the entire life cycle of a product, taking the name of analysis "from the cradle to the grave".

This tool assesses the impacts on human health, ecosystems and consumption of natural resources of a product, an activity, or a process through an evaluation of physical and chemical phenomena along all stages of the life cycle (extraction and treatment of raw materials, manufacturing, transport and distribution, use, reuse, recycling, and final disposal). This is done by quantifying the use of resources (inputs such as energy, raw materials, water) and emissions into the environment (discharges into the air, water, and soil) associated with the system subject to rating. This interdisciplinary method is also useful in identifying links between different phases of the life cycle.

The main standards for LCA are:

- ISO 14040: principles and framework
- ISO 14044: requirements and guidelines

The first standard considers the principles and structure of the LCA, while the second specifies the requirements and guidelines for conducting an LCA study. The LCA allows the detection of improvement opportunities through the identification of environmental critical points in the life cycle of a product. It also analyses the contribution of each phase of the life cycle on the overall environmental load, usually intending to give priority to product or process improvements. Furthermore, the LCA identifies the Key Performance Indicators (KPI) used in companies as a tool for managing the life cycle and as a support for decision-making processes. The structure of an LCA study, as proposed by the ISO 14040 standard, is divided into four main phases (Goedkoop et al., 2008):

1. **Goal and Scope Definition**: as any LCA makes sense only in relation to the objectives it intends to achieve and the object it aims to analyse. In this phase the client, the executor, the purpose and object of the study are declared. To calculate all flows, they must be related to a certain entity, called "functional unit" that must in any case be a defined and measurable unit of use and service. Product systems tend to be intricately related to each other. However, it is necessary to highlight and define the set of subsystems which flows are studied and calculated, or the "field of study" and the criteria for inclusion and exclusion of system inputs and outputs.
2. **Inventory***:* its purpose is to report and quantify all the flows of matter and energy in and out of the system. These flows refer to the functional unit and are expressed in physical units. The preparation of an inventory is therefore an operation of collection and organization, in a model, of data concerning the exchanges between the individual operations belonging to the production chain and between the overall industrial system and the environmental system. In this phase, it is important to build a flow chart of the operations that contribute to the system considered.
3. **Impact Assessment***:* the inventory data, which are made up of incoming and outgoing physical flows, are organized and aggregated through the classification and characterization operations. The contribution of the chain in question to the environmental impacts considered by the study is thus clarified. The first step consists of choosing the "impact categories" to be analysed, in other words in choosing which effects on the environment are to be taken into account. This choice is strictly connected to the objectives set. In fact, the main effects of the system on the environment are identified, and in the case of comparative LCA a more effective comparison between the life cycles of products or services in question is fulfilled.
4. ***Interpretation***: the last phase of the LCA involves the interpretation of obtained results, correlating outcomes of the inventory analysis and that of the impact analysis, in order to propose useful recommendations concerning the purposes and objectives of the study. This phase is often entrusted to external experts to validate the work carried out during the LCA.

Kloepffer extends the classic concept of life cycle assessment to achieve a complete evaluation of the three pillars of sustainability and therefore a life cycle management. The evaluation must also consider the economic and social aspects relating to the product or service. The life cycle sustainability assessment (LCSA) is thus defined as the combination of the environmental evaluation through the classic LCA, economic analysis through a life cycle costing (LCC), and social study through the social life cycle assessment (SLCA). LCC summarizes all costs associated with the life cycle of a

product that are attributable to one or more actors in that lifecycle. Alternatively, the SLCA places the impacts on the community and workers of the production under consideration at the heart of the analysis (Kloepffer, 2008).
According to Peng et al., nowadays numerous life cycle studies were conducted for assessing the sustainability of traditional processes, but few studies focused on AM processes. Figure 115 shows LCA phases, with energy sources and material consumed during the life cycle for SM and AM technologies. However, long-term impact assessments are extremely difficult to predict.

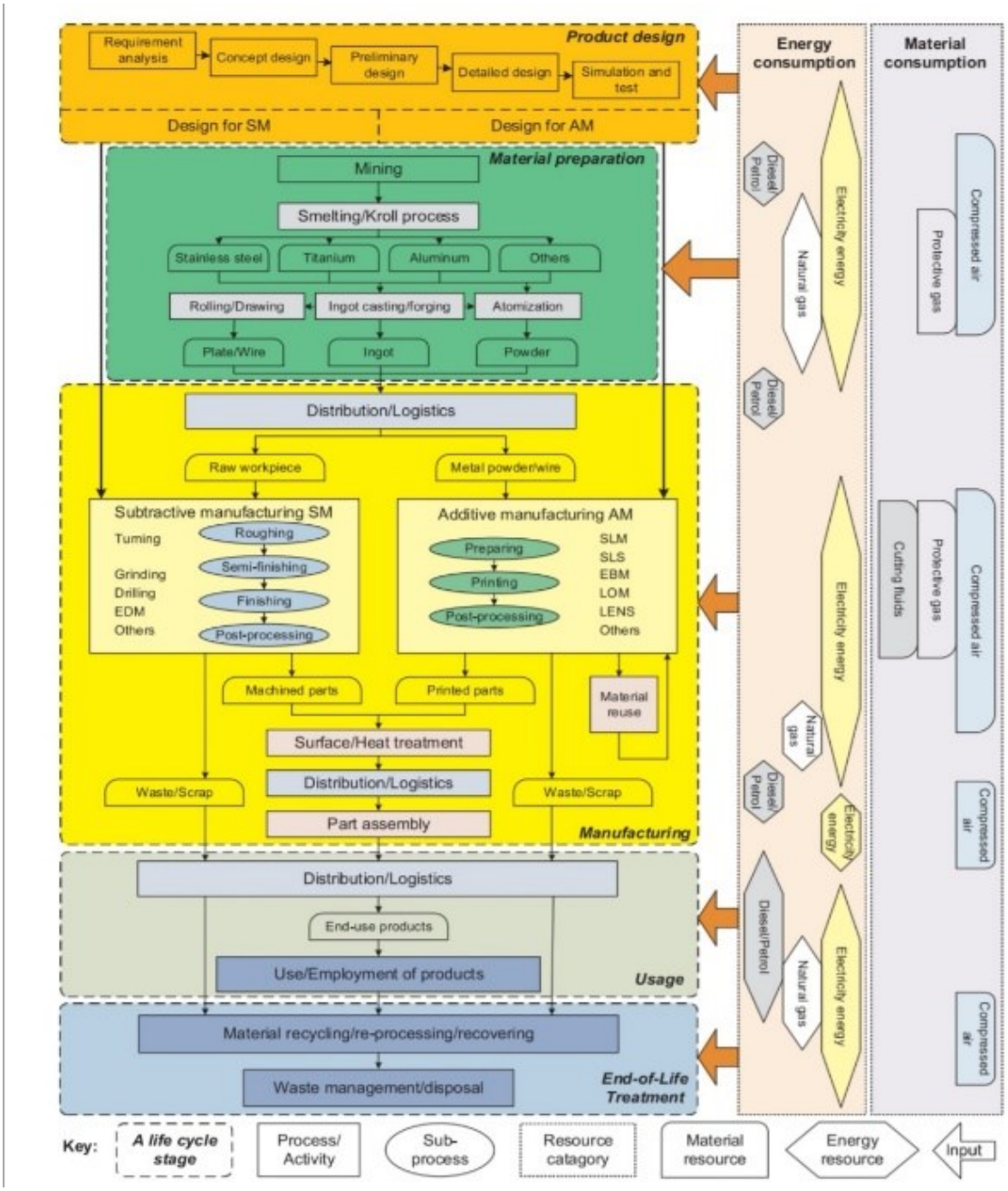

Figure 115 LCA of a metallic product made of AM and SM (Peng et al., 2018).

Peng et al. consider that logistics represent only a fraction of the environmental impact of the life cycle. Although as previously mentioned, the AM significantly changes the supply chain of companies. AM companies, in fact, could be strategically scattered close to their customers to reduce both the lead time of raw materials, intermediate parts, final products, or waste. However, a change in the supply chain is a complex operation, and therefore cannot be evaluated in the short term (Peng et al., 2018).
A methodology for accurately assessing the environmental impact of a component produced for AM from its CAD model, is shown by Le Bourhis et al. The comparison carried out on DLMD processes (MacroCLAD and MesoCLAD) does not

focus only on electrical consumption but also on consumption of fluids and materials that also contribute to the environmental impact. This methodology considers the different process settings and allows to take into account the different production strategies and their influences on the global environmental impact. The developed methodology is based on both analytical and experimental models. Some production strategies studied have highlighted that the environmental impact due to the electrical consumption is not always predominant. In the present assessment, powder consumption has an environmental impact of about 58% against 40% of the electricity. This is considered even more impactful if the recycling percentages of waste materials are minimal (Le Bourhis et al., 2014).
Kafara et al. compare additive manufacturing with conventional technologies with a cost and time effective assessment method for small-scale production of four types of mould cores. These are manufactured by casting of low-melting alloy, by milling from plaster-like material called Aquapour, by additive manufacturing using a High Impact Polystyrene (HIPS), and by additive manufacturing adopting a powder materials like salt. The comparison shows that the best environmental performance goes to additive manufacturing with salt as core material, while HIPS has an LCA only marginally disadvantageous compared to Aquapour (Kafara et al., 2017).
The environmental impact of wire arc additive manufacturing (WAAM) process of AISI 308L stainless steel is compared to that obtained from green sand casting and CNC milling. Figure 116 shows the result of the analysis carried out by Bekker and Verlinden, measured in ReCiPe endpoints (Pts), per kg of manufactured product. For WAAM, 44% of the impact is caused by energy input, while 48% is caused by the shielding gas. In all assessments, the markedly higher impact is caused by the use of materials. WAAM is one of the most efficient additive techniques in the use of materials (only 1.1% of waste) so it has the potential to reduce the environmental impact through the weight reduction of the topology optimization (Bekker and Verlinden, 2018).

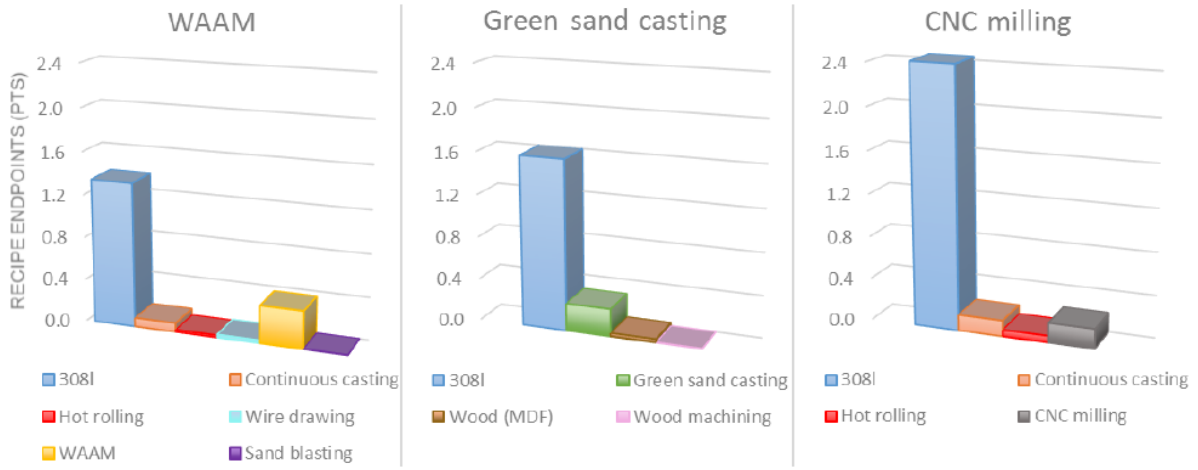

Figure 116 Environmental impacts of the processing steps of WAAM, green sand casting, and CNC milling respectively, in ReCiPe endpoints (Pts), per kg of manufactured 308l product (Bekker and Verlinden, 2018).

5.6 Exergy analysis

Sustainability is a dimension of an extremely multi-faceted production process. Today, the LCA is the most widespread method of analysis for calculating not only the environmental impact but also the economic and social impact through its various components, as seen before. Despite this, many approaches support the above to emphasize various aspects of the operation.
Exergetic analysis (EA) is based on the second law of thermodynamics and seeks to report the amount of useful work that can be extracted from a real system when it is brought into harmony with its environment. It is used to monitor the processes or a specific product from a thermodynamic point of view. As stated by Selicati et al., this approach is a fantastic concept that can strengthen and extend the conventional LCA (Selicati et al., 2020). In fact, the classic LCA approach focuses deeply on environmental emissions, while EA is much more centred on products, highlighting the availability of resources and system efficiency. EA and LCA can interact with each other to provide a more holistic view of the system/process to be assessed.
In an exergetic analysis, the irreversible process is always considered as part of a non-isolated environmental system with continuous thermodynamic exchanges. These exchanges modify the entropy of both, reducing that of the system, which produces work and disperses heat, and increasing that of the environment, which absorbs the heat produced. It follows

that EA is a strongly indicated method for this category of heat exchange process. This method is still slight used in the industrial sector and in particular in the field of additive manufacturing.

Renaldi et al. define the differences in exergy efficiency definitions for a selection of manufacturing processes, both subtractive and additive: laser cutting, selective laser sintering, and bending. The EA focuses on the process in a standalone machine, excluding auxiliary components that are not part of the actual process. The exergy efficiencies η_r and η_u are able to appropriately present the resource efficiency of subtractive and additive processes, respectively. While for the mass-conserving process there is still a need for a thorough study. Authors also performed a system-level analysis that shows how process-level exergetic efficiency definitions cannot encapsulate the variations in resource efficiency resulting from measures at the system-level (Renaldi et al., 2011).

A comparison between electron beam melting (EBM) and 5-axis milling using 10 environmental impacts selected from the Cumulative Exergy Demand (CExD) and "CML 2 Baseline 2000" methods is proposed by Paris at al. Additionally, combined indicators for the environmental impact ratio and the volume of material removal ratio are proposed. The EBM is more environmentally sustainable and also a good manufacturing option for parts with a complex shape that requires a strong removal of the material using subtractive methods. (Paris et al., 2016).

Nagarajana and Haapala proposed a generalized EA framework applied to two AM technologies: direct metal laser sintering (DMLS) with iron metal powder and fused deposition modelling (FDM) with acrylonitrile styrene acrylate polymer. A cradle-to-gate LCA methodology coupled with Cumulative Exergy Demand (CExD) analysis was performed to evaluate the environmental performance based on system-level resources and energy inputs. For both technologies, electricity was the main contributor to the exergy demand (88% for DMLS and 91 for FDM), as shown in Figure 117. Thus, 10% of the exergy input is related to the manufacturing of products, while 90% of the input is wasted in the form of bulk waste, heat, and work. Electricity consumption is a key contributor also for the LCA, where the damage to human health is considered the most relevant impact for both systems. The study shows the inefficiency of AM systems in managing material and energy inputs (Nagarajan and Haapala, 2018, 2017).

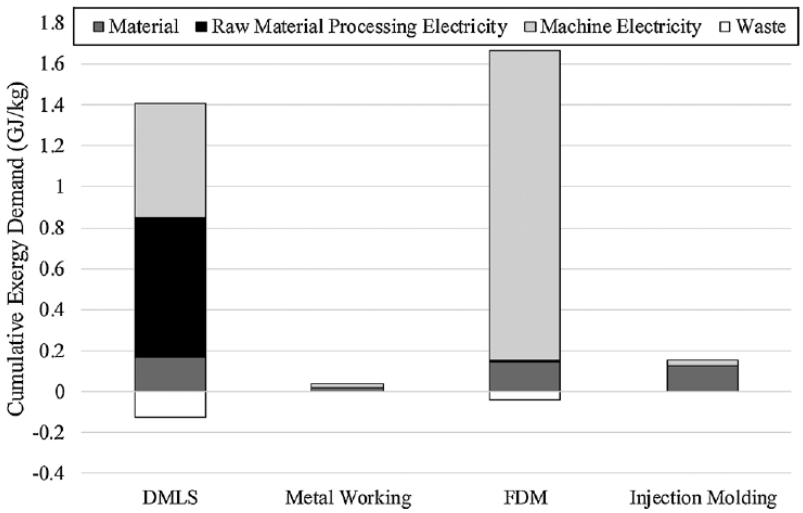

Figure 117 Cumulative exergy demand for the production of one kilogram of product for different manufacturing systems (Nagarajan and Haapala, 2018).

5.7 The thermodynamic modelling of EA-LCA method for DLMD process

Exergetic analysis coupled with Life Cycle Assessment (EA-LCA) brings considerable advantages: initially, they provide more objective-oriented evaluation results; secondly, they become a valuable tool for decision-making policies aimed at creating a retrofitting solution, allowing the system to avoid any potential failure automatically. Besides, they are useful instruments that help to understand process management alternatives to improve and innovate production process technologies (Cornelissen and Hirs, 2002).
Given the advantages of integrating EA-LCA, the description and selection of a detailed set of parameters and related cause-effect relationships for successful control of the discussed process, is the most important point (Selicati and Cardinale, 2020).
Of paramount importance is the definition of the set of parameters to be monitored, and the requirements for designing an ad-hoc architecture to monitor and control a manufacturing process.
EA-LCA enables the process to be efficiently split into unit functions, which have to be adequately analysed to determine the critical unit and to monitor the state of the critical parameters.
This method is entirely innovative because LCA and EA primarily serve to establish a model or a set of parameters that can be useful to obtain hidden knowledge of the process dynamics and, ultimately, to estimate the quality of the process and the impacts of mere consumption of resources and energy on the environment. Nowadays, no one has applied this concept to any AM method in the literature and EA and LCA are used only as indicators of sustainability.
Considering a basic control volume of a generic manufacturing process, Figure 118 shows an example of the main in and out streams that can occur. In grey, the EA's reference environment is outlined, and in blue the extension of the LCA's system boundary.

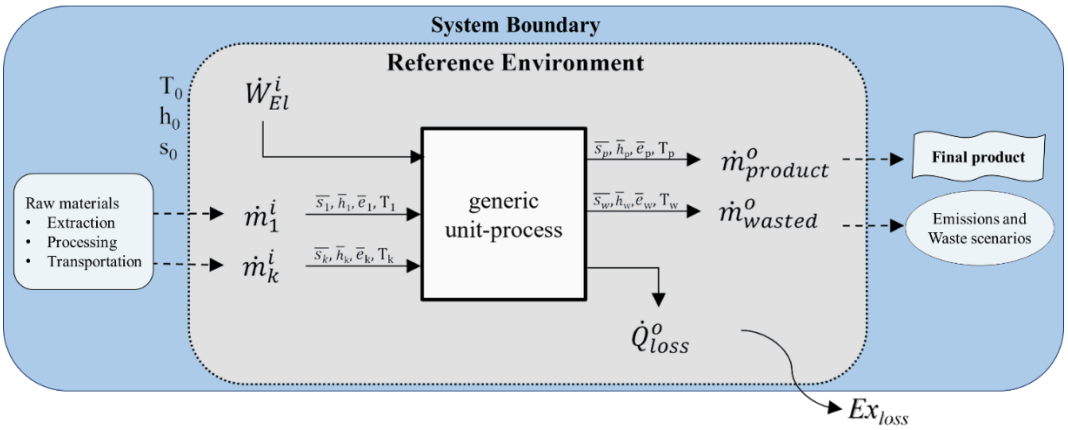

Figure 118 Control volume of a generic manufacturing process.

The thermodynamic laws behind the Exergetic Analysis are important to trace the set of parameters that need to be measured and monitored during the process, as well as variables that can be determined. In its balance equations, reference flows are uniquely described based on Szargut's studies. (Szargut et al., 1987):
Mass flow balance:

$$\sum_k \dot{m}_k^i = \sum_k \dot{m}_k^o \qquad (24)$$

Energy flow balance:

$$\sum_c \dot{H}_c^i + \sum_d \dot{W}_d^i + \sum_p \dot{Q}_p^i = \sum_c \dot{H}_c^o + \sum_d \dot{W}_d^o + \sum_p \dot{Q}_p^o \qquad (25)$$

Exergy flow balance:

$$\sum_c \dot{E}x_c^i + \sum_d \dot{W}_d^i + \sum_p \left(1 - \frac{T_0}{T_e}\right) \dot{Q}_p^i = \sum_c \dot{E}x_c^o + \sum_d \dot{W}_d^o + + \sum_p \left(1 - \frac{T_0}{T_e}\right) \dot{Q}_p^o + \boldsymbol{\dot{E}x_{loss}} \qquad (26)$$

$$Where\ T_e = \frac{T_k^i + T_k^o}{2} \quad (27)$$

While the following metrics can be determined by their thermodynamic laws:
Enthalpy, specific entropy, exergy:

$$H = \dot{m} \cdot c \cdot (T - T_0) \quad (28)$$

$$\bar{s} = c \cdot ln\left(\frac{T}{T_0}\right) \quad (29)$$

$$Ex = \dot{m} \cdot [\bar{h} - \bar{h}_0 - T_0 \cdot (\bar{s} - \bar{s}_0)] \quad (30)$$

In the following net and general efficiencies, the performance metrics of the process or its components are defined, depending on whether the objective is to evaluate the portion of useful exergy for the final product realization or to evaluate the overall exergy of the process:

$$\eta_n = \frac{\sum \dot{E}x^{product}}{\sum \dot{E}x^{in}} \quad (31)$$

$$\eta_g = \frac{\sum \dot{E}x^{out}}{\sum \dot{E}x^{in}} \quad (32)$$

The combination of EA and LCA implies the inclusion of other types of information: upstream processes for the supply of the raw materials and resources necessary for the process, as well as pollution and waste management scenarios.
The optimization procedure include the minimization of Ex_{loss}. This is the prominent factor in explaining the actual efficiency of the process that is lower than the theoretical one, calculated on the Carnot cycle. Temperature fluctuations in the exergetic equilibrium play a key role. In two transition phases, the greater the temperature difference, the greater the produced energy.
The energy balance is also important in terms of product quality optimisation. A very illustrative example is proposed by Paul and Anand, where authors concluded that energy is linked to the thickness of the finished product through an inversely proportional relationship. This means that energy analysis allows the quality of the finished product to be improved, its characteristics to be regulated and the energy costs of the process to be minimized at the same time (Paul and Anand, 2012).
According to the EA-LCA data inventory of the overall process, related to the functional unit, the set of essential thermodynamic parameters to be measured and monitored (M) and those calculated (C) with thermodynamic laws in a DLMD process are shown in Table 33.

Material/Energy	**Data flow in**	**Data flow out**	**M/C**
Metal powder	mass flow [kg/s]	mass flow [kg/s]	M
	temperature [K]	temperature [K]	M
Gasses	volume flow [l/s]	volume flow [l/s]	M
	temperature [K]	temperature [K]	M
Cooling fluid	volume flow [l/s]	volume flow [l/s]	M
	temperature [K]	temperature [K]	M
Electricity		electric power [W]	M
Heat		heat loss [J]	C
Exergy		exergy loss [J]	C
Environmental Impact		GWP_{100a} [$kgCO_{2eq}$]	C

Table 33 Essential thermodynamic parameters of DLMD process.

5.7.1 DLMD machine

The exergetic analysis of the DLMD process will be carried out below, considering the theoretical structure described above and the knowledge acquired on the monitoring systems described in the previous chapters.
Figure 119(a) and (b) show a schematic representation of the prototype DLMD system present at the Polytechnic University of Bari, and better described in Section 2.10. In summary, the prototype consists of:

- a fiber laser source with a nominal power of 4 kW and wavelength of 1.070 µm
- a 5-axis machine equipped with a deposition head and a coaxial nozzle
- an 11.57 kW laser chiller system
- a 600 W fiber chiller system
- a 1.10 kW nozzle chiller system
- a deposition head chiller system
- an external powder feeder
- a 2.20 kW powder suction system and gravimetric dispenser.

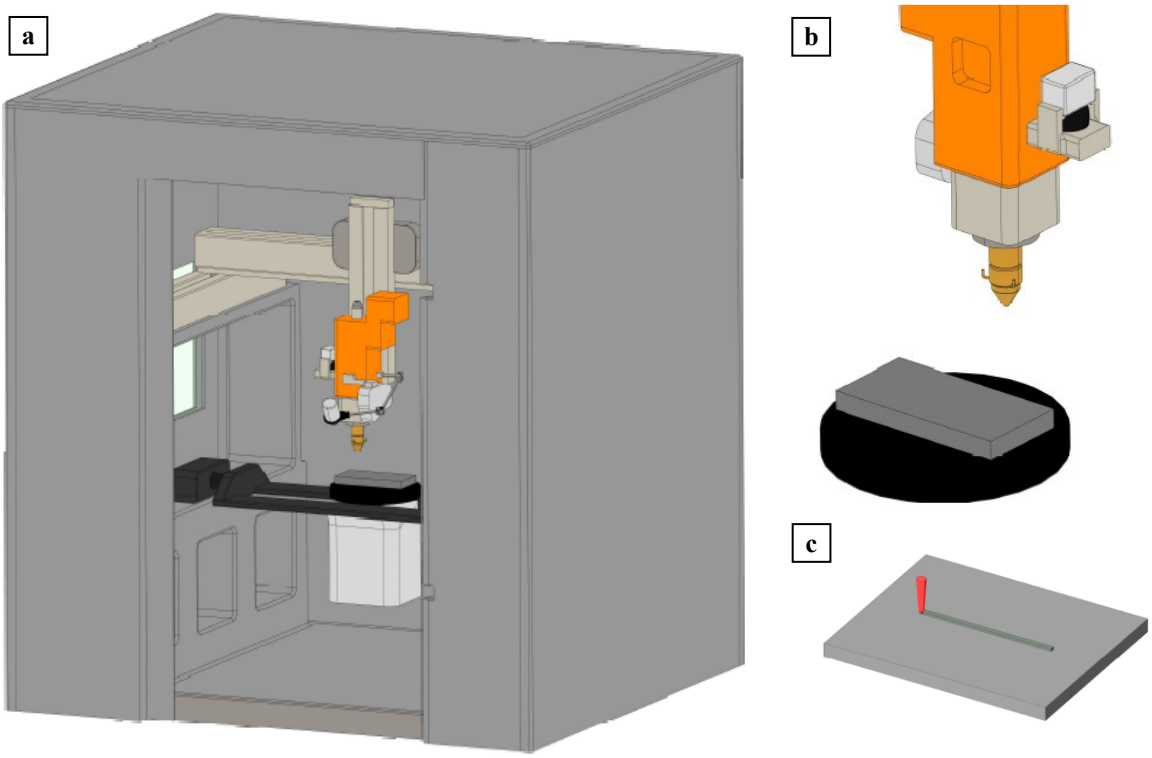

Figure 119 (a) Schematic representation of the prototype DLMD glovebox, (b) deposition head, and (c) deposition process of a single track.

In order to protect operators and avoid environmental pollution, the working area is bound by a glovebox. Inside are also located monitoring systems, such as a coaxial camera and a pyrometer. For this work, an AISI 316L stainless steel powder was deposited on a substrate of the same material, which composition is shown in Table 3. Argon was employed as a carrier gas for the powder and as a shielding gas to prevent clad oxidation.
In order to assess the feasibility of the purposed model single-track clad depositions were realized, as represented in Figure 119(c). To evaluate the influence of process parameters on the energy and exergetic efficiency of the DLMD process, a complete experimental plan as two key parameters vary were developed. The parameters with the greatest impact on energy consumption are laser power and translation speed, which were varied as shown in Table 34. Laser power governs the energy supplied to the process, and consequently the change in melt pool temperatures. The translation speed, on the other hand, changes the cycle times of the process and analysis, regulating energy balances and material consumption.

Process parameter	u.m.	Factor Levels			
		1	2	3	4
Laser power	W	600	900	1200	-
Spot diameter	mm	1.50	-	-	-
Translation speed	mm/min	500	1000	1500	2000
Powder feed rate	g/min	10	-	-	-
Carrier gas flow rate	l/min	10	-	-	-

Table 34 Experimental plan

5.7.2 The thermodynamic model

Based on the previously given guidelines, the model of the entire DLMD system whit its optimal sub-units and the description of all specific flows in and out were developed, resulting in sets of parameters to be monitored in real-time or with a sampling rate small enough to recognize trends in energy consumption and losses that make the process less efficient

In Figure 120 the complete design of the in and out streams of the entire laser deposition process are shown. This schematic representation is also useful to highlight the interconnection of parameters analysed by LCA and EA, and how their coupling can be extremely advantageous.

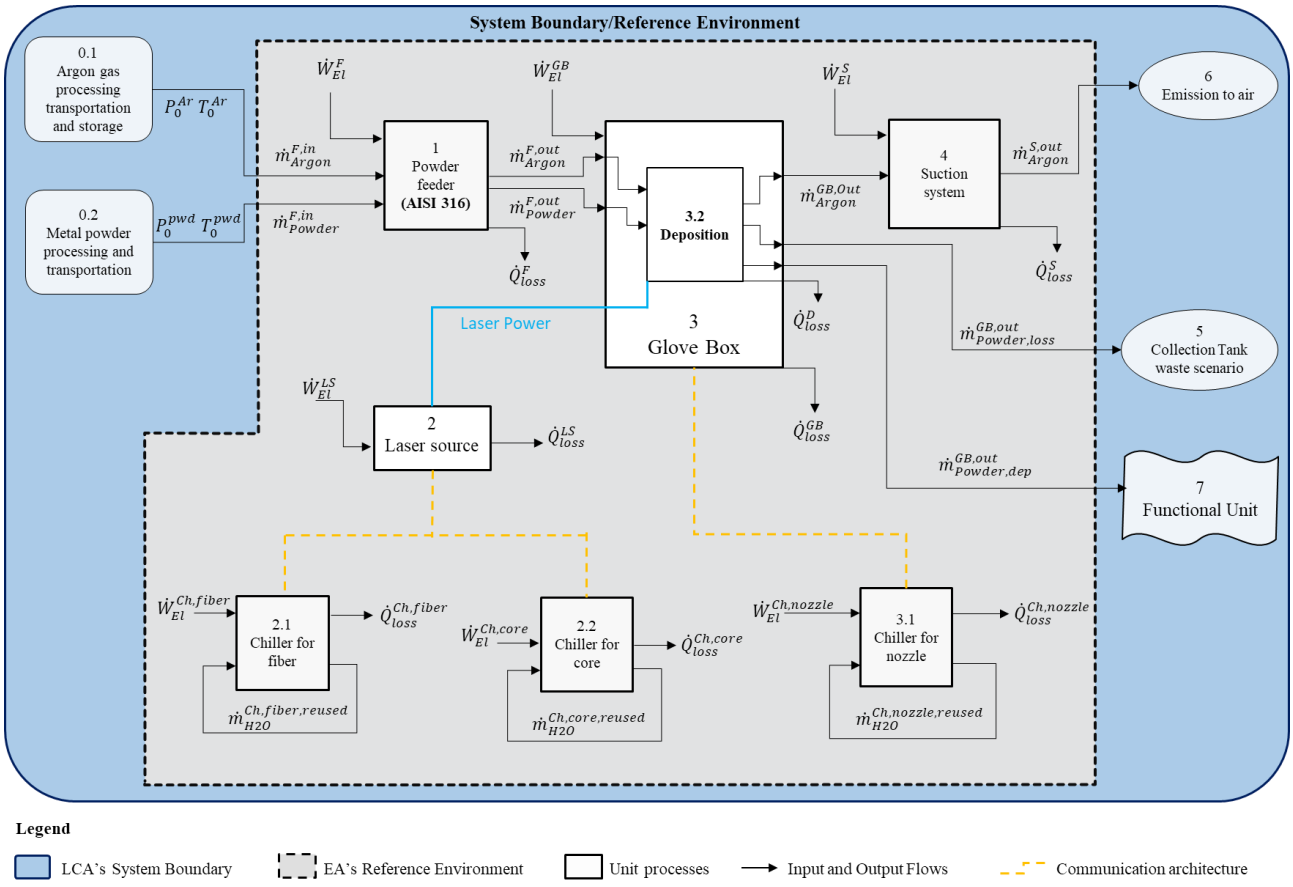

Figure 120 DLMD thermodynamic model.

The planning of the inventory of the data required for the EA has allowed highlighting the numerous key points of the system, of which it was found to have modest knowledge. In this first stage, controlled parameters are the global electricity consumptions by general meter and the temperature of the melt pool by the pyrometer. However, it was observed that the temperatures of the mass flows in and out of the plant are not tracked at any operational phase of each unit-process.

As things stand, there is insufficient knowledge to perform the appropriate analysis. This drawback shows how well before the analysis itself was carried out, the EA-LCA inventory has been useful for the detection of the first requirement for the measuring system as the real-time monitoring of the temperatures of the input and output material flows of the system and each unit process. To fill the database with the values of all the parameters required for analysis, a network of sensors is necessary. An additional significant criterion to synchronize all parameters that could be sensed with the sensing infrastructure to be mounted becomes the sampling frequency.

5.7.3 Description of the monitoring system

A sensing system were developed to meet DLMD requirements based on Raspberry Pi and Python v. 3.8. Due to the large range of software and hardware resources available, the first is distinguished by many advantages, such as small dimensions, low cost, and high flexibility. The latter is a fairly recent multi-platform interpreter commonly used in a real-time application, robotics, deep learning, image processing, database server, and monitoring systems by the scientific community. Due to its simplicity, intuitive syntax and its versatility, it has climbed to the top of the most used science applications in the last 10 years. In particular, in this specific application the Raspberry Pi 4 was selected, showing the following specifications:

- Broadcom BCM2711, Quad-core Cortex-A72 (ARM v8) 64-bit SoC @ 1.5 GHz
- 2 GB, 4 GB or 8 GB LPDDR4-3200 SDRAM (depending on model)
- Gigabit Ethernet

This choice guarantees both hardware and software flexibility, to perform the Exergetic Analysis.
The proposed sensing system aims to include energy meters, flow sensors, and, eventually, any other necessary acquisition device. In particular, the measurement of the process temperature was carried out through an off-axis pyrometer (CellaTemp®, Keller ITS) located solidly with the deposition head, to record the whole process. The emissivity value was set based on previous works and literature data relating to machining with AISI 316L stainless steel.
SIEMENS SENTRON PAC 3200 energy meter was employed for the electrical energy measurements. The energy meter has more than 200 parameters as float numbers. The acquired variables are: Active Power [kW], Reactive Power [kVar], Active Energy [kWh] Reactive Energy [kVarh], Voltage and Current Harmonics. The measuring accuracy of Actual Power is in the order of 0.5% (SIEMENS, n.d.).
In order to evaluate the maximum acquisition speed, the communication efficiency of the sensing device was evaluated using the SIEMENS SENTRON PAC 3200 energy meter. As a consequence of the preliminary test, the sensing system is capable of acquiring 100 WORD registers at 149 Hz from a Modbus TCP unit. This outcome is due to an acceptable strategy for acquisition. First of all, to speed up the acquisition process, the Python script reads data continuously on port 502 of the computer later data is elaborated and stored in a database. A schematic draw of the sensing system architecture is shown in Figure 121.

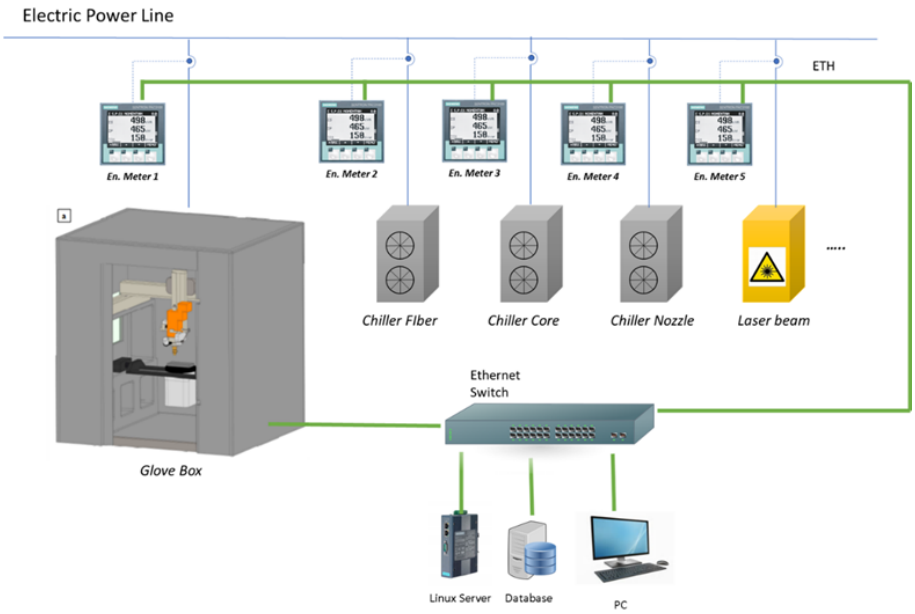

Figure 121 Sensing system architecture.

5.7.4 Electrical Energy Acquisition Test

Electrical energy acquisition tests were performed with the SIEMENS SENTRON PAC 3200, applied to each sub-component of the prototype DLMD system.

Figure 122 shows power input and output of the laser source during a testing deposition cycle of 2,4 seconds at laser output constant power of 600 W. The acquisition frequency is 40 Hz. The energy meter update frequency is about 4Hz. As the acquisition time is 10 times faster than the device update frequency, the plot has a typical stepped shape. The power input reaches a steady value after about 2 seconds.

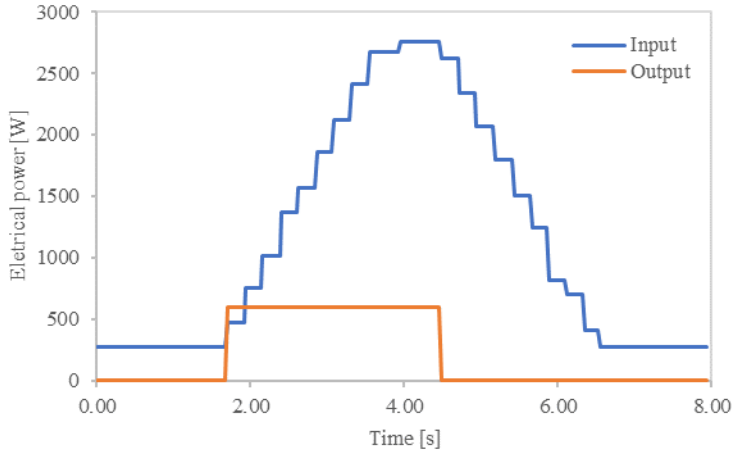

Figure 122 Laser Beam input and output power during the deposition cycle

The electricity consumption of the laser source was closely monitored as output power changes, revealing a linear proportion with the output, as shown in Figure 123(a). The efficiency of the device is therefore influenced by the basic electrical power of the system, which compromises its efficiency, especially at low intensities, as shown in Figure 123(b).

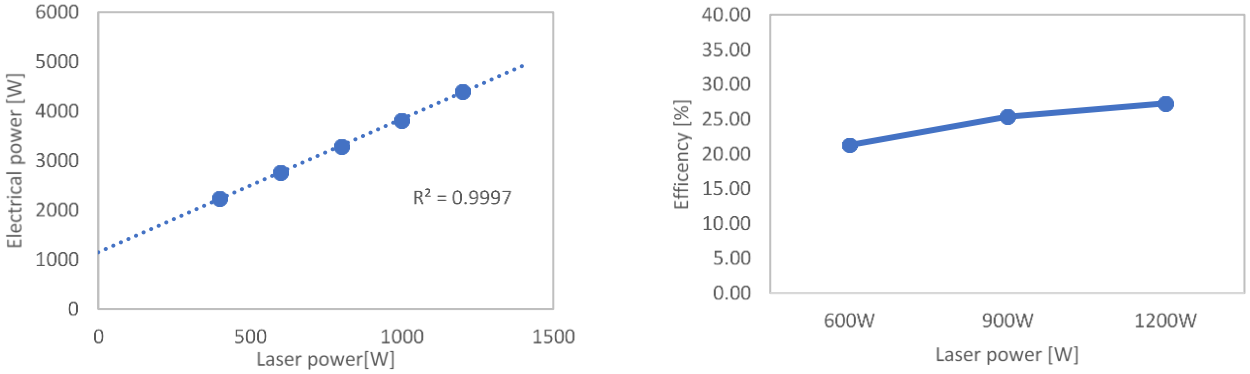

Figure 123 Laser source (a) electrical consumption and (b) efficiency.

Figure 124(a) shows the power input of the laser source chiller. The plot shows a basic 4800 W system power consumption with load cycles hitting peaks of 6800 W. The trend and frequency of peaks are strictly linked to the operation of the laser source and the laser power output required by the processing.

The laser source is a multipurpose device, used for different mechanical processing. Laser welding is a process in which very high energy densities are required to carry the material to instantaneous vaporization and operate in keyhole mode. On the other hand, laser deposition involving lower powers than the traditional laser welding. Therefore, the 4 kW laser source of the DLMD system will be used at an output level close to the minimum processing limit available, equivalent to 10% of the nominal capacity.

Figure 124(b) shows the input power of the chiller fibre. The device can be outlined as a simple heat exchanger without any power input control system. In fact, this power is not affected by work cycles of the source and stands at a constant value of 450 W.

Figure 124(c) plots the trend of the incoming electrical power for the nozzle chiller. Similar to the core chiller, this system has load cycles influenced by the deposition process and primarily by the energy reflected by the melt pool, which overheats the nozzle and the optics. The chiller manages a limited temperature variation of the deposition head during process downtime, which enables the device to be held on standby for a long time. This is less apparent for the core chiller since the laser source also produces a certain amount of waste heat that is handled by the chiller when is not generating the laser beam.

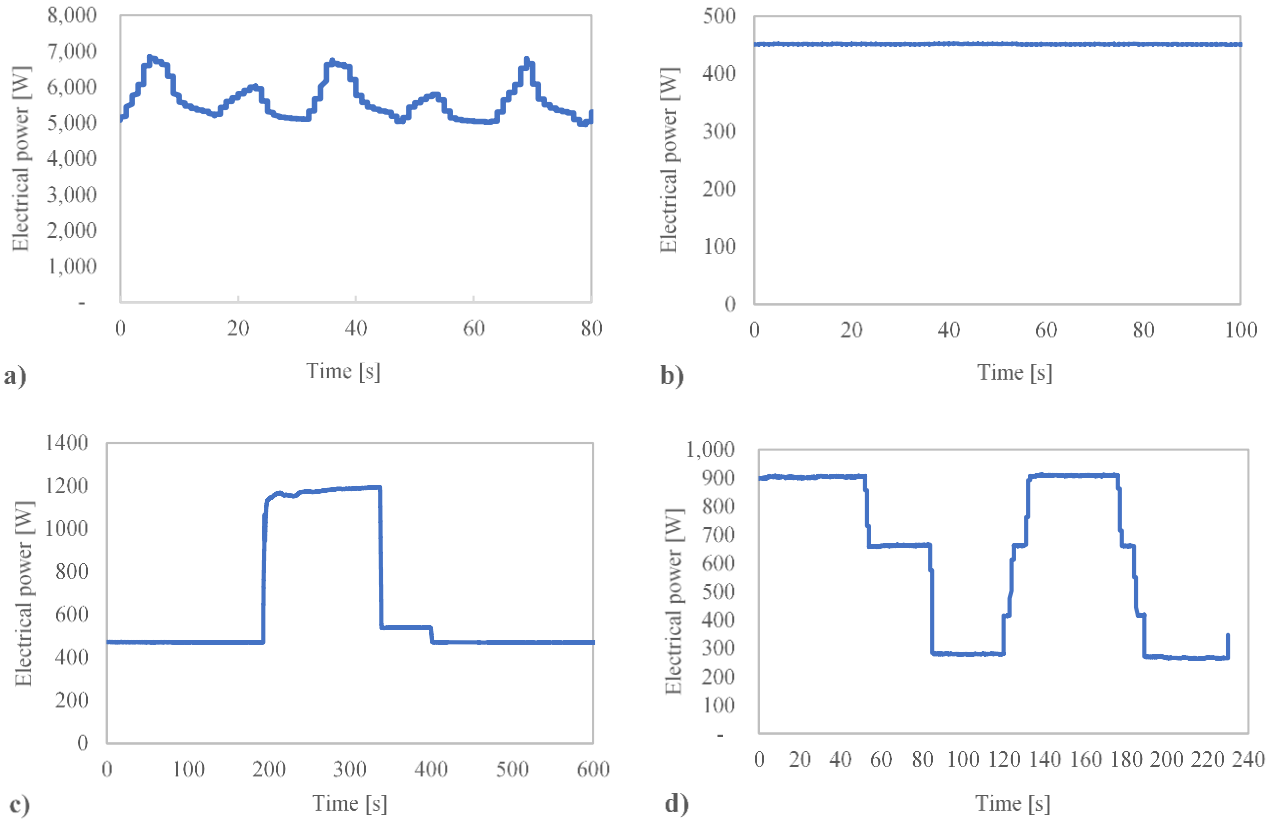

Figure 124 (a) Chiller fiber, (b) chiller core, and (c) chiller nozzle and (d) glove box input and output power during the deposition cycle.

In Figure 124(d) the consumptions of the glovebox are plotted. This apparatus is an agglomeration of various devices, such as the control PC, the deposition head movement system, and monitoring systems, which are useful for DLMD operations. As it is affected by the behaviour of different components during the deposition process, the trend over time of the electrical power input is irregular. However, there is an overall value of input power that reaches 900W and a minimum value that is about 300W.

Device	Parameter	u.m.	Max value	Min value
Powder Feeder	$W^{F}_{El,in}$	W	240	240
Laser Source	$W^{LS}_{El,in}$	W	2820	400
Clad	$W^{Clad}_{El,in}$	W	600	0
Glove Box	$W^{GB}_{El,in}$	W	900	300
Chiller for Fiber	$W^{Ch,Fiber}_{El,in}$	W	450	450
Chiller for Core	$W^{Ch,Core}_{El,in}$	W	6800	4800
Chiller for Nozzle	$W^{Ch,Nozzle}_{El,in}$	W	1200	500
Suction System	$W^{S}_{El,in}$	W	1500	300

Table 35 Electrical Power Distribution.

The power values recorded through the energy meter during preliminary tests on devices constituting the DLMD system and employed in the exergetic analysis have been summarized in Table 35. Maximum and minimum values were listed since during the actual deposition process, not all device components are involved. For example, only at the end of the

processing cycle is the suction system triggered, in order to clean the glovebox atmosphere from argon and the fraction of the remaining metal particles in suspension. The device is coupled with a gravimetric dispenser that doses calcium carbonate to reduce the risk of fine-metal powder processing explosions.
Exergetic analysis is a method mainly based on thermodynamics that evaluates the behaviour of systems by comparing them with the Carnot cycle. In order to obtain energy and exergy values of the system, it is essential to record the main thermal parameters of the system's material flows. Table 36 lists temperature, pressure, and specific heat values for argon, metal powder, and chiller water.

State functions	Symbol	u.m.	Metal Powder	Argon	Water for chiller
Dead state Temperature	T_0	K	298.15	293.15	293.15
Dead state Pressure	P_0	atm	0.987	4.935	0.987
Specific heat	c_p	J/kg K	500	520	4186

Table 36 Materials' properties.

Therefore, EA needs to evaluate the temperature variations during processing. These data were collected in various ways for each device component: directly through the use of special monitoring systems such as pyrometers; directly through component-integrated control systems; indirectly through data from the literature, data sheets, and numerical simulations. Figure 125 shows the plot of the maximum temperature of the single-track deposition process made by 600 W of laser power and a translation speed of 500 mm/min measured by the pyrometer.

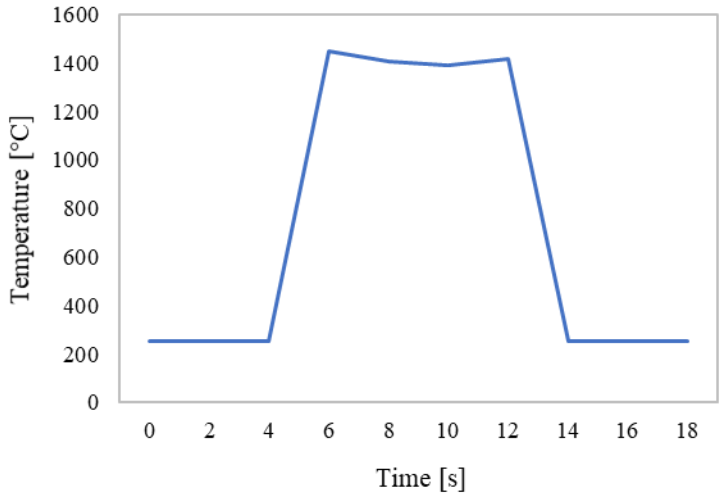

Figure 125 Temperatures measured by the pyrometer during deposition.

5.7.5 Mass, energy, exergy balance, and efficiencies

Initially, the energy and exergetic assessment focused on a specific deposition process, in which 600 W of laser power and 500 mm/min of translation speed were used, to describe in-depth the different phases of the analysis.
Since the flow of water inside the chillers is cyclic, net of negligible losses of the components during the process, and therefore the mass balance will always be equal to zero, only the mass balance of argon and powder is considered.

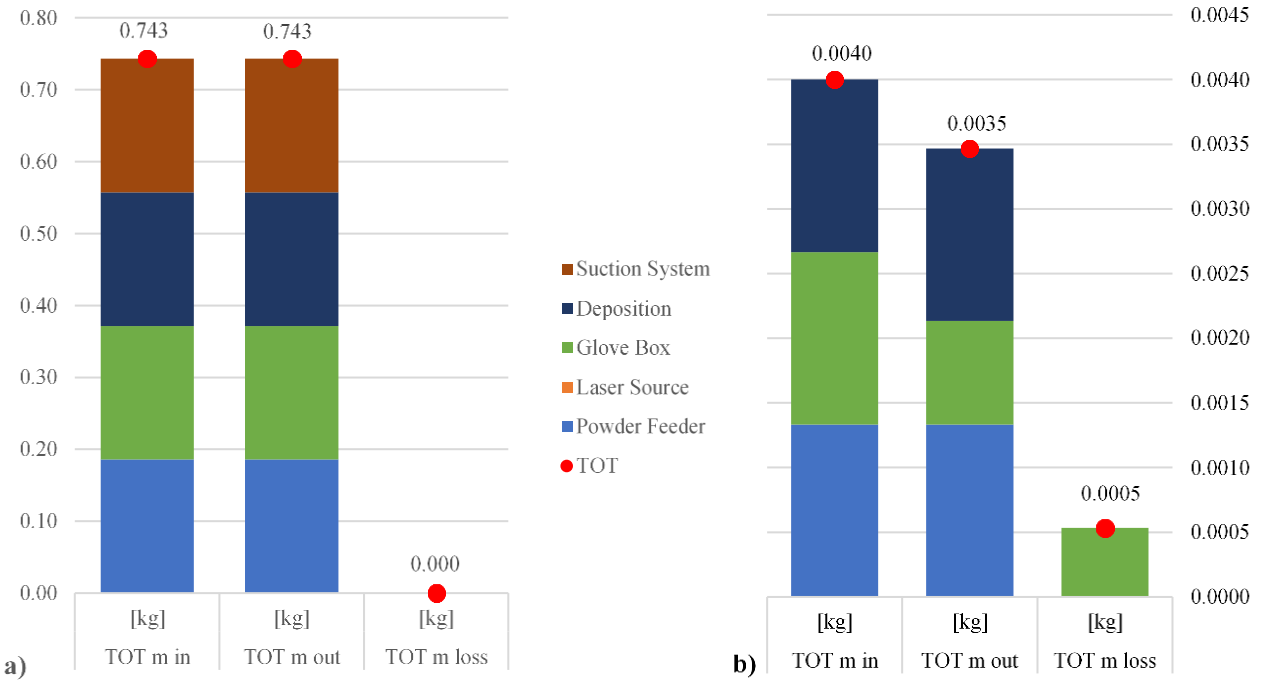

Figure 126 Mass balances of (a) Argon and (b) metal powder for 600 W and 500 mm/min deposition process.

Concerning the graph in Figure 126, the flow of argon is considered to be entirely necessary for the production of the clad, and for this reason, although it is not materially part of the final component, its output quantity is not to be considered lost. On the contrary, for a coaxial nozzle, the powder is considered 60% useful for cladding according to the deposition efficiency calculation provided by (Reddy et al., 2018) and 40% wasted inside the glove box and is therefore considered to have mass out loss.

Simplifying the process analysis, some assumptions have been made: (a) the system operates under steady-state conditions; (b) the pressure drops along the flow are negligible, and (c) each unit-process is insulated thus heat transfer between it and environment is negligible.

The graphs in Figure 126 were obtained through Eq. (23).

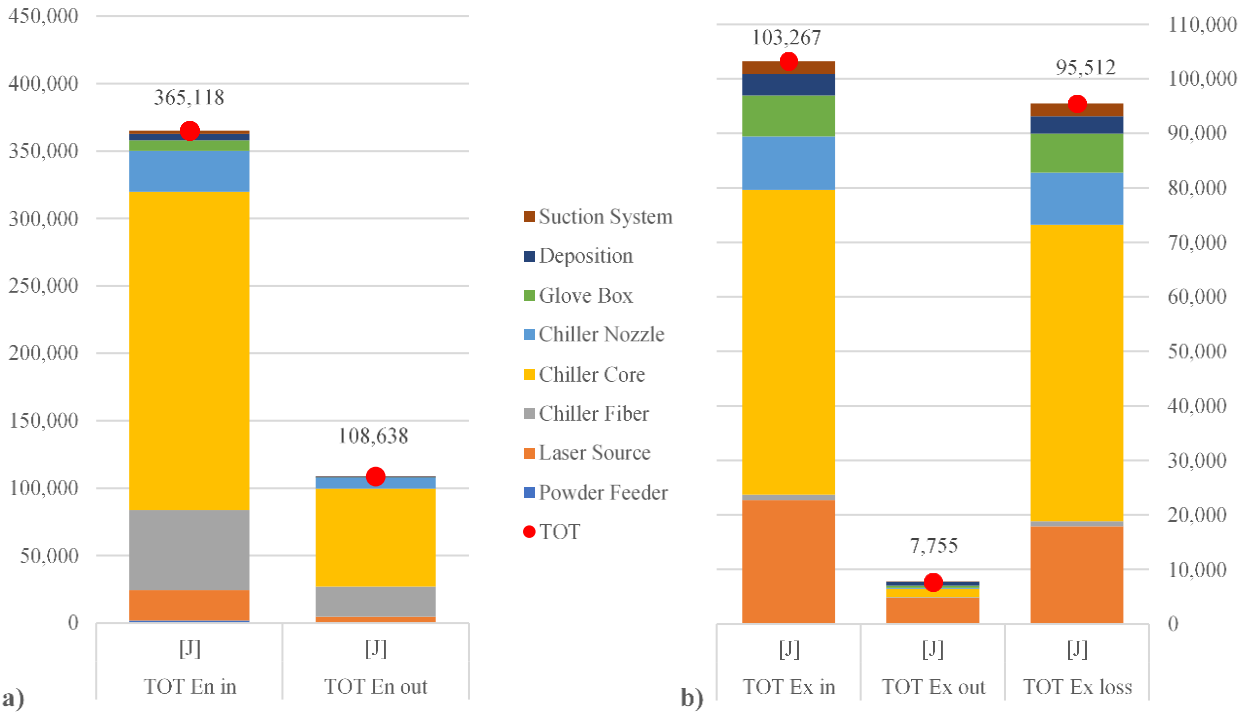

Figure 127 Energy (a) and Exergy (b) balances for 600W and 500mm/min deposition process.

The graphs in Figure 127 were obtained by means of Eq. (25) and (26), respectively.
Figure 127 shows that almost 70% of the incoming energy (Figure 127(a)) to the system during the process and almost 92% of the incoming exergy (Figure 127(b)) are lost. The input portion is determined by the electrical and material flows, which contribute to the balance through enthalpy, which depends on both the specific heat and the temperature difference between the dead state and the incoming temperature, sees Eq. (28). The lost portion corresponds to all the energy produced and dispersed, not directly useful for the deposition process.
As can be seen from the graphs, the three chillers appear to be the most energetic unit-process. The situation is slightly different regarding exergies, as the most active unit-process appears to be the core chiller, followed by the laser source.
Figure 128 shows the exergetic efficiency of each unit-process. The substantial difference between net use and general efficiency lies in the fact that the former considers only the exergies useful for the implementation of the deposition process, whereas, in the latter, all incoming and outgoing exergies are considered, as expressed in Eq. (31) and (32). Figure 128 shows the overall efficiencies of the entire process.
The laser source has an efficiency of about 21%, consistent with the literature on solid-state laser sources. As might have been expected, the efficiencies of the chillers turn out to be low, as they absorb more electrical power than they need to produce the work that is useful for the process. They are oversized compared to the process under consideration as the system is multipurpose and must also cover the needs arising from different processes, such as laser welding.
Figure 128 shows, on the right, the exergetic efficiency of the actual deposition process which takes place inside the glove box, but deserves a specific study as at this stage, the temperature differences of the materials change abruptly in a few moments. The value represents the energy (in the form of a laser beam) provided to the deposition point to create the clad but also wasted to heat other elements involved in this phase of the process, i.e., the powder dispersed in the glove box, the substrate and the argon that is dropped out by the suction system. Temperatures were measured with the pyrometer but a reference was taken to approximate how much the substrate overheated and to quantify the energy lost during deposition (Mazzarisi et al., 2020b).
Exergetic efficiencies are more complex than energy efficiencies because they consider useful work generated during the process and related to the maximum work of the Carnot machine. By controlling energy yields, they are higher and in line with the usual values: for example, the energy efficiency of the three chillers ranges from 25% to 40%.

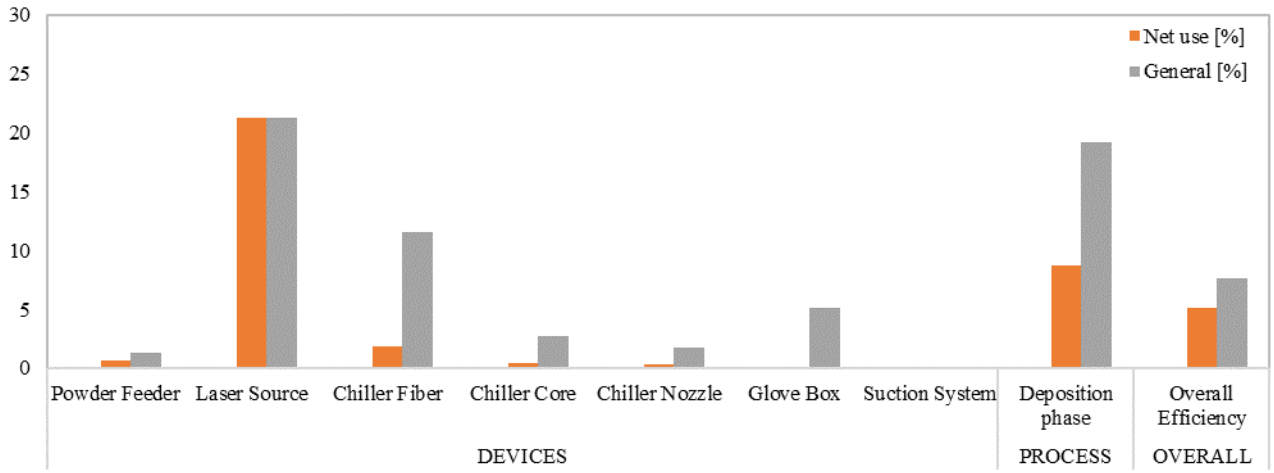

Figure 128 Unit-process devices, deposition phase, and overall process exergetic efficiencies for 600W and 500mm/min deposition process.

Analysing the energy balance, the larger fraction of energy consumed can be allocated to the generation of a laser beam. This result is consistent with other works in the literature that characterise DLMD as the most energetic additive manufacturing currently existing technology (7.779 MJ/kg) (Kellens et al., 2017).
Another food for thought regards the lack of bibliographical studies on the environmental impact on DLMD device systems that consider all components of the system agents in the process. For example, there is an almost total lack of studies on the impact of chillers on the efficiency of laser beam generation and the overall process.
Work carried out through exergetic modelling has the advantage of assessing both the general impact of the laser deposition process and the decomposition of the system into unit processes to be able to identify the energy and exergetic

contribution of each of them. Besides, it was possible to define the efficiency of the individual devices to plan for improvement on the most energy-intensive and therefore priority units.

5.7.6 Influence of process parameters on Exergetic analysis

After the in-depth explanation of the different phases of exergetic analysis, it deals here with the evaluation of the main process parameters of laser deposition on the energy impact of the process. In this way, the study wants to outline best practices for the development of sustainable additive manufacturing strategies.

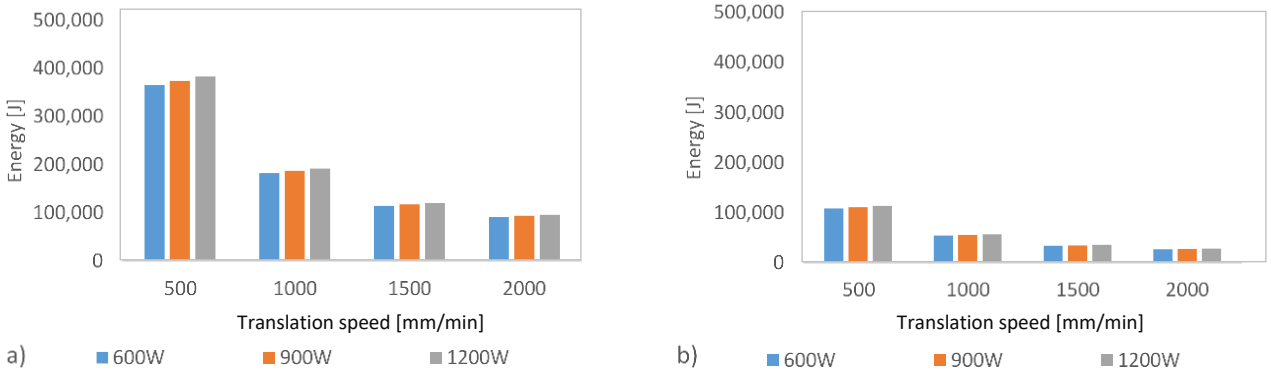

Figure 129 a) energy IN and b) energy OUT of energy balance of the experimental plan.

The energy balance in *Figure 129* shows a considerable influence on the translation speed both from the point of view of energy supply and demand of the whole system. The change in energy is proportional to the increase in processing speed, finding in the case of 2000 mm/min an energy consumption equal to 25% compared to chance with 500 mm/min. This is due to the change in the cycle times of all the systems constituting the DLMD system.

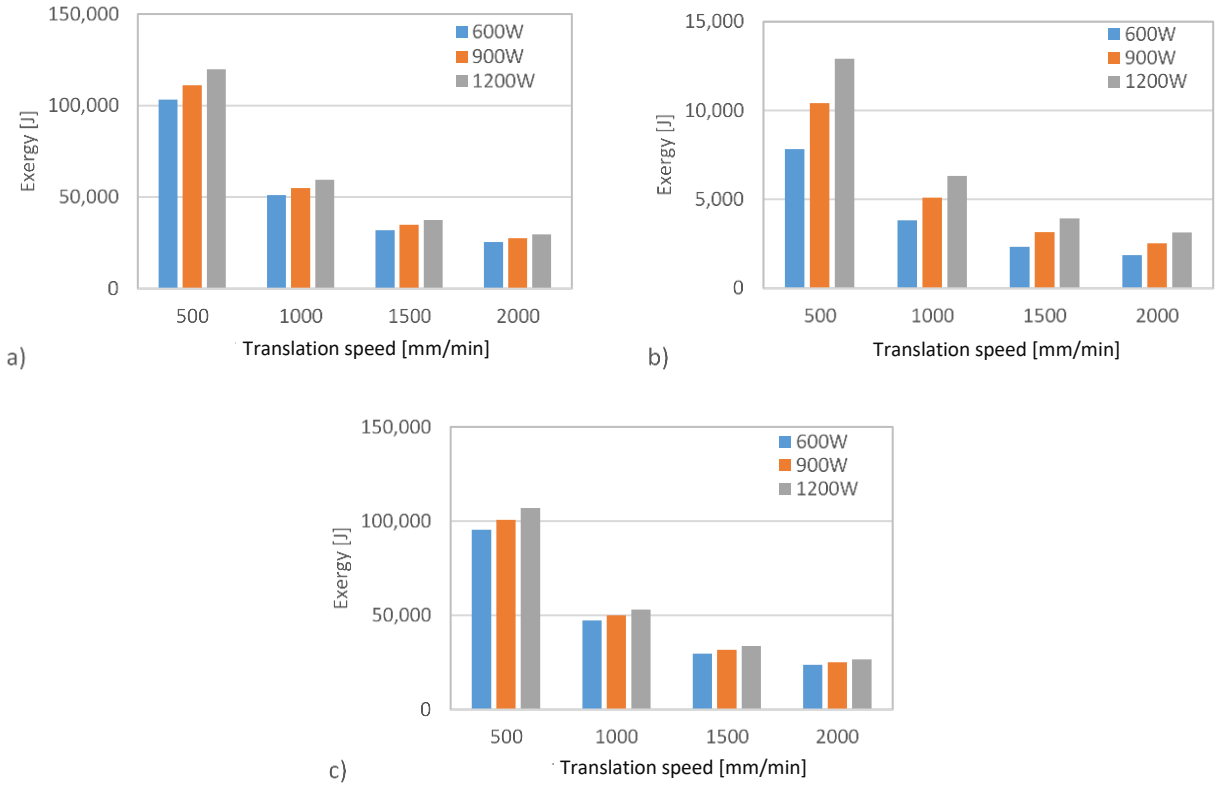

Figure 130 Exergy balance for the experimental plan: a) total exergy in, b) total exergy out, and c) total exergy loss of the experimental plan.

Conversely, laser power affects only one component of the DLMD system. This means a much smaller change in energy costs. In fact, a variation of only 5%, was found between the use of laser power of 1200 W and 600 W. This result was

easily foreseeable considering previous assessments of the impact of different chillers on total energy consumption, compared to the more energy-efficient laser source.
The ratio of energy supply to demand is almost stable for all combinations of the experimental plan around 30%.
From the exergetic point of view, the issue is slightly different, having to also consider the contributions due to the enthalpy and temperature of the system. Given the brevity of the deposition processes considered, which went from a maximum of 7.2 seconds to a minimum of 1.8 seconds, changes in chiller activation cycles here were not considered influential, but on longer processing would certainly be to be taken into account.
Trends already described for the energy balance here are even more evident. The most influential factor remains the processing time, but the laser power also has a much stronger impact, especially in exergy out. The large temperature changes due to the increase in laser power in the melt pool significantly increase the values obtained for tests with 1200 W, as can be seen in *Figure 130*(b). Nevertheless, the amount of exergy loss remains considerable, for all the cases considered shown in *Figure 130*(c)
The different proposition between exergetic input and output is also found in the efficiency of the system. In the graphs of the net and general use, there is a clear trend in operations with more massive use of laser power, of higher process efficiency. This again results from the increase in process temperature. While, from the point of view of translation speed, there is no effect on the overall efficiency of the DLMD system, as shown in *Figure 131*(a) and (b).

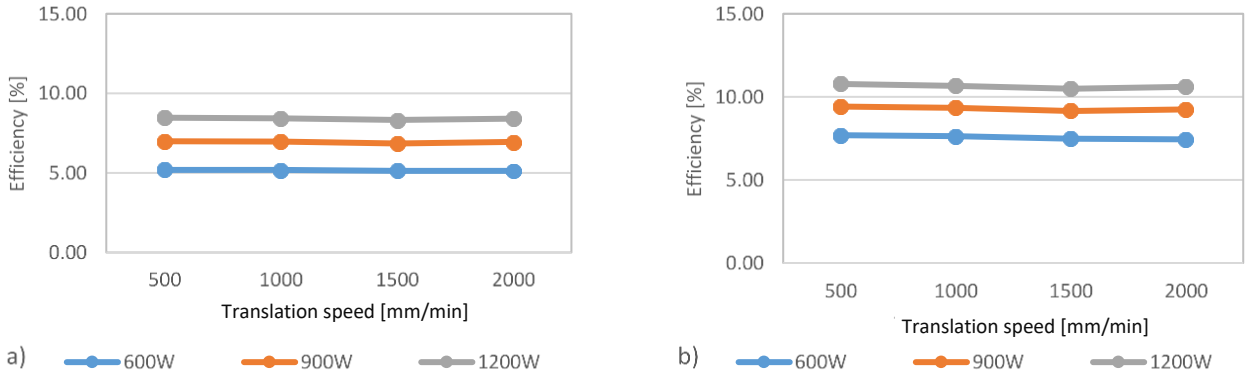

Figure 131 System exergetic efficiency: a) net use and b) general use of the experimental plan.

5.7.7 Conclusions and further developments

Given the aforementioned discussion, an appropriate system was developed to store, gather, and analyse a comprehensive set of parameters useful for sustainability assessment. This method may contribute to the accurate management of the quality and sustainability evaluation of the DLMD process under review. In addition, with a proper sensing and monitoring system, the EA-LCA will allow any practitioner to restructure both process hardware and software almost in real-time to smart I4.0 standards, thus improving cost efficiency.
The system let evaluating the influence of some process parameters of laser deposition on the efficiency and energy consumption of the DLMD system. The translation speed, which is strictly correlated to the deposition rate, was identified as a fundamental parameter for the reduction of energy and exergetic impacts. Instead, laser power has shown a great impact on the exergetic efficiency of the system, being the principal factor of the temperature variation of the melt pool.
In order to better monitor and control the DLMD process in real-time, the process modelling made it possible to recognize the open problems and relevant criticalities for the monitoring and control framework built in this work. Above all, the problem of synchronisation of sampling frequencies and integrating the data into a single system have to be considered.
Complex deposition strategies with idle times between contiguous sub-phases throughout the process will be the future application of the proposed method, which let be possible to see the current fluctuations in energy/exergetic loss for each sub-unit.
Moreover, the implementation of a nearly-real-time algorithm directly during the acquisition and a comprehensive EA-LCA on the DLMD process, via the data provided by the proposed acquisition system, will be the focus of the next works.

6 CONCLUSIONS

This doctoral thesis dealt with the monitoring and assessment of the sustainability of the Additive Manufacturing (AM) process of metal powders called Direct Laser Metal Deposition (DLMD). This technology, crucial in the Industry 4.0 paradigm, drew the attention of the scientific world and the results of this work have filled some knowledge gaps in the fields of modelling, monitoring, and assessment of the sustainability of the process, highlighted in the analysis of the state of the art.

The phenomenological model developed in chapter 3 has been useful to summarise various works in the literature that have developed predictive models using combined parameters ($Y = P^{\alpha} F^{\beta} V^{\gamma}$) as a function of specific working conditions. The proposed model has the capability to generalize the results of these works by relating the process parameters to the geometrical characteristics of the clad by using some physical characteristics of the employed materials. The most influent physical parameters were the thermal diffusivity of the base material and the density of the powders. The obtained results showed a remarkable predictive capacity of the model, supported by an experimental test carried out using a nickel-based superalloy, which reported high values of the coefficient of determination for almost all the analysed geometrical characteristics (e.g. $R^2 = 0.9778$ for the clad height fitting).

Further results were obtained in the analysis of process parameters characteristic of multilayer applications. An experimental plan in which the effects of the variation of the working distance were compared with the variation of the laser spot was developed. It has been noticed that the variation of the laser spot affects the clad width (in the range 1500 - 1800 µm) and the penetration depth (in the range 0 - 400 µm), resalting almost ineffective on the clad height. These experimental results, confirmed by an analysis of variance, validated a prediction formulation of the deposition width.

The work carried out on the relationships between process parameters and deposition quality provided the basis on which develop process monitoring activities. The thermal field has been extensively studied, thanks to the collaboration with the ENEA research centre of Brindisi. A monitoring system using thermal cameras was developed, which made it possible to highlight the influence on the thermal field of some process parameters that have not yet been analysed in the literature, such as the powder flow of nickel-based superalloy. This influence was recorded on the maximum temperatures with variations in the range 1491 - 1925 °C and on the cooling rates in the range of 580-1452 °C/s, with powder flows from 1.5 to 10 g/min. Besides, the thermal gradients, which underlie the development and diversification of the microstructure of the deposited material, were studied. A prediction model of the typology (from columnar to dendritic) and size of the microstructure was developed through solidification maps, based on the thermal gradient (G) and the growth rate of solidification (R). This method, usually adopted with data obtained from numerical simulations, has been modified to be used on experimental data. The encouraging results obtained from the investigation are validated by micrograph analysis.

The thermal monitoring was subsequently applied to deposition strategies. The influence of unidirectional and bidirectional strategies in the development of maximum temperatures and cooling rates was evaluated. Extremely regular thermal trends were obtained for the unidirectional depositions, while more discordant trends were obtained for the bidirectional depositions. The cooling rates reached 1000 °C/s for the former and over 1200 °C/s for the bidirectional strategy. The latter showed the presence of heat accumulation areas at the points of direction reversal. The maximum temperature of the melt pool was in the range 1400 - 1800 °C for unidirectional depositions, while it recorded values of 1500 - 1950 °C for bidirectional ones. The sudden temperature changes had consequences on the geometry, microstructure, and presence of defects in the deposition.

The unidirectional and bidirectional strategies were also monitored through a coaxial CCD camera. The melt pool geometry was examined by means of the “active contour” algorithm, employed for image analysis and segmentation. The melt pool showed to be strongly influenced by the process parameters and deposition strategies. The most influential parameter proved to be the dwelling times between layers, causing evident variations in the size of the melt pool in the construction of thin walls. A variation in the size of the melt pool of 1.781 mm^2 was recorded for the bidirectional deposition without dwelling times, 0.682 mm^2 by implementing 10 seconds of dwelling in the bidirectional deposition, ending with a variation of only 0.238 mm^2 for the unidirectional deposition with dwelling times. It is clear that in the last case there was an extremely more regular deposition.

The quality of the deposition was also evaluated by ultrasonic non-destructive techniques. These highlighted an exceptional capability to evaluate the main geometric factors of the deposition. Through the analysis of longitudinal and transverse waves, the clad height and the dilution with the substrate were determined. The latter is of paramount importance because it represents the mixing of the base material and powder material as well as determining the bond between clad and substrate. The ultrasonic analysis was useful for assessing the mechanical performance of components,

through Young's modulus, shear modulus, and Poisson's ratio, also highlighting how these are closely related to the dilution values.

Finally, the influence of the process parameters concerning treatment sustainability was assessed. Via the exergetic analysis, the critical issues of the equipment used in the laboratories of the Department of Mechanics, Mathematics and Management (DMMM) of the Polytechnic University of Bari were highlighted. The main fact to point out was a large amount of energy and exergy (over 88%) consumed by the chiller systems. The developed experimental plan was useful to establish how the energetic and exergetic impact of laser processing is influenced by the deposition rate. In fact, this parameter is linked to the work cycles of all system components, recording a reduction in energy load of more than 75% for processes carried out with speeds from 500 to 2000 mm/min. Conversely, the laser power has shown a marginal influence on the general energy and exergy balances, as this system-level parameter only constrains the laser source settings. However, the laser power was particularly impacting in terms of process efficiency, recording a value of 5% of net efficiency for the processes carried out using 600 W, increased to 8.5% for a deposition carried out with 1200 W. It was concluded that exergetically sustainable and efficient depositions can be achieved by using high deposition speeds and high laser powers.

7 FUTURE PERSPECTIVES

The investigations and experiments carried out in this doctoral thesis have contributed to the scientific development of Direct Laser Metal Deposition (DLMD) technology. The potentialities and weaknesses of the system were investigated. Some ideas and suggestions for future research topic have been pointed out and hopefully, they can be addressed when the global pandemic situation due to COVID-19 will be settled:

- The phenomenological model elaborated in chapter 3 can be expanded by taking into account additional process parameters, such as the laser spot diameter. This model can be validated on a wider range of materials of industrial interest, as well as on depositions with dissimilar materials and functionally-graded materials.
- The analysis of working distance and laser spot dimension influence can be applied to multilayer deposition strategies and included in an automated process monitoring and control system. In this way, closed-loop control systems that are not solely focused on laser power or translation speed can be developed.
- The thermal analysis carried out by using the thermal camera can be applied to the construction of thin-walls and complex 3D geometries. The modified solidification map method can be applied to the data deriving from layers to determine the variation of the whole microstructure of the component. Further process parameters can be investigated to broaden the spectrum of use of the proposed methodology.
- The study of the melt pool size and geometry using a coaxial CCD camera can be applied to complex geometries. Algorithms that can automatically identify deposition errors through the analysis of image brightness can be inserted. The system can be integrated into an automated control system.
- The ultrasonic evaluation of specimens using additive techniques can be carried out through more refined ultrasonic techniques (e.g. ultrasonic laser technique) capable to identify deposition defects of the order of a tenth of a millimetre. Depositions composed of numerous deposited layers can be examined, in order to validate the analysis reliability.
- The sustainability investigation of DLMD processes can be included in the life cycle assessment of the product/process, in order to have a comprehensive view of the environmental and energy impacts and of the efficiency proper of the technology. The analysis can be realized on complex deposition strategies in order to define guidelines and implement a standard for sustainable deposition process.

8 REFERENCES

Alekseev, A.V., Turichin, G.A., Klimova-Korsmik, O.G., Valdaytseva, E.A., Rashkovets, M.V., Nikulina, A.A., 2020. Simulation of the Ni3Al intermetallic inclusion growth process during direct laser deposition using Ni-based superalloy powder. Materials Today: Proceedings 30, 756–760. https://doi.org/10.1016/j.matpr.2020.01.562

Alfred, I., Nicolaus, M., Hermsdorf, J., Kaierle, S., Möhwald, K., Maier, H.-J., Wesling, V., 2018. Advanced high pressure turbine blade repair technologies. Procedia CIRP 74, 214–217. https://doi.org/10.1016/j.procir.2018.08.097

Alhaddi, H., 2015. Triple Bottom Line and Sustainability: A Literature Review. Business and Management Studies 1. https://doi.org/10.11114/bms.v1i2.752

Allwood, J.M., Ashby, M.F., Gutowski, T.G., Worrell, E., 2013. Material efficiency: providing material services with less material production. Philosophical Transactions of the Royal Society A: Mathematical, Physical and Engineering Sciences 371, 20120496. https://doi.org/10.1098/rsta.2012.0496

Anakhu, P., Bolu, C., Abioye, A., Azeta, J., 2018. Fused Deposition Modeling Printed Patterns for Sand Casting in a Nigerian Foundry: A Review. International Journal of Applied Engineering Research 13.

Angelastro, A., Campanelli, S.L., Casalino, G., 2017. Statistical analysis and optimization of direct metal laser deposition of 227-F Colmonoy nickel alloy. Optics & Laser Technology 94, 138–145. https://doi.org/10.1016/j.optlastec.2017.03.027

Angelastro, A., Campanelli, S.L., Casalino, G., Ludovico, A.D., Ferrara, S., 2011. A Methodology for Optimization of the Direct Laser Metal Deposition Process. Key Engineering Materials 473, 75–82. https://doi.org/10.4028/www.scientific.net/KEM.473.75

Angelastro, A., Latte, M., Rizzo, A., Palano, F., Campanelli, S.L., 2018. Thermal field monitoring and analysis of its influence on Direct Laser Deposition of single tracks of a nickel superalloy, in: Helvajian, H., Piqué, A., Gu, B. (Eds.), Laser 3D Manufacturing V. Presented at the Laser 3D Manufacturing V, SPIE, San Francisco, United States, p. 50. https://doi.org/10.1117/12.2297667

Ansari, M., Shoja Razavi, R., Barekat, M., 2016. An empirical-statistical model for coaxial laser cladding of NiCrAlY powder on Inconel 738 superalloy. Optics & Laser Technology 86, 136–144. https://doi.org/10.1016/j.optlastec.2016.06.014

Arrizubieta, J.I., Lamikiz, A., Klocke, F., Martínez, S., Arntz, K., Ukar, E., 2017. Evaluation of the relevance of melt pool dynamics in Laser Material Deposition process modeling. International Journal of Heat and Mass Transfer 115, 80–91. https://doi.org/10.1016/j.ijheatmasstransfer.2017.07.011

Arrizubieta, J.I., Wegener, M., Arntz, K., Lamikiz, A., Ruiz, J.E., 2016. Powder Flux Regulation in the Laser Material Deposition Process. Physics Procedia 83, 743–751. https://doi.org/10.1016/j.phpro.2016.08.076

Atzeni, E., Salmi, A., 2012. Economics of additive manufacturing for end-usable metal parts. The International Journal of Advanced Manufacturing Technology 62, 1147–1155. https://doi.org/10.1007/s00170-011-3878-1

Ayres, R., van den Berrgh, J., Gowdy, J., Center for Environmental Philosophy, The University of North Texas, 2001. Strong versus Weak Sustainability: Economics, Natural Sciences, and Consilience. Environmental Ethics 23, 155–168. https://doi.org/10.5840/enviroethics200123225

Bak, D., 2003. Rapid prototyping or rapid production? 3D printing processes move industry towards the latter. Assembly Automation 23, 340–345. https://doi.org/10.1108/01445150310501190

Barekat, M., Shoja Razavi, R., Ghasemi, A., 2016. Nd:YAG laser cladding of Co–Cr–Mo alloy on γ-TiAl substrate. Optics & Laser Technology 80, 145–152. https://doi.org/10.1016/j.optlastec.2016.01.003

Bax, B., Rajput, R., Kellet, R., Reisacher, M., 2018. Systematic evaluation of process parameter maps for laser cladding and directed energy deposition. Additive Manufacturing 21, 487–494. https://doi.org/10.1016/j.addma.2018.04.002

Bekker, A.C.M., Verlinden, J.C., 2018. Life cycle assessment of wire + arc additive manufacturing compared to green sand casting and CNC milling in stainless steel. Journal of Cleaner Production 177, 438–447. https://doi.org/10.1016/j.jclepro.2017.12.148

Bhavar, V., Kattire, P., Patil, V., Khot, S., Gujar, K., Singh, R., 2017. A review on powder bed fusion technology of metal additive manufacturing, in: Badiru, A.B., Valencia, V.V., Liu, D. (Eds.), Additive Manufacturing Handbook. CRC Press, pp. 251–253. https://doi.org/10.1201/9781315119106-15

Bian, L., Shamsaei, N., Usher, J.M. (Eds.), 2017. Laser-Based Additive Manufacturing of Metal Parts: Modeling, Optimization, and Control of Mechanical Properties, 1st ed. CRC Press, Boca Raton: CRC Press, Taylor & Francis, 2018. https://doi.org/10.1201/9781315151441

Blecher, J.J., Palmer, T.A., DebRoy, T., 2014. Solidification Map of a Nickel-Base Alloy. Metallurgical and Materials Transactions A 45, 2142–2151. https://doi.org/10.1007/s11661-013-2149-1

Boisselier, D., Sankaré, S., Engel, T., 2014. Improvement of the Laser Direct Metal Deposition Process in 5-axis Configuration. Physics Procedia 56, 239–249. https://doi.org/10.1016/j.phpro.2014.08.168

Bonilla, S., Silva, H., Terra da Silva, M., Franco Gonçalves, R., Sacomano, J., 2018. Industry 4.0 and Sustainability Implications: A Scenario-Based Analysis of the Impacts and Challenges. Sustainability 10, 3740. https://doi.org/10.3390/su10103740

Bourell, D., Kruth, J.P., Leu, M., Levy, G., Rosen, D., Beese, A.M., Clare, A., 2017. Materials for additive manufacturing. CIRP Annals 66, 659–681. https://doi.org/10.1016/j.cirp.2017.05.009

Butt, J., 2020. Exploring the Interrelationship between Additive Manufacturing and Industry 4.0. Designs 4, 13. https://doi.org/10.3390/designs4020013

Caiazzo, F., 2018. Laser-aided Directed Metal Deposition of Ni-based superalloy powder. Optics & Laser Technology 103, 193–198. https://doi.org/10.1016/j.optlastec.2018.01.042

Caiazzo, F., Alfieri, V., Argenio, P., Sergi, V., 2017. Additive manufacturing by means of laser-aided directed metal deposition of 2024 aluminium powder: Investigation and optimization. Advances in Mechanical Engineering 9, 168781401771498. https://doi.org/10.1177/1687814017714982

Caltanissetta, F., Grasso, M., Petrò, S., Colosimo, B.M., 2018. Characterization of in-situ measurements based on layerwise imaging in laser powder bed fusion. Additive Manufacturing 24, 183–199. https://doi.org/10.1016/j.addma.2018.09.017

Campanelli, S.L., Angelastro, A., Signorile, C.G., Casalino, G., 2017a. Investigation on direct laser powder deposition of 18 Ni (300) marage steel using mathematical model and experimental characterisation. The International Journal of Advanced Manufacturing Technology 89, 885–895. https://doi.org/10.1007/s00170-016-9135-x

Campanelli, S.L., Angelastro, A., Signorile, C.G., Casalino, G., 2017b. Investigation on direct laser powder deposition of 18 Ni (300) marage steel using mathematical model and experimental characterisation. The International Journal of Advanced Manufacturing Technology 89, 885–895. https://doi.org/10.1007/s00170-016-9135-x

Campbell, F.C., 2006. Manufacturing technology for aerospace structural materials, 1st ed. ed. Elsevier, Amsterdam ; Boston.

Casalino, G., Angelastro, A., Perulli, P., Casavola, C., Moramarco, V., 2018. Study on the fiber laser/TIG weldability of AISI 304 and AISI 410 dissimilar weld. Journal of Manufacturing Processes 35, 216–225. https://doi.org/10.1016/j.jmapro.2018.08.005

Castellano, A., Foti, P., Fraddosio, A., Marzano, S., Piccioni, M.D., 2014. Mechanical characterization of CFRP composites by ultrasonic immersion tests: Experimental and numerical approaches. Composites Part B: Engineering 66, 299–310. https://doi.org/10.1016/j.compositesb.2014.04.024

Castellano, A., Mazzarisi, M., Campanelli, S.L., Angelastro, A., Fraddosio, A., Piccioni, M.D., 2020. Ultrasonic Characterization of Components Manufactured by Direct Laser Metal Deposition. Materials 13, 2658. https://doi.org/10.3390/ma13112658

Cerniglia, D., Scafidi, M., Pantano, A., Rudlin, J., 2015. Inspection of additive-manufactured layered components. Ultrasonics 62, 292–298. https://doi.org/10.1016/j.ultras.2015.06.001

Chartrain, N.A., Williams, C.B., Whittington, A.R., 2018. A review on fabricating tissue scaffolds using vat photopolymerization. Acta Biomaterialia 74, 90–111. https://doi.org/10.1016/j.actbio.2018.05.010

Chen, D., Heyer, S., Ibbotson, S., Salonitis, K., Steingrímsson, J.G., Thiede, S., 2015. Direct digital manufacturing: definition, evolution, and sustainability implications. Journal of Cleaner Production 107, 615–625. https://doi.org/10.1016/j.jclepro.2015.05.009

Chunming Li, Chiu-Yen Kao, Gore, J.C., Zhaohua Ding, 2008. Minimization of Region-Scalable Fitting Energy for Image Segmentation. IEEE Transactions on Image Processing 17, 1940–1949. https://doi.org/10.1109/TIP.2008.2002304

Colosimo, B.M., Grasso, M., n.d. In- situ Monitoring of Metal Additive Manufacturing Processes: Sensing and Intelligent Data Analysis 6.

Cooke, K.O., Richardson, A., Khan, T.I., Shar, M.A., 2020. High-Temperature Diffusion Bonding of Ti–6Al–4V and Super-Duplex Stainless Steel Using a Cu Interlayer Embedded with Alumina Nanoparticles. Journal of Manufacturing and Materials Processing 4, 3. https://doi.org/10.3390/jmmp4010003

Cornelissen, R.L., Hirs, G.G., 2002. The value of the exergetic life cycle assessment besides the LCA. Energy Conversion and Management 43, 1417–1424. https://doi.org/10.1016/S0196-8904(02)00025-0

Costa, L., Felde, I., Réti, T., Kálazi, Z., Colaço, R., Vilar, R., Verő, B., 2003. A Simplified Semi-Empirical Method to Select the Processing Parameters for Laser Clad Coatings. Materials Science Forum 414–415, 385–394. https://doi.org/10.4028/www.scientific.net/MSF.414-415.385

Dalibozhko, A., Krakovetskaya, I., 2018. Youth entrepreneurial projects for the sustainable development of global community: evidence from Enactus program. SHS Web of Conferences 57, 01009. https://doi.org/10.1051/shsconf/20185701009

Dass, A., Moridi, A., 2019. State of the Art in Directed Energy Deposition: From Additive Manufacturing to Materials Design. Coatings 9, 418. https://doi.org/10.3390/coatings9070418

de Oliveira, U., Ocelík, V., De Hosson, J.Th.M., 2005. Analysis of coaxial laser cladding processing conditions. Surface and Coatings Technology 197, 127–136. https://doi.org/10.1016/j.surfcoat.2004.06.029

DebRoy, T., Wei, H.L., Zuback, J.S., Mukherjee, T., Elmer, J.W., Milewski, J.O., Beese, A.M., Wilson-Heid, A., De, A., Zhang, W., 2018. Additive manufacturing of metallic components – Process, structure and properties. Progress in Materials Science 92, 112–224. https://doi.org/10.1016/j.pmatsci.2017.10.001

Di Pierro, B., Sangiorgio, V., Fiume, G., Fanti, M.P., 2019. Analysis of Industrial Changes and Enabling Technologies in Industry 4.0, in: 2019 IEEE International Conference on Systems, Man and Cybernetics (SMC). Presented at the 2019 IEEE International Conference on Systems, Man and Cybernetics (SMC), IEEE, Bari, Italy, pp. 581–586. https://doi.org/10.1109/SMC.2019.8914610

Dilberoglu, U.M., Gharehpapagh, B., Yaman, U., Dolen, M., 2017. The Role of Additive Manufacturing in the Era of Industry 4.0. Procedia Manufacturing 11, 545–554. https://doi.org/10.1016/j.promfg.2017.07.148

Ding, Y., Warton, J., Kovacevic, R., 2016. Development of sensing and control system for robotized laser-based direct metal addition system. Additive Manufacturing 10, 24–35. https://doi.org/10.1016/j.addma.2016.01.002

Doubenskaia, M., Pavlov, M., Grigoriev, S., Smurov, I., 2013. Definition of brightness temperature and restoration of true temperature in laser cladding using infrared camera. Surface and Coatings Technology 220, 244–247. https://doi.org/10.1016/j.surfcoat.2012.10.044

Du, L., Gu, D., Dai, D., Shi, Q., Ma, C., Xia, M., 2018. Relation of thermal behavior and microstructure evolution during multi-track laser melting deposition of Ni-based material. Optics & Laser Technology 108, 207–217. https://doi.org/10.1016/j.optlastec.2018.06.042

Dubourg, L., St-Georges, L., 2006. Optimization of Laser Cladding Process Using Taguchi and EM Methods for MMC Coating Production. Journal of Thermal Spray Technology 15, 790–795. https://doi.org/10.1361/105996306X146785

Dutta Majumdar, J., Manna, I., 2011. Laser material processing. International Materials Reviews 56, 341–388. https://doi.org/10.1179/1743280411Y.0000000003

El Cheikh, H., Courant, B., Hascoët, J.-Y., Guillén, R., 2012. Prediction and analytical description of the single laser track geometry in direct laser fabrication from process parameters and energy balance reasoning. Journal of Materials Processing Technology 212, 1832–1839. https://doi.org/10.1016/j.jmatprotec.2012.03.016

Emamian, A., Alimardani, M., Khajepour, A., 2014. Effect of cooling rate and laser process parameters on additive manufactured Fe–Ti–C metal matrix composites microstructure and carbide morphology. Journal of Manufacturing Processes 16, 511–517. https://doi.org/10.1016/j.jmapro.2014.07.002

Emamian, A., Farshidianfar, M.H., Khajepour, A., 2017. Thermal monitoring of microstructure and carbide morphology in direct metal deposition of Fe-Ti-C metal matrix composites. Journal of Alloys and Compounds 710, 20–28. https://doi.org/10.1016/j.jallcom.2017.03.207

Erfanmanesh, M., Abdollah-Pour, H., Mohammadian-Semnani, H., Shoja-Razavi, R., 2017. An empirical-statistical model for laser cladding of WC-12Co powder on AISI 321 stainless steel. Optics & Laser Technology 97, 180–186. https://doi.org/10.1016/j.optlastec.2017.06.026

Errico, V., Campanelli, S.L., Angelastro, A., Mazzarisi, M., Casalino, G., 2020. On the feasibility of AISI 304 stainless steel laser welding with metal powder. Journal of Manufacturing Processes 56, 96–105. https://doi.org/10.1016/j.jmapro.2020.04.065

Everton, S.K., Hirsch, M., Stravroulakis, P., Leach, R.K., Clare, A.T., 2016. Review of in-situ process monitoring and in-situ metrology for metal additive manufacturing. Materials & Design 95, 431–445. https://doi.org/10.1016/j.matdes.2016.01.099

Farshidianfar, M.H., Khajepour, A., Gerlich, A., 2016a. Real-time control of microstructure in laser additive manufacturing. The International Journal of Advanced Manufacturing Technology 82, 1173–1186. https://doi.org/10.1007/s00170-015-7423-5

Farshidianfar, M.H., Khajepour, A., Gerlich, A.P., 2016b. Effect of real-time cooling rate on microstructure in Laser Additive Manufacturing. Journal of Materials Processing Technology 231, 468–478. https://doi.org/10.1016/j.jmatprotec.2016.01.017

Flemings, M.C., 2006. Solidification Processing, in: Cahn, R.W., Haasen, P., Kramer, E.J. (Eds.), Materials Science and Technology. Wiley-VCH Verlag GmbH & Co. KGaA, Weinheim, Germany. https://doi.org/10.1002/9783527603978.mst0173

G Marshall, W J Young Ii, N Shamsaei, J Craig, T Wakeman, S M Thompson, 2015. Dual Thermographic Monitoring of Ti-6Al-4V Cylinders during Direct Laser Deposition. Unpublished. https://doi.org/10.13140/rg.2.1.3373.6401

Gaja, H., Liou, F., 2018. Defect classification of laser metal deposition using logistic regression and artificial neural networks for pattern recognition. The International Journal of Advanced Manufacturing Technology 94, 315–326. https://doi.org/10.1007/s00170-017-0878-9

Gan, Z., Yu, G., He, X., Li, S., 2017. Numerical simulation of thermal behavior and multicomponent mass transfer in direct laser deposition of Co-base alloy on steel. International Journal of Heat and Mass Transfer 104, 28–38. https://doi.org/10.1016/j.ijheatmasstransfer.2016.08.049

Gao, W., Zhang, Y., Ramanujan, D., Ramani, K., Chen, Y., Williams, C.B., Wang, C.C.L., Shin, Y.C., Zhang, S., Zavattieri, P.D., 2015. The status, challenges, and future of additive manufacturing in engineering. Computer-Aided Design 69, 65–89. https://doi.org/10.1016/j.cad.2015.04.001

Ghobakhloo, M., 2018. The future of manufacturing industry: a strategic roadmap toward Industry 4.0. Journal of Manufacturing Technology Management 29, 910–936. https://doi.org/10.1108/JMTM-02-2018-0057

Gibson, I., Rosen, D., Stucker, B., 2015. Additive Manufacturing Technologies. Springer New York, New York, NY. https://doi.org/10.1007/978-1-4939-2113-3

Gisario, A., Kazarian, M., Martina, F., Mehrpouya, M., 2019. Metal additive manufacturing in the commercial aviation industry: A review. Journal of Manufacturing Systems 53, 124–149. https://doi.org/10.1016/j.jmsy.2019.08.005

Goedkoop, M., Oele, M., Schrywer, A., Vieira, M., 2008. SimaPro Database Manual: Methods Library.

Guan, X., Zhao, Y.F., 2020. Modeling of the laser powder–based directed energy deposition process for additive manufacturing: a review. The International Journal of Advanced Manufacturing Technology 107, 1959–1982. https://doi.org/10.1007/s00170-020-05027-0

Haleem, A., Javaid, M., 2019. Additive Manufacturing Applications in Industry 4.0: A Review. Journal of Industrial Integration and Management 04, 1930001. https://doi.org/10.1142/S2424862219300011

He, W., Shi, W., Li, J., Xie, H., 2019. In-situ monitoring and deformation characterization by optical techniques; part I: Laser-aided direct metal deposition for additive manufacturing. Optics and Lasers in Engineering 122, 74–88. https://doi.org/10.1016/j.optlaseng.2019.05.020

Herzog, D., Seyda, V., Wycisk, E., Emmelmann, C., 2016. Additive manufacturing of metals. Acta Materialia 117, 371–392. https://doi.org/10.1016/j.actamat.2016.07.019

Hopkinson, N., Dicknes, P., 2003. Analysis of rapid manufacturing—using layer manufacturing processes for production. Proceedings of the Institution of Mechanical Engineers, Part C: Journal of Mechanical Engineering Science 217, 31–39. https://doi.org/10.1243/095440603762554596

Hopkinson, N., Hague, R.J.M., Dickens, P.M. (Eds.), 2006. Rapid manufacturing: an industrial revolution for the digital age. John Wiley, Chichester, England.

Hsu, H.-W., Lo, Y.-L., Lee, M.-H., 2019. Vision-based inspection system for cladding height measurement in Direct Energy Deposition (DED). Additive Manufacturing 27, 372–378. https://doi.org/10.1016/j.addma.2019.03.017

Huang, S.H., Liu, P., Mokasdar, A., Hou, L., 2013. Additive manufacturing and its societal impact: a literature review. The International Journal of Advanced Manufacturing Technology 67, 1191–1203. https://doi.org/10.1007/s00170-012-4558-5

Jayal, A.D., Badurdeen, F., Dillon, O.W., Jawahir, I.S., 2010. Sustainable manufacturing: Modeling and optimization challenges at the product, process and system levels. CIRP Journal of Manufacturing Science and Technology 2, 144–152. https://doi.org/10.1016/j.cirpj.2010.03.006

Jiang, J., Xu, X., Stringer, J., 2019. Optimization of process planning for reducing material waste in extrusion based additive manufacturing. Robotics and Computer-Integrated Manufacturing 59, 317–325. https://doi.org/10.1016/j.rcim.2019.05.007

Jones, J., Whittaker, M., Buckingham, R., Johnston, R., Bache, M., Clark, D., 2017. Microstructural characterisation of a nickel alloy processed via blown powder direct laser deposition (DLD). Materials & Design 117, 47–57. https://doi.org/10.1016/j.matdes.2016.12.062

Jovane, F., Westkämper, E., Williams, D., 2009. The manufuture road: towards competitive and sustainable high-adding-value manufacturing. Springer-Verlag, Germany.

Kafara, M., Süchting, M., Kemnitzer, J., Westermann, H.-H., Steinhilper, R., 2017. Comparative Life Cycle Assessment of Conventional and Additive Manufacturing in Mold Core Making for CFRP Production. Procedia Manufacturing 8, 223–230. https://doi.org/10.1016/j.promfg.2017.02.028

Kaierle, S., Overmeyer, L., Alfred, I., Rottwinkel, B., Hermsdorf, J., Wesling, V., Weidlich, N., 2017. Single-crystal turbine blade tip repair by laser cladding and remelting. CIRP Journal of Manufacturing Science and Technology 19, 196–199. https://doi.org/10.1016/j.cirpj.2017.04.001

Kellens, K., Baumers, M., Gutowski, T.G., Flanagan, W., Lifset, R., Duflou, J.R., 2017. Environmental Dimensions of Additive Manufacturing: Mapping Application Domains and Their Environmental Implications: Environmental Dimensions of Additive Manufacturing. Journal of Industrial Ecology 21, S49–S68. https://doi.org/10.1111/jiec.12629

Khajavi, S.H., Partanen, J., Holmström, J., 2014. Additive manufacturing in the spare parts supply chain. Computers in Industry 65, 50–63. https://doi.org/10.1016/j.compind.2013.07.008

Khorram Niaki, M., Nonino, F., 2018. The Management of Additive Manufacturing, Springer Series in Advanced Manufacturing. Springer International Publishing, Cham. https://doi.org/10.1007/978-3-319-56309-1

Kim, F.H., Moylan, S.P., 2018. Literature review of metal additive manufacturing defects (No. NIST AMS 100-16). National Institute of Standards and Technology, Gaithersburg, MD. https://doi.org/10.6028/NIST.AMS.100-16

Kloepffer, W., 2008. Life cycle sustainability assessment of products: (with Comments by Helias A. Udo de Haes, p. 95). The International Journal of Life Cycle Assessment 13, 89–95. https://doi.org/10.1065/lca2008.02.376

Knezović, N., Topić, A., 2019. Wire and Arc Additive Manufacturing (WAAM) – A New Advance in Manufacturing, in: Karabegović, I. (Ed.), New Technologies, Development and Application, Lecture Notes in Networks and Systems. Springer International Publishing, Cham, pp. 65–71. https://doi.org/10.1007/978-3-319-90893-9_7

Kodama, H., 1981. Automatic method for fabricating a three-dimensional plastic model with photo-hardening polymer. Review of Scientific Instruments 52, 1770–1773. https://doi.org/10.1063/1.1136492

Le Bourhis, F., Kerbrat, O., Dembinski, L., Hascoet, J.-Y., Mognol, P., 2014. Predictive Model for Environmental Assessment in Additive Manufacturing Process. Procedia CIRP 15, 26–31. https://doi.org/10.1016/j.procir.2014.06.031

Lee, Y., Nordin, M., Babu, S.S., Farson, D.F., 2014. Effect of Fluid Convection on Dendrite Arm Spacing in Laser Deposition. Metallurgical and Materials Transactions B 45, 1520–1529. https://doi.org/10.1007/s11663-014-0054-7

Lei, K., Qin, X., Liu, H., Ni, M., 2018. Analysis and modeling of melt pool morphology for high power diode laser cladding with a rectangle beam spot. Optics and Lasers in Engineering 110, 89–99. https://doi.org/10.1016/j.optlaseng.2018.05.022

Lei, Z., Zhang, K., Zhou, H., Ni, L., Chen, Y., 2018. A comparative study of microstructure and tensile properties of Ti2AlNb joints prepared by laser welding and laser-additive welding with the addition of filler powder. Journal of Materials Processing Technology 255, 477–487. https://doi.org/10.1016/j.jmatprotec.2017.12.044

Li, W., Liou, F., Newkirk, J., Taminger, K.M.B., Seufzer, W.J., 2017. Investigation on Ti6Al4V-V-Cr-Fe-SS316 Multi-layers Metallic Structure Fabricated by Laser 3D Printing. Scientific Reports 7. https://doi.org/10.1038/s41598-017-08580-z

Liu, J., Li, L., 2005. Effects of powder concentration distribution on fabrication of thin-wall parts in coaxial laser cladding. Optics & Laser Technology 37, 287–292. https://doi.org/10.1016/j.optlastec.2004.04.009

Liu, W.-W., Tang, Z.-J., Liu, X.-Y., Wang, H.-J., Zhang, H.-C., 2017. A Review on In-situ Monitoring and Adaptive Control Technology for Laser Cladding Remanufacturing. Procedia CIRP 61, 235–240. https://doi.org/10.1016/j.procir.2016.11.217

Liu, Z., Li, T., Ning, F., Cong, W., Kim, H., Jiang, Q., Zhang, H., 2019. Effects of deposition variables on molten pool temperature during laser engineered net shaping of Inconel 718 superalloy. The International Journal of Advanced Manufacturing Technology 102, 969–976. https://doi.org/10.1007/s00170-018-03245-1

Long, J., Huang, W., Xiang, J., Guan, Q., Ma, Z., 2018. Parameter optimization of laser welding of steel to Al with pre-placed metal powders using the Taguchi-response surface method. Optics & Laser Technology 108, 97–106. https://doi.org/10.1016/j.optlastec.2018.06.026

Lu, C., Lin, Q., Li, B., Wu, J., Zhang, Y., 2019. Effect of powder feeding rate on heat and mass transfer behaviors during filler powder laser welding. Optics & Laser Technology 120, 105711. https://doi.org/10.1016/j.optlastec.2019.105711

Ludovico, A.D., Angelastro, A., L., S., 2010. Experimental Analysis of the Direct Laser Metal Deposition Process, in: Joo, M. (Ed.), New Trends in Technologies: Devices, Computer, Communication and Industrial Systems. Sciyo. https://doi.org/10.5772/10431

Luigi De Filippis, Livia Serio, Davide Palumbo, Rosa De Finis, Umberto Galietti, 2017. Optimization and Characterization of the Friction Stir Welded Sheets of AA 5754-H111: Monitoring of the Quality of Joints with Thermographic Techniques. Materials 10, 1165. https://doi.org/10.3390/ma10101165

Lundbäck, A., Lindgren, L.-E., 2017. Finite Element Simulation to Support Sustainable Production by Additive Manufacturing. Procedia Manufacturing 7, 127–130. https://doi.org/10.1016/j.promfg.2016.12.033

Mahamood, R.M., Akinlabi, E.T., 2017. Scanning speed and powder flow rate influence on the properties of laser metal deposition of titanium alloy. The International Journal of Advanced Manufacturing Technology 91, 2419–2426. https://doi.org/10.1007/s00170-016-9954-9

Marzban, J., Ghaseminejad, P., Ahmadzadeh, M.H., Teimouri, R., 2015. Experimental investigation and statistical optimization of laser surface cladding parameters. The International Journal of Advanced Manufacturing Technology 76, 1163–1172. https://doi.org/10.1007/s00170-014-6338-x

Matos, F., Godina, R., Jacinto, C., Carvalho, H., Ribeiro, I., Peças, P., 2019. Additive Manufacturing: Exploring the Social Changes and Impacts. Sustainability 11, 3757. https://doi.org/10.3390/su11143757

Mazzarisi, M., Campanelli, S.L., Angelastro, A., Dassisti, M., 2020a. Phenomenological modelling of direct laser metal deposition for single tracks. The International Journal of Advanced Manufacturing Technology 111, 1955–1970. https://doi.org/10.1007/s00170-020-06204-x

Mazzarisi, M., Campanelli, S.L., Angelastro, A., Palano, F., Dassisti, M., 2020b. In situ monitoring of direct laser metal deposition of a nickel-based superalloy using infrared thermography. Int J Adv Manuf Technol. https://doi.org/10.1007/s00170-020-06344-0

Mebratu, D., 1998. Sustainability and sustainable development. Environmental Impact Assessment Review 18, 493–520. https://doi.org/10.1016/S0195-9255(98)00019-5

Menzel, R. (Ed.), 2007. Lasers, in: Photonics: Linear and Nonlinear Interactions of Laser Light and Matter. Springer Berlin Heidelberg, Berlin, Heidelberg, pp. 359–531. https://doi.org/10.1007/978-3-540-45158-7_6

Milewski, J.O., Lewis, G.K., Thoma, D.J., Keel, G.I., Nemec, R.B., Reinert, R.A., 1998. Directed light fabrication of a solid metal hemisphere using 5-axis powder deposition. Journal of Materials Processing Technology 75, 165–172. https://doi.org/10.1016/S0924-0136(97)00321-X

Mirkoohi, E., Ning, J., Bocchini, P., Fergani, O., Chiang, K.-N., Liang, S., 2018. Thermal Modeling of Temperature Distribution in Metal Additive Manufacturing Considering Effects of Build Layers, Latent Heat, and Temperature-Sensitivity of Material Properties. Journal of Manufacturing and Materials Processing 2, 63. https://doi.org/10.3390/jmmp2030063

Muthu, S.S., Savalani, M.M. (Eds.), 2016. Handbook of Sustainability in Additive Manufacturing, Environmental Footprints and Eco-design of Products and Processes. Springer Singapore, Singapore. https://doi.org/10.1007/978-981-10-0549-7

Muvvala, G., Patra Karmakar, D., Nath, A.K., 2017. Online monitoring of thermo-cycles and its correlation with microstructure in laser cladding of nickel based super alloy. Optics and Lasers in Engineering 88, 139–152. https://doi.org/10.1016/j.optlaseng.2016.08.005

Nabhani, M., Razavi, R.S., Barekat, M., 2018. An empirical-statistical model for laser cladding of Ti-6Al-4V powder on Ti-6Al-4V substrate. Optics & Laser Technology 100, 265–271. https://doi.org/10.1016/j.optlastec.2017.10.015

Nagarajan, H.P.N., Haapala, K.R., 2018. Characterizing the influence of resource-energy-exergy factors on the environmental performance of additive manufacturing systems. Journal of Manufacturing Systems 48, 87–96. https://doi.org/10.1016/j.jmsy.2018.06.005

Nagarajan, H.P.N., Haapala, K.R., 2017. Environmental Performance Evaluation of Direct Metal Laser Sintering through Exergy Analysis. Procedia Manufacturing 10, 957–967. https://doi.org/10.1016/j.promfg.2017.07.087

Nenadl, O., Kuipers, W., Koelewijn, N., Ocelík, V., De Hosson, J.Th.M., 2016. A versatile model for the prediction of complex geometry in 3D direct laser deposition. Surface and Coatings Technology 307, 292–300. https://doi.org/10.1016/j.surfcoat.2016.08.090

Nowotny, S., Scharek, S., Beyer, E., Richter, K.-H., 2007. Laser Beam Build-Up Welding: Precision in Repair, Surface Cladding, and Direct 3D Metal Deposition. Journal of Thermal Spray Technology 16, 344–348. https://doi.org/10.1007/s11666-007-9028-5

Ocelík, V., de Oliveira, U., de Boer, M., de Hosson, J.Th.M., 2007. Thick Co-based coating on cast iron by side laser cladding: Analysis of processing conditions and coating properties. Surface and Coatings Technology 201, 5875–5883. https://doi.org/10.1016/j.surfcoat.2006.10.044

Ocylok, S., Alexeev, E., Mann, S., Weisheit, A., Wissenbach, K., Kelbassa, I., 2014. Correlations of Melt Pool Geometry and Process Parameters During Laser Metal Deposition by Coaxial Process Monitoring. Physics Procedia 56, 228–238. https://doi.org/10.1016/j.phpro.2014.08.167

Paris, H., Mokhtarian, H., Coatanéa, E., Museau, M., Ituarte, I.F., 2016. Comparative environmental impacts of additive and subtractive manufacturing technologies. CIRP Annals 65, 29–32. https://doi.org/10.1016/j.cirp.2016.04.036

Paul, R., Anand, S., 2012. Process energy analysis and optimization in selective laser sintering. Journal of Manufacturing Systems 31, 429–437. https://doi.org/10.1016/j.jmsy.2012.07.004

Peng, T., Kellens, K., Tang, R., Chen, C., Chen, G., 2018. Sustainability of additive manufacturing: An overview on its energy demand and environmental impact. Additive Manufacturing 21, 694–704. https://doi.org/10.1016/j.addma.2018.04.022

Pinkerton, Andrew J, Li, L., 2004. Modelling the geometry of a moving laser melt pool and deposition track via energy and mass balances. Journal of Physics D: Applied Physics 37, 1885–1895. https://doi.org/10.1088/0022-3727/37/14/003

Pinkerton, Andrew J., Li, L., 2004. The significance of deposition point standoff variations in multiple-layer coaxial laser cladding (coaxial cladding standoff effects). International Journal of Machine Tools and Manufacture 44, 573–584. https://doi.org/10.1016/j.ijmachtools.2004.01.001

Purtonen, T., Kalliosaari, A., Salminen, A., 2014. Monitoring and Adaptive Control of Laser Processes. Physics Procedia 56, 1218–1231. https://doi.org/10.1016/j.phpro.2014.08.038

Quinlan, H.E., Hasan, T., Jaddou, J., Hart, A.J., 2017. Industrial and Consumer Uses of Additive Manufacturing: A Discussion of Capabilities, Trajectories, and Challenges: Industrial and Consumer Uses of Additive Manufacturing. Journal of Industrial Ecology 21, S15–S20. https://doi.org/10.1111/jiec.12609

Rashkovets, M., Mazzarisi, M., Nikulina, A.A., Casalino, G., 2020. Analysis of laser direct stainless steel powder deposition on Ti6Al4V substrate. Materials Letters 274, 128064. https://doi.org/10.1016/j.matlet.2020.128064

Ready, J.F., 1997. Industrial applications of lasers, 2nd ed. ed. Academic Press, San Diego.

Reddy, L., Preston, S.P., Shipway, P.H., Davis, C., Hussain, T., 2018. Process parameter optimisation of laser clad iron based alloy: Predictive models of deposition efficiency, porosity and dilution. Surface and Coatings Technology 349, 198–207. https://doi.org/10.1016/j.surfcoat.2018.05.054

Rejeski, D., Zhao, F., Huang, Y., 2018. Research needs and recommendations on environmental implications of additive manufacturing. Additive Manufacturing 19, 21–28. https://doi.org/10.1016/j.addma.2017.10.019

Renaldi, Kellens, K., Dewulf, W., Duflou, J.R., 2011. Exergy Efficiency Definitions for Manufacturing Processes, in: Hesselbach, J., Herrmann, C. (Eds.), Glocalized Solutions for Sustainability in Manufacturing. Springer Berlin Heidelberg, Berlin, Heidelberg, pp. 329–334. https://doi.org/10.1007/978-3-642-19692-8_57

Ri-sheng, L., Shao-ni, S., Zi-sheng, L., 2016. The influence of scanning methods on the cracking failure of thin-wall metal parts fabricated by laser direct deposition shaping. Engineering Failure Analysis 59, 269–278. https://doi.org/10.1016/j.engfailanal.2015.10.011

Satyanarayana, D.V.V., Eswara Prasad, N., 2017. Nickel-Based Superalloys, in: Prasad, N.E., Wanhill, R.J.H. (Eds.), Aerospace Materials and Material Technologies. Springer Singapore, Singapore, pp. 199–228. https://doi.org/10.1007/978-981-10-2134-3_9

Selicati, V., Cardinale, N., 2020. Benchmarking Sustainability on an Industrial Case Within Industry 4.0 Paradigm: Advantages of Involving Exergetic Analysis in Life Cycle Thinking. TI-IJES 64, 244–250. https://doi.org/10.18280/ti-ijes.642-418

Selicati, V., Cardinale, N., Dassisti, M., 2020. The interoperability of exergy and Life Cycle Thinking in assessing manufacturing sustainability: A review of hybrid approaches. Journal of Cleaner Production 124932. https://doi.org/10.1016/j.jclepro.2020.124932

Shi, T., Lu, B., Shen, T., Zhang, R., Shi, S., Fu, G., 2018. Closed-loop control of variable width deposition in laser metal deposition. The International Journal of Advanced Manufacturing Technology 97, 4167–4178. https://doi.org/10.1007/s00170-018-1895-z

SIEMENS, n.d. SENTRON PAC3200 - Reliable and precise monitoring of electrical power systems [WWW Document]. Datasheet Available at: URL https://www.mc-mc.com/ASSETS/DOCUMENTS/ITEMS/EN/Siemens_93_47ADAPTER_Datasheet.pdf (accessed 3.27.20).

Sireesha, M., Lee, J., Kranthi Kiran, A.S., Babu, V.J., Kee, B.B.T., Ramakrishna, S., 2018. A review on additive manufacturing and its way into the oil and gas industry. RSC Advances 8, 22460–22468. https://doi.org/10.1039/C8RA03194K

Siva Shashidhara Reddy, S., Balasubramaniam, K., Krishnamurthy, C.V., Shankar, M., 2005. Ultrasonic goniometry immersion techniques for the measurement of elastic moduli. Composite Structures 67, 3–17. https://doi.org/10.1016/j.compstruct.2004.01.008

Sobczak, J.J., Drenchev, L., 2013. Metallic Functionally Graded Materials: A Specific Class of Advanced Composites. Journal of Materials Science & Technology 29, 297–316. https://doi.org/10.1016/j.jmst.2013.02.006

Sol, T., Hayun, S., Noiman, D., Tiferet, E., Yeheskel, O., Tevet, O., 2018. Nondestructive ultrasonic evaluation of additively manufactured AlSi10Mg samples. Additive Manufacturing 22, 700–707. https://doi.org/10.1016/j.addma.2018.06.016

Song, B., Yu, T., Jiang, X., Xi, W., 2019. Numerical model of transient convection pattern and forming mechanism of molten pool in laser cladding. Numerical Heat Transfer, Part A: Applications 75, 855–873. https://doi.org/10.1080/10407782.2019.1608777

Spranger, F., Graf, B., Schuch, M., Hilgenberg, K., Rethmeier, M., 2018. Build-up strategies for additive manufacturing of three dimensional Ti-6Al-4V-parts produced by laser metal deposition. Journal of Laser Applications 30, 022001. https://doi.org/10.2351/1.4997852

Steen, W.M., Mazumder, J., 2010. Laser Material Processing. Springer London, London. https://doi.org/10.1007/978-1-84996-062-5

Stephens, B., Azimi, P., El Orch, Z., Ramos, T., 2013. Ultrafine particle emissions from desktop 3D printers. Atmospheric Environment 79, 334–339. https://doi.org/10.1016/j.atmosenv.2013.06.050

Stock, T., Seliger, G., 2016. Opportunities of Sustainable Manufacturing in Industry 4.0. Procedia CIRP 40, 536–541. https://doi.org/10.1016/j.procir.2016.01.129

Sun, G.F., Shen, X.T., Wang, Z.D., Zhan, M.J., Yao, S., Zhou, R., Ni, Z.H., 2019. Laser metal deposition as repair technology for 316L stainless steel: Influence of feeding powder compositions on microstructure and mechanical properties. Optics & Laser Technology 109, 71–83. https://doi.org/10.1016/j.optlastec.2018.07.051

Sun, G.F., Yao, S., Wang, Z.D., Shen, X.T., Yan, Y., Zhou, R., Ni, Z.H., 2018. Microstructure and mechanical properties of HSLA-100 steel repaired by laser metal deposition. Surface and Coatings Technology 351, 198–211. https://doi.org/10.1016/j.surfcoat.2018.07.048

Sun, Y., Hao, M., 2012. Statistical analysis and optimization of process parameters in Ti6Al4V laser cladding using Nd:YAG laser. Optics and Lasers in Engineering 50, 985–995. https://doi.org/10.1016/j.optlaseng.2012.01.018

Szargut, J., Morris, D.R., Steward, F.R., 1987. Exergy analysis of thermal, chemical, and metallurgical processes.

Tabernero, I., Lamikiz, A., Ukar, E., López de Lacalle, L.N., Angulo, C., Urbikain, G., 2010. Numerical simulation and experimental validation of powder flux distribution in coaxial laser cladding. Journal of Materials Processing Technology 210, 2125–2134. https://doi.org/10.1016/j.jmatprotec.2010.07.036

Tan, H., Zhang, F., Wen, R., Chen, J., Huang, W., 2012. Experiment study of powder flow feed behavior of laser solid forming. Optics and Lasers in Engineering 50, 391–398. https://doi.org/10.1016/j.optlaseng.2011.10.017

Tapia, G., Elwany, A., 2014. A Review on Process Monitoring and Control in Metal-Based Additive Manufacturing. Journal of Manufacturing Science and Engineering 136. https://doi.org/10.1115/1.4028540

Tay, S.I., Malaysia, T.H.O., Raja, P., Pahat, B., Hamid, N.A.A., Ahmad, A.N.A., 2018. An Overview of Industry 4.0: Definition, Components, and Government Initiatives. Control Systems 10, 10.

Thompson, M.K., Moroni, G., Vaneker, T., Fadel, G., Campbell, R.I., Gibson, I., Bernard, A., Schulz, J., Graf, P., Ahuja, B., Martina, F., 2016. Design for Additive Manufacturing: Trends, opportunities, considerations, and constraints. CIRP Annals 65, 737–760. https://doi.org/10.1016/j.cirp.2016.05.004

Thompson, S.M., Bian, L., Shamsaei, N., Yadollahi, A., 2015. An overview of Direct Laser Deposition for additive manufacturing; Part I: Transport phenomena, modeling and diagnostics. Additive Manufacturing 8, 36–62. https://doi.org/10.1016/j.addma.2015.07.001

Torims, T., 2013. The Application of Laser Cladding to Mechanical Component Repair, Renovation and Regeneration, in: Katalinic, B., Tekic, Z. (Eds.), DAAAM International Scientific Book. DAAAM International Vienna, pp. 587–608. https://doi.org/10.2507/daaam.scibook.2013.32

Toyserkani, E., Khajepour, A., Corbin, S., 2005. Laser cladding. CRC Press, Boca Raton, Fl.

Vaidya, S., Ambad, P., Bhosle, S., 2018. Industry 4.0 – A Glimpse. Procedia Manufacturing 20, 233–238. https://doi.org/10.1016/j.promfg.2018.02.034

Vandone, A., Baraldo, S., Valente, A., 2018. Multisensor Data Fusion for Additive Manufacturing Process Control. IEEE Robotics and Automation Letters 3, 3279–3284. https://doi.org/10.1109/LRA.2018.2851792

Verdi, D., Múnez, C.J., Garrido, M.A., Poza, P., 2017. Process parameter selection for Inconel 625-Cr3C2 laser cladded coatings. The International Journal of Advanced Manufacturing Technology 92, 3033–3042. https://doi.org/10.1007/s00170-017-0372-4

Wirth, F., Arpagaus, S., Wegener, K., 2018. Analysis of melt pool dynamics in laser cladding and direct metal deposition by automated high-speed camera image evaluation. Additive Manufacturing 21, 369–382. https://doi.org/10.1016/j.addma.2018.03.025

Wittbrodt, B.T., Glover, A.G., Laureto, J., Anzalone, G.C., Oppliger, D., Irwin, J.L., Pearce, J.M., 2013. Life-cycle economic analysis of distributed manufacturing with open-source 3-D printers. Mechatronics 23, 713–726. https://doi.org/10.1016/j.mechatronics.2013.06.002

Wohlers, T., 2014. Wohlers Report 2014: 3D printing and additive manufacturing state of the industry; annual worldwide progress report. Wohlers Associates, Fort Collins, Colo.

Wohlers, T., Campbell, R.I., 2017. Wohlers report 2017: 3D printing and additive manufacturing state of the industry : annual worldwide progress report.

Wolf, M., 2016. Improving the Efficiency of the DMLD Process: How particle size and laser spot size influence process quality and efficiency. Laser Technik Journal 13, 32–34. https://doi.org/10.1002/latj.201600028

Wolff, S.J., Gan, Z., Lin, S., Bennett, J.L., Yan, W., Hyatt, G., Ehmann, K.F., Wagner, G.J., Liu, W.K., Cao, J., 2019. Experimentally validated predictions of thermal history and microhardness in laser-deposited Inconel 718 on carbon steel. Additive Manufacturing 27, 540–551. https://doi.org/10.1016/j.addma.2019.03.019

Xi, W., Song, B., Zhao, Y., Yu, T., Wang, J., 2019. Geometry and dilution rate analysis and prediction of laser cladding. The International Journal of Advanced Manufacturing Technology 103, 4695–4702. https://doi.org/10.1007/s00170-019-03932-7

Yang, Q., Yuan, Z., Zhi, X., Yan, Z., Tian, H., Chen, X., 2020. Real-time width control of molten pool in laser engineered net shaping based on dual-color image. Optics & Laser Technology 123, 105925. https://doi.org/10.1016/j.optlastec.2019.105925

Yosofi, M., Kerbrat, O., Mognol, P., 2018. Energy and material flow modelling of additive manufacturing processes. Virtual and Physical Prototyping 13, 83–96. https://doi.org/10.1080/17452759.2017.1418900

Yu, J., Lin, X., Ma, L., Wang, J., Fu, X., Chen, J., Huang, W., 2011. Influence of laser deposition patterns on part distortion, interior quality and mechanical properties by laser solid forming (LSF). Materials Science and Engineering: A 528, 1094–1104. https://doi.org/10.1016/j.msea.2010.09.078

Yu, T., Yang, L., Zhao, Y., Sun, J., Li, B., 2018. Experimental research and multi-response multi-parameter optimization of laser cladding Fe313. Optics & Laser Technology 108, 321–332. https://doi.org/10.1016/j.optlastec.2018.06.030

Yuan, K., Guo, W., Li, P., Wang, J., Su, Y., Lin, X., Li, Y., 2018. Influence of process parameters and heat treatments on the microstructures and dynamic mechanical behaviors of Inconel 718 superalloy manufactured by laser metal deposition. Materials Science and Engineering: A 721, 215–225. https://doi.org/10.1016/j.msea.2018.02.014

Zhan, X., Meng, Y., Zhou, J., Qi, C., Zhang, C., Gu, D., 2018. Quantitative research on microstructure and thermal physical mechanism in laser melting deposition for Invar alloy. Journal of Manufacturing Processes 31, 221–231. https://doi.org/10.1016/j.jmapro.2017.11.018

Zhang, K., Liu, W., Shang, X., 2007. Research on the processing experiments of laser metal deposition shaping. Optics & Laser Technology 39, 549–557. https://doi.org/10.1016/j.optlastec.2005.10.009

Zhang, X., Li, W., Cui, W., Liou, F., 2018. Modeling of worn surface geometry for engine blade repair using Laser-aided Direct Metal Deposition process. Manufacturing Letters 15, 1–4. https://doi.org/10.1016/j.mfglet.2017.11.001

Zhang, Y., Guo, G., Li, F., Wang, G., Wei, H., 2017. The interface control of butt joints in laser braze welding of aluminium-steel with coaxial powder feeding. Journal of Materials Processing Technology 246, 313–320. https://doi.org/10.1016/j.jmatprotec.2017.03.020

Zhang, Z., Ge, P., Yao, X.X., Li, T., Liu, W.W., 2020. Numerical studies of residual states and scaling effects in laser-directed energy deposition additive manufacturing. The International Journal of Advanced Manufacturing Technology 108, 1233–1247. https://doi.org/10.1007/s00170-020-05300-2

Zhu, G., Li, D., Zhang, A., Pi, G., Tang, Y., 2012. The influence of laser and powder defocusing characteristics on the surface quality in laser direct metal deposition. Optics & Laser Technology 44, 349–356. https://doi.org/10.1016/j.optlastec.2011.07.013

Zobler, M., Mantwill, E., 2018. Cooling Solutions for Laser Applications: Why a tailor-made chiller supports the optimal performance of the laser and reduces energy costs. Laser Technik Journal 15, 50–55. https://doi.org/10.1002/latj.201800020